Magnetic Particle Imaging (MPI) Tracers for In Vivo Applications

Hamed Arami

A dissertation
submitted in partial fulfillment of the
requirements for the degree of

Doctor of Philosophy

University of Washington

2015

Committee:
Kannan M. Krishnan, Chair
Christine K. Luscombe
Denny Liggitt
Buddy Ratner, GSR

Programs Authorized to Offer Degree:
Materials Science & Engineering
&
Nanotechnology and Molecular Engineering

University of Washington

Abstract

Magnetic Particle Imaging (MPI) Tracers for In Vivo Applications

Hamed Arami

Chair of the Supervisory Committee:
Professor Kannan M. Krishnan
Materials Science & Engineering

Magnetic particle imaging (MPI) is a real-time, quantitative and clinically safe imaging technique, potentially applicable for future clinical applications such as cancer imaging, cardiovascular imaging or stem cell labeling and tracking. MPI performance (i.e. spatial resolution and sensitivity) is highly dependent on nanoparticles (NPs) size distribution, magnetization and environment. Therefore, NPs MPI signal is different after distribution into tissues or binding to the cells. In this project, we evaluated the potential capabilities of MPI for tissue targeted imaging applications such as cancer imaging. To do this, we used two preliminary experimental models to predict the performance of the tracers in a tissue equivalent environment and an acidic lysosome-like solution. For efficient targeting and specific binding of the NPs to specific cells (e.g. cancers), it is required to conjugate additional biomolecules that can be recognized by receptors on the membranes of these cells. Therefore, we introduced functional groups (such as amine, carboxyl and maleimide groups) to the surface of our optimized MPI tracers and used them for bonding of a brain cancer targeting peptide (lactoferrin) to the NPs and evaluated the targeting

efficacy of these MPI tracers using an in vivo glioma xenograft model. We also conjugated Cy5.5 near infra-red fluorescent (NIRF) molecules to these functional groups and evaluated NPs performance as multimodal MPI tracers. This additional modality enabled us to study the biodistribution and pharmacokinetics of our optimized MPI tracers more accurately, since NIRF revealed more details of microstructural distribution of the NPs in different organs. In addition, we investigated the pharmacokinetics and biodistribution of the intravenously injected NPs and evaluated MPI performance of the NPs after their accumulation in reticuloendothelial system (RES) organs (e.g. liver and spleen), and glioma xenografts.

TABLE OF CONTENTS

Dedication

To My Family

Acknowledgments

I would like to thank my advisor, Professor Kannan Krishnan for all his kind supports during my PhD studies. Without his great inspirations, encouragements and directions, it was impossible to complete this thesis. I also want to thank my committee members, Prof. Denny Liggitt (UW, Department of Comparative Medicine), Prof. Christine Luscombe (UW, MSE Dept.) and Prof. Buddy Ratner (UW, Bioengineering) for their time and insight, which helped to make this work complete.

I also thank our collaborators, Prof. Steven Conolly and Dr. Patrick Goodwill (Bioengineering, UC Berkeley), Prof. Urs Hafeli and Dr. Kathayoun Saatchi (Faculty of Pharmaceutical Science, University of British Columbia) and Prof. Jeff Bulte (Dept. of Radiology, Johns Hopkins University). I would also like to acknowledge the great trainings for animal handling and experiments provided by UW, Department of Comparative Medicine. I would like to thank UW Medicine South Lake Union for facilitating histology and MRI studies, UW Molecular Engineering and Science (MolEs) center for TEM analyses and Fred Hutchinson Cancer Research Center for providing near infra-red tissue imaging tools and equipment.

My group colleagues have also given me tremendous help in the past sevral years. I want to express the same gratitude to many current and former group members, especially Dr. Matthew Ferguson, Dr. Amit Khandhar, Dr. Asahi Tomitaka, Dr. Sonu Gandhi, Dr. Scott Kemp, Dr. Saqlain A. Shah, Dr. Wei Zhang, Dr. Youfeng Hou, Dr. Zheng Li, Eric Teeman, Haydin Bradshaw, Alyssa Troska, Ryan Hufschmid, Olivia Lenz, Zheng Li, Byung Kwon, Mark Brunson and Hillary Kaufman for their helpful suggestions and technical assistances. Finally, I really appreciate my family's supports during these years.

Chapter 1.

INTRODUCTION

Magnetic particle imaging is a quantitative tomographic imaging technique for visualizing magnetic nanoparticle tracers in a wide range of potential diagnostic and therapeutic applications, such as cardiovascular imaging and early cancer detection. When MPI tracers are in blood circulation, their magnetic response to applied magnetic field can be used for construction of images, revealing their flow in the blood vessels. As we will show in this thesis (Chapters 2, 3 and 4), biocompatible iron oxide nanoparticles are the only type of tracers being developed for MPI. Therefore, MPI can be used as an alternative, but clinically safer method for computed tomography (CT), because CT is based on using iodinated contrast agents that are not safe for patients with chronic kidney disease (CKD). When MPI tracers are accumulated in targeted tissues such as cancers or heart lesions, they can be used to visualize these tissues for various diagnosis purposes. Similarly, using iron oxide nanoparticles as MPI tracers will facilitate translation of this technique to the clinics as a safer method compared with positron emission tomography (PET) and magnetic resonance imaging (MRI), which respectively use radionuclides and gadolinium based contrast agents for imaging. In this chapter, we discuss the basic concepts of MPI for image generation along with physiochemical properties of iron oxide nanoparticles as its contrast agents.

1.1. Magnetic Particle Imaging (MPI)

Theoretical models of MPI pedict a mass sensitivity of the order of nanograms (Fe) and a spatial resolution of 0.2-0.5mm (assuming magnetite nanoparticle tracers of optimum size (23-27nm) and field gradient of about 3 $T\mu_0^{-1}m^{-1}$), making it a promising tool for full-body imaging, in comparison with other techniques such as PET and MRI.[1, 2] High sensitivity and contrast are promising for cancer imaging; for example, direct imaging of the intra-tumor distribution of therapeutic magnetic NPs to

verify if they are distributed in the layers around the tumor cortex rather than the desired accumulation in the core for effective theranostic application.[3] Also, linearity of the signals and higher tracer sensitivity without any interfering background signal makes MPI a potentially non-invasive technique for cellular imaging applications such as *in vivo* stem cell tracking.[4, 5]

The first animal MPI image obtained from the blood flow in mouse heart is shown in Fig. 1.1. Here, the NPs (Resovist^{TM}) were injected through mouse tail vein and NPs flowing through the heart was recorded after about 8 seconds. Also, recently reported MPI images of a rat 2 hours after injection of the monodisperse nanoparticles are shown in Fig. 1.2. As it can be seen in the images, MPI features depth independent signal and outstanding contrast, since signal is generated solely by magnetic nanoparticles and there is no interfering signal from diamagnetic tissues surrounding the nanoparticles.[6, 7] Also, MPI can provide real-time positive-contrast images of the nanoparticles uptake by various organs.[6] Such characteristics make MPI a suitable technique with higher tracer localization accuracy, specially when compared with other methods such as MRI and fluorescent imaging. In MRI, surrounding tissues generate a background signal due to their unavoidable relaxivity. Background signals in fluorescent imaging is also usually generated due to auto-fluorescence of the surrounding tissues.

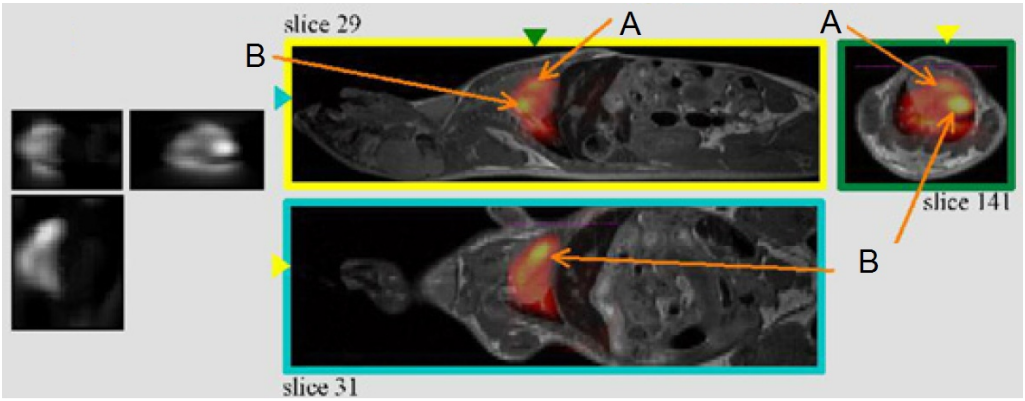

Fig. 1.1. Cardiovascular MPI image of the blood flow in mouse heart fused with MRI images. Adapted from [6].

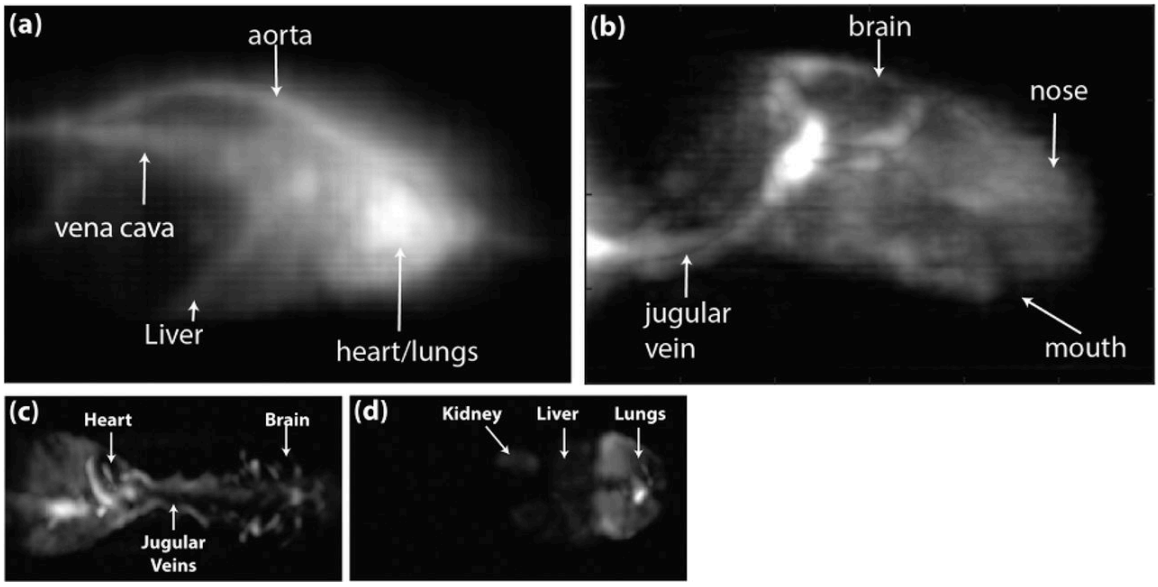

Fig. 1.2. MPI images generated 2 hours after injection of highly monodisperse iron oxide nanoparticles into an anesthetized Fisher 344 rat. Parts (a) and (b) show the saggital images of the abdominal and thorax (part of the body between neck and diaphragm) regions and anterior (head and neck), [Field of view (FOV): 6 cm × 4 cm; Scan time 20 min]. Parts (c) and (d) show the coronal images of a sacrificed rat [FOV: 11 cm × 4.5 cm × 3.75 cm, Scan time: 10 min]. Note that the jugular vein and heart are brighter due to presence of nanoparticles in blood. Also, the signal blushing was correlated to the nanoparticles present in the blood pool.[8]

Note that even though these theoretically predicted values for spatial resolution and spatial resolution mentioned earlier, were reported more than a decade ago by MPI inventors at Philips,[1] there are still challenges to achieve highest quality MPI images, specially in biological environments such as blood and tissues. This is due to the fact that the most important effect of the magnetic relaxation mechanism and possibly magnetic interaction of the nanoparticles during MPI measurements were not considered in the first experimental analyses. As we will show later in Chapters 3, the magnetic relaxation of the nanoparticles and therefore their MPI performance is highly dependent on their core size (median size and monodispersity) and environment. Therefore, the MPI signals (i.e. spatial resolution and signal intensity) are different after nanoparticles internalization into cells or tissues. In addition, the MPI instrumentation is still under development to find the

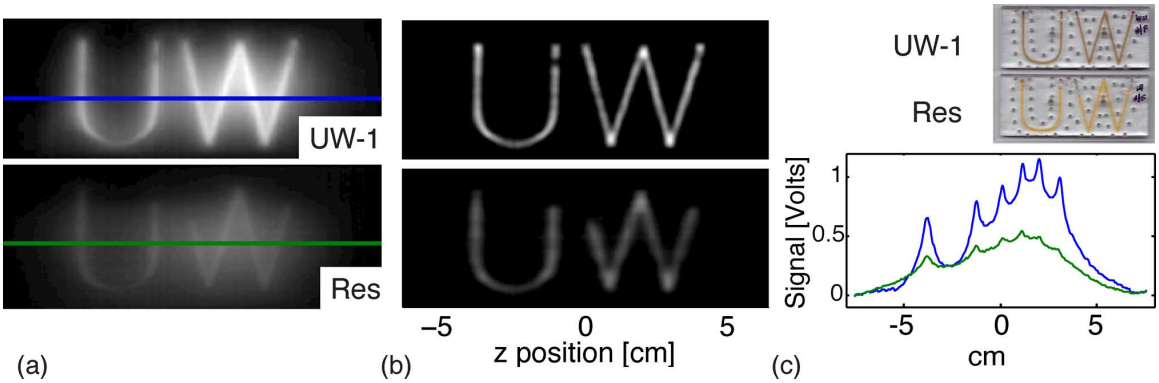

Fig. 1.3. Phantom images generated by highly monodisperse iron oxide nanoparticles with a median core size of about 23-27nm (shown as UW-1), compared with Resovist (Res), at the same iron concentrations. The images show improved signal intensity and spatial resolution when optimized nanoparticles were used for imaging. The channels in the phantoms were 1.5mm wide and 1.5mm deep.[9]

optimal nanoparticles excitation parameters (e.g. magnetic field frequencies and amplitudes) for each application. Such MPI scanner optimizations should be done using highly monodisperse types of tracers with a median core size of 23-27nm, synthesized by thermal decomposition and optimized for MPI (Appendix A). However, unfortunately, most of the MPI optimization studies have been done using a commercially available tracer (Resovist), which is formed from non-uniform clusters of iron oxide nanoparticles, as the magnetic core, coated with a dextran polysaccharide layer. Resovist was originally synthesized as a MRI contrast agent and is not optimal for MPI. In addition, its short blood half-life limits its application for biomedical purposes.[10] A comparison between MPI images of a phantom filled with Resovist and highly monodispersed nanoparticles with a median core size of 23-27nm, prepared in our laboratory is shown in Fig. 1.3.

Generally, in MPI, time-dependent magnetization of the nanoparticles (NPs) caused by an alternating magnetic field (typically in the range of 3-25kHz) induces a voltage in a receiver coil.[1, 2] This signal is proportional to dm/dt, in which m is the NPs magnetic moment. Later in Chapter 3 and Appendix A, we will show that this parameter is highly dependent on nanoparticles size and monodispersity. Furthermore, it is the non-linear magnetization of superparamagnetic NPs that enables signal localization and makes MPI possible. Note that MPI signal intensity is changing linearly with

concentration of the NPs, but it varies non-linearly with field (see Chapter 3). A gradient field is applied which features a field-free point (FFP), or a field free line (FFL),[11] and to form an image, the FFP is scanned across the sample; NPs located at the FFP experience a rapid change in magnetization as the FFP passes and generate signal, while NPs spatially removed from the FFP have saturated magnetization, and therefore experience no change in magnetization and thus generate no signal (Fig. 1.4).[7]

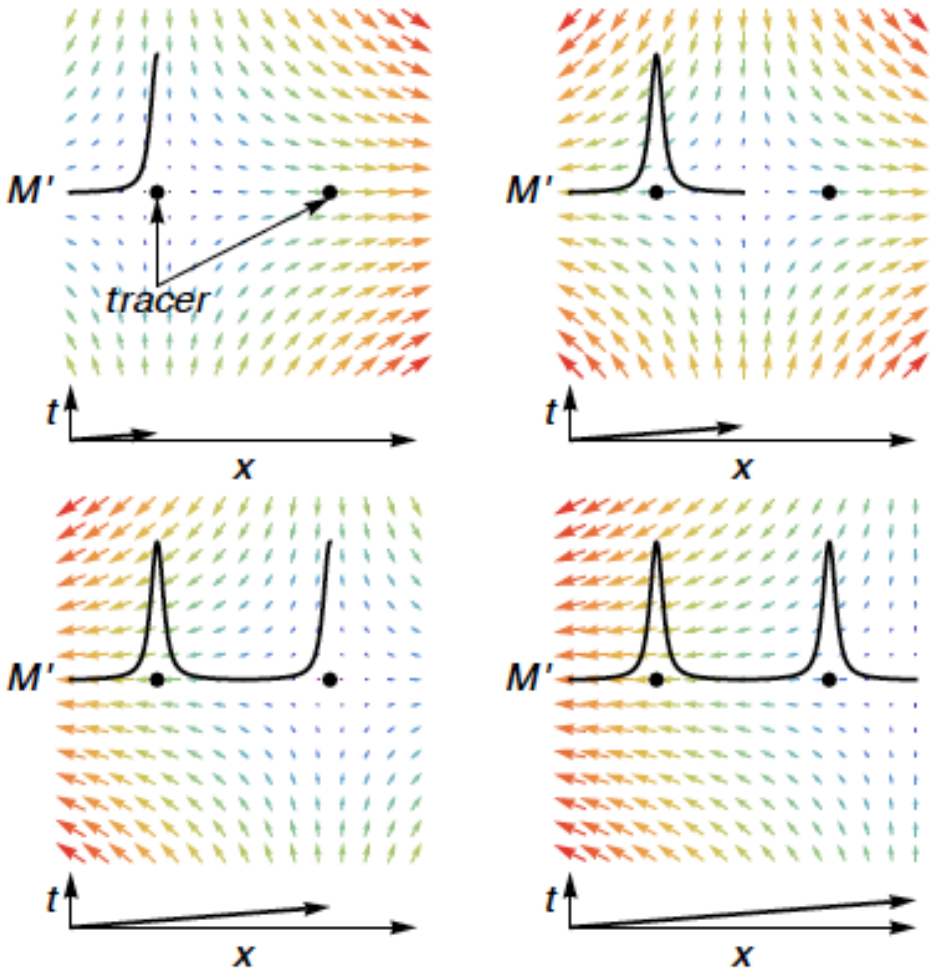

Fig. 1.4. Schematic showing the signal localization mechanism in MPI. A gradient field, featuring a field free point (FFP) or field free line (FFL) surrounded by non-zero fields is scanned across an imaging volume (voxel). When this FFP (or FFL) reaches a nanoparticle or a point source (shown here by black dots), it generates a signal originated from the nanoparticles magnetic relaxation.[12]

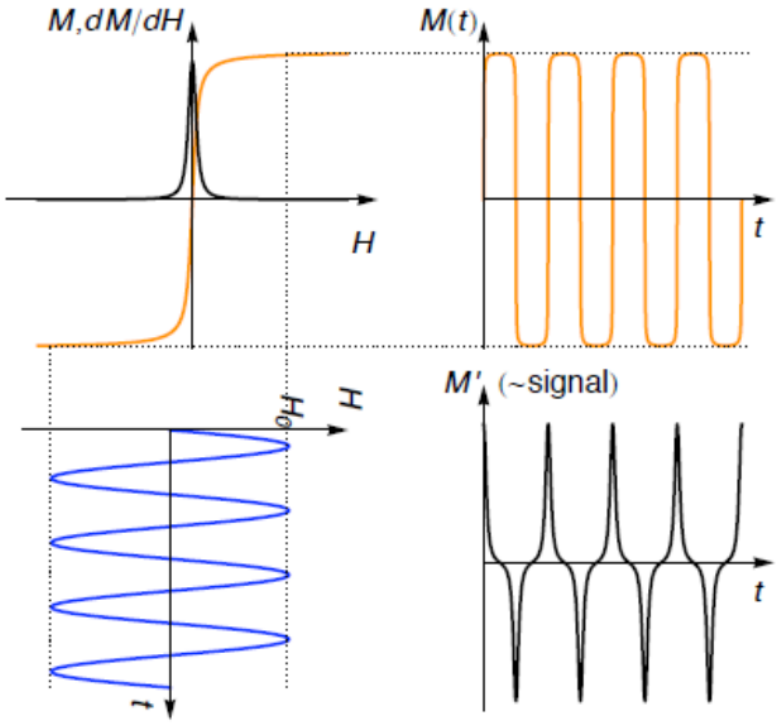

Fig. 1.5. Nonlinear magnetization of the tracers in the presence of an AC magnetic field generates a time-dependent signal, dm/dt, which is proportional to the rate of variation of the magnetization with field, dm/dH.[12] We use this dm/dH as the basis for evaluation of the resolution and sensitivity levels of our NPs as MPI tracers.

Based upon this simple principle, two approaches for MPI image reconstruction have been developed: *system matrix* and *x-space*. In *system matrix* reconstruction, the signal's higher-order harmonic content can be distinguished from the applied AC field using Fourier analysis.[1, 13, 14] In the *x-space* reconstruction, which is the approach used for most of the discussions related to MPI data in this thesis, an image is formed by relating signal intensity to FFP location at all points within the imaging volume.[11, 15, 16] As shown in Fig. 1.5, in *x-space* MPI, the Point Spread Function (PSF) is a product of the derivative of the magnetization, dm/dH, which is purely a property of the tracer, and the instrument-dependent field gradient, dH/dx, in which x is the distance.[10, 17] We emphasize that the principles of tracer optimization are the same for both reconstruction approaches, which are simply linked by the Fourier transform. The time-

rate of change of tracer magnetization should be maximized for a given alternating applied field. Relevant to *system matrix* reconstruction the number of measurable harmonics and their relative intensity will thus both be maximized. Relevant for *x*-space reconstruction, the dm/dH height is maximized for sensitivity and its full width at half maximum (FHWM) is minimized for spatial resolution.[18] In our lab, we use a home-built Magnetic Particle Spectormetery (MPS) to determine the dm/dH response of the NPs and use it to predict the spatial resolution and signal intensity that can be generated in a MPI scanner. MPS is now an established method for rapid screening of NPs to determine their suitability for MPI.[16, 19, 20] In the next parts of this thesis, we will discuss NPs characteristics required for efficient magnetic particle imaging.

1.2. MPI tracers

In spite of all the advantages highlighted above, in practice it remains a challenge to optimize MPI tracers for maximum resolution and signal intensity. Superparamagnetic iron oxide is the most favorable tracer for MPI, due to its biocompatibility and adequate magnetic properties,[21] with several formulations of superparamagnetic iron oxides having already been approved by the FDA for clinical applications such as MRI or iron delivery in anemia.[22-25] However, iron oxide NPs prepared for MPI should be designed delicately to have the highest size monodispersity and lowest magnetic anisotropy, in order to provide highest spatial resolution and signal intensity during applications [13, 21] within the constraints of limits set by peripheral nerve stimulation and specific absorption.[15]

Superparamagnetic behavior of the NPs is the key characteristic of the tracers in MPI and iron oxide with the crystallographic structure of magnetite (Fe_3O_4) has been reported as the best candidate for this application. Magnetite has both divalent (Fe^{2+}) and trivalent (Fe^{3+}) iron ions in an inverse spinel lattice structure, in which 32 oxygen ions make a face centered cubic (FCC), and eight Fe^{3+} and eight Fe^{2+} ions occupy the tetrahedral sites and eight additional Fe^{3+} sit on octahedral sites, as shown in Figs. 1.6 and 1.7. Bulk magnetite is a ferrimagnetic material, and its magnetic hysteresis is similar to

ferromagnetic materials, with remnant magnetization and coercively. As shown in Fig. 1.7, 16 octahedral sites of magnetite unit cell are occupied by 8 Fe^{3+} ions (S=2, magnetic moments $\mu \approx 4\mu_B$, spheres with down arrows) and 8 Fe^{2+} ions (S=5/2, $\mu \approx 5\mu_B$, spheres

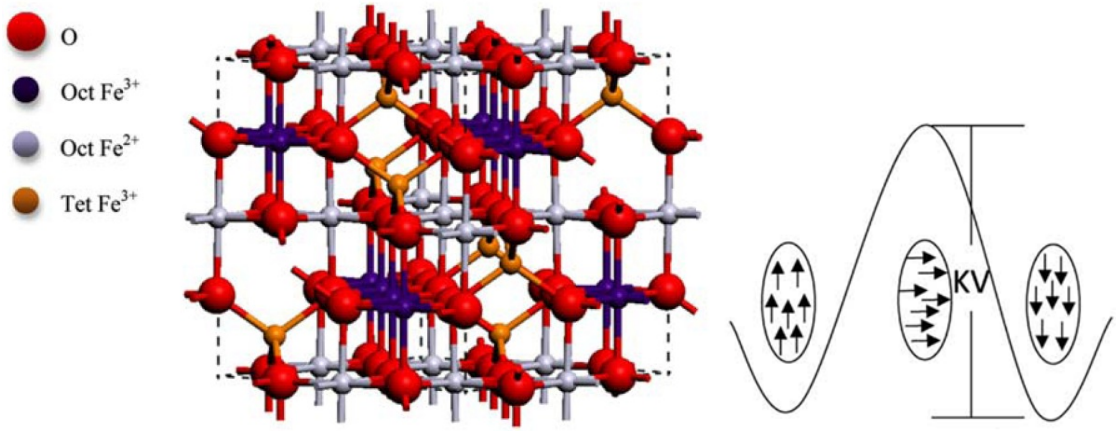

Fig. 1.6. Crystal structure of the magnetite (left) and criterion needed for superparamagnetism (right).[21]

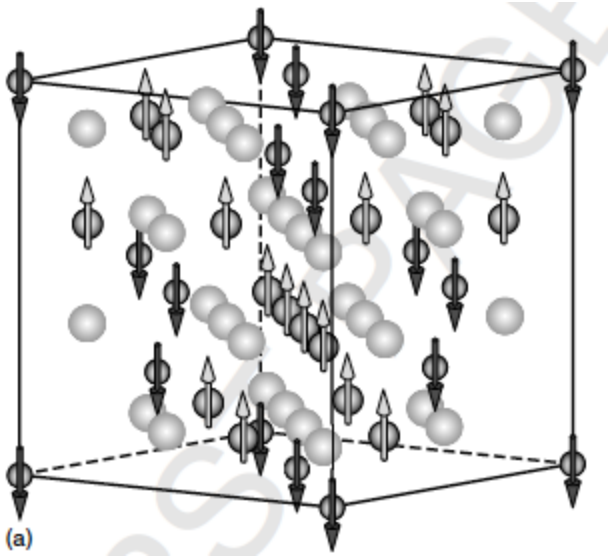

Fig. 1.7. Spin lattice structure showing the origin of ferrimagnetic behavior in magnetite (Fe_3O_4). Magnetite unit cell contains, 32 oxygen anions (O^{2-}, shown here by larger and brighter spheres) and 24 iron cations (Fe^{2+} and Fe^{3+}, shown here by smaller and darker spheres).[26]

with up arrows). In addition, there are 8 other co-aligned Fe^{3+} ions (again S=2, $\mu \approx 4\mu_B$, spheres with down arrows) in the unit cells, occupying the tetrahedral cites. Such atomic arrangement results in a net ferrimagnetic moment of 4μB per unit cell in magnetite. However, considering a single domain particle, and a measurement time of about 100s (used in routine magnetic measurement techniques such as a vibrating sample magnetometer or VSM used in this thesis), with decreasing the size below a critical value of about 27nm, the magnetic properties of this material changes to superparamagnetic.[27]

Superparamagnetic magnetite has a closed magnetization loop, and follows the Langevine function for magnetization. The NPs are very small and therefore their magnetic anisotropy energy, KV (K: magnetic anisotropy energy per unit volume; V: NP volume) is smaller than the available thermal energy barrier, K_BT, (K_B: Boltzman's constant and T: temperature) for rotating between easy magnetization axes (Fig. 1.6). Therefore, they show spontaneous reversal of the magnetic moments with zero net magnetization, even in the absence of an external field.[21] Later in section 3.1, we will discuss the details of these reversal mechanisms in correlation with the amplitudes and frequency of the applied magnetic fields in MPI systems.

In this thesis, we first review general NPs physiochemical properties required for any diagnostic and therapeutic application, including MPI, in Chapter 2. Also, we present strategies for synthesis and phase transfer of highly monodisperse iron oxide core nanoparticles with optimum size range and crystalline structure (Chapter 3 and Appendix A). As it will be discussed later, tuning the size and phase purity of iron oxide nanoparticles can significantly improve the MPI signal intensity and spatial resolution (Appendix A and Chapter 5). We also report strategies for phase transfer of the NPs to aqueous media and their surface functionalization in Chapters 3-5, based on the desired applications. We show that using a proper phase transfer approach by coating the nanoparticles with specific polymers, such as polyethylene glycol (PEG) and its derivatives or co-polymers, can significantly improve the stability, blood circulation half-life and targeting efficiency of the NPs during *in vivo* applications (Chapter 4). Also, we

discuss how various surface functionalization approaches, such as functionalization of the NPs with amine groups or maleimide groups enable us to conjugate various types of molecules (e.g. fluorescent tags and targeting peptides) to the NPs for multimodal imaging and targeting purposes. Finally, in Chapter 5, we evaluate MPI for targeted imaging of cancers using athymic nude mice with glioma (brain tumor) xenografts generated in them by subcutaneous injection of the C6 brain cancer cells.

Chapter 2.

IN VIVO DELIVERY, PHARMACOKINETICS, BIODISTRIBUTION AND TOXICITY OF IRON OXIDE NANOPARTICLES

As discussed earlier in Chapter 1, iron oxide nanoparticles (IONPs) are the only type of tracers that have been used for MPI, due to their long-term successful history in various biomedical applications. In fact, IONPs are the only type of magnetic nanoparticles approved by US Food and Drug Administration (FDA). IONPs have been extensively used during the last two decades, either as effective bio-imaging contrast agents or as carriers of biomolecules such as drugs, nucleic acids and peptides for controlled delivery to specific organs and tissues. Most of these novel applications (including MPI) require elaborate tuning of the physiochemical and surface properties of the IONPs. As new IONPs designs are envisioned, synergistic consideration of the body's innate biological barriers against the administered nanoparticles and the short and long-term side effects of the IONPs become even more essential.

There are several important criteria (*e.g*. size and size-distribution, charge, coating molecules, and plasma protein adsorption) that can be effectively tuned to control the *in vivo* pharmacokinetics and biodistribution of the IONPs. These important parameters, also define the performance of the tracers in different kinds of MPI applications. In this chapter, we review the crucial IONPs parameters, in light of biological barriers in the body, and the latest IONPs design strategies used to overcome them. These strategies should be carefully considered for design of the effective MPI tracers and their potential translation to the clinics. For example, blood half-life of the nanoparticles, which is one of the most critical factors in MPI cardiovascular and cancer imaging (since longer circulation time increases the chance of nanoparticles uptake by tumors), is highly dependent on their size and surface charge (Chapter 5). We will show in Chapter 4, that choosing a proper functionalization method can increase the blood circulation time of

MPI tracers in mice, by decreasing their hydrodynamic size. We will also discuss the size dependent performance of the MPI tracers in tissue-equivalent environments (Chapter 3).

A careful review of the long-term biodistribution and side effects of the IONPs in relation to nanoparticle design has to be considered for proper design and screening of the efficient MPI tracers. This is specially important for evaluation of IONPs with larger core sizes (~23-27nm), which have shown significant improvements in MPI spatial resolution and signal intensity, due to their size-dependent higher saturation magnetizations (Appendix A). Finally, while the discussions presented in this chapter are specific to IONPs, some of the information can be readily applied to other nanoparticle systems, such as gold, silver, silica, calcium phosphates and various polymers.

2.1. Introduction

Superparamagnetic iron oxide (γ-Fe_2O_3 and Fe_3O_4) nanoparticles (IONPs) are biocompatible, biodegradable, and non-toxic, and have been used for a wide range of biomedical applications such as tumors or vascular imaging,[21, 28, 29] drug delivery,[22] gene therapy,[30] *in vivo* tracking of labeled cells,[5] magnetic separation of cells or molecules,[31] or as an iron supplement for patients with anemia.[32] Immediately after their administration *in vivo*, a host of innate immunological mechanisms start to recognize and collect these foreign particles and direct them to the major elimination pathways of the body.[33] Therefore, there is always a competition between the desired distributions of the IONPs in specific organs and their highly active clearance mechanisms.[34] The amount and distribution pattern of the IONPs in different organs and tissues, during or after any clinical diagnostic or therapeutic application (ranging from several minutes to several years, depending on the application), is generally considered as biodistribution and the rate of their recognition and removal by the immune system, metabolism and excretion from the body is usually referred to as pharmacokinetics. Knowing these two parameters is crucial to enhance the expected functionality of the IONPs in any selected region or organ of the body, and to minimize

their toxicological side effects due to any undesirable biodistribution or pharmacokinetic behavior.[35]

Recent progress in synthesis, characterization and most importantly, surface functionality of the IONPs have enabled researchers to improve these two important parameters and answer some important questions related to their clinical applications.[36] It is well known that whilst the size of the iron oxide crystals determines the magnetic properties of IONPs, the additional molecules on their surface act as the main interface between the IONPs and the body's immune system.[21] Therefore, depending on how the IONPs were synthesized, their surface chemistry, the desired application and administration methods, the expected pharmacokinetic and biodistribution behavior of the IONPs may be different.[37]

Iron oxide nanoparticles are prepared by two major chemical methods. Co-precipitation of Fe^{2+} (ferrous) and Fe^{3+} (ferric) ions in an alkaline solution is a well-established conventional IONPs synthesis method.[38] Further, these IONPs can be coated *in situ* with different types of polymers (*e.g.* dextran,[39] chitosan[22] and starch[40]) by the synthesis of the IONPs in the presence of these molecules in solution. These types of IONPs have been extensively investigated during the last two decades and have been successfully translated to the clinic.[41] While the method can be easily scaled up for mass production of the IONPs, it is difficult to obtain uniform iron oxide core sizes with narrow size distributions and controlled magnetic properties using such aqueous co-precipitation methods.[22] Alternatively, thermal decomposition of organic complexes of iron (*e.g.* iron pentacarbonyl, iron oleate or FeOOH) in the presence of capping agents (*e.g.* oleic acid and oleyl amine), results in excellent control of size, shape and monodispersity of the IONPs, and the desired magnetic properties.[10, 42-44] We have developed highly standard procedures for repeatable and large-scale synthesis of these types of nanoparticles,[45] by significant modification of previously reported methods.[46-48] The main drawback of this approach is the hydrophobicity of the synthesized IONPs, which requires elaborate, multi-step surface modifications to transfer them to aqueous media and improve their bio-functionality.[22, 36]

This chapter provides a comprehensive review of the *in vivo* biological barriers encountered by IONPs. Furthermore, parameters that play key roles in the clearance pathways, body distribution and ultimate fate of IONPs are discussed. We will show that synergistic consideration of all these parameters is required in order to develop standard criteria for tuning the pharmacokinetics and biodistribution of the IONPs for a specific clinical application. If this information is carefully considered in future studies, it will help decrease costs associated with clinical trials and potentially reduce the number of animal studies by avoiding unnecessary experiments. Also, it can expedite the clinical translation of the IONPs to various imaging or therapeutic applications (*e.g.* early diagnosis and treatment of cancers, heart and brain plaques and lesions and efficient regenerative tissue engineering). Additionally, pharmacokinetics, biodistribution and clearance pathway of the IONPs administrated through various *in vivo* routes such as intravenous and retro-orbital injection, intrapulmonary or oral delivery, will be discussed along with their physiological limitations and the IONPs properties required for each one of them. Note that, even though we only show MPI applications for intravenously injected IONPs in this thesis, MPI can be potentially used for various other applications such as imaging of the respiration system and gastro-intenstinal (GI) pathway (similar to MRI). Also, retro-orbital injection of the IONPs has been used for some cancer imaging applications. Therefore, here, we briefly review their relevant biodistribution and clearance mechanisms for future references. Recent progress in successful clinical applications of IONPs and any reported side-effects on humans will be also discussed in detail.

2.2. IONPs pharmacokinetics

Depending on the desired biomedical application, iron oxide nanoparticles have been mostly administrated through intravenous injection (IV), oral delivery or intranasal (inhalation) pathway (also see section 2.2.2). Regardless of the biological barriers (*e.g.* acidic gastric pH and the general stability of the IONPs) specific to each administration method, the body's immune system responds quickly to the presence of IONPs, trying to

eliminate them through phagocytic, metabolic and degradative processes in immune cells (*i.e*. circulating white blood cells such as monocytes and residential tissue macrophages, discussed in section 2.2.1.2). Based on previous reports, summarized in this chapter, tissue (*e.g.* liver and spleen) macrophages are the most critical cells in the elimination of IONPs from the blood circulation. In this section, we describe the pharmacokinetic performance and the desired characteristics of the IONPs for each administration method.

2.2.1. Intravenously injected IONPs

Intravenous injection is the most commonly used approach for administration of IONPs. It is the only administration method used for MPI up to now. Fortunately, this method has been extensively used for MRI applications. Therefore, a review of MRI related literature helps to estimate biodistribution, pharmacokinetics and clearance mechanisms of the MPI tracers. Basic characteristics of some of the IONPs that are approved for clinical use as intravenously injected contrast agents for MRI are shown in Table 2.1. In the 1990's, ultrasmall superparamagnetic iron oxide (USPIO) nanoparticles were developed for diagnostic and therapeutic clinical applications of MRI by Weissleder *et al.*[49] and other research groups,[50] with the most commonly used ones being AMI-227 (Sinerem® by Guerbet, and Combidex® by Advanced Magnetics, also called as monocrystalline iron oxide nanoparticle or MION[50, 51]), SHU55C (Schering AG) and NC100150 (Clariscan, Nycomed). Compared to the first generation of IONPs with hydrodynamic size, d_H ~ 150nm, USPIOs were smaller (d_H ~20-30nm) and showed a longer blood circulation time (*e.g*. 4h 30min in rats).[52, 53] This enabled the use of USPIOs extensively as blood pool MRI contrast agents. Later, cross-linked iron oxide (CLIO) nanoparticles were prepared to prevent the detachment of the dextran coating because of its weak bonding with hydroxyl groups on the surface of the IONPs.[54] In contrast to USPIOs, CLIO series of IONPs had several iron oxide crystallites as their core.[53, 54] This group of IONPs has also been widely investigated for different types of biomedical imaging applications. Considering these MRI studies are important since Resovist, one of the commonly used MPI tracers, is synthesized by using a similar

approach (note that Resovist was originally synthesized as a MRI contrast agent). Generally, for each MPI application, it is important to know the blood circulation time of the injected IONPs (*i.e.*, the time between injection and elimination from the blood) and utilize this data to tune the IONPs characteristics based on the desired circulation time for that specific application.

2.2.1.1. Blood half-life

Blood or plasma half-life ($t_{1/2}$) of the NPs is the time it takes for the concentration of the injected NPs in the blood to decrease to half its initial value and is a helpful measure to monitor the pharmacokinetics of the NPs. This decrease in concentration is due to the elimination of the NPs through various organs (details to be discussed in the next sections of this chapter). For magnetic nanoparticles (*i.e.* IONPs) the half-life can also be defined as the time in which the magnetic signal intensity generated from the blood (e.g. MRI T_2 or T_1 relaxation rates of the blood) reduces to half its initial value immediately (ranging from second to several minutes, depending on the measurements technique) after the injection of the NPs.[55, 56] Assuming a one-compartment pharmacokinetic model for IONPs, *i.e.* they do not disintegrate after injection and their distribution in blood after injection remains uniform, the decrease in concentration often follows a mono-exponential decay function (equation 1). A simple fitting of the data (e.g. IONPs concentrations or changes in MRI contrast or fluorescent signal intensity of the blood samples) to this equation is used to calculate half-life ($t_{1/2}$) accurately (equation 3).[40, 49] The general form of the expression is as follows:

$$ED = ID \exp(-t * R) \qquad (1)$$

where, R is the elimination rate constant that can be simply determined by data analysis softwares such as Excel, ED is the effective dose (the dose remaining in the blood plasma at the desired therapeutic time point, t) and ID is the injected dose. To calculate the blood half-life ($t_{1/2}$) we have:[50]

$$\frac{ED}{ID} = \frac{1}{2} = \exp(-t_{1/2} * R) \qquad (2)$$

By rearranging the above equation, we get the following expression for blood half-life of the IONPs:

$$t_{1/2} = \frac{\ln(2)}{R} \qquad (3)$$

The blood half-life of different types of IONPs, shown in Table 2.1, ranges from several minutes[49] to several days[57] in rodents and from 1 hour (VSOP-C184)[58] to 24 hours (AMI-227)[59] in humans. These values depend on various IONPs characteristics that will be discussed in next sections of this chapter. Further, blood half-life values are highly dependent on dose levels of the injected IONPs (this parameter is discussed later in section 2.2.1.4).

Table 2.1. Blood half-lives ($t_{1/2}$) of the different types of iron oxide nanoparticles (IONPs) after their injection into animal models or human. The iron dosages are reported here based on mg Fe/kg body weight unit for easier comparison.

CS/HS	Coating molecule	Name	Charge (mV)	Model	Dose (mg Fe/kg)	$t^{1/2}$	Applications/Notes	Ref.
4-7/72	Dextran	SPIO (AMI25)	NA	Rats	0.224	6m	General MRI applications	[49]
4-6/150					1.12	16m		[50]
4-6/20		USPIO (AMI 227)	NA		1.12	2h		[50]
4-7/17		MION-46	NA		0.224	81m	MRI/Made by size fractionation of AMI-25	[49, 60]
4-6/NA		USPIO	NA		15	2h	MRI of spinal cord	[61]
NA/35		Ferumoxtran-10 (Sinerem)	NA	Rabbits	56	Several days	MRI of Atherosclerotic Plaque	[62, 63]
5/30			NA	Human	2.6	21-30h	MRI of lymph nodes	[64]
5/30		BMS 180549/USPIO	NA	Rats	0.14-1.68	3.7h	General MRI evaluation	[65]
			NA	Human	1.7	>24h	General MRI evaluation	[59]
5/30		USPIO Sinerem	NA	Rats	11.2	4h30m	Tumor MRI	[53]
4-6/227		Ferumoxides (Feridex) or Endorem	NA	Human	0.56-0.84	2h	Liver MRI	[66]
NA/121		Feridex	NA	Rabbits	4.8	0.46h	MR Imaging of Atherosclerosis	[67]
NA/15		Fractionated Feridex				15.9h		
NA/50-80	Dextran (20kDa)	Amino-dextran SPIO-Micromod	–4.95 to –0.77	Mice	4	5-60m	Protein adsorption analysis	[68]
12/50	Dextran (40kDa)	NA	0	Rats	5	50m	MRI of myocardial infarction and brain tumor	[69, 70]
3-5/60-80	Carboxy dextran	SHU 555 C (Resovist)	Anionic	Rats	5.6	56±17m	Imaging of Inflammatory Bowel Disease	[71]
				Rats	2.8	35m	General MRI applications	[72]
				Human	NR	6h		
NA/25		SPIO	-20	Rats	11.2	90m	MR Lymphography	[73]
		USPIO	NA	Rabbits		6h	MRI of atherosclerotic plaques	[74]
7/30		Ferumoxytol (AMI7228)	Anionic	Human	<4	10-14h	MR angiography	[72, 75]
				Rats	2.24	67m		[72]
20/42	Dextran+ antibody	Ocean Nanotech	NA	Mice	NR	7.5h	Brain tumor targeting and MRI (0.2mL, concentration NR)	[76]
30/30×70	Dextran-PEG	Nanoworms	NA	Mice	3	16-19h	Tumor targeting	[77]
NA/30	Dextran-PEG+ targeting molecule	NA	NA			17.9-19.6h		
NA		Nanoworms	NA	Mice	3.3[(a)]	12h[(b)]	Atherosclerotic plaques/one dimensional clusters with 80-110nm length and 30nm width	[78]

NA/250	Cross-linked dextran (20kDa)	Nanoworms	NA	Mice	~5[a]	10h	MRI, protein adsorption and blood half-life analysis	[79]
5-7/20	Starch	FeO-BPA	NA	Pigs	4	150m	Abdominal MR Angiography	[80]
				Rodents	1-3	45-100m		
NA/60-90		NA	-12.3 to 3.9	Rats	11.2	13m	MR Lymphography	[73]
5-7/20	PEG+ starch	NC100150 (Clariscan)	Anionic	Rabbits	0.25-1	45-120m	MRI of renal perfusion	[81]
5-7/25				Human	3-4	3-4h	MR angiography	[82]
<10/142	PEG (5kDa)-starch[c]	NA	+24.4	Rats	12	7.29h	Tumor targeting-By increasing the PEG MW to 20kDa, HS and half-life increased to 168nm 11.75h	[40]
7/30	Chitosan-PEG-chlorotoxin-cy5.5	NA	0	Mice	6.7[a]	7-8h	Cancer targeting and imaging/NIR fluorescence Scanner for half blood life/	[83]
5/10	PEG+ lipid	NA	NA	Rats	6	45m	Kidney targeting /imaging (Υ-Fe_2O_3 core crystals)	[84]
10-15/35		LSPIO	NA	Mice	3.9	1.02h [b]	MRI detection of atherosclerotic lesions / The Half-lives in wild type mice reduced to 1.01 (no targeting) and 1.12 (with targeting) for LSPIO and reduced to 1.41 (no targeting) and 1.55 (with targeting) for LUSPIO	[85]
NA/10		LUSPIO	NA			1.52h [b]		
10-15/36	PEG+ lipid+ antibody	LSPIO	NA			7.28-7.42h [b]		
NA/12-16		LUSPIO	NA			9-9.3h[b]		
4/8.6	Citrate coating	VSOP-C184	NA	Rats	2.52	21±5m	MRI Pre-clinical characterizations	[86]
				Pigs		36±4m		
4/7			NA	Human	0.84-4.2	0.5-1.5h	General MRI applications	[58]
NA/12		VSOP-C43	NA	Rats	1.68	8.4 ±0.9m	Effect of age on half-life/ half-life increased to 15.9±2.4 in old rats	[87]
19.6/117.3	PEG+ polyaniline+BCNU drug	NA	NA	Mice	15	62h[d]	Brain tumor imaging and drug delivery	[57]
8/24	DMSA	NA	Anionic	Mice	22.4	Several hours	Tumor MRI and targeting (Maghemite core crystals)	[88]
12/42	DMSA	NA	-35	Rats	5	10m	General MRI application/ highly monodisperse cores	[89]
12/49	DMSA-PEG(2kDa)		-15			20m		
17/86	PMAO-PEG(5kDa)	NA	Neutral	Mice	7	4m	Designed for magnetic particle imaging (MPI)/highly monodisperse cores	[90, 91]
20/42						19m		
27/78	PMAO-PEG(20kDa)					160m		
19.7/98	PEG	NA	-3 to -7	Mice	7	12-14m		[92]
19.7/43						12-14m		
10/63	Polyacrilamide +PEG (0, 0.6, 2, 10kDa)	NA	NA	Rats	7	28, 25, 38 and 150m	Brain tumor MRI/Larger PEG MWs increase the half-life time.	[93]

4-8/21	phosphonate	P904	NA	Rabbits	56	3.5h	MRI of atherosclerotic plaques	[62, 63]
70/NA	Silica+PEG	NA	NA	Rats	5.7	2.5h	General MRI	[56]
NA/1.6μm	P(S/V-COOH) polymer	MPIO-Bangs	NA	Mice	0.0145	1m	MRI of myocardial infarction	[94, 95]

Abbreviations: [Core size and hydrodynamic size (**CS/HS**)]-[Blood half-life ($\mathbf{t^{1/2}}$)]-[Not available (**NA**)]-[monocrystalline iron oxide nanoparticles (**MION**)]-[Lipid-coated ultra-small superparamagnetic iron particles (**LUSPIOs**)]-[larger lipid-coated superparamagnetic iron oxide particles (**LSPIOs**)]-[meso-2,3-dimercaptosuccinic acid (**DMSA**)]-[1,3-bis(2-chloro-ethyl)-1-nitroso-urea (**BCNU**)]-[poly(maleic anhydride-alt-1-octadecene) **(PMAO)**]

[(a)] Assuming that each mouse weighed 30g.

[(b)] IONPs injected through retro-orbital route.

[(c)] cross-linked starch

[(d)] Half-life reported for the BCNU drug loaded to the IONPs.

2.2.1.2. Mononuclear phagocytic system (MPS): the major clearance route

Intravenously injected IONPs, are selectively taken up by the liver and spleen (see our mice biodistribution study results in Chapter 4.8), with few reports also showing the presence of a smaller fraction of the injected IONPs in the lung.[96, 97] Liver and spleen are, in fact, the major clearance pathways for the IONPs in the blood and these organs form part of the important immune system known as mononuclear phagocytic system (MPS) or monocyte-macrophage system also known classically as reticuloendothelial system (RES).[98, 99] Note that using MPS terminology for this clearance system is more more consistent with the current literature. However, we use RES for monocyte-macrophage clearance system to avoid confusions with magnetic particle spectrometry (MPS), which is commonly used in this thesis. In this section, details about the various physiological components of the RES and their role in the clearance pathways are provided. Later (section 2.2.1.4), we will consider the physicochemical properties of IONPs (*e.g.* size, surface charge, surface coating density) that affect their biodistribution and clearance by the RES.[100]

The RES system includes monocytes circulating in the blood and macrophages located in different organs, such as liver, spleen, lymph nodes, bone marrow, lung and brain.[101] Generally, macrophage precursor cells form from hematopoietic stem cells in bone marrow and then get released into circulation as monocytes. These circulating

monocytes then extravasate through the endothelium and migrate to tissues followed by differentiation into various larger size macrophage subsets, depending on their anatomical location and functional phenotype.[102] The major specialized tissue-resident macrophages are Kupffer cells in liver, alveolar macrophages in lungs, osteoclasts in bones and histiocytes in interstitial connective tissues. Distinct macrophage populations also exist in secondary lymphoid organs, including the macrophages residing in spleen marginal zones and sub-capsular sinus macrophages in lymph nodes. Tissue-specific macrophages also patrol highly immune-privileged organs such as brain (microglia), eyes and testes.[103] All these tissue-distributed macrophages clear the body of the presence of pathogens or foreign bodies such as bacteria, viruses, abnormal and old cells and IONPs, by phagocytosis (*i.e.* engulfing them followed by their degradation and metabolism, as discussed in section 2.3), or by recruiting additional macrophages from circulation to strengthen the innate defense mechanisms (during infections or injuries).[104]

In general, liver and spleen are usually the dominant organs for clearance of the nanoparticles from the bloodstream.[83] However, when injected in high dosages, the liver and spleen macrophages can only eliminate a fraction of the IONPs from the bloodstream and the excess IONPs get accumulated in other macrophage-rich tissues such as lung and adipose tissue.[105] Uptake of the IONPs by the macrophages of liver and spleen is usually preceded by a) opsonization, b) recognition by the macrophages and c) phagocytosis (Fig. 2.1). Briefly, during the opsonization process, plasma proteins deposit on the surface of the injected IONPs, a process similar to other immunogenic species (*e.g.* viruses and bacteria) and one that specifically signals the Kupffer or reticular macrophages to recognize and eliminate them from the circulation.[54, 55]

Kupffer cells are located inside the sinusoidal blood vessels of the liver (Fig. 2.2) and are the most active phagocytes in uptaking the IONPs. Kupffer cells first attach themselves to the approaching IONPs. Then they form foot-like extrusions around the IONPs, called pseudopodia, and encapsulate them in phagocytic vesicles or phagosomes. The wall of the phagosomes comes in contact with lysosomes, which are intracellular

organelles containing an acidic environment responsible for degradation and metabolism of internalized species, and their membranes fuse with each other. Then, digestive enzymes are released from the lysosomes, which degrade the IONPs. The exact intracellular degradation rates of the IONPs remain unknown.

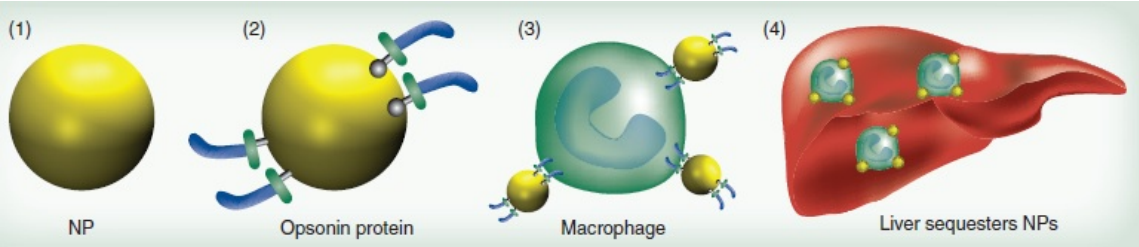

Fig. 2.1. Adsorption of the plasma proteins on the IONPs followed by their uptake by Kupffer cells and their accumulation in liver; Presence of PEG prevents the opsonization and decreases the uptake of the IONPs by macrophages.[106]

IONPs that are carefully synthesized to stealthily pass the Kupffer cells, usually have longer circulation time but may have greater uptake by phagocytic cells of RES organs other than liver. For example, Cole *et al.*[107] reported a higher uptake of the nanoparticles in spleen compared to liver, after addition of a polyethylene glycol (PEG) layer around the cross-linked starch-coated IONPs. The exact mechanism of such selective uptake of these IONPs by spleen macrophages is still unknown. The authors reported two possible scenarios for this observation: first, PEGylation reduced the uptake by liver Kupffer cells, increased the half-life from 7.29h to 11.75h, and therefore macrophages in spleen had more time to remove the IONPs from the blood. Second, the higher spleen uptake might be due to increase of the hydrodynamic size of the IONPs to values larger than 200nm after injection, because of plasma proteins adsorption or possible aggregation. The critical role of the hydrodynamic size on liver and spleen uptake will be discussed later in section 2.2.1.4.

Recent reports also demonstrate that either nanoparticles or monocyte-macrophages can be selectively manipulated to facilitate their phagocytosis and targeting abilities.[108, 109] For instance by either specific coating of nanoparticles (e.g. Immunoglobulin G or

IgG coated IONPs[108]) or by pre-treating phagocytic cells with specific cytokines[109] the phagocytic and tissue or lesion homing capabilities of particle containing phagocytes can be influenced. These approaches can potentially enable nanoparticle containing monocytes or macrophages to be targeted to sites of infection, inflammation or neoplasia for therapeutic or imaging purposes.[110]

It is also possible to manipulate the immune system of the body to prolong the circulation time of the IONPs. For example, reducing the number of active Kupffer cells by pre-injection of another material, such as liposome particles coated with a chelated Ni^{2+} layer. Ni^{2+} has a higher affinity to adsorb the plasma protein through opsonization and therefore it has a high rate of initial macrophage uptake. The IONPs injected after this pre-treatment step showed a prolonged half-life up to 5 times more than the IONPs directly injected without administration of decoy liposome particles.[111] However, for further clinical applications of this approach, it is also necessary to evaluate the long-term toxicity of these decoy particles, in addition to all other concerns related to safety of the IONPs. As an alternative approach, Wang *et al.*[112] labeled red blood cells with IONPs and observed a significantly longer blood circulation time and efficient tumor targeting after intravenous administration of these cells.

It is important to note that macrophage uptake of the IONPs can have either beneficial or detrimental effects, based on the desired application.[113] For example, for targeting cancers in various tissues,[114] or identifying metastatic cancers in the lymph nodes,[115, 116] and vascular angiography,[117, 118] longer circulation time as a result of lower macrophage uptake is desired. On the other hand, for some other imaging applications such as evaluation of brain lesions,[119-121] assessment of rejection of the transplants or grafts,[122] visualization of heart plaques[74, 123] and various other inflammation-mediated diseases[54, 124-126] higher uptake rates of the injected IONPs by specific macrophages (other than the Kupffer cells) or circulating monocytes and their subsequent homing to specific tissues is desired.

• ***Liver:***

Liver blood vessels contain highly fenestrated sinusoids, with a certain average pore size of 100-200nm (depending on the animal or human species), lined by Kupffer cells (Fig. 2.2).[127, 128] As described earlier, Kupffer cells are the most effective macrophages to quickly phagocytize the nearby IONPs from the blood.[129] Liver uptake of IONPs has been reported as the most effective elimination pathway of the nanoparticles, even when the IONPs are tuned for specific targeting of tissues or organs (*e.g*. tumors).[85] Due to the high rate of IONPs accumulation in the liver,[130] the organ can be easily imaged using the IONPs as T_2 contrast enhancement agents in MRI or as tracers for MPI (see Chapter 4).[92] As we will show later (Chapters 4, 5 and Appendix A), the optimal core size for MPI tracers is 20-27nm. Phase transfer of these larger core sizes, usually results in larger hydrodynamic sizes and therefore faster uptake of these ideal MPI tracers by liver. In particular, rapid uptake of the IONPs by liver is helpful in MR imaging of potential liver cancers, since the IONPs that are taken up by the Kupffer cells in the healthy liver generate a dark contrast in T_2-weighted MRI, on the other hand, the tumor sites, lack Kupffer cells and thus phagocytized IONPs, and appear as bright regions.[131, 132] However, this rapid liver uptake is a challenge in MPI, since currently available MPI scanners lack the required sub-millimeter high resolution to detect these microstructural regions in organs, similar to MRI. T_2-weighted MRI images and their use for quantification of the IONPs in organs are discussed in section 4.7.

Hepatocytes are physically separated from the sinusoids in the liver by a region called the space of Disse (Fig. 2.2).[133] As discussed in section 2.3.1, hepatocytes also accumulate the biodegradation byproducts of IONPs in the form of a protein-iron complex, called ferritin. Although the Kupffer cells found in the sinusoids are normally the main entrapment sites,[134] if suitably functionalized, IONPs can also accumulate in hepatocytes.[135] Hepatocyte delivery of the IONPs can be enhanced by addition of molecules with high hepatocyte binding affinities (*e.g*. linoleic acid[136] and lactobionic acid[137]) to the surface of the IONPs, or by increasing the percentage of antifouling

molecules such as PEG[133] on the surface of the IONPs to decrease their rate of opsonization.

Accurate mapping of the distribution of IONPs in the liver demands detailed experimental studies. For example, Van Beers *et al.*[138] used different imaging techniques to study the distribution of ultrasmall dextran coated IONPs (Ferumoxtran, core size, d_C ~5nm, d_H ~30-35nm) in the liver using a rat model. They used chemical staining of the ferric ions (Fe^{3+}), in liver sections and showed by light microscopy analyses that maximum uptake of the IONPs (injection dose of 15 μmol Fe/kg) by the Kupffer cells occurred after 1-4 hours of injection. This peak was delayed to 8-24 hours when the dosage was increased to 150 μmol Fe/kg. MR images on the other hand, showed a change in liver contrast, 1 hour after injection of the higher dosage (150 μmol Fe/kg), suggesting IONPs were still distributed in the extracellular blood and interstitum, rather than Kupffer cells or hepatocytes. Closer inspection using electron microscopy analysis in ultrathin sections of the liver showed only sparse IONP uptake in the hepatocytes after 24 hours of administering the higher dosage (150 μmol Fe/kg).

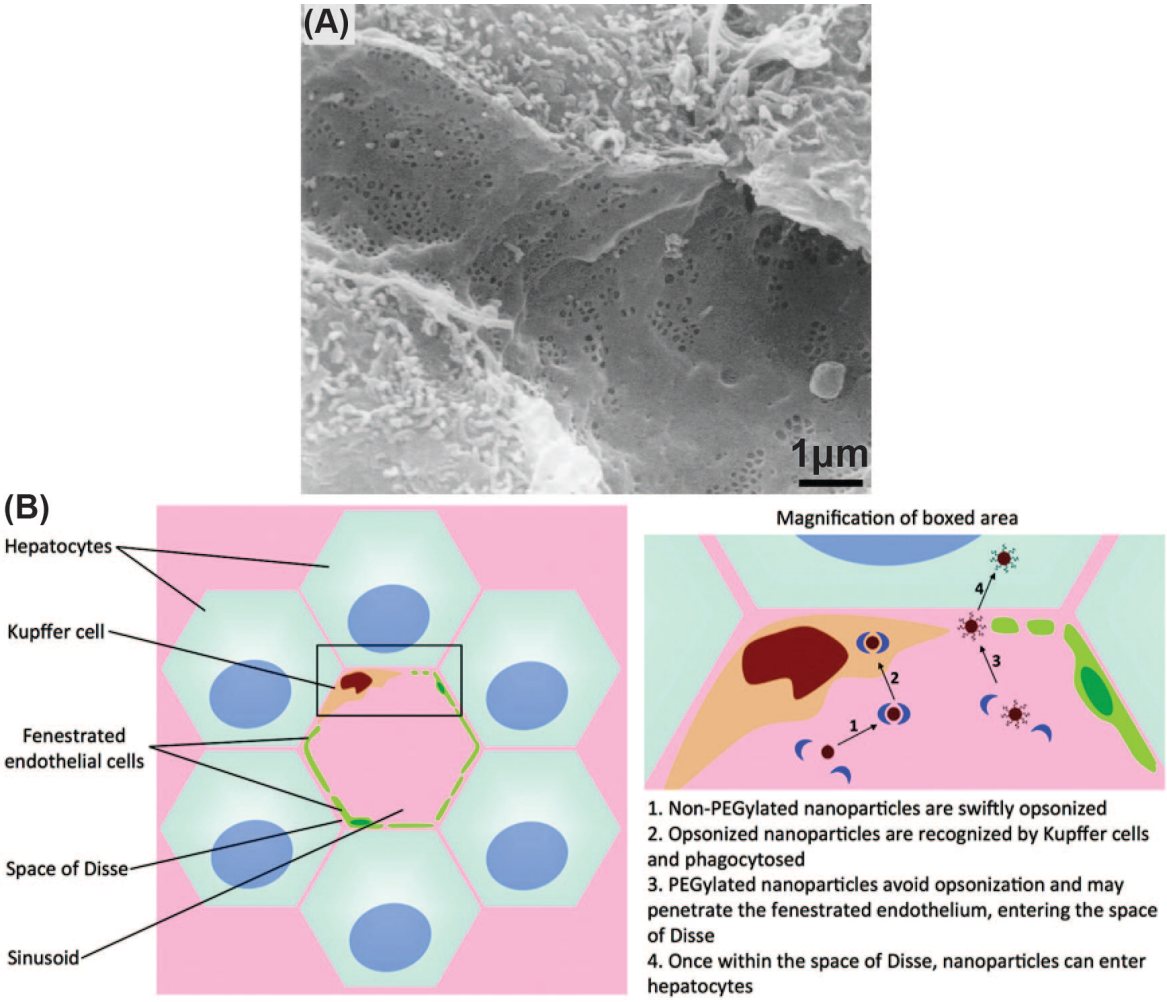

Fig. 2.2. (a) Scanning electron microscopy (SEM) image of the liver sinusoids. (b) Kupffer cells located in liver sinusoids phagocytize the IONPs from the bloodstream.[127, 133]

- ***Spleen:***

Macrophages residing in the reticular meshwork of the spleen and bone marrow also act as efficient filters for removing the IONPs from the bloodstream. For example, an artery entering the splenic pulp terminates in small, highly porous capillaries that allow the blood to enter into the marginal and red pulp zones and then get squeezed into collecting veins through the fenestrated venules in the red pulp regions (Fig. 2.3).[139] The macrophages present in marginal and red pulp zones of the spleen phagocytize the IONPs (see section 4.8.3).[140] Studies on rats and mice have shown the presence of the

IONPs either in the red pulp or particularly in the marginal zones around the white pulp regions of the spleen.[92, 141] The filtered blood then passes through the endothelial walls of the venous sinusoids and finally returns to circulation. Macrophages lining these venous sinuses also act as the secondary filtering barrier for the IONPs.[139]

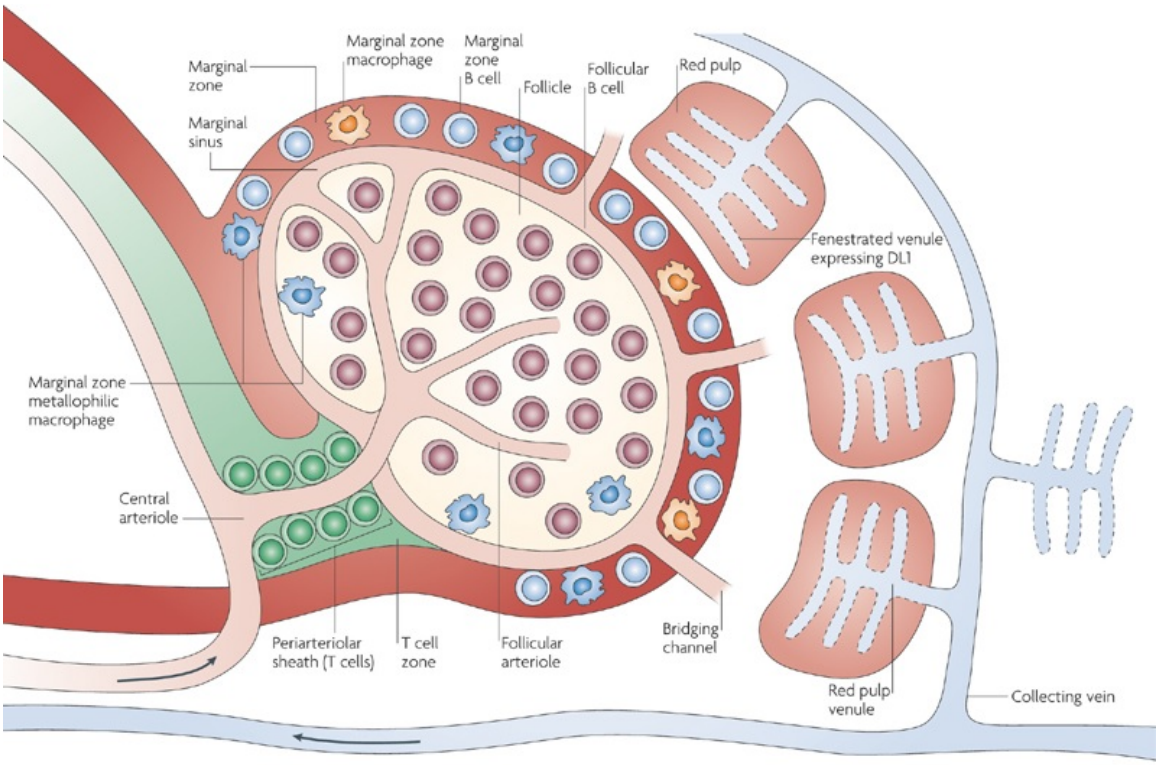

Fig. 2.3. The spleen microstructural anatomy and pathway of the IONPs entering the spleen through its central arteriole. This artery terminates in highly porous small capillaries that direct the IONP into the marginal zones around the white pulp where macrophages actively take up the nanoparticles.[142]

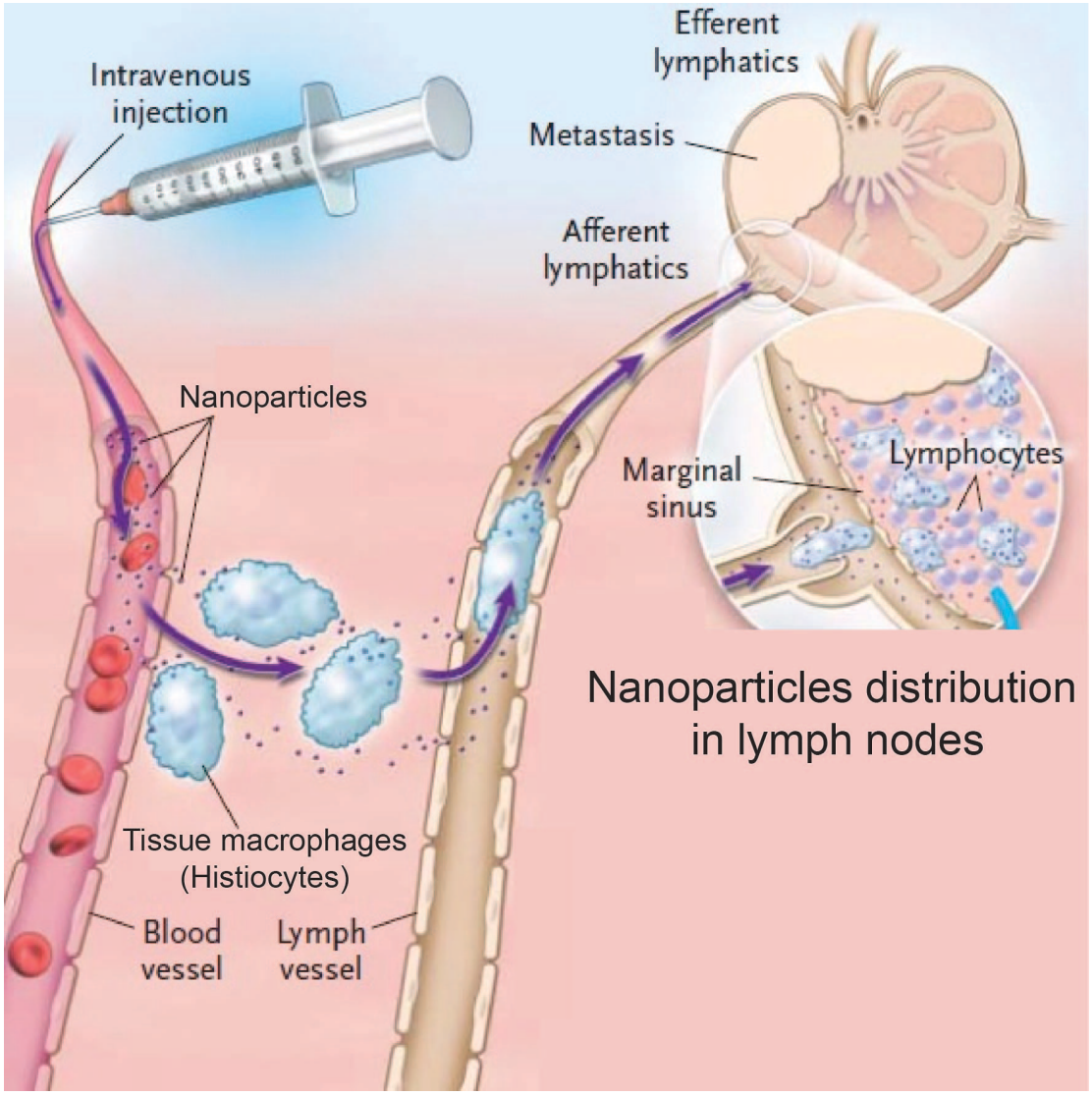

Fig. 2.4. Pathway of the IONPs in lymph node system. IONPs get taken up from the blood vessel by the lymph node macrophages (histiocytes) and then get shuttled to the lymph vessel through afferent lymphatics.[143]

• ***Lymph nodes:***

Lymph nodes are widely distributed in the body and linked together by a network of lymphatic vessels. If IONPs enter a tissue, they ultimately may enter the lymph surrounding that tissue.[139] They, then get directed to the regional lymph nodes by way of afferent lymphatics and get trapped in the sinusoidal reticular meshwork lined with macrophages.[143-145] The IONPs in tissues may also be phagocytized by histiocytes

present in the interstitum. These histiocytes then migrate to the lymph nodes through lymph vessels as shown in Fig 2.4.[143, 144] The filtered lymph passes out of the node through efferent lymphatic vessels and finally reaches the venous blood.[145] The major fraction of the IV injected IONPs usually get filtered first by the liver and spleen, before reaching any other organs and their surrounding lymph nodes. An exception would be IONPs that are injected intramuscularly or subcutaneously. In these cases regional lymph nodes may be the initial filter point.

2.2.1.3. Renal clearance: a non-phagocytizing pathway

Nephrons are the major functional and structural units of the kidney and each kidney has over a million nephrons. They help the kidneys maintain the homeostasis of body fluids and electrolytes among intracellular, extracellular, and extravascular compartments. They are also responsible for selective filtering of carbohydrates and proteins from the blood, as well as ions and even nanoparticles with d_H < 10-15nm, if present. The generally agreed size range constraints for clearance of the nanoparticles through kidneys and other organs (e.g. liver and spleen)[34, 146, 147] will be discussed in detail in section 2.2.1.4.

The intravenously injected IONPs enter the blood vessels of the nephrons through the renal hilum and are eventually excreted in urine via the ureter, then via the urinary bladder. However, first they must pass through the glomerulus. During this clearance pathway, the IONPs or their degradation products, first reach the glomerular capillaries – the blood filtration sites in the nephrons – through afferent arterioles and the filtered blood leaves the glomeruli through efferent arterioles. The elements for excretion that are filtered from the blood (ultrafiltrates), enter Bowman's space after passing through gaps between the podocytes (Fig. 2.5), forming the glomerular basement layer of the capsules.[148] These intercellular filtering slits are also referred to as fenestrae. Note that the filtration mechanism in the kidney is physically different from the mechanisms in liver and spleen. The kidney fenestrae act as filters that only allow species *smaller* than a certain size (d_H~10-15nm) to leave the bloodstream and get excreted from the body, but

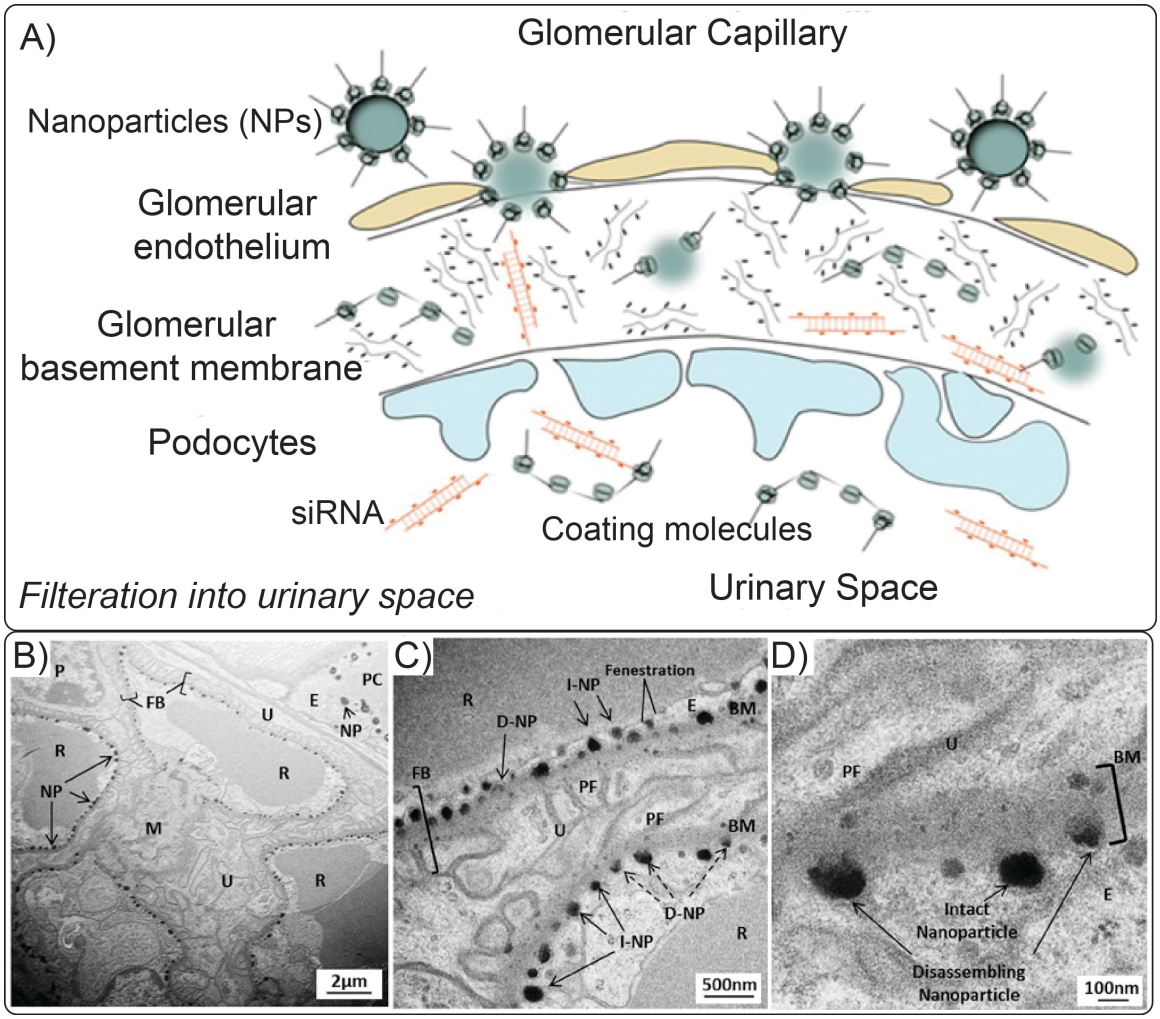

Fig. 2.5. (A) Excretion pathway of the IONPs or their degradation products through kidney. IONPs enter the glomerular capillaries through the afferent arterioles. IONPs smaller than 10-15nm, their detached coating molecules, therapeutic agents (e.g. siRNA) or degradation bi-products present in the blood can pass the glomerular endothelium and fenestrations between the podocytes, where they actually get transferred to renal tubules and are excreted in the urine via the bladder. Transmission electron microscopy (TEM) images in parts (B), (C) and (D) show that nanoparticles (NP) were trapped in these fenestrae due to their large sizes (~60-100nm). (BM: Basement membrane; FB: Filtration barrier, (I/D)-NP: (intact/disassembling) nanoparticle; P: podoyctes; U: Urinary space; PF: podocyte foot process; M: Mesangium, PC: peritubule capillary; E: Endothelial cell; R: Erythrocyte).[149]

liver and spleen sinusoids act as filters that entrap blood borne elements *larger* than a certain size (see section 2.2.1.4). The hydrodynamics of the blood pressure, flow and

viscosity and the filterable elements size and charge determine the filtering efficiency of the nephrons.[150] In addition, the number and size of these channels is controlled by physiological and pathological conditions and varies from species to species. Eventually, the ultrafiltrate solution containing any IONPs reaches the renal pelvis, where they get transferred to the urinary bladder via the ureters.

If renal clearance is the appropriate clearance route for a specific type of IONPs, a large percentage of the administrated IONPs dosage should be excreted through urine.[146] However, due to size constraints, no specific reports describe the presence of the non-degraded IONPs in urine.[151] However, small coating molecules that are detached from the surface of the IONPs due to their weak bonding and other small biodegradation byproducts may be excreted through kidney (Fig. 5).[149, 152]

Note that labeling of IONPs by coating molecules (*e.g.* by fluorescent molecules) is not necessarily a reliable approach to prove the presence of the IONPs in urine, since in most of the cases the coating materials (even those covalently bonded to IONPs surface) can get degraded and independently be cleared out of the body through the kidneys much faster than the iron oxide core of the IONPs.[153, 154] When IONPs coating molecules are labeled with fluorophores, it is possible to study the co-localization of the IONPs and their coatings in tissue sections by confirming the presence of blue foci generated by the Prussian Blue staining of the iron in the core and the fluorescent signal from the coating of the IONPs at the same location in tissues.[83] Even though there are some reports of the accumulation of the IONPs in kidney,[155, 156] the critical evidence for renal clearance, *i.e.* traces of IONPs in urine, were not presented in these studies. The observed MRI or fluorescent contrast enhancements in the kidney might be only due to the presence of the blood circulating IONPs or their micron size aggregates in the efferent and afferent blood in the capillaries and arterioles in the renal cortex and not necessarily from the glomerular uptake.[83, 107, 157, 158]

2.2.1.4. Parameters determining the blood clearance pharmacokinetics

- ***Hydrodynamic size and stability of the IONPs:***

Hydrodynamic size of the IONPs is one of the most important factors that determines their biodistribution kinetics.[159] This is the most important parameter that should be carefully considered for development of efficient MPI tracers, since the MPI performance of the nanoparticles (i.e. signal intensity and resolution and blood circulation time) is usually dependent on their size and stability in biological environments. The effect of hydrodynamic size, d_H, on the pharmacokinetics of polymer and gold nanoparticles have been discussed at length,[33, 146, 147, 160, 161] and it is reasonable to expect similar behavior for IONPs as well. A recent study has clearly shown the decrease of the blood half-life of IONPs from 50 to 3 minutes by increasing their hydrodynamic size from 20 to 85nm.[162] As shown in Fig. 2.6, IONPs with d_H > 100nm quickly accumulate in the liver and spleen through macrophage phagocytosis and entrapment in liver and spleen sinusoids (section 2.2.1.2).[85, 163] In addition, it has been reported that IONPs with d_H > 200nm have higher rates of uptake by the spleen when compared with the liver, due to their mechanical filtration followed by macrophage phagocytosis in spleen.[107, 164, 165] Pinocytosis (a mechanism for cellular uptake of the smaller nanoparticles occurring by a non-specific and non-receptor mediated cell membrane absorption) by liver and spleen macrophages has been reported as the main internalization pathway for dextran-coated IONPs with d_H < 20nm.[166, 167] Larger IONPs can get internalized through receptor-dependent endocytosis.[166] In both cases, the internalized IONPs get transferred to lysosomes. Finally, it is highly likely that IONPs with d_H, < 10-15nm[100, 146] are eliminated via the kidneys according to the mechanisms discussed earlier in section 2.2.1.3 (Fig. 2.6). Due to variation in IONPs characteristics and experimental parameters(such as animal models, quantification techniques *etc.*) used in different studies, the exact upper and lower size limits to avoid, or enhance hepatic and renal clearance, are not well-defined, but the range of sizes provided here are the most agreed upon values for each of the IONPs elimination mechanism discussed above.[37] Therefore, based on these size limits, we try to adjust the synthesis

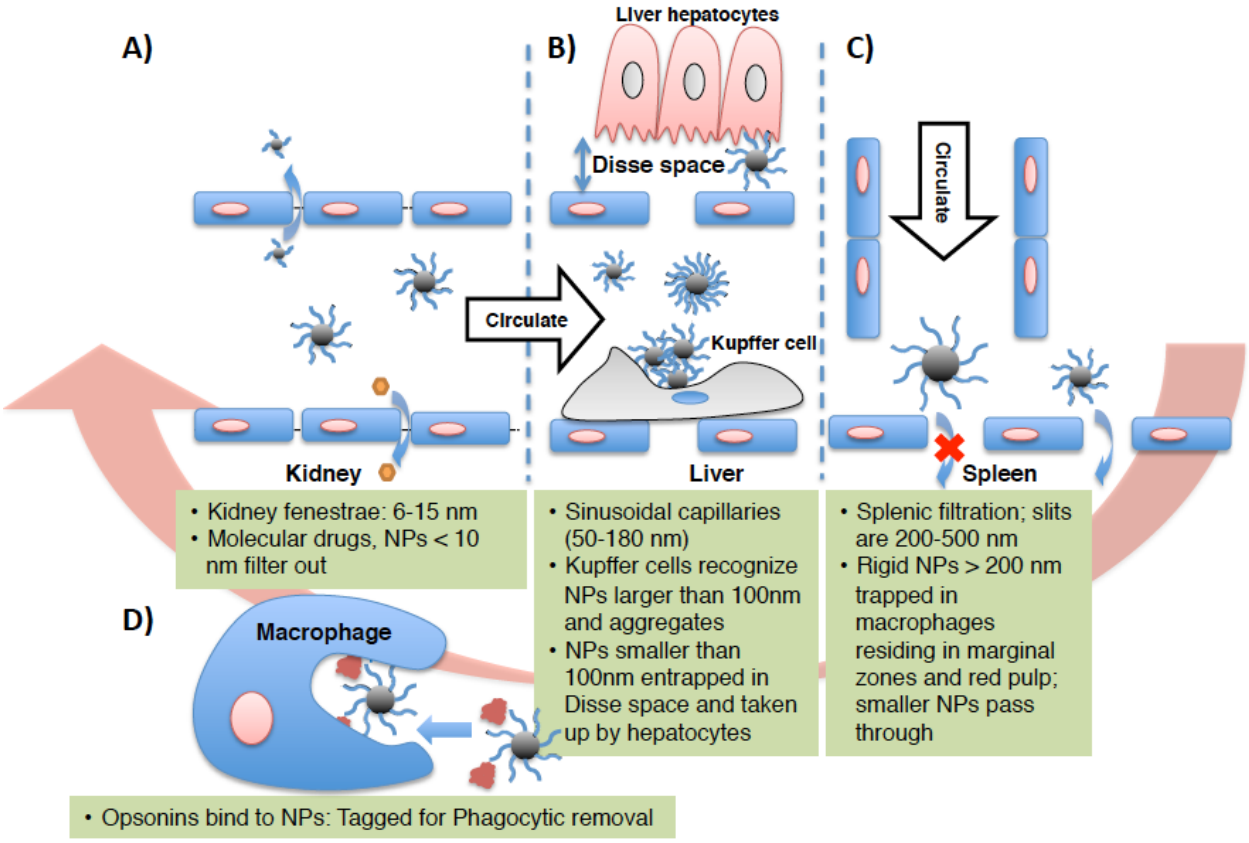

Fig. 2.6. Schematic showing the size dependent physiological barriers against nanoparticles blood circulation. (A) In human kidneys, nanoparticles with d_H < 15 nm in diameter are filtered out, thus imposing a lower size limit for designing long circulating nanoparticles. (B) Sinusoidal capillaries in the liver are fenestrated (50-180 nm) and lined with the Kupffer cells, which rapidly uptake large nanoparticles or agglomerates tagged with opsonins, and smaller nanoparticles are trapped in the Disse space and can be taken up by hepatocytes. Meanwhile, nanoparticles <100 nm in diameter with non-fouling (prevent protein adsorption) and non-immunogenic (prevent immune response) coatings continue circulating. (C) The Spleen imposes a true upper limit in optimal size for circulation – nanoparticles larger than about 200 nm get trapped in the marginal zones and red pulp, where they are sequestered by the splenic macrophages. (D) Finally, opsonization is the tagging of nanoparticles with specialized proteins called opsonins for removal by phagocytic cells of mononuclear phagocytic system (or RES), which includes the Kupffer cells in the liver and the splenic macrophages in the marginal zones and red pulp.[168, 169]

and surface functionalization of our MPI tracers in a way to end up with hydrodynamic sizes of ~20-100nm, to minimize clearance through liver, spleen and kidneys. Note that

the optimal core size of the IONPs as optimal MPI tracers is ~20-27nm (see Chapters 3, 4 and Appendix A).

Blood half-lives of different types of IONPs with a wide range of hydrodynamic sizes are briefly listed in Table 2.1. Note that due to novelty of MPI, only a few IONPs formulations presented in this table were specifically designed for MPI. However, considering the wide range of hydrodynamic sizes, surface charges and coating molecules of other formulations (even thought they were not designed for MPI) can be used for future design of various MPI tracers with different functionalities. Generally, RES elimination of the IONPs is the dominant mechanism since the hydrodynamic size of the IONPs are usually larger than the size limits for renal elimination.[170] Therefore, as a simple rule of thumb, by tuning the hydrodynamic diameter of the IONPs between approximately 20-100nm, it is possible to extend their blood half-life and increase the access of the IONPs to other organs such as lymph nodes,[171, 172] arterial walls,[85] brain[173] or tumors.[28] However, it is important to note that even if d_H=10-100nm on average, there may be some fraction of the IONPs (or their aggregates) with sizes beyond this range. The percentage of these fractions depends on the distribution, or the polydispersity index (PDI) of the hydrodynamic size of the IONPs, which is typically determined in solution using dynamic light scattering (DLS). PDI is a dimensionless number, usually ranging from 0.05 to 0.7 and describing the amount of non-uniformity of nanoparticles hydrodynamic size distribution. PDI values smaller than 0.05 are rarely seen, only for highly monodisperse standards and values greater than 0.7 show that the nanoparticles are highly polydisperse, having a very broad hydrodynamic size distribution. A high PDI indicates a broad distribution of nanoparticle diameters, which results in their multi-stage clearance since larger nanoparticles circulate for shorter periods compared to smaller IONPs.[174] For instance, Briley-Saebo *et al.*[67] used filtration to fractionate Feridex (d_H= 121nm, with polydispersity index, PDI, of 0.4) IONPs based on their size and only used the smaller size (d_H=15nm, PDI=0.2) portion of the original batch for biodistribution studies. They found that fractionation of Feridex increased the blood half-life in mice from 0.46h to 15.9h and decreased the liver

accumulation dosage from 60% of the injected dose to only 6.4% after 44h post-injection. In general, the lowest possible PDI is preferred in order to get more reliable and repeatable *in vivo* blood clearance pharmacokinetics and subsequent biodistribution results.

Size instability caused by aggregation of the injected IONPs also plays a detrimental role in their clearance kinetics.[40] When the injected IONPs are not stable in the blood, they form aggregates to decrease their surface energy, which results in their rapid entrapment by the RES system. IONPs aggregates can form due to various reasons; for example, they form when the steric hindrance or electrostatic repulsion forces between the individual IONPs are not strong enough to prevent the nanoparticles from forming these clusters.[175] Alternatively, when the coating molecules are weakly bound to the IONP cores, they are easily detached in the presence of highly ionic species in the surrounding biological media, resulting in IONP aggregation.[176] Usually, in these cases, cross-linking of the coating molecules can improve the IONPs stability and blood half-life.[39, 79] Adsorption of plasma proteins on the IONPs can also increase the size and RES elimination rate of the IONPs.[177] Therefore, by utilization of a proper surface modification approach (see Coating Molecules section below), both stability and circulation time of the IONPs can be improved.[178]

• ***Core size:***

Biomedical IONPs are usually made of crystalline iron oxide cores with superparamagnetic properties.[21] Core size, d_C, of the iron oxide nanoparticles plays a very important role in determining their saturation magnetization and dictates their T_2, T_2* and T_1 relaxation times when used as MRI contrast agents.[43, 179, 180] For example, increasing d_C of IONPs from 5 to 14nm, increases T_2 relaxation rate of the surrounding protons (r_2 relaxivity) by a factor of three.[181] In MPI, IONPs behave as tracers – unlike MRI, where the IONPs simply alter contrast of surrounding tissue, IONPs in MPI are the source of the imaging signal – and larger crystallite sizes (d_C ~ 23-27) generate images with higher resolution and brightness.[9, 42] However, faster

biodegradation rates in liver and spleen has been recently reported for monodisperse 5nm iron oxide cores in comparison with 15 and 30nm IONPs and coated with the same coating molecules.[134] This may raise long-term toxicity issues for larger core sizes, because of a longer dwell time.

In an ideal surface modification process that results in a uniform coating thickness with the same type of molecules, larger core sizes should result in larger hydrodynamic sizes. However, larger crystal sizes have strong magnetostatic or dipolar interactions with each other, which often results in the formation of clusters of the cores with larger hydrodynamic sizes. This also makes their surface modification more challenging. As discussed in the previous section, for larger hydrodynamic sizes, especially when d_H > 200nm, a shorter half-life is expected due to the rapid hepatic and splenic filtration of the nanoparticles. Also, for a constant iron dosage, the total surface area is less for larger core sizes, which mean less chemically or physically active sites are available for conjugation or loading of the desired polymer coatings and therapeutic biomolecules on the IONPs.[182] Therefore, there is always a competing role between higher imaging efficiency and longer blood residence time with accompanying therapeutic performance of these larger contrast agents both in MPI and a wide range of T_2 MRI applications.

For example, as shown in Table 2.2, r_2 relaxivity of the ultrasmall IONPs (lipid coated ultrasmall iron oxide nanoparticles or LUSPIO) with smaller core (d_C ~2-5nm) and hydrodynamic (d_H ~ 10nm) sizes was about one third of larger SPIO (LSPIO) nanoparticles, (d_C ~7-12 and d_H ~35nm).[85] However, the blood half-life of LUSPIO was ~1.5 times more and its liver accumulation was 30% lower than the LSPIO nanoparticles. When different antibodies were conjugated to these IONPs for targeting of heart lesions, the blood half-life of the LUSPIO was again 30% more and the liver uptake was about 10-15% less than LSPIO. Note that smaller IONPs have a higher r_1 (the T_1 relaxation rate of the water protons surrounding each nanoparticle) and are thus often used as contrast agents, which provide brighter images in T_1-weighted MRI.[43] A longer circulation time is generally expected due to their smaller sizes, but more systematic studies are needed to evaluate their short-term and long-term size-dependent

biodistribution.[159] Note that this example is based on contrast agents designed for MRI. However, the general concepts are almost the same for MPI tracers too. MPI tracers with larger core sizes (up to 25-27nm, which is superparamagnetic to ferromagnetic transition borderline size range) generate higher signal intensity and spatial resolution (Chapter 3 and Appendix A), but their half-life gets shorter due to their unavoidable larger hydrodynamic sizes. Selection of proper coating molecules, such as coating with larger PEG molecules (i.e. >20kDa), may help to prolong their circulation time.

In addition to size, monodispersity and shape uniformity of the iron oxide cores – important parameters often tuned to improve the imaging performance of the IONPs – may also affect their biodistribution and pharmacokinetics. Controlled high temperature decomposition of iron organometallics (*e.g.* iron pentacarbonyl and iron oleate) results in highly uniform and monodisperse IONPs.[16, 45] However, these IONPs are coated with hydrophobic surfactant molecules (*e.g.* oleic acid and oleyl amine) and complex surface modification processes are usually needed to transfer them to aqueous media. Due to limitations of the phase transfer approaches, these IONPs have shown shorter blood circulation times compared to some IONPs synthesized by conventional co-precipitation in the presence of polymers such as dextran (Table 2.1).

Table 2.2. Effect of hydrodynamic size (d_H) of the IONPs on their r_1 and r_2 relaxivities in MRI, their blood half-lives in normal and wild type mice and dosage percentage accumulated in the liver. The hydrodynamic sizes were based on number percentage average and the injection dose (ID) was 3.9 mg Fe/kg body weight.($ApoE^{-/-}$: apolipoprotein E deficient: WT: wild type mice; IK17: human antibody; LSPIO: lipid-coated superparamagnetic iron oxide particle; LUSPIO: lipid-coated ultra-small superparamagnetic iron particle; MDA2 and E06: murine antibodies).[85]

Formulation	Size (nm) (d_H)	r1 (s^{-1} mmol/l^{-1})	r2 (s^{-1} mmol/l^{-1})	Blood Half-Life $ApoE^{-/-}$ (h)	Blood Half-Life WT (h)	%ID in Liver (24 h p.i.)
Untargeted LUSPIO	10 ± 3	14 ± 1	35 ± 2	1.52	1.41	25
Untargeted LSPIO	35 ± 5	12 ± 1	103 ± 4	1.02	1.01	35
MDA2 LUSPIO	14 ± 3	13 ± 1	37 ± 2	9.01	1.55	31
MDA2 LSPIO	38 ± 4	11 ± 1	117 ± 5	7.28	1.12	37
IK17 LUSPIO	12 ± 2	14 ± 1	35 ± 2	9.12		31
IK17 LSPIO	36 ± 4	10 ± 1	106 ± 5	7.30		34
E06 LUSPIO	16 ± 4	12 ± 1	38 ± 2	9.32		30
E06 LSPIO	39 ± 5	11 ± 1	119 ± 6	7.42		35

• ***Core morphology:***

Generally, one-dimensional nanostructures such as polymer filaments,[183] carbon nanotubes[184] and gold nanorods[185] with a high length to width aspect ratio have shown longer blood circulation times over the spherical counterparts.[186] The longer circulation time of one-dimensional nanoparticles has been attributed to lesser uptake by macrophages due to an opsonin-independent phagocytosis phenomenon.[185] The same trend is expected for iron oxide nanostructures with high aspect ratios.[35] For example, a prolonged blood half-life of up to 19h has been reported for iron oxide "nanoworms" with longitudinal size of 70nm, comprising a linearly aligned set of IONPs (~25nm) encapsulated in dextran-PEG copolymer.[77] However, the largest fraction of the injected nanoworms accumulated in the lymph nodes (~40%), followed by the spleen (~15%) and liver (~9%).[187] This is in contrast with the more frequently reported results for spherical IONPs, in which liver has the highest uptake rate among the other RES organs. Other recent studies [188, 189] indicate that more systematic comparative analyses are needed to identify the exact clearance mechanisms and the optimum aspect ratios that enhance the blood half-life and pharmacokinetic performance of one-dimensional nanoparticles. It is also important to note that, experimentally, it is a difficult fabrication process to maintain all the other parameters (such as number of coating molecules, polydispersity and stability) effectively the same, and only change the core morphology and compare the pharmacokinetics and biodistribution results.[40, 190] Such studies are even more complex when hybrids of iron oxide with other materials such as gold, carbon nanotubes, quantum dots, gadolinium or silica are used for *in vivo* investigations.[140, 156, 191-199]

Other IONPs morphologies such as cubes have also been used for in-vivo studies, but the effects of these specific shape on their pharmacokinetics and biodistribution mechanisms are still unknown.[200] A recent study has shown that iron oxide nanocubes tend to form aggregates in the endosomes of the liver and spleen macrophages at the earlier stages of uptake, which decreases their endosomal degradation rate.[201] When shuttled from endosomes to lysosomes, the lysosome enzymes and proteins redispersed

the aggregated nanocubes and subsequently increased their degradation rate.[201] TEM analyses showed that degradation happens faster at edges of these cubes (along (220) lattice planes), which are thermodynamically less stable crystallographic sites (Fig. 2.7).[201]

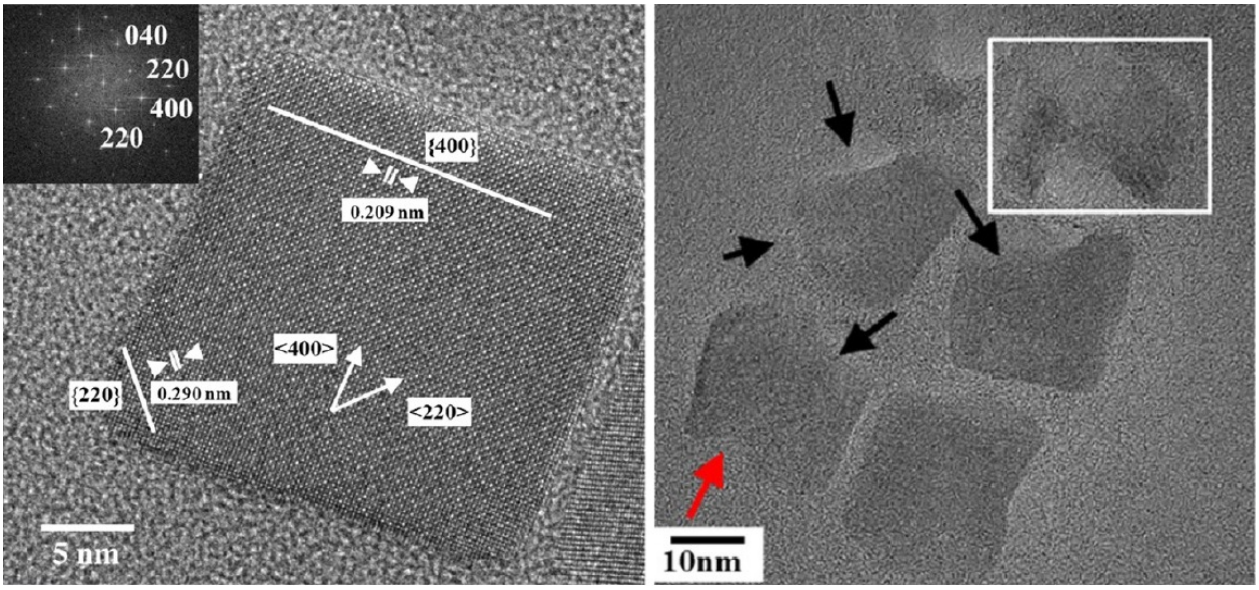

Fig. 2.7. Single crystalline iron oxide nanocubes (left) and their biodegradation in crystallographic directions with higher atomic surface energies after incubation in lysosome-like solution (right).[201]

• ***Coating molecules:***

Un-coated IONPs are often colloidally unstable, form aggregates and get eliminated by the RES system quickly. The biodegredataion rate of these aggregates is slower than the individual IONPs and can cause serious long-term safety issues, as discussed in Section 2.3.[201] There are some recent methods reported for developing colloidally stable un-coated IONPs.[202-205] However, further studies are required to evaluate the *in vivo* performance of these IONPs formulations. Different types of natural (*e.g.* dextran,[68] chitosan,[22] starch,[40, 107] human serum albumin (HSA)[206] and phospholipids or liposomes[207, 208]) and synthetic polymers (PEG,[134] Pluronic,[24] and different types of co-polymers[154]) have been used to improve the blood circulation

time of the IONPs. Table 2.1 lists some of the most commonly used types of coating materials and the blood half-life of the corresponding IONPs. All these polymers and their prospective alternates are relatively non-toxic.[180]

Among these different types of the polymers, PEG has been the most popular coating option. It stabilizes IONPs primarily via steric hindrance, and has excellent anti-fouling characteristics (resists interaction with blood and serum proteins and therefore, reduces opsonization, macrophage uptake and subsequent RES clearance of the IONPs).[106] Multiple mechanisms have been proposed in the literature regarding the stealth behavior of the PEGylated IONPs; the most accepted one is based on the shielding of the surface charge of the IONPs and increasing their hydrophilicity, which results in their reduced interactions with opsonin proteins.[209] For a wide range of therapeutic applications, it is desirable to combine the stealth characteristics of PEG with the novel functionalities of other polymers that enable conjugation of drugs or targeting molecules,[83] or sensitivity to pH and temperature changes in the surrounding environment.[210, 211] Table 2.1 shows some examples of PEG-grafted-polymers that have been used for this purpose.

Although PEG is still the best candidate for coating of IONPs, there are some recent studies showing some possible drawbacks regarding its role in the enhancement of the nanoparticles pharmacokinetics when multiple injections are required (*e.g.* multiple IONPs administration is required to monitor tumor sizes over a specific period); specifically, the pharmacokinetics of the nanoparticles can be different with repeated injections. For instance, a very high rate of RES uptake has been reported for some types of PEGylated IONPs in their second run of injection.[212] This phenomenon is called accelerated blood clearance (ABC) and its mechanism is not well understood.[213] A suggested mechanism is that anti-PEG IgM antibodies form in the spleen after the first IONPs injection, which remain in the blood and bind to PEGylated IONPs administered through subsequent injections; as a result, their uptake by Kupffer cells in the liver is enhanced.[214, 215] ABC not only decreases the therapeutic performance of the IONPs by reducing half-life, but also raises serious concerns regarding the potential for liver damage, especially when IONPs act as carriers for highly toxic anticancer drugs.[216,

217] Zwitterionic (or dipolar) materials such as dopamine sulfonate[218] and poly(amino acids),[219] polymers with heteroatoms in the main chain (polyglycerol[155]) and vinyl polymers (poly(vinylpyrrolidone)[131, 220]) have been introduced as the best alternative materials for PEG.[221] The preliminary results show that nanoparticles coated with these novel polymers can have a long circulation time in blood.[222] However, the occurrence of ABC phenomenon for repeated administration of these novel polymers is still unknown.

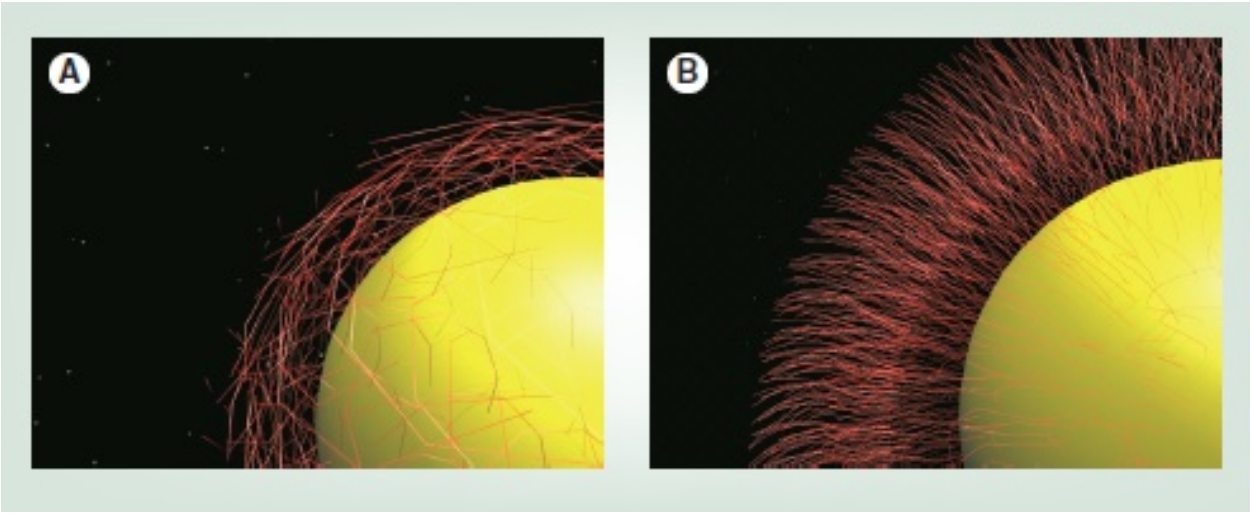

Fig. 2.8. (A) Mushroom-like configuration of the coating molecules on the surface of the IONPs which results in a lower density of the coating molecules and (B) brush-type assembly of the coating molecules which provides a high density coating layer.[106]

The molecular weight, shape, charge and grafting density of the coating molecules on the surface of individual IONPs can also change the pharmacokinetic performance of the IONP.[40, 133, 190] For example, increasing the molecular weight of the PEG molecules enhances the stealth characteristics of the IONPs by covering a larger surface area of the IONPs, which results in their slower elimination and degradation by RES macrophages.[40, 107] Also, when the distance between the attachment sites of the coating molecules to the IONPs surface is large (low surface density), a “mushroom-like” coating forms, with a shorter half-life in comparison with the “brush-like” conformation observed in high surface density coatings (Fig. 2.8).[106, 223] This is due to better shielding of the IONPs surface against the opsonin proteins, provided by the denser brush

like coatings.[209, 224, 225] The effect of charge on IONPs circulation will be discussed in the next section.

Some coating polymers such as PEG have highly flexible chains, with a large number of possible conformations. This makes a conformational "cloud" around the IONPs.[221] Statistically, when the rate of the transition of the coating molecules between their different conformations is high, the probability of the interaction of the plasma proteins with the IONPs is reduced and the blood half-life of the IONPs is longer.[226] The flexibility and stiffness of these polymers depends on their molecular structure parameters, such as size of the side groups and presence of polar groups or side chains in their backbone.[227] Polymers with higher glass transition temperatures (T_g) usually have higher rigidity.[228] Thermogravimetric (TG) studies are the standard way to determine T_g of the different polymers. More systematic studies are needed to identify exactly the role of parameters such as flexibility, rigidity and glass transition temperature of the coating polymers on pharmacokinetics of the IONPs.[146]

The uniformity of the molecular weight of the polymer used for functionalizing the IONPs can also be an effective parameter for determining the circulation time of individual IONPs. For example, natural polymers such as chitosan and dextran usually have higher molecular weight polydispersity index (PDI, explained in the beginning of section 2.2.1.4 where we discussed the effects of hydrodynamic size and stability of the IONPs) compared to synthetic polymers prepared by controlled chemical routes such as reversible addition fragmentation chain transfer (RAFT) polymerization.[229] In terms of producing uniform biodistribution performance, a low PDI might be more desirable.

Circulation time of the IONPs usually decreases when additional biomolecules, such as cancer targeting agents and drugs, are conjugated to the surface of the IONPs.[77] Increasing the average number of these molecules on IONPs decreases the blood half-life and consequently the targeting ability of the IONPs.[77] This is due to the increase in the hydrodynamic size of the IONPs after loading of these targeting agents. Therefore, there should be an optimum number of these molecules required on each IONP in order to get the highest therapeutic performance. This variation depends directly on the type, size and

charge of the targeting molecule.[77] A PEG linker between the IONPs surface and the targeting molecules increases their residence time in the blood stream, due to steric hindrance and anti-fouling characteristics of PEG molecules.[77, 154]

Finally, the binding strength of coating molecules with IONP cores has an effect on circulation time. Coatings that form weak non-covalent bonding to IONPs are prone to detachment from the IONPs *in vivo* after injection;[54] as a result, a large fraction of these separated small molecules or their biodegradation by-products accumulate in the kidney and are cleared via urine, while the remaining IONPs get aggregated and are delivered to the liver.[149, 154, 221] Cross-linking of the coating molecules forms a hydrogel around the IONPs that protects them against opsonization and increases their blood half-life.[230] For example, dextran molecules have a weak interaction with the surface of the IONPs through the hydrogen bonds between the hydroxyl groups of the dextran moiety and surface oxide hydroxide groups.[231] When the dextran molecules are cross-linked with each other using 1-chloro-2,3-epoxypropane (or epichlorohydrin) as an alkylating cross-linker, the blood half-life of the IONPs is increased up to 12h in mice.[77, 232] Increasing the dextran cross-linking percentage decreases the protein adsorption and prolongs the blood circulation time of the IONPs.[79] The same effects were reported recently for IONPs coated with cross-linked starch.[40] Note that these dextran or starch coated IONPs are synthesized by co-precipitation method. IONPs synthesized by thermal decomposition method (Chapter 3) are usually coated with a thin layer of oleic acid or oleyl amine surfactant, which is strongly bonded to the surface of the nanoparticles. There is no report showing the detachment of these surfactant molecules from the IONPs during the in vivo applications. We think radiolabeling of iron oxide core and surfactants with different radionuclides can help to monitor this phenomenon accurately. This is specially an important question for future MPI, since the optimal MPI tracers are usually synthesized by this method (as shown in the next chapters of this thesis and previous works published by our group[10]).

• ***Surface charge and zeta potential***

The surface charge of IONPs directly depends on the molecular structure of the coating materials. For example, a positive charge is expected for IONPs with a higher number of amine groups,[40, 233] while hydroxyl, sulphate and carboxyl groups usually contribute to a negative charge on IONPs.[36, 222] Since charge affects the degree of protein adsorption on IONP surface, the types of the functional groups present on the surface of the IONPs are important in determining the blood circulation time of the IONPs.[233] Unfortunately, there is only limited information available regarding the direct role of these functional groups on the pharmacokinetic and biodistribution of the IONPs.

Zeta potential (which is measured in units of mV) has been routinely used as a parameter for estimating the surface charge of the nanoparticles. However, it is important to note that this parameter is calculated from the electrophoretic mobility (speed of the IONPs in an electric field) of the IONPs and is not an accurate representative of the nanoparticles surface charge.[234] Therefore, it is possible to see similar zeta potential values for different batches of IONPs that are coated with different numbers of the charged species on their surface.[235] These different charge densities on the surface of the IONPs might change their electrostatic interactions with the surrounding proteins and cell membranes and alter the blood circulation pharmacokinetics.[236] Therefore, considerable care must be taken to comparatively interpret the pharmacokinetic behavior of the IONPs based only on their zeta potential values.

The blood half-life of some IONPs with neutral, positive or negative charges are shown in Table 2.1. It is generally agreed that IONPs with a neutral surface charge have a slower rate of RES or renal elimination.[100, 237, 238] For example, for IONPs with the same size and coating type (*i.e.* dextran), the half-life of the neutral Ferumoxtran-10 (d_H = 35nm) IONPs in human body was longer than that of anionic Ferumoxytol (d_H = 17-31nm) IONPs (24-36h vs. 10-14h).[75, 163] A much faster blood clearance is generally expected for positive charge IONPs in comparison with negative charge IONPs,[239]

because positively charged IONPs have a higher affinity to adsorb plasma proteins[240] and bind to macrophage or other cell membranes.[241]

However, there are still some discrepancies about the exact role of zeta potential ranges on the RES clearance rates in different studies. For example, some reports link higher liver uptake of the IONPs only to positive charged IONPs with d_H > 100nm.[146] But, on the other hand, it is also reported that negatively charged USPIO (SHU555C, d_H = 21nm) coated with carboxydextran have a much higher uptake by macrophages as compared with non-ionic Ferumoxtran-10 (d_H = 20-50nm) IONPs coated with unmodified dextran.[242] In another study, liver accumulation of different sizes of PVP-coated IONPs with zeta potentials ranging from +12-14mV were compared with Feridex (d_H = 58nm and -25mV).[131] It was shown that liver uptake of the positively charged IONPs was less than Feridex with slightly more accumulation observed in the liver for PVP coated IONPs, with d_H = 118nm. In a separate study, Sakulkhu *et al.*[240] reported an almost similar blood circulation time for negatively charged (zeta potential~-6mV) and neutral (zeta potential~1.5mV) PVA coated IONPs, with respective hydrodynamic sizes of ~38 and ~28nm. Also, Cole *et al.*[40] reported a half-life of up to 12 hours in rats for PEG-modified starch coated IONPs with a zeta potential of about +25mV.

These apparently controversial conclusions might be due to the fact that blood clearance of the IONPs is a complex phenomenon depending on the combination of the various parameters discussed above, *i.e.* size, shape, charge and the nature and density of coating molecules. In fact, it is technically difficult to maintain all the other parameters the same and compare the biodistribution results based only on one parameter such as zeta potential.[33]

- ***Proteins adsorption***

As discussed in section 2.2.1.2, opsonization is a process by which the IONPs get encased by plasma opsonin proteins, making them recognizable by macrophages (Figs. 2.1 & 2.6).[243] Opsonization is usually followed by receptor-mediated phagocytosis of the nanoparticles by these macrophages or other phagocytic cells.[244] In addition,

surface protein accumulation usually increases the hydrodynamic size of the IONPs, which accelerates their hepatic clearance.[131, 233]

Various parameters determine the thickness and composition of the plasma protein corona forming around IONPs.[245] For example, the type, functional groups (*e.g.* amines, carboxyls or maleimides) and charge of the coating molecules can significantly change the composition of the protein corona forming around IONPs.[240, 246] Also, the amount of the adsorbed proteins per nanoparticles is enhanced by increasing the size and surface roughness of the nanoparticles.[247, 248] Mahmoudi *et al.*[233] incubated different sizes of IONPs with fetal bovine serum (FBS) and analyzed the composition of the protein corona formed around the nanoparticles. They reported that the larger molecular weight fraction of the proteins showed higher adsorption onto the surface of the larger IONPs, and smaller proteins interacted more with smaller IONPs. This is because protein molecules have a different conformational arrangement on nanoparticle surfaces compared to flat surfaces of the same material – a phenomenon that depends on the curvature of the binding surface.[248] The relatively larger curvature of smaller size nanoparticles limits the binding of large protein molecules, thus decreasing the corona size.[249] However, their larger total surface area increases the total amount of the proteins adsorption. Also, the physiochemical and mechanical characteristics of the coating molecules can significantly alter the rate of the protein adsorption by the IONPs.[180, 250] Anti-fouling coatings (such as PEG[251] and zwitterionic materials[218]) help minimize interactions with opsonin proteins. This can be achieved by either shielding the surface charge, increasing the hydrophilicity, or decreasing the interfacial surface tension of the IONPs.[209, 248] Also, protein interactions with nanoparticles decrease when the coating molecules have a high vibrational mobility and flexibility.[209] Additionally, some coatings have a high affinity for adsorbing dysopsonin proteins that suppress the macrophage uptake.[209, 245] Finally, it is still not clear whether adsorption of a specific type of protein or a combination thereof is the most critical factor for the rapid recognition of the IONPs by RES macrophages.[146]

Depending on their net charge, plasma proteins bind either to the iron oxide core or the coating layer; for instance, differential proteomic studies of dextran coated IONPs incubated with different types of plasma proteins has shown that cationic plasma proteins such as histidine-proline rich glycoprotein (HPRG) and high molecular weight kininogen (HMWK) bind to anionic magnetite cores, while immunoglobulins (IgG) and mannan-binding lectins (MBL) bind to the cationic dextran coating.[68] The slightly anionic characteristic of the core crystals was due to partial dissociation of $Fe(OH)_3$ during the co-precipitation synthesis.[252, 253] Simberg *et al.*[68] compared the half-life of the IONPs in knockout mice and wild type (WT) mice (without any genetic manipulation and with all proteins existing in blood plasma) to find which plasma proteins play the dominant role in opsonization and recognition of the IONPs by liver macrophages. They also measured the half-life of Clodronate liposome nanoparticles in mice with impaired liver uptake as a control for circulation of IONPs. It was shown that these plasma proteins do not play a significant role in blood clearance of the IONPs (Fig. 2.9(a)). Liver Kupffer cells recognized the IONPs with the same rate, regardless of the specific type of adsorbed proteins present in plasma (Fig. 2.9(b)).[68] Also their results showed that the proteins present in plasma do not completely mask the surface of the dextran coating or iron oxide core, suggesting that the IONPs could be directly recognized by Kupffer cells, with minimal influence from the opsonin protein coating.

Similar studies were used to determine the role of protein adsorption on blood residence time of IONPs nanoworms, coated with a cross-linked dextran layer.[230] Cross-linking created a stealth hydrogel around the IONPs and increased their half-life in mice from less than 1 hour to about 10 hours. It has been assumed for more than a decade that the cross-linked layer forms a barrier around the IONPs, preventing the adsorption of the opsonin proteins and diminishing their recognition by RES macrophages.[77, 232] However, the results of this recent study showed that while cross-linking increased the half-life of the IONPs, it did not change the adsorption of the plasma proteins to the iron oxide core or coating layers. The longer circulation time of the cross-linked IONPs was attributed to the diminished binding rate of the anti-dextran antibody to the surface of the

IONPs due to decreased number of surface hydroxyl groups after cross-linking. These two studies show that to prolong IONPs circulation time, it is not necessary to completely prevent proteins adsorption on the nanoparticles. More investigations are needed to show if these results are specifically related to dextran coated nanoworms studied in these reports or they can be generalized to other types of IONPs and coatings.

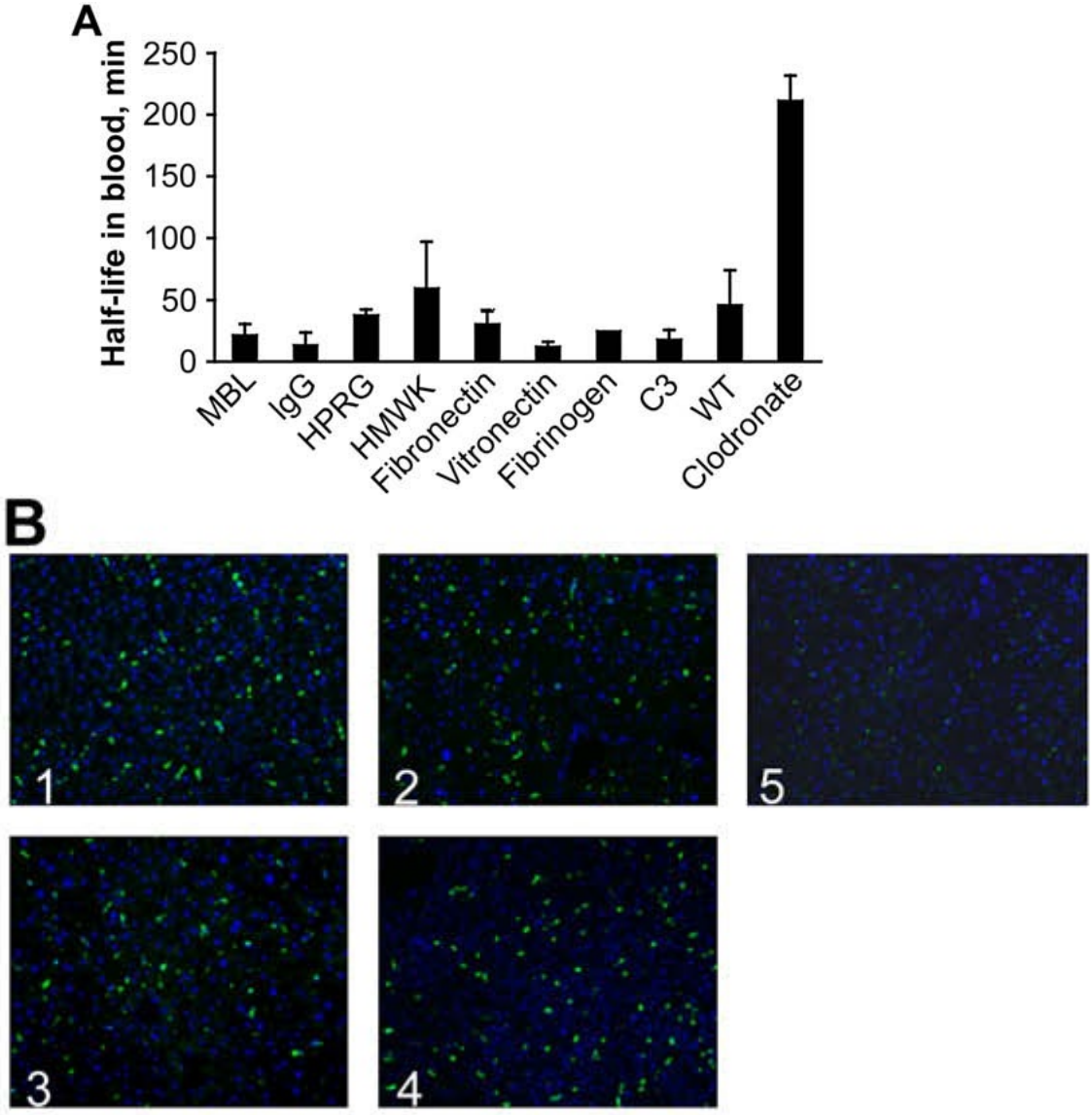

Fig. 2.9. (A) The half-lives of the dextran coated IONPs in different types of knockout mice (each lacking a specific plasma protein). The half-lives in various genetically engineered knockout mice (MBL, IgG, HPRG, HMWK, Fibronectin, Vitronectin, Fibrinogen and complement C3 deficient mice) were almost similar to their half-life in wild type (WT) control mice with all plasma proteins present in blood. Mice treated with Clodronate liposomes had impaired liver phagocytic function which served as a control (right bar). (MBL: mannose-binding lectins; Immunoglobulin G: IgG; HPRG: histidine–proline rich glycoprotein; HMWK: high molecular weight kininogen (HMWK)). (B) Histology of the liver sections confirm the results in part (A) and show that the Kupffer cells recognize and take up these IONPs (green dots due to presence of fluorescent molecules on their surface) regardless of the type of the proteins adsorbed to the surface of the nanoparticles after their injection. (Panel labels: 1, HMWK-deficient; 2, wild type; 3, complement C3-deficient; 4, MBL-deficient; 5, clodronate-treated mice).[68]

- ***Technical factors (e.g. nanoparticles dosage and animals phenotypes):***

In addition to the characteristics of the IONPs described above, there are some important technical factors that can affect the circulation and pharmacokinetics of the IONPs. For example, the blood half-life of the IONPs is dose-dependent in both animal models[94] and humans.[82, 254] An earlier study has shown that RES elimination of the nanoparticles by macrophages in rat liver and spleen, gets saturated, when more than 10^{15} nanoparticles are injected.[255] The remaining nanoparticles usually circulate in the blood for longer times and have more chance to reach other organs.[94] A recent study in rodents has shown that the clearance rate of the nanoparticles is also dependent on the mice strain type and their particular immune systems.[109] Further, the circulation time usually increases with age, due to the reduced phagocytic activity.[87]

Except for a limited number of the iron oxide nanoparticles that are clinically approved (such as Ferumoxytol or Ferumoxide), or those that are undergoing clinical trials, most of the available half-life information of IONPs are limited to data derived from animal models. Therefore, it is important to know how to correlate the half-lives in different species for better prediction of IONPs circulation times in human patients. Usually, the blood half-lives in rodents are much shorter than in human due to faster heart rates and circulation time in rodent models (e.g. about 670, 420 and 75 beats per minute for mice, rats and human, respectively).[161] For example, the blood half-life of 45 μmol Fe/kg of AMI-227 IONPs is 24h and 2h in humans and rats, respectively.[256]

2.2.2 Pharmacokinetics and clearance of IONPs in other administration methods

Intrapulmonary delivery (inhalation or intratracheal instillation) of the IONPs is predominantly used for imaging and treatment of lung diseases.[257] IONPs administrated using the intranasal pathway eventually enter the alveoli spaces in the lungs.[258] In studies of mice, the inhaled IONPs mostly accumulated in the central lung region – about 2.5 times more than in the peripheral lung zones – without any considerable difference between the right and left lungs.[259] The respiratory innate immune system acts as the major barrier against their entrance into blood and other

organs.[260, 261] The macrophages that are present in the alveolar spaces phagocytize the IONPs, digest them and their by-products get released into the pulmonary lymphatics or they are swallowed.[262, 263] A recent study has shown that the presence of the IONPs can increase the number of lung macrophages by the migration of monocytes into the lung, which enables faster ingestion of the IONPs.[264] The intranasal pathway is also known as a feasible way to deliver molecules to the brain.[265] However, the reported results related to IONPs are still controversial and the mechanisms for overcoming the BBB through this method are still unknown.[266-268]

The size, charge, coating and state of agglomeration of IONPs also play an important role in their clearance kinetics through the lung macrophages. Al Faraj *et al.*[260] instilled uncoated IONPs (d_c = 20-30nm) *via* an intratracheal plastic catheter and showed that even 14 days after administration of the IONPs, about 88% of the dosage was still present in the lung but other organs were not different from control values (Table 2.3). The biodistribution of the injected IONPs was also presented in this table for comparison, showing that major part of the IV administrated IONPs were accumulated in the RES organs. Cho *et al.*[261] used negatively charged cross-linked IONPs (d_H = 36nm) after labeling them with fluorescent molecules (Cy5.5) and reported that major fraction of the IONPs were cleared from the lung 3h after administration due to increased macrophage uptake in the lung. Using a fluorescent tag, they showed that the nanoparticles were mostly excreted in the urine in 24h. Additional studies are required to confirm if these observed fluorescent signals in urine were from the degradation by-products or detachment of the coating molecules after administration of the IONPs or not. Also, the presence of any excreted magnetic iron oxide cores in urine could be quantified by determination of any magnetic signal from the urine. Other studies by Kwon *et al*.[268, 269] also showed that after 28 days of inhalation exposure to silica coated IONPs (d_H = 50nm) a high percentage of the IONPs were accumulated in the liver, kidney and testis and the percentage of the IONPs remaining in the lung was similar to other tissues (*e.g.* brain, heart, spleen, *etc.*). Further studies are required to clarify the degradation

mechanisms, clearance pharmacokinetics and exact biodistribution of the IONPs administered by this method.

Table 2.3. Biodistribution of the IONPs administered through intratracheal instillation in comparison with intravenously (IV) injected IONPs and control mice instilled with saline. The instilled IONPs are mostly accumulated in the lung, while the IV injected IONPs are mainly entrapped in RES system.[260]

Iron Assay by ICP-OES in μg/g of Organ in the Follow-up Study after Sacrifice at Day 14

Iron Assay	Control (n = 2)	Instilled (n = 4)	Injected (n = 2)
Lung	67.9 ± 5.6	278.1 ± 6.8	93.5 ± 6.7
Liver	103.5 ± 30.4	104.6 ± 21.6	339.5
Spleen	347.9 ± 45.5	341.8 ± 64.7	492.3 ± 78.7
Kidneys	68.2 ± 9.5	59.7 ± 8.1	91.4 ± 12.3
Blood	384.8 ± 9.6	410.2 ± 61.4	487.8 ± 45.8
Brain	13.8 ± 0.9	17.6 ± 2	22.3 ± 4.5
Heart	91.9 ± 28.1	95.8 ± 20.6	96.1 ± 24.4
Thymus + LN	32.8 ± 11	35.0 ± 9.9	39.1 ± 9.4
Testicles	15.1 ± 1.4	14.2 ± 1.3	13.7 ± 1.8

Oral administration of the IONPs has been mainly used for MR imaging of the gastrointestinal (GI) tract. The IONPs used for this method are usually larger than the IONPs used for IV or inhalation.[270] For example, Ferumoxsil (AMI-121, coated by silica, d_H =300nm diameter) has been tested for pioneering clinical studies in the 1990's.[271, 272] There are some major biological barriers against the successful GI delivery of the IONPs. For example, the gastric acids and enzymes can degrade the IONPs in a short time. However, proper coating materials (such as casein protein, silica and poly(lactide-co-glycolide acid)) with pKa values lower than 3-5, helps to efficiently protect the nanoparticles against these active digestion mechanisms.[273-276] Here, pKa is a constant parameter for each type of coating and is defined as a pH value above which the coating starts to dissociate.

Depending on the type of application, the IONPs that survive the extreme acidic environment in the GI tract (pH~1-4) might need to pass the transport barrier of the intestinal epithelium. This can be achieved by using epithelial permeation enhancers such as peptides that can specifically bind to FcRn receptors in intestine epithelial layer.[277]

Then, IONPs should pass through the liver sinusoids before entering the general blood circulation system. This means that most of the surviving IONPs might be taken up and eliminated by the Kupffer cells present in these sinusoids. In fact, the liver is again the major clearance organ in the pathway of these IONPs, unless special surface modifications have been used to enable stealthy behavior to resist phagocytosis by these macrophages. The IONPs remaining in the intestine are excreted through the feces, as reported recently by Smith *et al*.[278] The iron ions and detached or decomposed coating molecules, formed by digestion of the IONPs can also get shuttled to the portal blood or excreted from the GI track following the intestinal fluid flow.[279]

Other injection routes such as intra-peritoneal (IP),[280-282] retroorbital,[78, 85] intravitreal (inner cavity of the eyes for intraocular drug delivery),[283, 284] intra-muscular and subcutaneous injections have also been used as alternative methods for administration of the IONPs. Tsuchiya *et al*.[280] showed that intra-peritoneally injected IONPs mainly distributed in liver, lymph nodes and lung. Kim *et al.*[281] showed that IP injected IONPs can pass the blood-brain- and blood–testis-barriers in addition to usual accumulation in RES organs. Biodistribution of the IONPs injected via the eye depends on their route of administration. For example, IONPs can enter into general blood circulation pool by retroorbital (as opposed to intraorbital) injection and reach other organs such as liver and targeted tissues.[78, 85] However, no traces of the IONPs were observed in other organs after their intravitreal injection.[283, 284] Nanoparticles administered by this method accumulated at corneal, retinal, scleral and optic nerves.[285] Intra-muscular and subcutaneous injections of the IONPs have been recently used for adjuvant-free malaria vaccine delivery[286] or non-invasive imaging of the sentinel lymph nodes to monitor breast cancer metastasis.[287, 288] However, more studies are required to determine the long-term biodistribution and clearance of the IONPs injected by these methods.

2.2.3. Biodistribution of IONPs in other organs and tissues

- **Brain:**

The blood capillaries found in different locations of the body are formed from endothelial cells and the exchange of small molecules (such as gasses, inorganic ions, monosaccharides and amino acids) between the blood and interstitial fluids occurs through the gaps between these cells. In the brain, endothelial cells are tightly fused in the capillary walls, due to some contribution by astrocytes. This forms a minimally penetrable layer, known as the blood brain barrier (BBB), that protects the brain from some toxins, hydrophilic molecules and in general, against many infectious agents (Fig. 2.10). Gasses and other hydrophobic molecules such as transport facilitating peptides can pass this barrier by diffusion through the hydrophobic lipid bilayer membrane of the cells. These peptides facilitate the transport of hydrophilic molecules (*e.g.* carbohydrates and amino acids) through the BBB.

Unfortunately, the BBB also prevents the delivery to the brain of desired therapeutics such as drugs and nanoparticles needed for a wide range of tumor diagnosis and treatment trials; consequently requiring more direct and invasive administration methods such as intracranial injections.[289] In order to avoid such invasive administration routes, researchers are taking advantage of the selective permeability of BBB transport facilitating peptides or sugars and other penetrating molecules to deliver therapeutic agents to the brain [290, 291] For example, it has been shown that when the IONPs are coated with a co-polymer of chitosan (a polysaccharide natural polymer) and PEG (d_H=30nm), they can pass the BBB.[114] This was attributed to 1.) the high lipid solubility of the amphiphilic PEG that increases the endothelial permeability of the IONPs, 2.) the electrostatic interaction between the cationic chitosan and negatively charged brain endothelium that may facilitate the adsorptive-mediated transport across the BBB and 3.) the small hydrodynamic size of the IONPs.[114] As another example, intra-peritoneal injection of silica coated magnetic nanoparticles has been reported as an effective method for facilitating the passage of the IONPs through the BBB.[281] This was described based on probable entry of the nanoparticles into the brain from

discontinuities of the BBB in ganglia. Raut *et al.*[292] have shown that application of an external magnetic field can also enhance the permeability of the BBB; however, the mechanisms of overcoming this barrier through these approaches and possible adverse effects when nanoparticles pass BBB are still under investigation.[293] A recent study used stereotactic injection of the IONPs to brain for effective stimulation of the neurons at deep brain tissues using an external magnetic field.[294] This opens new possibilities for treatment of various brain diseases such as Alzheimer or Parkinson using IONPs. The nanoparticles were in the injected area one month after their administration. However, the long-term biodistribution and clearance mechanisms and kinetics of these nanoparticles require further investigations. Preliminary studies by Engberink *et al.*[295] suggest that cervical lymph nodes play a key role as a drainage pathway for the IONPs accumulated in the brain after passing the BBB. The exact clearance mechanisms of the IONPs from the brain and their probable side-effects (*e.g.* human neurodegenerative diseases due to changes in brain iron homeostasis) require extensive studies.[296]

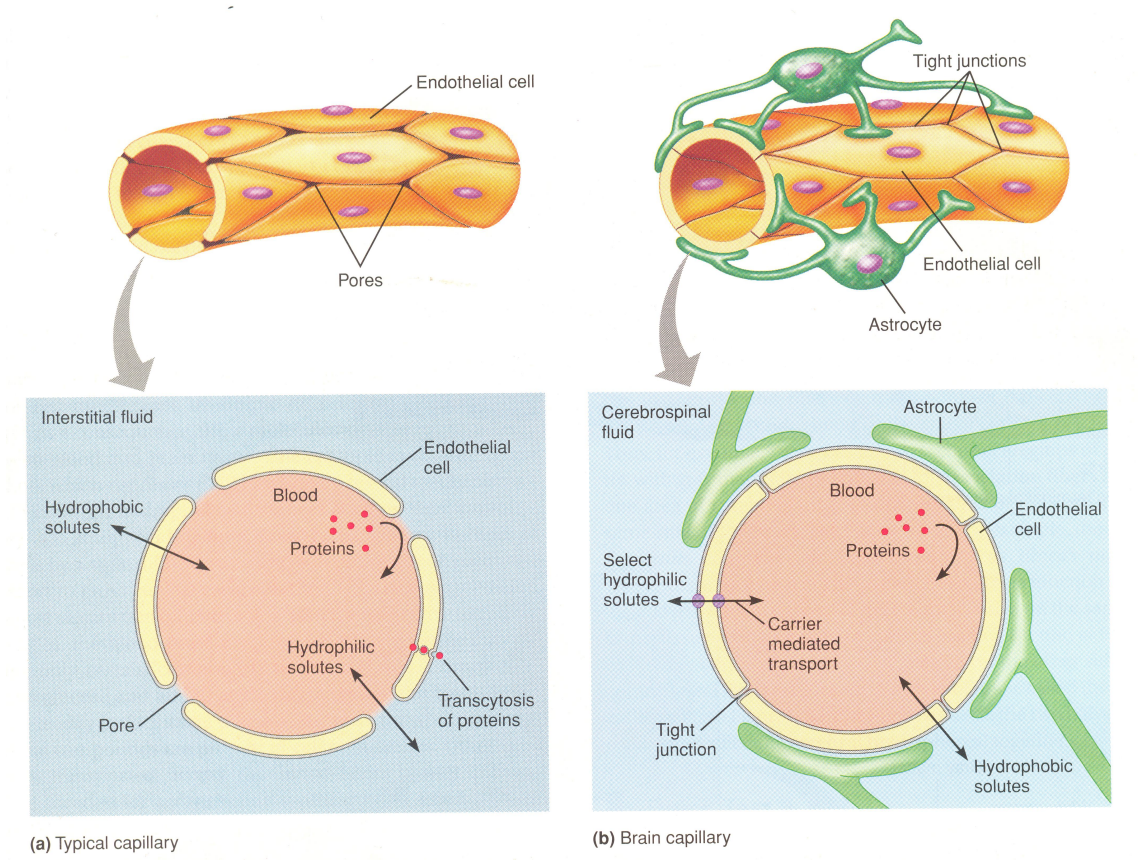

Fig. 2.10. Comparison of the typical blood capillaries found in most parts of the body (left) with the blood brain barrier (BBB, right). Small hydrophilic molecules can diffuse between blood and interstitial fluids through the pores between the endothelial cells in normal capillaries. Hydrophobic molecules and large size proteins can only pass this barrier by transcytosis. Endothelial cells in brain capillaries are connected by tight junctions. Proteins transcytosis is not possible in BBB and only selected hydrophilic molecules can pass the barrier by mediated carriers. Hydrophobic molecules can cross the BBB by transcytosis.[297]

• ***Tumors:***

Fast growing tumors require new blood vessels (tumor angiogenesis or neovascularization) or rerouting of the existing vessels adjacent to the tumors to provide enough oxygen and nutrition for their survival.[298] This generates abnormal fenestrated endothelial structures around the tumors that are highly permeable for IONPs.[225, 299] These leaky vessels, which lack any associated lymphatic drainage drive a unique process

known as the enhanced permeability and retention (EPR) effect (Fig. 2.11) that is helpful in the effective delivery of the IONPs to the solid tumors.[300] These inter-endothelial pores can be as large as a few micrometers.[298, 301] However, the desired nanoparticle hydrodynamic size (d_H) range to evade RES and renal elimination and enter the tumors by EPR is variably reported to be 30-200nm by Albanese *et al.*[34], 10-100nm by Ranganathan *et al.*[302] and 50-600nm (preferably smaller than 100nm) by Melancon *et al.*[100] Further, the exact range of the pore sizes and effective NPs size can vary in different species and different types of tumors. Nanoparticles larger than 100nm mainly get trapped in the extracellular spaces and cannot penetrate further after extravasation from these leaky blood vessels.[34, 303] However, smaller IONPs (d_H < 20nm) can penetrate deep into the perivascular area of the tumors, but they may have a short retention time because of hydraulic forces that can easily push them out of the tumor tissue.[34, 100, 304] After administration, these smaller nanoparticles can effectively evade liver and spleen uptake, but are rapidly eliminated from the blood by kidneys, specially for hydrodynamic sizes below 10-15nm.[305] A recent study has shown that IONPs decorated with tumor-homing peptides that can specifically bind to fibrin and fibrin-associated clotted plasma in tumor vessels can block blood flow through leaky tumor blood vessels and subsequently inhibit tumor growth.[306] Variations in the tumor targeted delivery of the IONPs through the EPR effect, might be due to differences in animal models and biological diversity of the tumors.[307]

In addition to the passive targeting mechanism described above, the IONPs can be directed to tumors, by attaching tumor specific antibodies or peptides to them.[308] These targeting molecules have high affinity for the unique receptor molecules found in specific tumor cells. Also, a magnetic field gradient can be used to drive the IONPs toward the desired location in the body.[57, 309] A recent study, for example, shows that using an external magnet around the tumor sites, significantly enhances the targeting ability of the peptide loaded IONPs and decreases the liver uptake.[310] However, in some cases IONPs redistribution through the RES organs (mainly liver and spleen) has been reported after removing the external magnetic field.[311] Such directed

accumulation of the IONPs in the tumors is called active targeting.[100] The effect of active targeting on enhancing the accumulation of the IONPs in the tumor tissue is currently unclear, because of contradictory findings reported in the literature.[34] For effective targeting the nanoparticles loaded with antibodies or targeting peptides should have a long blood circulation time, which requires evading the elimination through RES organs and kidneys. Therefore, as discussed in section 2.2.1.4, the hydrodynamic size range of 10nm $<d_H<$100nm is required to minimize the RES and renal clearance.[312] Usually the hydrodynamic size increases considerably after conjugation of the targeting molecules to nanoparticles. This decreases the targeting ability due to shorter blood half-life. On the other hand, larger number of the targeting molecules can improve the targeting efficiency of the nanoparticles. Therefore, optimum numbers of targeting molecules should be added to IONPs in order to ensure the longest blood half-life.[313, 314] The required number of targeting molecules on NPs depends on the type of the tumors and the affinity of these molecules for specific and selective binding to tumor cells.

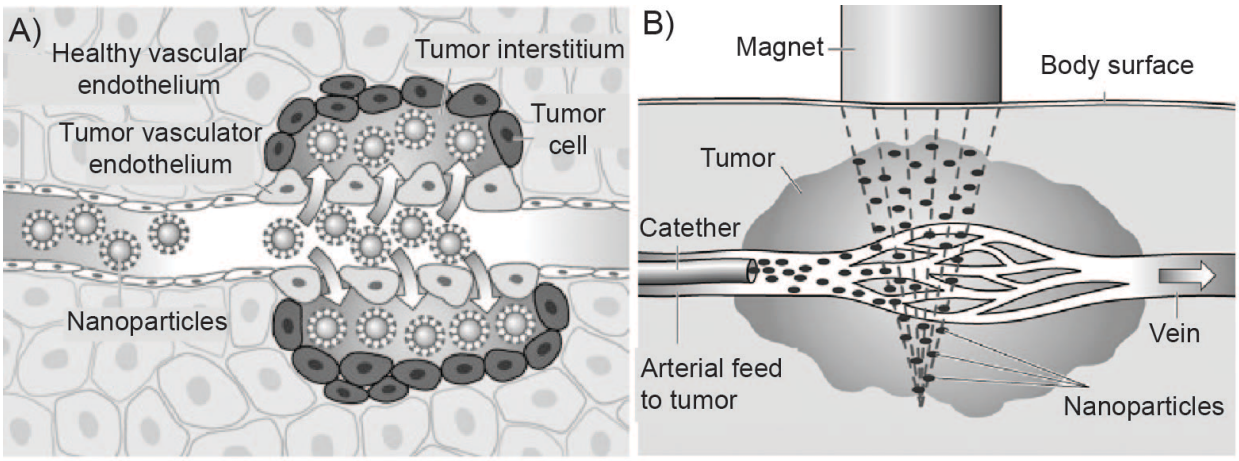

Fig. 2.11. (A) Tumors leaky vasculators and their enhanced permeability and retention (EPR). (B) Presence of an externally applied magnetic field can increase the accumulation of the IONPs in tumor area.[311]

• ***Skin:***

For all the administration methods and routes (*e.g.* IV, oral, intrapulmonary and intratracheal delivery) described in this chapter, there is usually no distribution of the IONPs to the skin. Recent studies, however, showed a transdermal pathway and distribution of the IONPs directed through an incision in the skin. Lee *et al.*[315] studied the penetration of the IONPs into the skin when physical (sonophoresis) and chemical (oleic acid) stimuli were used to enhance the permeability of the stratum corneum (SC) by disrupting its lipid bilayer structure. It was shown that even in the presence of these enhancers, only restricted penetration of the IONPs to SC-stratum granulosum (SG) interface or upper SG layer was observed. Baroli *et al.*[316], however, showed earlier that metallic nanoparticles can penetrate hair follicles and the SC layer and reach the skin epidermis, without application of any enhancer.

Ziv-Polat *et al.*[317] studied the clearance kinetics of the IONPs (d_c=20nm) from the incised rat skin. They found that 3 days after administration of the IONPs, they mostly resided in the extracellular spaces within the fibrin clot. The macrophages and fibroblasts actively took up the IONPs, so that after 8-14 days, IONPs were observed in both extracellular and intracellular spaces of these cells. Later, after 28 days, the majority of IONPs were cleared from the skin tissue with only negligible traces in intracellular vesicles of these cells. No further analyses were used to track the cleared IONPs or their degradation by-products in liver, spleen or kidneys.

2.3. Biodegradation and the fate of the IONPs in the body

2.3.1. Metabolic pathway of the IONPs

In a normal human body, 65% of the iron is present within the hemoglobin protein, 4% in myoglobin, 0.1% in transferrin and 15-30% in ferritin, which is mainly stored in the liver hepatocytes.[139] Ferritin (d_H~13nm) is composed of a protein shell surrounding an ultrasmall iron oxide nanoparticle in their central cavity (d_C~8nm) (Fig. 2.12).[151] Different types of protein coating structures have been reported for various animal

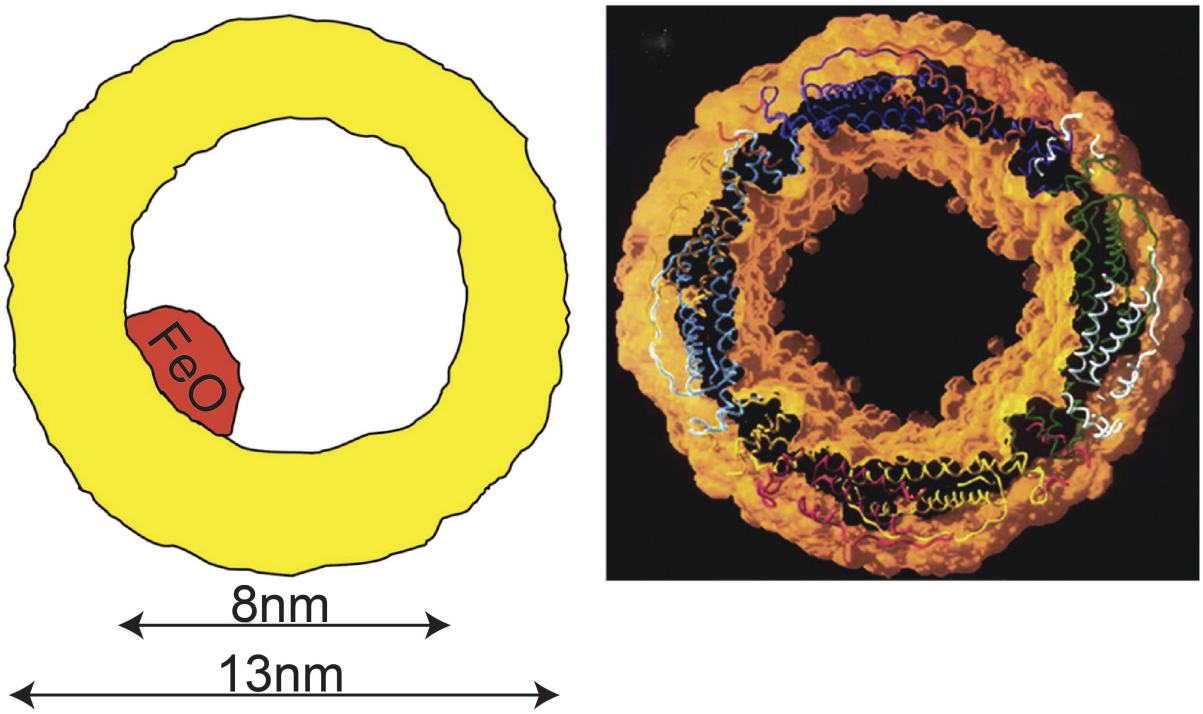

Fig. 2.12. Ferritin (~13nm) is the main form of iron storage in the liver after degradation of IONPs in macrophages. It is formed from a protein shell (~13nm) surrounding iron oxide ultrasmall nanoparticles in their central cavity (~8nm).[151]

models and human.[318] It is believed that the mechanisms involved in intracellular degradation of any IONPs are very similar to those related to ferritin. In ferritin, the protein shell first gets dissolved by lysosomal proteases and then the internal iron oxide nanoparticles get released followed by rapid dissolution in acidic environment of the lysosomes.[151]

After degradation of the IONPs, there is an excess of iron in the organs, which needs to be regulated through the innate clearance mechanisms of the body (Figs. 2.13 and 2.14).[319] Transferrin and ferritin are two principal iron-protein complexes that help to shuttle and store the iron ions resulting from the degradation of the IONPs in the body.[89] Nissim[320] and Richter[321] were the pioneering researchers who reported the *in vivo* biodegradation of the iron oxide particles and role of transferrin and ferritin in the biodistribution of their degradation by-products more than six decades ago. Related

investigations are still ongoing with the development of more advanced types of IONPs and characterization methods; for example, Levy *et al.*[105], recently used a combination of multiple magnetic characterization techniques (EPR and SQUID) accompanied by intracellular TEM imaging and ICP quantification techniques (see section 2.4. for description of these characterization methods) to precisely monitor the long-term (over three months) transformation of the iron oxide to ferritin in mouse liver and spleen.

Intravenously injected IONPs, taken up by the macrophages in different RES organs, especially liver and spleen, get dissolved in the acidic environment of the lysosome compartments of these cells.[322, 323] A slower IONPs degradation rate has been shown in spleen macrophages in comparison with liver Kupffer cells, as a result of the presence of less iron storage proteins available in spleen.[201] The degradation rate is also highly dependent on the type of materials coating the surface of the IONPs.[324] IONPs with coatings that allow limited water diffusion to their cores usually degrade slower in the macrophages.[325] Also, the degradation rate is slower for higher dosages of the injected IONPs.[326, 327] The released iron ions bind to iron-binding apoferritin proteins existing in the cytoplasm of the macrophages and form ferritin.[145] Iron ions can easily detach from the ferritin and bind to apotransferrin to form transferrin.[328] Plasma transferrin circulates in the body to transport iron to different tissues such as bone marrow and muscles (Fig. 2.13). In bone marrow they transform into hemoglobin in red blood cells (RBC) and in muscles they become myoglobin, an iron and oxygen binding protein responsible for carrying oxygen to muscle tissues in vertebrates.

In the bone marrow, transferrin can strongly bind to the receptors on the membrane of the erythroblasts, followed by endocytosis and release of the iron ions into the mitochondria to form hemoglobin, which later gets stored in the red blood cells as the principal oxygen carrier.[139, 145] Senescent RBCs (the lifespan of RBCs is about 120 days in humans) are fragile and burst in the tight capillary spaces of the red pulp in the spleen, thus releasing their hemoglobin. This can cause an increase in the amount of iron in the spleen as reported by Levy *et al.*[105] RES macrophages then phagocytize these hemoglobin molecules and transform a part of them into ferritin and then transferrin, which can again

go back to bone marrow, be used to make new RBCs or get stored in the liver hepatocytes in the form of ferritin.[329] This ongoing cycle maintains the iron ions in the body for a long time with a slow clearance rate (Figs. 2.13 and 2.14).[328, 330] Macrophages also transform a fraction of these hemoglobin molecules to bilirubin (a normal breakdown product of heme catabolism), which then gets excreted in bile and urine. If the amount of iron in the body is more than the available amount of apoferritin, large microscopic insoluble aggregates known as hemosiderin, form in the liver cells.[331] The iron-releasing rate from hemosiderin is much slower than ferritin.[331]

The iron ions released from the IONPs administered orally into the GI tract usually get absorbed through the small intestine. The apotransferrin protein secreted by the liver flows to the small intestine through the bile and then binds to these iron ions to form transferrin.[139] Transferrin molecules bind to the receptors of the intestinal epithelial cells and get internalized by pinocytosis and finally reach the plasma.[139] Transferrin transfers the iron ions into liver hepatocytes, where they release their loosely bound iron ions into the cytoplasm of these cells. Iron ions immediately bind with apoferritin to form ferritin as the main iron storage supply of the body and again iron enters the same metabolic cycle as the IV injected IONPs (Figs. 2.13 and 2.14). Generally, the GI absorption mechanism is much slower and less efficient than iron absorbed followed by IV injection of the IONPs, which is an important factor to consider when the IONPs are administrated for increasing the iron supply in the body for patients with anemia.[23, 332] However, delivery of iron orally is safer since overdosing via this route is difficult.

The clearance of the iron released from inhaled IONPs in the lung also follows the same mechanism by incorporation of ferritin and transferrin. Alveolar macrophages take up and degrade the IONPs and form intracellular ferritin. Released ferritin transforms to transferrin in the bronchial and epithelial lining fluids and eventually gets cleared quickly by lung mucociliary system.[262] Transferrin can be also transported to the RES system for the long-term storage, as described above.

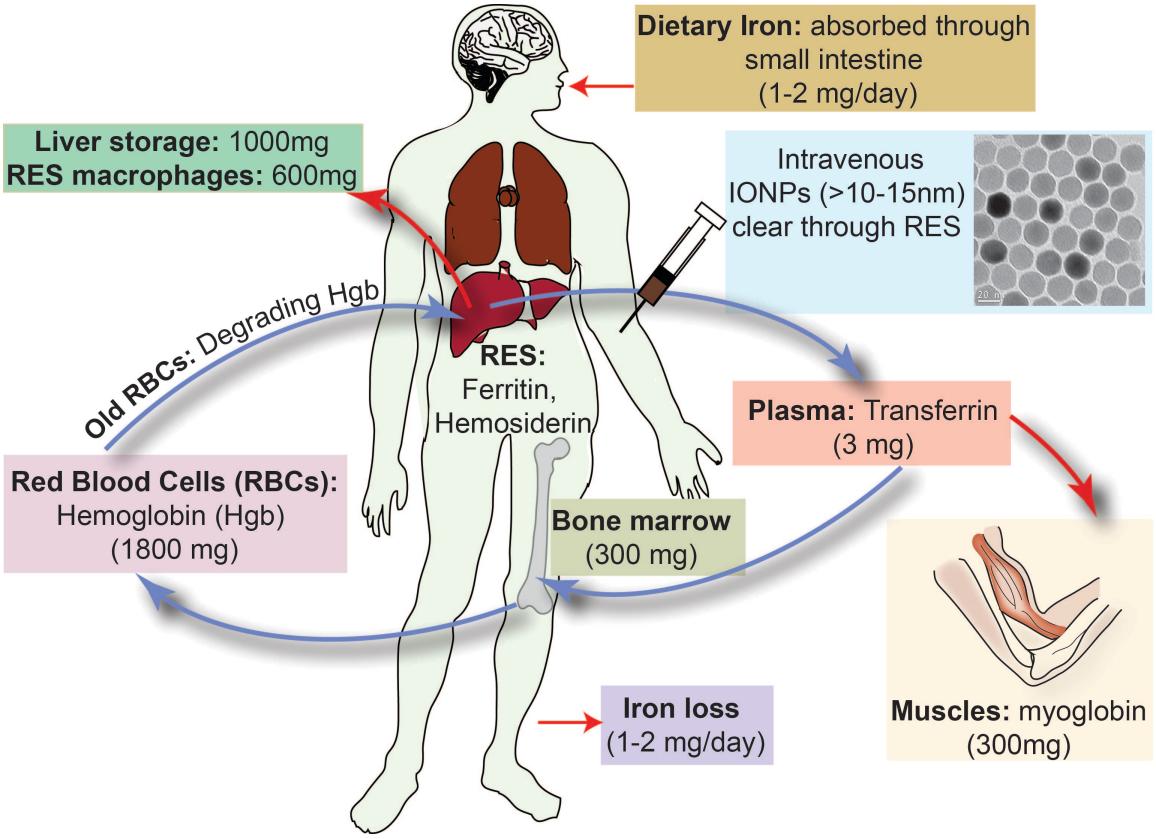

Fig. 2.13. IONPs biodegradation and general iron transport and metabolism pathway in the body. The intravenously injected IONPs, with hydrodynamic sizes larger than 10-15nm, get degraded in RES (or MPS) macrophages and free iron ions transform to ferritin and hemosiderin iron-protein complexes. Ferritin can transform to transferrin and then get transported to bone marrow, where they are used for making hemoglobin in red blood cells (RBC) that circulate in the body. A part of this iron also forms myoglobin, an iron-protein complex carrying oxygen to muscles. Senescent RBCs are fragile and burst in the tight capillary spaces of the red pulp in the spleen and release their hemoglobin. This can cause an increase in the amount of iron in the spleen. RES macrophages then phagocytize these hemoglobin molecules, form ferritin and again transform them into transferrin, which can go back to bone marrow to make new RBCs or get stored in the liver hepatocytes in the form of ferritin.

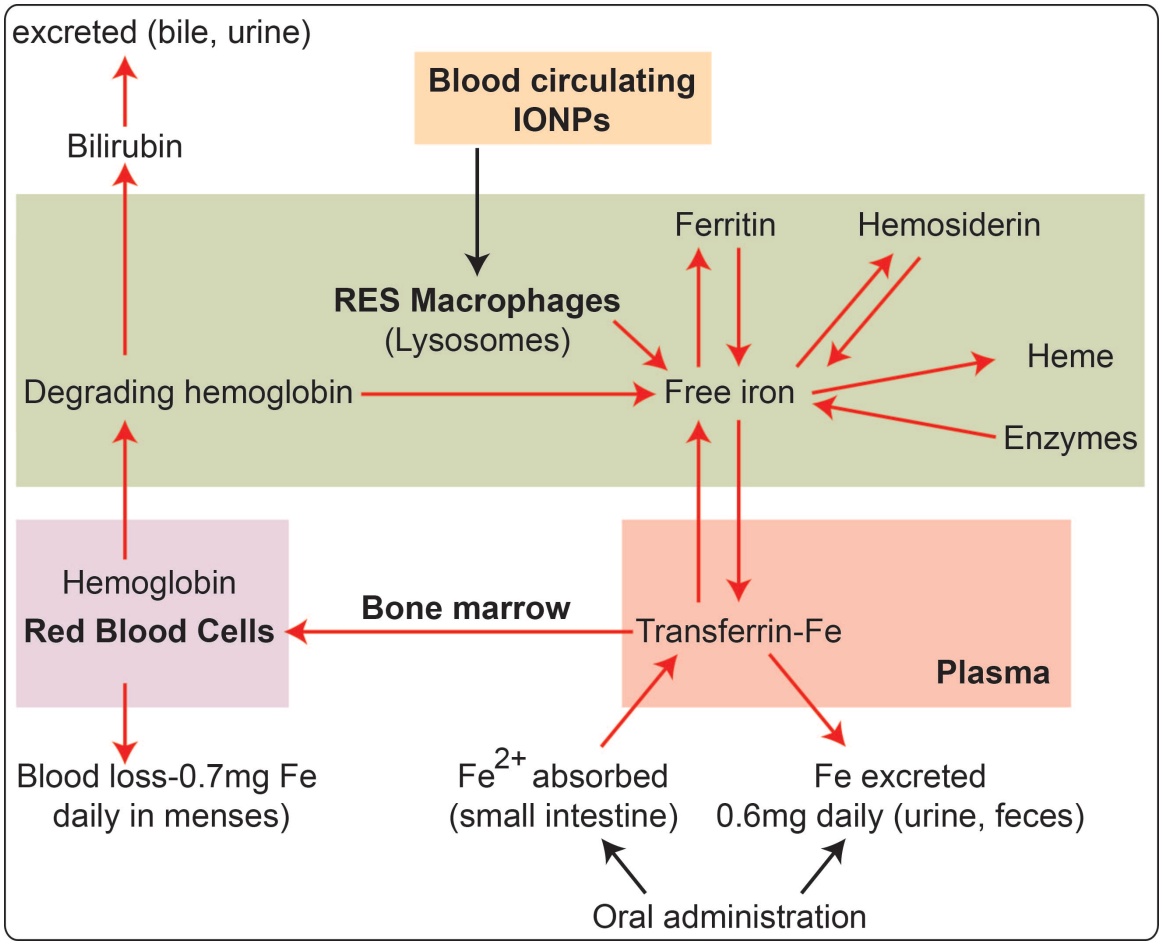

Fig. 2.14. Biodegradation, metabolic pathway and clearance of the IONPs after their intravenous injection or oral administration. Similar to Fig. 2.13, administered IONPs degrade and transform to ferritin and transferrin iron-protein complexes and enter the innate storage, blood circulation and recycling path, which usually takes a long time (up to several years) to get fully cleared from the body. Note that this slow clearance has been successfully used to increase the level of iron in blood for anemia patients.

The degradability and clearance of the coating materials should also be considered as an additional criterion for evaluation of the biodistribution of the IONPs. Radiolabeling of the iron oxide core and coating molecules is a common method for tracking of their movements along different excretion routes[333-335] or monitoring their integrity in blood circulation after administration.[336, 337] For example, labeling of the iron oxide core by ^{56}Fe and dextran coating by ^{14}C tags, showed that dextran molecules have a much

faster clearance kinetics compared to the iron core.[338] In a rat model, ~88.6% and ~12.9% of the injected coating molecules got degraded and cleared through urine and feces, respectively, after 56 days. On the other hand, only 16.8-21.8% and 1% of the administered iron was excreted in the feces and urine, respectively, and the remaining dosage was still circulating in the body as part of the iron metabolic cycle even 84 days after injection. Alternatively, conjugation of fluorophores to the coating molecules and optical microscopy of the urine and feces have also been used to monitor clearance through the kidneys and the hepato-billiary pathways.[152] However, it is important to test the co-localization of the iron and fluorescent signals to make sure that the fluorescent signal is not just from the detached coating or fluorescent molecules due to their faster degradation and clearance rates. In a separate study, Tate *et al.*[339] determined the amount of the IONPs in mice organs, 14 and 580 days after injection, and showed the complete clearance (e.g. through feces and urine) of the IONPs after 580 days. Note that this report only showed the results 14 and 580 days after injection without any intermediate time points and therefore the exact clearance time cannot be exactly established.

Iron ions resulting from the degradation of the IONPs can be incorporated in the RBC hemoglobin either as ferrous (Fe^{2+}) or ferric (Fe^{3+}) ions. However, only Fe^{2+} ions are active in transporting the oxygen molecules between lung and other tissues.[340] Simply put, this is because ferric ions are at their highest state of oxidation and cannot react with the oxygen molecules.[341] Ferrous ions from hemoglobin, on the other hand, make weak and reversible bond with oxygen molecules, which are then released from red blood cells as they circulate.[139] Methemoglobin reductase enzyme can reactivate the non-functional ferric ions of the hemoglobin by reducing their oxidation state to ferrous.[341] Therefore, there might be some additional variations in the metabolic pathway of the different forms of IONPs (*i.e.* FeO, Fe_2O_3 or Fe_3O_4) and future studies can be helpful to investigate their pharmacokinetics more precisely.[342] This is specially important for translation of MPI to clinics, since we have shown that magnetite (Fe_3O_4) is the desired iron oxide phase for ideal MPI tracers (Appendix A). Also, knowing the degradation rate

and final body clearance mechanisms of these ideal MPI tracers and their possible side-effects due to their larger core sizes (i.e. 23-27nm) is unknown and requires long-term biodistribution studies. Also, note that hemoglobin also transports carbon dioxide (CO_2), by forming a carbamate group between its terminal amino groups and CO_2 molecules.[343]

2.3.2. Organs half-lives

For safer application of the IONPs, the degradation rate of the IONPs in RES organs should be specified by their half-life in each organ.[87] For example, it has been shown that for lower injected dosages (1mg/kg body weight), IONP degradation in rat liver follows a mono-exponential decreasing rate, but for higher dosages (2 and 5mg/kg body weight), it is a bi-exponential function comprising two separate fast and slow decay curves.[330] Knowing the tissue half-life is also important in monitoring the retention time of the IONPs in tumors when their therapeutic applications such as controlled release of the drugs are desired.[93, 100, 344] The half-lives of the IONPs in different organs can be determined using the same techniques that are used for measuring their blood half-lives.[345]

2.4. Methods for determining pharamacokinetics and biodistribution of IONPS

Various methods have been used for the detection of very low concentration of IONPs in blood and organs (*i.e.* nanomoles of iron per gram of the tissue).[346] These methods can be roughly categorized into imaging, spectroscopy and magnetometry. Imaging methods used for characterizing biodistribution of IONPs include, but are not limited to, transmission electron microscopy (TEM), optical microscopy, MRI and MPI – a novel imaging modality that is sensitive solely to the magnetic signal from IONPs. The high magnification and resolution capabilities of TEM are helpful for observing IONPs distributed in the intracellular and extracellular regions of ultrathin tissue slices (*i.e.* 0.2μm).[347] Furthermore, TEM offers additional tools such as electron beam

diffraction[326] and elemental analysis[348, 349] that can be used to differentiate iron oxides encapsulated in ferritin from the crystalline and superparamagnetic IONPs encapsulated in the lysosomes of liver and spleen macrophages; thus, TEM can provide detailed information about the pharmacokinetic and degradation pathways of IONPs.[105] It should be noted, however, that TEM needs electron transparent samples requiring costly and elaborate preparation procedures. Furthermore, due to its small field of view, TEM only provides limited information from selected regions of the sample. New emerging techniques can be used as more feasible alternatives for TEM. For example, in a recent study by Abe *et al.*[157], a new non-destructive method called X-ray scanning analytical microscopy (XSAM) has been introduced for elemental mapping of iron in whole mice based on the analysis of energy-dispersed fluorescent X-rays in air, even when the samples contain water.

Histology, which is the analysis of tissue sections using optical microscopes, is a routine method that is usually more cost-effective than TEM and can provide helpful information about the distribution of iron ions (from the blood or IONPs) in larger areas of tissue. Tissue sections are chemically stained with Prussian Blue or similar chemical agents that are specific for identifying iron ions. However, Prussian Blue staining for histology has its limitations – the technique is only usable for visualization of the iron ions and may not detect IONPs prior to degradation.[107] Also, it can't distinguish the endogenous iron in tissues from the administered iron. For quantitative studies, tissue sections (*e.g.* 100-200mg) should be first dissolved in an acidic solution (*e.g.* 1mL, aqua regia). Then Prussian Blue should be added to this solution, followed by absorbance measurements at 690 nm to quantify the amount of iron in each sample compared to tissues excised from control mice.[350] As an alternative method, IONPs intrinsic peroxidase-mimicking activity can be used to catalyze the oxidation of peroxidase substrates and produce a color foci at the site of the nanoparticles accumulation in tissues. Zhuang *et al.*[351] reported a higher sensitivity and therefore more accurate quantification of iron in tissues by using this method compared with traditional Prussian Blue staining.

In addition to *ex vivo* imaging methods described above, *in vivo* imaging with MRI and MPI can be used for characterizing biodistribution of IONPs. MRI is a non-destructive method that has been extensively used for biodistribution studies of IONPs in live animals.[352] Although MRI with T_2 contrast has been extensively used for *in vivo* tracking of the IONPs, it is not optimal when high concentrations of IONPs are localized in the organs (specially liver and spleen), which saturates the T_2 signal and results in dark images without any specifically useful information. Hoopes *et al.*[353] used a new technique named as ultra-short T_2 MRI to generate positive contrast from the IONPs and overcome the sensitivity limitations of the conventional MRI. MPI can also generate real-time positive contrast images that are solely generated from the IONPs. The technique is based on the nonlinear magnetic response of the IONPs to an applied AC magnetic field which induces a signal that is localized with a strong DC magnetic field gradient – additional details about the imaging technique can be found Chapter 1.[1, 7] This method is still under extensive investigations and will be commercially available in the near future.[354, 355] Both MRI and MPI can detect very low iron concentrations down to nanograms per liter (ng/L) in solutions.[42, 356]

Elemental analysis with spectroscopic methods, such as inductively coupled plasma-atomic emission spectroscopy (ICP-AES), is often used for quantitative chemical analysis. It is a destructive method that is used for quantifying the amount of elemental iron in the acid digested tissues.[225] Reports have shown that this technique can determine the iron concentrations down to orders of nanomoles of iron per gram of the tissue (nM Fe/gr tissue)[346] However, like Prussian Blue staining, ICP-AES cannot differentiate the endogenous iron originating from the blood from the exogenous iron released from IONPs.[105, 134, 346] To resolve this challenge, Bellusci *et al.*[357] synthesized $MnFe_2O_4$ nanoparticles instead of pure magnetite (Fe_3O_4) and then using ICP, they measured the manganese concentration in organs to monitor the biodistribution of the injected nanoparticles in mice liver, spleen and kidneys. They reported that the maximum amounts of Mn in these organs were observed 6 hours after injection of these nanoparticles. However, addition of manganese may raise some toxicity concerns or

significantly change the magnetic performance of the IONPs. Also, the pharmacokinetics and clearance mechanisms of the released Mn ions might be significantly different from iron ions and we think such methods are only reliable for determining the biodistribution of the nanoparticles before their degradation.

Electron paramagnetic resonance (EPR), ferromagnetic resonance spectroscopy (FMR), magnetic susceptibility measurement (MSM) and superconducting quantum interference device (SQUID) are magnetometry techniques that can detect IONPs based on their superparamagnetic properties and can be efficiently used to delineate iron from the IONPs and the endogenous iron in the blood pool. EPR has been recently used as a convenient method for quantification of the IONPs in tissues with very high sensitivity (*i.e*. nM Fe/gr tissue).[310, 346, 350, 358] Sample preparation is easy, but destructive and only usable for pieces of tissues excised from organs.[105, 346, 350] SQUID magnetometry is also a highly sensitive method that can detect even very weak magnetic fields in the body, such as mapping the brain or gastric activities (*i.e.* magnetoencephalography and magnetogastrography, respectively). For biodistribution studies, however, it has been used for quantifying IONPs from tissues excised and prepared similar to EPR method. Due to technical limitations and high costs of the device, it has been used only for limited number of IONPs biodistribution studies.[77, 105, 134]

Labeling of the IONPs by radioactive atoms (*e.g.* ^{59}Fe,[338, 359], ^{111}In[360], ^{51}Cr[361] or ^{69}Ge[335]) or near infrared fluorescent molecules (*e.g.* Cy5.5,[83, 114, 362] SBD/SDA[363] or VivoTag 800[300] fluorophores) have also been used for quantification of the IONPs in the tissues. These methods are based on loading of these radiating species onto IONPs and then measuring the emitted radioactive or fluorescent signals of the tissue samples or organs at different stages of the pharmacokinetic studies. Both techniques are relatively costly and require special training and facility, particularly for radioactive labeling. Also, loading of the fluorophores might change the hydrodynamic size of the IONPs. A non-radiation approach has been introduced for biodistribution studies of the IONPs. Crayton *et al.*[364] first doped different types of

lanthanides (*i.e.* Ho, Eu, Gd and Sm) into different batches of IONPs with various sizes (d_H~15, 29 and 70nm) and surface charges (ranging from -20 to +14mV). They simultaneously injected these different types of IONPs to the same group of animals and then they used ICP to quantify each of these lanthanides in tissues to compare the pharmacokinetics and biodistribution pattern of these IONPs with different characteristics. Their biodistribution results confirm our conclusions discussed in previous sections of this chapter. However, we think using such multiplex studies help to determine the pharmacokinetics and biodistribution of different types of the MPI tracers (e.g. similar core sizes coated with different types of molecules) synergistically in only one experiment, without any concern for subject-to-subject variability. This can expedite screening of the MPI tracers for future in vivo application. However, in a recent study, Naha *et al.*[365] doped bismuth into IONPs, since this element enhances the contrast in computed tomography (CT) imaging. They showed a significantly different clearance pharmacokinetics for iron and bismuth ions after degradation of the nanoparticles and therefore, such studies are only valid before the degradation of the IONPs starts. Also, similar to drugs and small molecules, theoretical modeling of the pharmacokinetics of the IONPs can be used as an efficient and cost-effective approach to predict the biodistribution of the IONPs.[366] However, these studies are still in their early stages.

2.5. *In vivo* toxicity of the IONPs

Iron oxide nanoparticles are generally considered as safe, biocompatible and non-toxic materials. LD-50 (the median lethal dose or the dose required to kill half of the tested animals during a specified time) of the uncoated iron oxide nanoparticles was reported to be 300-600 mgFe/kg body weight.[367] This value was increased to 2000-6000 mgFe/kg when the IONPs were coated with stabilizing and biocompatible dextran molecules.[367] A LD-50 value of 35 mmol Fe/kg was also reported for carboxy-dextran coated IONPs.[74] However, systematic toxicity studies are required when different types of molecules such as synthetic capping agents (*e.g.* oleic acid and oleyl amine) or

different types of polymers, fluorophores and radioactive tags, or other therapeutic molecules are incorporated into the coating layer of the IONPs.[134]

2.5.1. Toxicity of the IONPs in animal models

In vivo toxicity studies of IONPs in animal models usually need long-term monitoring investigations for months or even years,[338, 339] due to prolonged circulation of the degraded IONPs in the body. Measurement of the LD-50 of the materials historically raised some ethical concerns due to sacrificing of a large number of the animals.[368] However, use of traditional LD-50 testing is no longer required by the FDA. Different degradation rates and pharmacokinetics of the iron oxide cores and coating molecules make the studies even more complicated.[159] For example, while almost all the dextran molecules coating the IONPs were cleared from rats 56 days post-injection, about 80% of the injected IONPs were still circulating as iron-protein complexes in the blood after 84 days.[338] Due to this complexity, most of the toxicity results reported for IONPs are based on *in vitro* assays, in which the metabolic activity of a limited number of cell lines are measured for toxicity evaluation of IONPs. Although these experiments provide very helpful preliminary information, their results might not be necessarily applicable for all the different cell types and organs present in the body.[369] Nor may they satisfy regulatory requirements.

Toxicity in animal models is studied by evaluating changes in blood chemistries and variation of blood cell parameters, gene expression profiles in liver or change in gross or histologic features of organs as well as monitoring clinical and weight changes (among other endpoints) after administration of the IONPs.[134, 159, 370] Jain *et al.*[371] studied the toxicity of Pluronic coated IONPs (d_H=186-206nm in water) in rats, by monitoring the amount of alanine aminotransferase (ALT), aspartate aminotransferase (AST) and alkaline phosphatase (AKP) in serum after injection of the nanoparticles. Also, the amount of lipid hydroperoxide (LHPO) in different tissues were used to analyze the levels of their oxidative stresses due to administration of the IONPs. They showed that the IONPs only caused minor transient changes, over a period of 6-24h in the liver

enzyme levels. The small amount of oxidative stresses in different tissues also declined after 3 days. These results were also confirmed, by histological analyses of the organs, showing no apparent abnormal changes. In a recent study, Yang *et al.*[159], analyzed the gene expression changes in mice liver after injection of IONPs with core sizes of 10, 20, 30 and 40nm and hydrodynamic sizes of 14, 25, 34 and 43nm, respectively. Their preliminary results (1 and 7 days after injection) showed that smaller nanoparticles (i.e. 10 and 20nm IONPs) induced more changes in expression level of some susceptible genes such as Pcsk9 (proprotein convertase subtilisin/kexin type 9) and Hmox1 (heme oxygenase 1), indicating oxidative stress and possible changes in metabolic processes.

Gu *et al.*[134] also studied the *in vivo* toxicity of the monodisperse oleic acid capped IONPs (d_C = 5, 15 and 30nm), coated with a layer of phospholipid-PEG co-polymer. Their hematology studies showed an increase in the number of neutrophils, 1 day after injection, which returned back to its normal amount through the next 30 days. This was attributed to the host defense response of the body to the presence of IONPs. There was also a consistent increase in ALT and AST enzymes possibly due to transfer of oleic acid molecules from liver macrophages to hepatocytes. No consistent effect of core size on these parameters was reported in this investigation. All the other parameters were within the normal range. The differences between the results of this report and those shown by Jain *et al.*[371] for Pluronic coated IONPs was attributed to different species (mouse vs. rat) and the IONPs preparation approaches.

Monge-Fuentes *et al.*[370] also did a series of toxicity evaluations for dimercaptosuccinic acid (DMSA) coated IONPs in monkeys. Previous reports have shown some preferential accumulation in lung[372, 373] and brain[374] for DMSA coated IONPs, due to some unknown mechanisms. However, no significant toxicity issue was observed in the nonhuman primate models during the 120-day study period.[370]

Feng *et al*.[375, 376] reported that surface chemistry and size of the IONPs can affect the lipid, glucose and amino acid metabolism pathways, by disturbance of renal, hepatic and cardiac performance. Using high-resolution nuclear magnetic resonance (NMR) coupled with multivariate statistical analysis, they analyzed urine, plasma, spleen, liver

and kidney in rats after administration of the dextran coated and uncoated IONPs. They observed metabolic changes such as elevation of urinary α-hydroxy-n-valerate, o- and p-HPA, and nicotinate, decreasing levels of urinary α-ketoglutarate, succinate and citrate, gradual increase in plasma glucose, saturated fatty acid, and individual amino acids and decrease of plasma unsaturated fatty acid and triacylglycerol.

Similar to IV injected IONPs, the type of the coating material plays an important role in toxicity level of the IONPs administrated through intranasal pathway. Park *et al.*[377] showed that intratracheal instillation of uncoated IONPs causes multiple adverse effects such as decreasing the level of intracellular reduced glutathione in the cells of bronchoalveolar lavage (BAL) fluid, increasing of pro-inflammatory cytokines in BAL fluid, expression of inflammation related genes and formation of microgranuloma. No toxicity was found when IONPs were coated by an anti-biofouling cross-linked polymer and administered through the same pathway.[261] However, silica coated IONPs did not show any pulmonary effect, but changed the level of the white blood cells in the blood and caused extramedullary hematopoiesis in the spleen.[269]

The oral administration of lower doses of the IONPs has also been reported as a generally safe route, with mild side effects such as nausea, vomiting or flatulence.[378] A study reported by Wang *et al*.[379] showed that increasing the dose of the IONPs ($d_H \sim$ 44nm, from 300 to 1200 mg Fe/kg mice weight, did not change the splenocyte proliferation and release of cytokines but changed the proportions of the T-lymphocyte subsets in peripheral blood, showing that higher doses influenced the immune function of the mice. Also, acute oral exposure to IONPs can cause severe side effects such as inhibition of acetylcholinestrase in red blood cells, inhibition of $Na^{(+)}$-$K^{(+)}$, $Mg^{(2+)}$, and $Ca^{(2+)}$-ATPases activities in brain and activation of the hepatotoxicity marker enzymes in serum and liver.[380] Di Bona *et al.*[381] also reported that intra-peritoneally injected IONPs can easily cross the placental barrier in pregnant mice and increase the risk of fetal deaths due to excessive accumulation of the IONPs in the fetal liver.

Overall, IONPs have shown a promising performance in numerous *in vivo* experiments during the last three decades, specially compared with contrast agents of

other imaging techniques, such as Gd-based agents for MRI or radionuclides for PET. Therefore, IONPs seem to be the most clinically safe type of contrast agents for MPI. IONPs long-term successful history in pre-clinical and clinical trials expedites the development of MPI and its translation to clinics. In the next section, we will summarize the most recent results of IONPs clinical trials, which further supports the general safety of these type of contrast agents for MPI.

2.5.2. Clinical safety of the IONPs for human

Extensive pre-clinical and clinical research has been done during the last two decades to evaluate the side effects of IONPs administered to humans. However, these studies have been limited to dextran coated IONPs (*e.g.* Ferumoxide or Feridex, Fermoxytol or Feraheme, Resovist) by IV injection and silica coated IONPs (Ferumoxsil) by oral administration. Satisfactory toxicological profiles with no clinically significant side effects have been reported for these IONPs according to the standard pharmacological tests, following either IV injection[382] or oral administration.[378] A recent study using Ferucarbotran (Resovist) to map lymph node metastasis in 22 patients with thoracic squamous cell esophageal cancer showed no side effects from the IONPs.[383] Howarth *et al.*[384] used another type of dextran coated IONPs (Sinerem) for diagnosis of carotid inflammatory plaques in 20 patients without any adverse side effect. In another human trial, the safety of Ferumoxtran-10 was tested in 1777 adults and at least one adverse effect (*e.g.* back pain, pruritus, headache, and urticarial) was reported for 23.7% of the patients.[385] 7 patients (0.42%) experienced severe adverse effects (*e.g.* anaphylactic shock, chest pain, dyspnea, skin rash, oxygen saturation decreased, and 2 cases of hypotension). Also, one death was reported due to bolus injection of un-diluted IONPs. Bolus IV administration is no longer recommended for IONPs. This resulted in development of a safer formulation using lower molecular weight dextran to coat IONPs (Ferumoxytol or Feraheme).[382]

One of the most recent developments in the clinical applications of IONPs, is the approval of Ferumoxytol (or Feraheme) in June 2009 by the US Food and Drug

Administration (FDA) for the treatment of iron deficiency in adults with chronic kidney disease.[32] Later in 2012, these IONPs also received European authorization, with a brand name of Rienso.[386] A high dose tolerability of up to 510mg in one injection and an increase in hemoglobin level has been reported in patients using this product.[387] In a recent study, no serious adverse events were observed in 396 US patients following a total of 570 IV injections of these IONPs.[41] 22 patients reported minor adverse side effects such as headache, myalgia, nausea, chest discomfort, flushing, nasal congestion and pruritus or needed modified injections. Also, Hasan *et al.*[388] studied the unstable cerebral aneurysm by early uptake of these IONPs and none of the 22 patients experienced any adverse events. In a one-year retrospective observational study of 8666 US patients treated with IONPs, some severe adverse effects, including hypotension (0.12%), hypersensitivity (0.06%), dyspnoea (0.05%), loss of consciousness (0.03%), syncope (0.02%), unresponsive to stimuli (0.02%) and anaphylactoid reaction (0.02%) were reported.[382, 389] Gastrointestinal effects such as nausea, vomiting, abdominal pain, diarrhea and constipation were among the most frequent adverse effects reported in a clinical study of 1562 patients reported from Europe and ~7.9% of the patients experienced some adverse effect.[386] However, some investigators still believe that the possible long-term safety effects of these IONPs have not been fully evaluated.[390] Also, note that this 510mg is a relatively high dosage and for MPI applications in human (e.g. cardiovascular or cancer imaging), we estimate a much lower dosage of intravenously injected IONPs, due to high tracer mass sensitivity of the MPI. The exact dosage range for human MPI applications is still unknown and requires preliminary animal experiments.

2.6. Chapter Summary and future outlook

Iron oxide nanoparticles incorporate excellent biocompatibility and safety factors with their unique magnetic properties, which can be easily optimized by tuning their size and distribution. Therefore, they are one of the most reliable candidates to be used in a wide range of biomedical applications such as cancer imaging and therapy, magnetic

separation of malignant cells and stem cells labeling. These factors have made IONPs the most favorite type of tracers for MPI, too. Generally, clinical success of the IONPs in any clinical application, including MPI, depends on three major parameters: pharmacokinetics, short and long-term tolerability in the body and therapeutic or diagnostic functionality in the desired organ. Biodistribution and toxicity of injected dextran coated iron oxide was first tested in animal models in the 1940's by Nissim.[320, 391] In spite of the extensive research accompanied by development of more advanced characterization techniques and instruments during the previous six decades, there are still major un-answered questions regarding the preparation of safe and effective IONPs for different types of clinical diagnostic and therapeutic applications. These questions (as discussed in this chapter) are potentially among the most important challenges against the translation of MPI to clinics, too.

For example, different types of IONPs prepared by various synthesis methods and functionalized with a diverse range of coating molecules have been introduced for various diagnostic and therapeutic applications, during the last decades. However, clinical trials have been done for only two families of IONPs, *i.e.* those coated with polysaccharides or silica. Therefore, careful consideration of the barriers against the clinical approval of conventional IONP formulations facilitates development of safe MPI tracers. In reality, various IONPs characteristics such as core and hydrodynamic size, morphology, size polydispersity, surface charge and type of the coating molecules affect the *in vivo* performance of the IONPs significantly. Other experimental variations such as method of administration, variations between animal models and humans, and different characterization techniques used can be also considered as influential factors. Preparation of standard databases for categorizing different pharmacokinetics, biodistribution and toxicity results based on specific IONPs characteristics and well-defined experimental factors can help investigators to find the required information in a much faster and cost effective way. The same approach has been successfully used for categorizing the mechanical, physical and chemical properties of a wide range of metallic alloys and compounds based on their elemental composition and complex processing parameters.

These materials databases have been used as one of the key tools during the industrial revolution of 20th century. This can help to efficiently address various clinical challenges by providing a wide range of valuable proof-of-concept results. It can also expedite advancement of translational MPI researches.

As another example, the effects of various additional molecular parameters such as mechanical flexibility or rigidity, molecular weight, density on the surface of the nanoparticles and molecular structure (*e.g.* presence of side-chains, functional groups on the backbone) of the coating molecules on pharmacokinetic performance and consistency of the IONPs need to be studied systematically. Also, effects of size, administered dose and crystalline structure of the iron oxide (amorphous, FeO, Fe_2O_3 or Fe_3O_4) on their degradation rates in RES macrophages and transformation to plasma ferritin are still unknown. This is specially important for optimal MPI tracers (see next chapters) synthesized by thermal decomposition method, since there is no systematic report showing the size dependent degradation and clearance of these type of IONPs in animal models. Recently developed characterization tools with higher mass sensitivities should be utilized to study these effects in more accurate ways.

The parameters summarized above should be carefully considered for designing of tracers for MPI applications. In addition, MPI signal quality (i.e. spatial resolution and intensity) is highly dependent on core size of the iron oxide nanoparticles (see Chapter 3). We will show later in this thesis that optimum core size for getting the best MPI image quality is about 23-27nm (Appendix A). In addition, using larger core sizes results in larger hydrodynamic sizes and shorter blood circulation half-life (see section 2.21.4). Such shorter half-life may decrease the effective targeting of the tissues (such as cancers or heart lesions). Therefore, controlled surface chemistry approaches used for phase transfer and functionalization of these larger core sizes should be consistent with optimal MPI performance. For example, we have seen that using PEG molecules with larger molecular weights (i.e. 20 or 30kDa) enhances the stability of MPI tracers with larger core sizes (see Appendix B) and increases their blood half-life. Also, conjugating targeting peptides (e.g. lactoferrin or RGD) to IONPs or using external magnets to direct

them to desired tissues help to increase the targeting efficiency of these optimal MPI tracers. However, the addition of these targeting peptides increases their hydrodynamic size and therefore, decreases their blood circulation half-life. Also, degradation rate and long-term side-effect of these larger core sizes (d_c~23-27nm) are still unknown. In addition, phase transfer and functionalization of these larger core sizes is much more challenging compared with smaller core sizes, probably due to magnetic interaction of these larger core sizes which are close to the borderline size limits of superparamegnetic to ferromagnetic transition.

In summary, we suggest considering the following criteria and parameters for designing optimal MPI tracers:

1 - MPI signal intensity and spatial resolution improves significantly by increasing the core size of the IONPs to 23-27nm. In Chapter 3, we study the effect of core sizes. We also show that increasing the core size to 25-27nm can significantly improve the MPI signals (Chapter 5 and Appendix A).

2- Phase transfer and functionalization of these larger core sizes is more challenging, requiring larger coating molecules such as 20kDa PEG. In Chapter 5 and Appendix A)., we show that using a co-polymer of PMAO and PEG (20kDa) can effectively enhance the stability of these larger size IONPs.

3- Specific surface chemistry approaches should be used to increase the blood circulation time of the MPI tracers, specially when conjugation of targeting peptides to IONPs is desired for tissue targeted MPI application. For example, in Chapter 4 we show that selection of a proper PEG derivative (i.e. heterofunctional PEG, NH_2-PEG-NH-FMOC) can increase the blood circulation half life, compared with bi-fucntional PEG (NH_2-PEG-NH_2) . Also, in Chapter 5, we show that using a co-polymer of PMAO-PEG (20kDa), in which the PEG chains are functionalized with maleimide groups can be effectively used for conjugation of a brain cancer targeting peptide (lactoferrin).

4- Long-term side effects, degradation rate and clearance mechanisms of the monodispersed IONPs with optimal core sizes need more systematic *in vivo* studies.

Chapter 3.

MPI PERFORMANCE OF IRON OXIDE NANOPARTICLES IN BIOLOGICAL ENVIRONMENTS

MPI signals can be generated from a combination of Néel relaxation, Brownian rotational diffusion and hysteretic reversal mechanisms of NPs in response to applied magnetic fields. These mechanisms will be discussed in section 3.1.When specific targeting of organs, such as carcinoma and endothelial cardiovascular cells are needed, different behavior may be expected in immobilized NPs, due to complete or partial elimination of the Brownian motion. Also, after cellular uptake, the internalized nanoparticles, mostly accumulate in endosomes or lysosomes. This may lead to nanoparticles showing different MPI performance, due to their aggregation or degradation in acidic environment of these organelles (Section 3.2). In this chapter, we evaluate the MPI performance of the MPI tracers in different biological environments. We also present surface chemistry strategies to prolong the size stability and MPI signal consistency of our nanoparticles in biological media (Section 3.3).

3.1. Size-dependent ferrohydrodynamic relaxometry of MPI tracers in different environments

3.1.1. Introduction

Previously in our lab, we have investigated how the core-size, hydrodynamic-size, and the size distribution of the tracer, determine the MPI resolution and intensity.[13, 16, 392] These studies were performed when the NPs, dispersed in aqueous media, were able to move freely in response to the applied magnetic field. However, during *in vivo* imaging, the environment of the NPs is quite complex and free NP motion cannot be assumed. For example, in the case of specific targeted imaging, NPs may bind to the cell membranes and their magnetic relaxation behavior may be considerably different from

their free state.[28] Here, we are interested in understanding very generally how NPs will respond to an MPI excitation field in a variety of potential circumstances, as determined by the NP's magnetic properties, their surrounding environment, and the field amplitude and frequency. Therefore, it is important to understand the different magnetic reversal mechanisms, i.e. Brownian rotational diffusion, Néel relaxation, and hysteretic reversal, available to NPs when an alternating field is applied.[21] Brownian rotational diffusion occurs by the free rotation of magnetically blocked NPs with respect to the fluid to achieve an equilibrium orientation under an applied field.[393, 394] On the other hand, Néel relaxation occurs by thermally activated reversal of the moment within the NPs, and involves no physical movement of the NPs. Finally, for magnetically blocked NPs, hysteretic reversal can also occur if the applied field exceeds the NP coercivity, H_c. These mechanisms are shown in Figs. 3.1 and 3.2. The measurement time is also relevant, and when multiple mechanisms are available, the fastest one is expected to dominate, where reversal time is determined by NP core and hydrodynamic sizes, field amplitude, and field ramp rate.[395, 396] Therefore, in designing MPI tracers for any application, it is crucial to understand the contributions of these three reversal mechanisms, and how they relate to the NPs properties and environment, and to the frequency and amplitude of the applied AC field.[19]

In this part of the thesis, we investigated the size-dependent performance of MPI tracers under idealized local environments representing bound and free states, using MPS to evaluate tracer relevance in both the *system matrix* and *x-space* MPI formulations. To accomplish this, a thermal decomposition process was used to prepare hydrophobic iron oxide nanoparticles with various median core sizes, ranging from 7 to 22nm, all with narrow (~ ±3-5 nm) size-distributions.[392, 397] The nanoparticles were then transferred from chloroform to aqueous media using an amphiphilic co-polymer.[397] To create idealized bound states, in which NP motion was prohibited and to monitor the contribution of the relaxation regimes prior to and after phase transfer, the NPs were homogeneously dispersed and immobilized in tri-octyl-phosphine oxide (TOPO), which is solid at room temperature, and tissue equivalent agarose gel, respectively, and the

resultant MPS signal intensities (obtained from both *system matrix* and *x-space* approaches; see section 1.1 for details) and resolution (obtained from dm/dH measurements analyzed using *x-space* theory) were compared with freely moving NPs. Since the frequency is fixed (25 kHz) in our MPS system, we used different field amplitudes to study the contribution of the hysteretic reversal in the received signals. These comparisons enabled us to investigate the size and environmental dependence of NP's relaxation behavior. In particular, we hoped to better understand the NPs' response during targeted-imaging (Chapter 5), when Brownian rotation may be inhibited due to specific binding or perfusion into host tissue, as shown schematically in Fig. 3.1(a).

In summary, as it will be discussed in details during the next sections, we found that immobilized NPs with core diameters smaller than ~20nm have similar spatial resolution, but lower signal intensities when compared with their free rotating counterparts. Compared to their performance in solution, spatial resolution was improved, but signal intensity was lower, when larger NPs with core size of 22nm were immobilized in agarose. Same trends were observed in signal intensities, when considering either system matrix or *x*-space approaches. The harmonic and dm/dH signal intensities changed linearly and the spatial resolution did not change with decreasing NP concentration up to 15μg/mL.

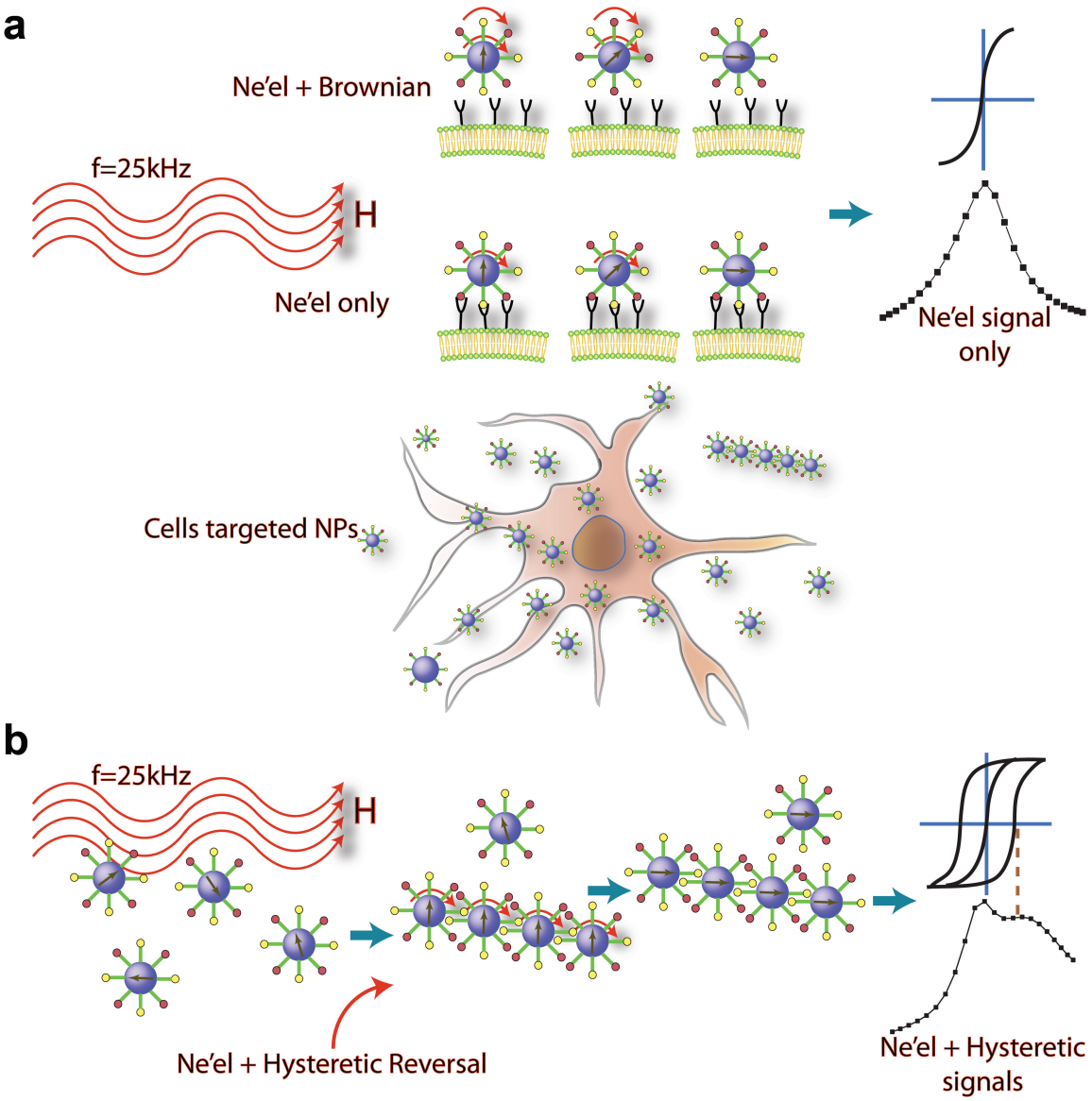

Fig. 3.1. Schematic showing the proposed contribution of Néel relaxation and hysteretic reversal on the tracer dm/dH obtained from a zero dimensional magnetic particles spectrometer. The relaxation of the NPs induced by the external sinusoidal magnetic field and the resultant MPI spatial resolutions are shown for immobilized and free-rotating NPs. The black arrows inside the NPs are representative of the intrinsic magnetic moment of the NPs. While, only Néel relaxation is expected for immobilized NPs (a), large NPs and clusters of NPs have non-zero coercivities, increasing the peak width or spatial resolution (b). It is assumed that the NPs shown in (a) have an ideal size distribution and do not show any hysteretic reversal. Also, Brownian relaxation is slower than Néel relaxation and has a substantially lower contribution to our measurements.

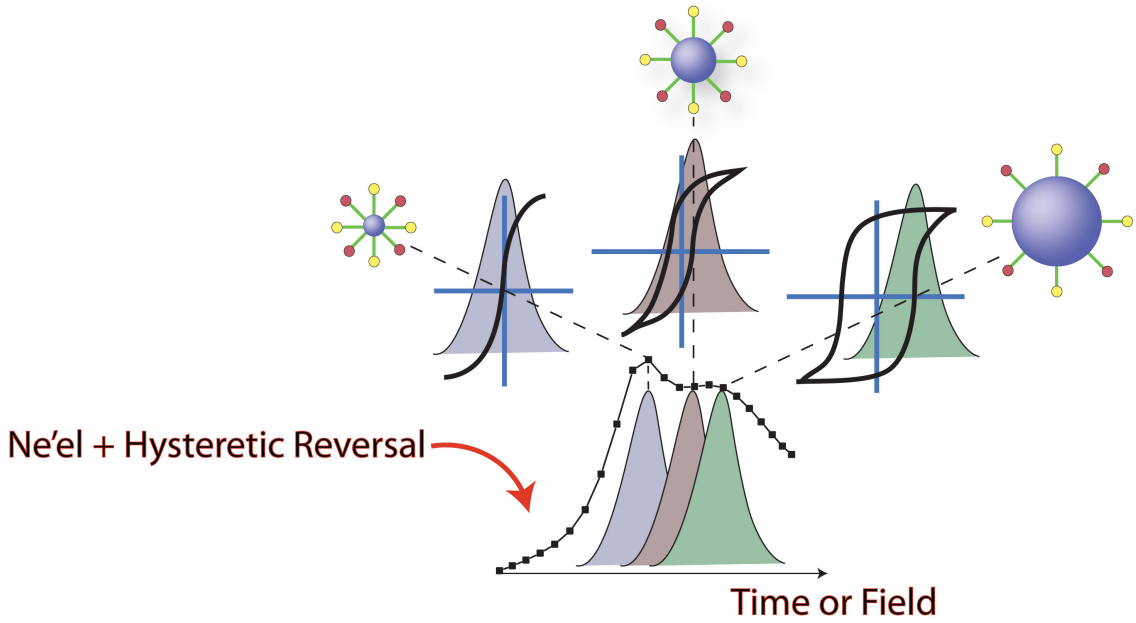

Fig. 3.2. Schematic showing that coercivity increases with increasing the core size of the NPs and therefore, monodispersity is crucial in order to get the highest resolution and intensity (c).

3.1.2. Synthesis of different sizes of magnetite tracers and their phase transfer

Iron oxide NPs were synthesized from pyrolysis of iron oleate (Fe-Ol) fatty acid salt, in the presence of oleic acid (OAc, tech grade 90%, Sigma-Aldrich, St. Louis, MO) and 1-octadecene (ODE, technical grade 90%, Sigma-Aldrich, St. Louis, MO), according to established protocols.[45, 392, 397] Iron oleate (Fe-Ol) was prepared by reacting sodium hydroxide (NaOH, 97%, Sigma-Aldrich, St. Louis, MO) with anhydrous iron chloride ($FeCl_3$, 98%, Alfa Aesar, MA) and OAc, following the method reported before.[398, 399] The purified Fe-Ol was stored in ODE with a concentration of 18 wt. % Fe-Ol. NPs were prepared by refluxing a mixture of Fe-Ol and OAc at 320°C for 24h under argon atmosphere. Median core sizes of the NPs were tuned accurately by adjusting the molar ratios of Fe-Ol:OAc as 1:0, 10, 15, 18, 19 and 20.

Phase transfer of the NPs was performed following our previous reports.[392, 400, 401] Amphiphilic co-polymer of poly(maleic anhydride-alt-1-octadecene) (PMAO, Mn =30,000-50,000, Sigma-Aldrich, St. Louis, MO) and methoxy poly(ethylene glycol)

(PEG, Mn = 5,000, Sigma-Aldrich, St. Louis, MO), was used for coating and phase transfer of the iron oxide NPs. PMAO-PEG was prepared by acid catalysis of mPEG and its ester bonding with anhydride ring of PMAO as we described elsewhere.[397] Purified NPs were collected by a strong magnet and dried in vacuum for 1h. 10mg of the hydrophobic NPs were dispersed in 1-2 ml of chloroform by sonication for about 1h. 10mg of PMAO-PEG co-polymer was added to this mixture. After sonication for about 1h the NPs were dried in argon and re-dispersed in 1mL of Tris-acetate-EDTA (TAE, 1x) buffer by sonication for 30min, followed by size exclusion purification (Sephacryl$_{TM}$ S-200 gel, GE healthcare Life Sciences, US) to remove un-bound polymer molecules and transfer the NPs to water. The NPs were stored in the refrigerator (~4°C) for further analysis.

3.1.3. Structural Characterization of the nanoparticles

Inductively Coupled Plasma Atomic Emission Spectrophotometer (ICP-AES, Jarrell Ash 955, MA) was used to determine the concentration of iron in the samples. The hydrodynamic sizes of NPs dispersed in water were measured by Dynamic Light Scattering (DLS, Zetasizer Nano, Malvern Instruments, UK), with mean diameters (intensity distribution) used for comparing samples and calculating Brownian relaxation times. Morphology and crystallographic phase structure of the NPs were investigated, by bright field imaging and selected area diffraction, respectively, using a Transmission Electron Microscope (TEM, FEI TecnaiTM G2 F20, 200 KeV, Hillsboro, OR), equipped with a Gatan CCD camera (Pleasanton, CA). TEM samples were prepared by depositing and drying a drop of diluted NPs suspension on carbon coated copper grids. The TEM and DLS results of the samples with different sizes are shown in Fig. 3.3.

3.1.4. Immobilization of the NPs

Certified molecular biology agarose (BioRad, Herculus, CA) and trioctyl-phosphine oxide (TOPO, 99%, Sigma-Aldrich, St. Louis, MO), were used for immobilization of the hydrophilic and hydrophobic NPs, respectively. The water dispersed NPs were mixed

with a 3 wt.% solution of the agarose (1:1 v/v) and were stored in the fridge for 2h, allowing for mixture gelation. Final agarose concentration was 1.5wt%, which is a standard value defined for having tissue-equivalent characteristics.[402] Pore sizes smaller than ~250nm were reported for Agarose gel prepared with the same concentration.[403] Solid TOPO was placed in a water bath (~50°C) and after complete melting was mixed thoroughly with chloroform dispersed NPs (1:1 v/v). Solidification of the TOPO occurs after about 5min at room temperature. Concentrations of the NPs were known in all liquid (1 to 2 mg/mL) and frozen (0.3-0.5 mg/mL) samples and vigorous mixing was used to assure their homogeneous dispersion in gel and TOPO. The saturation magnetization and MPI performance of these immobilized NPs were studied by VSM and MPS, respectively.

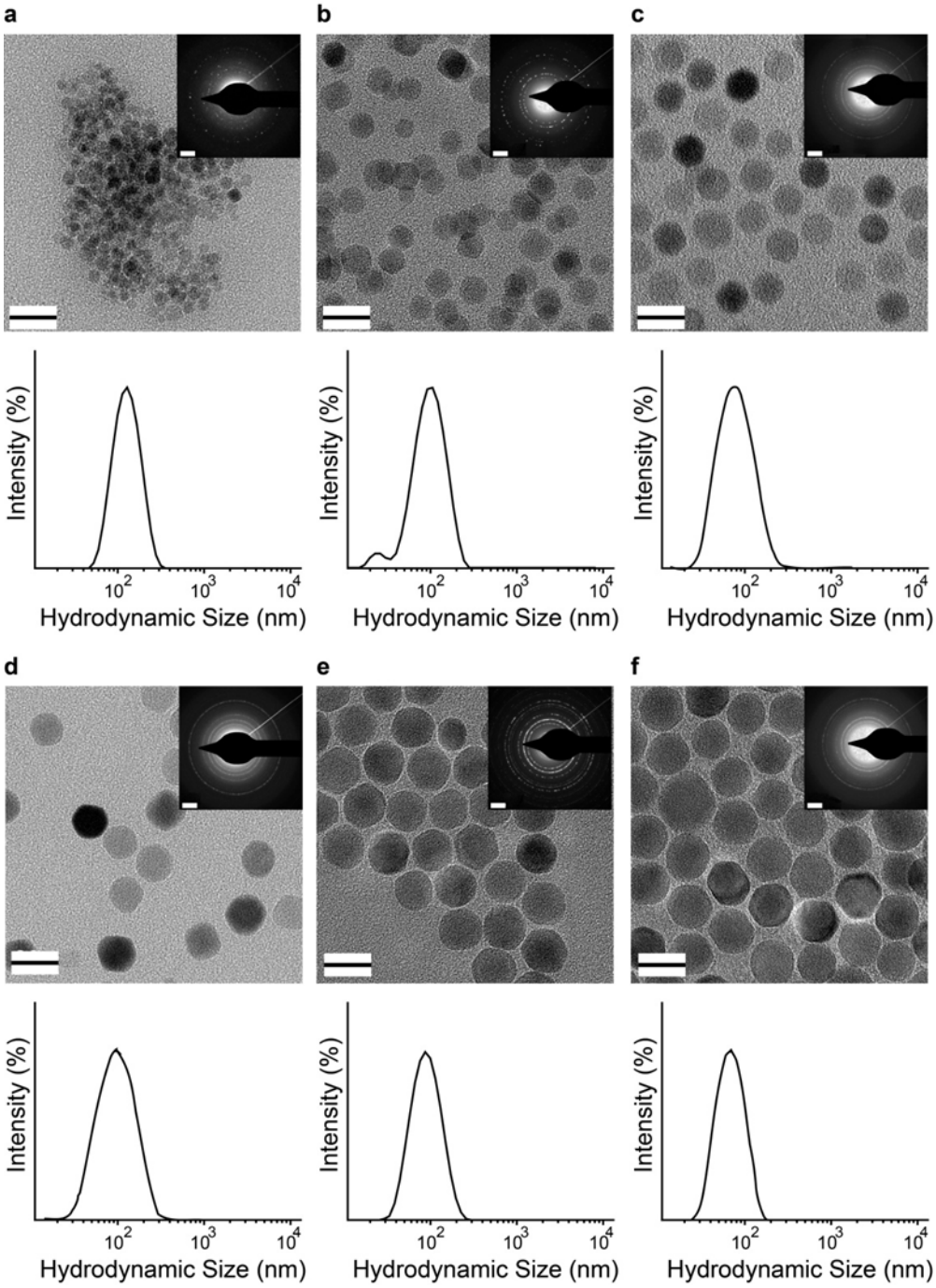

Fig. 3.3. Characterization of the NPs with different core sizes of (a) ~7, (b) ~12, (c) ~16, (d) ~18 (e) ~20 and (f) ~22nm: TEM, diffraction pattern and intensity based DLS. The TEM scale bars are all 20nm. The hydrodynamic sizes of these nanoparticles were in a range of 55-95nm. TEM images match well with magnetic core sizes of the NPs (shown in Figs. 3.4, 3.5 and 3.5) calculated using the Chantrell fitting.[404]

3.1.5. Magnetic characterization of the NPs

Liquid samples (~100μL, containing 100-200μg of NPs) were used to study the magnetization behavior (M vs. H) of the NPs by a room temperature vibrating sample magnetometer (VSM, Lakeshore, Weterville, OH). Agarose and TOPO dispersed samples were transferred to measurement vials before their gelation or freezing and then cooled down in the fridge in order to immobilize the NPs. The magnetization curve was fit to the Langevin function, using the Chantrell method, to determine the median magnetic core size (d_0) of the NPs.[404] This method is volumetric and gives the median core size distribution of a statistically significant number of NPs, better representing the total sample than TEM measurements.

The Brownian rotational diffusion time constant, τ_B,[393, 394] is

$$\tau_B = \frac{3V\eta}{K_B T} \quad (1)$$

where V is the hydrodynamic volume ($V = \pi * d_H^3/6$) of the NPs, η is the viscosity of the environment, K_B is the Boltzman's constant and T is the ambient temperature (Kelvin) and where small angles of rotation and small fields ($H \ll H_k$, where $H_k = 2K/M_s$ is the anisotropy field) are assumed. The Néel relaxation time (τ_N) for thermal excitation of the magnetization over an anisotropy barrier (KV) under an applied field, H, comparable in magnitude to H_k, a property of the material, is given by:

$$\tau_N = \tau_0 * \exp\left(\frac{KV*(1-\frac{H}{H_K})^2}{k_B T}\right) \quad (2)$$

Here, τ_0 is 10^{-10}s, V is the volume of the core iron oxide, H is the magnetic field [T/μ_0], and K (11 kJ/m^3) is the magnetocrystalline anisotropy constant for bulk iron oxide.[13, 17, 18] Note that for small field amplitudes, when $H << H_K$, the term $(1-H/H_K)^2$ can be dropped in the exponent.[405]

3.1.6. MPI signal testing of the NPs

As discussed before, MPI is a magnetic inductive measurement technique, in which a sufficiently large alternating magnetic field results in a non-linear magnetization response, M(t), from the magnetic tracers.[1] In a MPI scanner, signal localization for imaging is achieved by scanning a field-free point (FFP) across the imaging volume. In the *x-space* approach to MPI image reconstruction,[7] the imaging performance can be simply described by the point spread function (PSF), which is a product of the dm/dH, and the field gradient, dH/dx. Field gradient is a MPI scanner property. However, dm/dH is highly dependent on NPs (e.g. nanoparticles size and magnetization in different environments). Therefore, for a given imaging system, with a well defined field gradient, the spatial resolution and signal intensity in MPI can be maximized by decreasing the dm/dH full width at half maximum (FWHM) and increasing its peak height.[15, 406] Alternatively, in the frequency domain approach to MPI image reconstruction, a Fourier transform (**F**) of the signal, **F**(dM/dt) at each point in the imaging volume is performed and compared to a predetermined system function.[13, 14] **F**(dM/dt) is unique to the tracer performance and can be used, alternatively, to evaluate imaging performance.

Here, we used a custom-built MPS for MPI signal analysis of the NPs with various median core sizes, ranging from 7 to 22nm as well as commercial NPs Resovist^{TM} and Feridex^{TM}. The MPS excites magnetization in NPs using a transmit coil, and measures the voltage, V(t), induced in a receiver coil by the changing NP magnetization (details of the spectrometer can be found in our previous report).[16] The MPS signals, (dm/dH and harmonic spectrum) are calculated from the received voltage, V(t), (using a MATLAB program running with our MPS system, generated by Dr. Mathew Fergusson) and is used to evaluate the MPI performance of the NPs in the *system matrix* or *x-space* approaches, respectively. Procedures for obtaining these data are discussed in sections 3.1.6.1 and 3.1.6.2. For each measurement, 200μL of the samples with known iron concentrations were transferred to a 0.6mL microcentrifuge tube and each vial was inserted into the MPS coils, applying sinusoidal excitation fields of 5.1 to 18.6mTμ_0^{-1} (peak-peak, f_0=25kHz). The sample holder and instrument are designed to

ensure that the sample's position is always the same in the center of the coil. All MPS measurements were repeated three times and their average with standard deviation are shown in this thesis. However, the error bars were sometimes very small and are not seen in the plots.

3.1.6.1. Determination of NP dm/dH

Similar to other imaging systems, in MPI the PSF describes variation of the signal intensity with distance in the space around a point source in the imaging volume. It is the smallest observable signal source in the system, and therefore defines the spatial resolution of the image. The PSF can be recorded in one or more dimensions around this central point.[11] An image can be formulated as a convolution of the PSF with the distribution of point sources (tracer NPs) within the image volume. Full width at half maximum of the PSF determines the image resolution.

The MPS, which has no field gradient but only a sinusoidal excitation field, measures dm/dH(t). The dm/dH is essentially the instrument-independent PSF, in that it measures purely the NP tracer response to the excitation field. In *x-space* MPI, the PSF is simply the product of dm/dH and the known field gradient of the instrument and therefore the dm/dH gives the spatial resolution and signal intensity, along the excitation field direction of an arbitrary imaging system. [10, 11] The applied magnetic field in our MPS can be described as:

$$H(t) = H_0 \sin(\omega t) \tag{3}$$

Here, H_0 is the peak excitation amplitude listed above and ω is the field angular frequency ($2\pi f_0$), in which f_0 was 25kHz for all measurements described in this work.

The induced voltage can be calculated considering the rate of variation of the magnetic moment of the NPs with applied field, m(H), using the following equation:[19, 407]

$$V(t) = -\mu_0 . S. \left(\frac{d}{dt} m(t)\right) = -\mu_0 . S. \left(\frac{d}{dH} m(H)\right) . \left(\frac{d}{dt} H(t)\right) \tag{4}$$

in which, μ_0 is the magnetic permeability of vacuum equal to $4\pi\times10^{-7}$ Vs/Am and S is the coil sensitivity with unit of 1/m. Considering equation (3) and re-arranging equation (4), we have:

$$\frac{d}{dH}m(H) = \frac{-1}{\mu_0.S.\omega.H_0}.\frac{V(t)}{\cos(\omega t)} \quad (5)$$

Generally, dm/dH, which has units of (m^3), should be normalized by the quantity of iron in the sample. The resulting data [m^3/g Fe] is a useful metric for evaluating tracers performance in a MPI system, that is a function of only the applied field and the tracer properties. Here, we generated the dm/dH graphs according to equation (5), and normalized by iron mass as measured by ICP.

3.1.6.2. MPI harmonic spectra

The received voltage signal (V(t)) was divided by μ_0.S , defined above, to determine the magnetization as a function of time and then divided by field ramping rate ($\omega.H_0$). Then, harmonic spectra were generated by Fourier transform of the resulting data.[16] Again, all the harmonic values were normalized by the amount of the iron in each sample, to make the results comparable for all different core sizes.

3.1.7. Results

We considered several environments to demonstrate the range of responses available from our tracers: hydrophobic magnetic particles, with only an oleic acid ligand coating, were dispersed either in chloroform or immobilized in TOPO; biocompatible particles coated with PMAO-PEG were suspended in water, or immobilized in agarose gel. Gelatinous agarose is a tissue equivalent material that has been used extensively for modeling and evaluating NP relaxation behavior in MRI. Gelled samples represented the expected signal for NPs that have perfused into tissue.[402] TOPO is a dense solid at room temperature that inhibited the motion of the hydrophobic NPs.

MPS signals (both dm/dH and harmonic spectra) and hysteresis loops for different sizes of the NPs dispersed in four different media are shown in Figs. 3.4-3.6. Concentration normalized plots shown in Figs. 3.4-3.6 (left side columns) are generated according to sections 3.1.6.1 and 3.1.6.2. Inset graphs show dm/dH after normalizing intensity to compare the full width at half maximum of the peaks and correlate it to nominal spatial resolution. The range of measured harmonics (from third to thirty ninth) is also presented in Figs. 3.4-3.6 (middle column). The harmonic signals are shown after normalization by the amount of iron in the samples. Corresponding median core sizes of the NPs and their standard deviations were determined using Chantrell[404] fitting to the measured m(H) data shown in the right side column. As in previous experiments, we observed that NP size strongly influenced MPS performance.[16, 392] In each of the model environments we investigated, the equilibrium magnetization (m-H curve) and MPS signal (dm/dH and harmonics) both varied substantially with the magnetic core size as measured from 7 nm to 22 nm (Figs. 3.4 and 3.5).

Note that the number of harmonics detected depends on the drive frequency, and the MPS hardware. The MPS hardware, specifically the sampling rate of the data acquisition card, determines the highest harmonic that can be detected. In our case, our card samples at 2MHz, so 1MHz is the highest frequency signal we can detect. So with a 25 kHz drive field, we can get 40 harmonics, though the odd harmonics are much stronger, which is why we say we measure 39. If we decreased the frequency, we could measure more harmonics. With higher frequency we would measure fewer harmonics. However, we used 25kHz frequency for all measurements presented in this thesis.

Different values of peak excitation amplitude (H_0), were applied for analysis of the role of the hysteretic reversal on the behavior of the largest NPs (d_0=22nm, σ=0.38), in free-rotating (water) and immobilized (agarose), states. The corresponding dm/dH data and harmonic spectra are shown in Fig. 3.7(a) and (b). Plots of dm/dH are shown after scaling by iron concentration (mm^3/mg Fe), and scaled to one to enable comparison of their FWHM (inset). The harmonic spectra also show the intensity of the NPs responses at different amplitudes.

Generally, the magnetic properties of iron oxide NPs are highly sensitive to size, morphology and crystallographic structure.[22] Direct observation of the NPs with TEM revealed the typical morphology and structure of these NPs. As shown in Figs. 3.4 and 3.5, the median core sizes of the NPs increases from ~7 to 22nm, with increasing the molar ratio of the oleic acid to iron oleate from 0 to 20. The selected area electron diffraction patterns of the NPs (insets, Fig. 3.3), show bright and sharp spots, arranged as individual rings indexed as (200), (220), (311) and (400) of magnetite, from inner rings to outer rings, respectively. Finally, electron energy-loss fine structure measurements[408] and analysis,[409] has confirmed that the nanoparticles are predominantly magnetite (Fe_3O_4).

Since the hydrated size of the NPs is very important in determining their biological performance, the hydrodynamic size distributions of the NPs in aqueous media are also shown in Fig. 3.3. Hydrodynamic size also determines the Brownian relaxation time of the NPs, which – according to equation (1) – varies between 84 and 283 microseconds for the measured range (55 – 95nm) of diameters.[13] The DLS results shown here are based on the intensity percentage distribution of the NPs after surface modification with PMAO-PEG co-polymer. The results show that the hydrodynamic size (Z-average) of the NPs are distributed in a narrow range of 55-95nm with polydispersity index (PDI) of 0.18-0.23 for all core sizes. A single peak in the DLS spectrum also shows that the phase transfer typically resulted in uniform hydrodynamic size distribution and individually polymer-coated stable NPs.

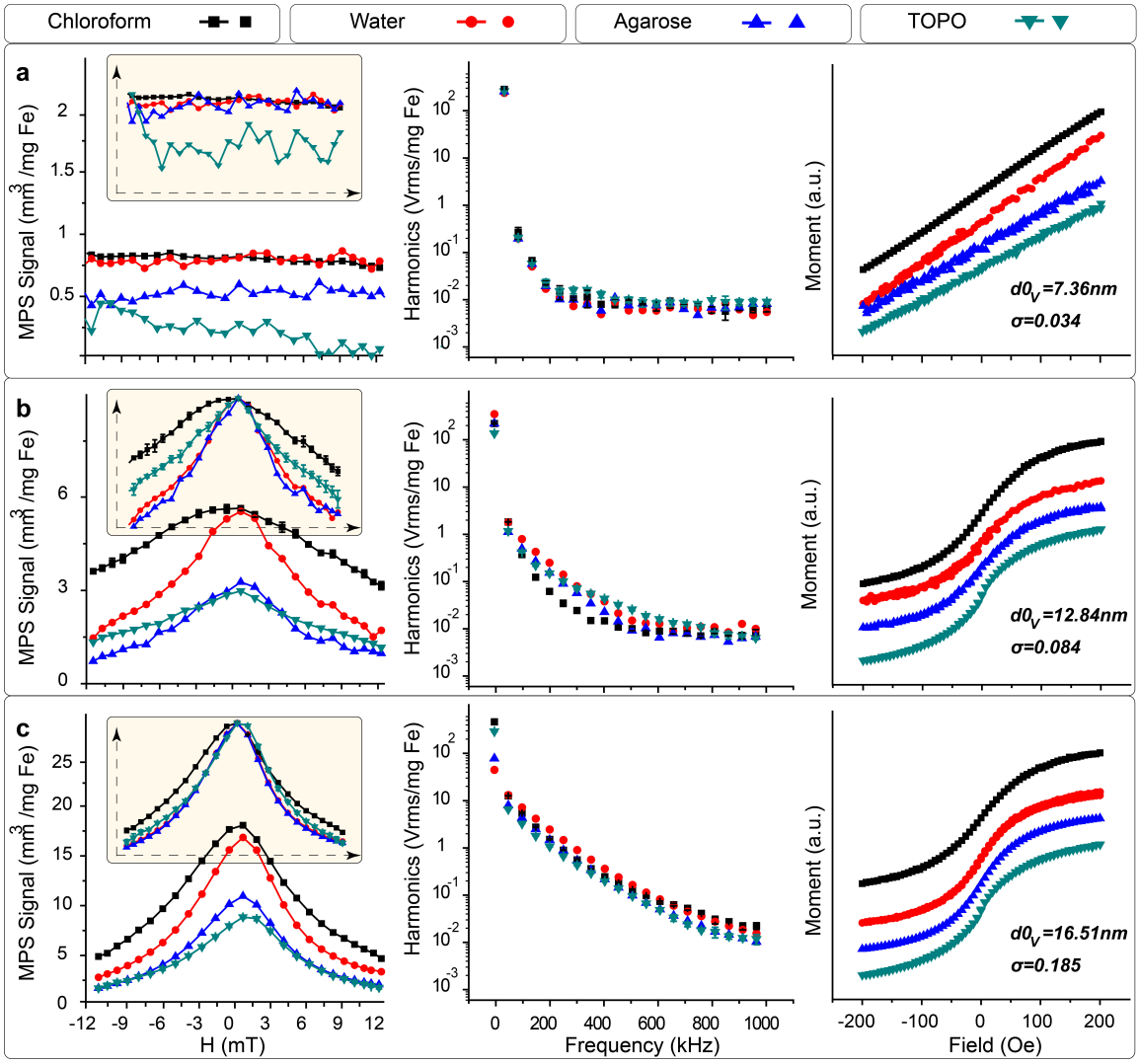

Fig. 3.4. dm/dH (left column) and harmonic spectra (middle column) divided by the amount of iron in each sample and normalized to one (inset, left column) and normalized VSM (right column) data for the NPs with different core sizes before (free in chloroform and immobilized in TOPO) and after (free in water and immobilized in agarose) the aqueous phase transfer. The data in (a)-(c) are for NPs ranging in core diameter from ~7 to 16nm as indicated. Median core sizes and standard deviations (σ) were calculated from the VSM results, using Chantrell size fitting.[404] Both dm/dH and harmonics based MPS signal intensities increase with median size and decrease with standard deviation of the NPs, in agreement with the slope of the m-H curves.

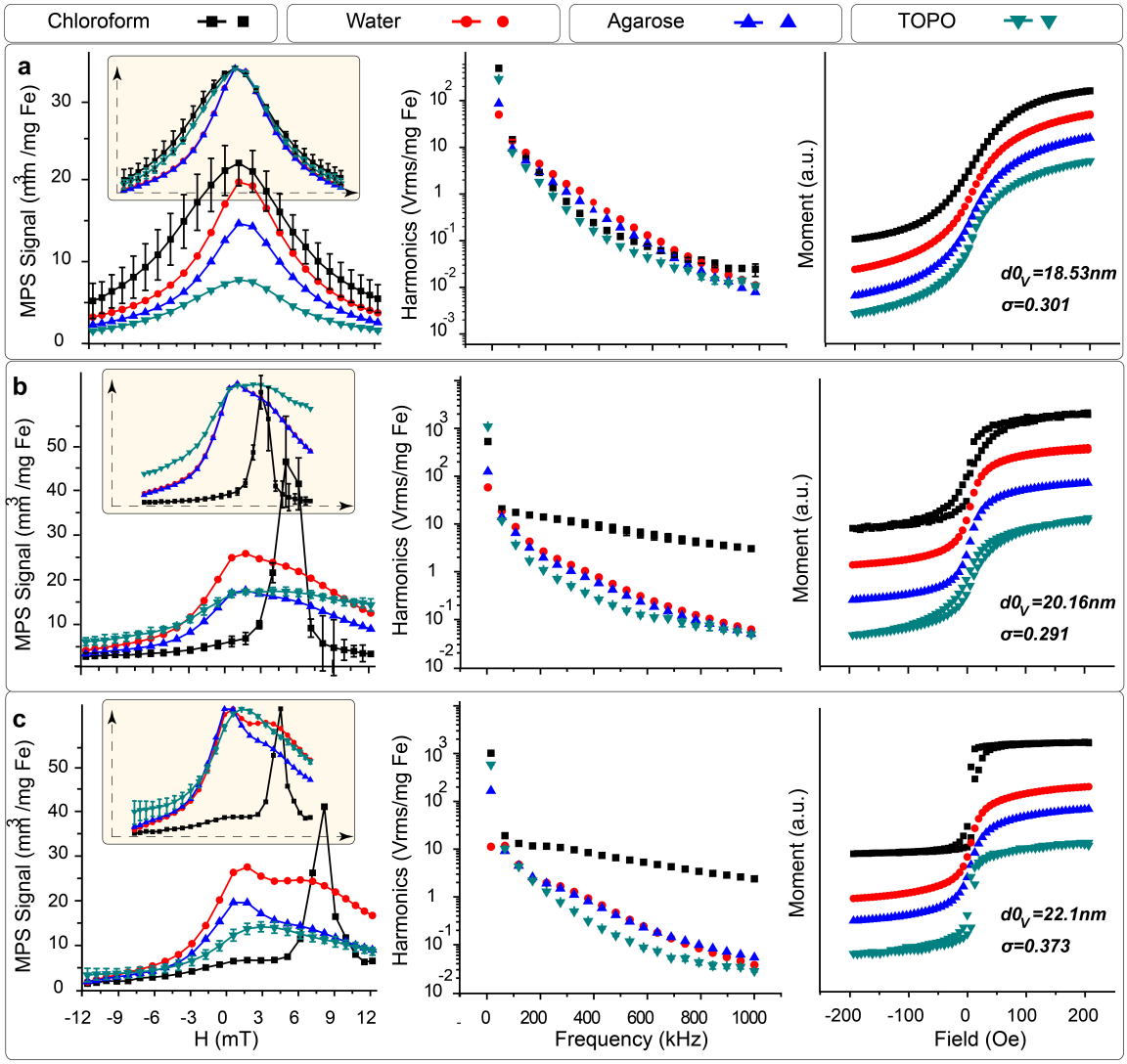

Fig. 3.5. All the graphs are presented similar to Fig. 3.4. Both dm/dH and harmonics based MPS signal intensities increase with median size and decrease with standard deviation of the NPs, in agreement with the slope of the m-H curves. Néel relaxation is the dominant mechanism for NPs up to 20nm, while a combination of Néel and hysteretic reversal generate the signal in the largest (22nm) NPs.

Fig. 3.8 shows the linear variation of the MPS signal with iron concentration. Water dispersed NPs were diluted up to ~15µg/mL and their MPS signals were measured three times. The full harmonics spectra, the average values of their third to thirty ninth harmonics versus iron concentration and their corresponding dm/dH peak widths (normalized to one) and intensities are shown in Figs 3.8(a)-(d), respectively.

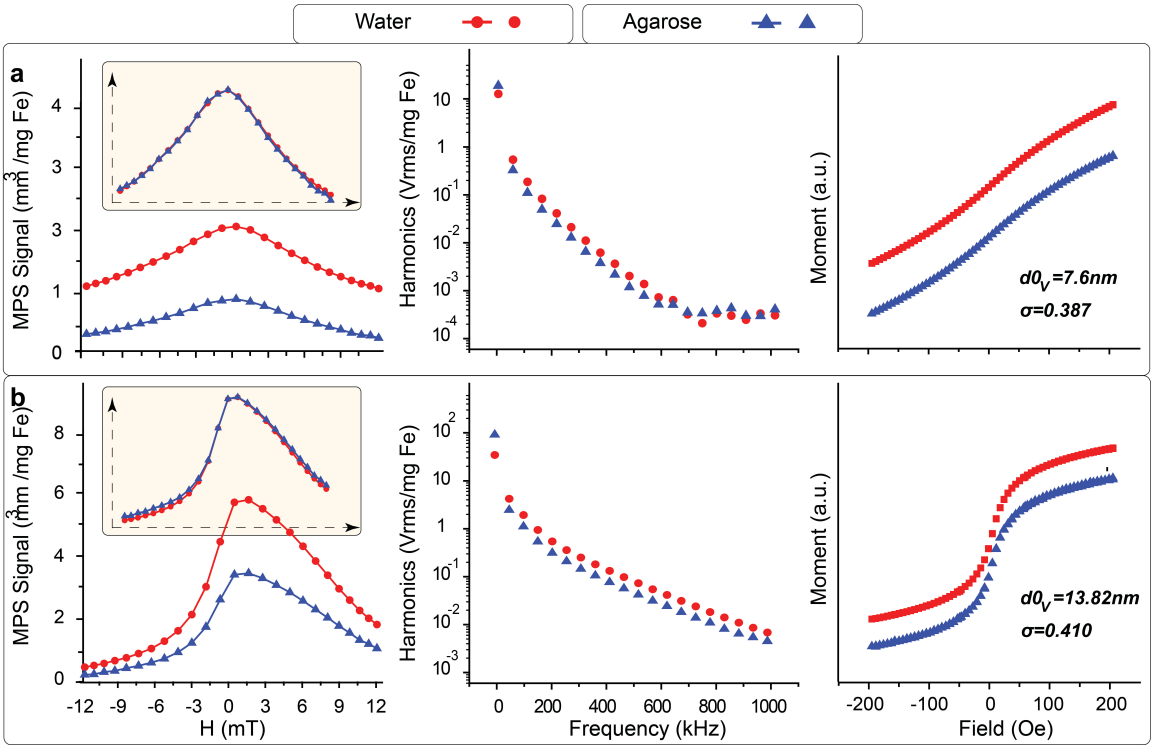

Fig. 3.6. MPS dm/dH and harmonics graphs of commercial iron oxide nanoparticles (Feridex™ (a) and Resovist™ (b)). Details of the graphs are provided in Figs. 3.4 and 3.5.

3.1.8. Discussions

Previous researchers have shown that MPI offers the prospect of high resolution and high-sensitivity medical imaging.[16, 19, 392, 410-412] MPI is sensitive to variations in tracer size,[16] and it has also been shown that the MPI signal is sensitive to tracer fluid viscosity,[413-415] as well as freezing of the fluid.[19] We are interested in optimizing tracers for specific MPI applications, such as cancer targeting, stem cell tracking or angiography. Idealized models of bound and free tracer environments help to understand how MPI tracers behave, and how their performance may be impacted by, for example, perfusion of tracer particles into a tumor, or targeting to the surface of a tumor cell by specific affinity or functionalization. In our MPI experiments, where the excitation frequency was fixed at 25 kHz and field amplitude varied from 5.1 to 18.6 mT.μ_0^{-1}, the

tracer's environment did influence MPI performance, due to differences in tracer responses to applied magnetic field. Furthermore, we can conclude that MPI imaging of immobilized particles is certainly possible, and with optimized tracers, performance should equal that of free-moving tracers.

We observed a transition in behavior with increasing NP core size, corresponding to a change from superparamagnetism to ferromagnetism, around 20nm (Figs. 3.4 and 3.5). This matches well with the blocking size of the NPs (~20.6nm) calculated using the following:

$$KV = k_B T \log \frac{\tau_{meas}}{\tau_0} \quad (6)$$

where K is the magnetocrystalline anisotropy constant (equation (2)), V is the volume of the iron oxide core, k_B is Boltzmann's constant, τ_{meas} is the field switching time or the measurement time (20 microseconds, calculated from applied frequency, 25kHz) and τ_0 is 10^{-10} s. Here, blocking means that for a given measurement time, the thermal energy is not sufficient to overcome the NP anisotropy energy barrier (KV). The aggregated or clustered NPs can effectively act like NPs of larger size and show ferromagnetic behavior exhibiting open loops in their m-H curves. This effect was much more pronounced in 20 and 22nm NPs when they were dispersed in chloroform. In MPS measurements, these transitions caused a shift from zero field (Figs. 3.4 and 3.5) in small sized NPs, to non-zero values of the field for larger NPs (20 and 22nm), in the location of the dm/dH peak, which corresponds to maximum dm/dH (Fig. 3.1(b)). The peak changed systematically with increasing NP magnetic size (Fig. 3.2) and sometimes featured an asymmetric "tail" at larger sizes. Physically, we interpret these changes to correspond to an evolution in magnetic reversal, from Néel-dominated relaxation in the smaller sizes (Fig. 3.1(a)), to Brownian or hysteresis-dominated reversal for larger sizes.[13, 392] Assuming highly monodisperse NPs without any aggregates, Néel relaxation times of the NPs with core sizes smaller than 22 nm were calculated to be less than ~5 microseconds (equation (2), assuming zero applied field). However, Brownian or hysteretic reversal is expected to lead to a shift in the dm/dH maximum toward later times (phase lag) or larger fields, respectively, relative to the time at which the applied field is zero (Figs. 3.1 and 3.2).

Generally, the relative contributions of Brownian and hysteretic reversal will be determined by the applied field amplitude and frequency. In these experiments, hysteretic reversal was expected to dominate compared to Brownian relaxation, due to the relatively large field amplitude ($\mu H \sim 14.6$mT, of the order of H_K) and relatively high frequency (25 kHz) magnetic field. Assuming that the viscosity of water is 10^{-3} N.s.m^{-2} at room temperature, the Brownian relaxation time, calculated for the range of measured hydrodynamic diameters (60-90 nm) is 84-283 microseconds – longer than the period of the applied field (~40 microseconds) (Note that in a single period of the applied field, the NP magnetization was observed to reverse twice, although only one reversal is shown in the figures).[13] While the Brownian relaxation time (equation 1) is defined for small fields ($H<<H_K$), it provides a 1st-order approximation of the relaxation time when it is assumed that the moment cannot rotate within the crystal itself: since rotation from saturation to saturation (180 deg) is desired in MPI, to begin the magnetic reversal some small initial rotation would need to occur by random collisions before the moment could experience a torque from the applied field. Given these factors, it is unlikely that Brownian relaxation is the dominant relaxation mechanism under the experimental conditions described here, however, as will be discussed below, it could contribute measurably by aligning the NP easy axes when they are dispersed in solution.

To further probe the reversal mechanism of the largest NPs, we varied the excitation field amplitude between 5.1 and 18.6 mTμ_0^{-1} (Fig. 3.7) (All other MPS results presented in this study were performed using an excitation amplitude of 14.8 mTμ_0^{-1}). As shown in Fig. 3.7(a), the tails (ranging from ~7-15mT) in the dm/dH data are more pronounced at higher field amplitudes (i.e. 14.8 and 18.6 mTμ_0^{-1}), showing more contribution from hysteretic reversal. Here, MPS intensity, which depends on the number of moments that are reversed by the driving field, increases with increasing field amplitude (the same trend is observed in dm/dH plots and harmonic spectra). We note also that, as the field amplitude increased, the dm/dH peak location shifted to higher fields, while the harmonic spectrum displayed an increasing slope with relatively greater contribution from higher harmonics (most notably after the 7th harmonic). These effects

are likely due to reversal of the fraction of the sample with larger size, by the higher field amplitudes [395, 396] and corresponding to their larger coercivity due to their larger volume and reversal energy barrier. Therefore, monodispersity of the NPs plays a key role to get the optimum signal intensity and spatial resolution. As discussed above, this effect is less pronounced for the immobilized NPs dispersed in gel. Note that, since the excitation frequency in all measurements was constant (25kHz), increasing the field amplitude increased the field ramping rate. However, all the dm/dH and harmonic data were divided by field ramp rate (equations 3 and 4), and therefore the signal intensity is only dependent on tracer performance and it is not proportional to ramp rate. It is important to note that similar evolution was observed with field amplitude for both gel and water samples (the causes of difference between the water and gel samples at each amplitude will be discussed later).

The smallest NPs (~7nm) showed the weakest MPS signal (Fig. 3.4), measured by dm/dH height, and the fewest measurable harmonics (up to 15th harmonics). In general, as size increased, the dm/dH height increased, dm/dH FWHM decreased, and the number of harmonics and their intensity increased, such that larger NPs featured spectra with good SNR even up to the 39th harmonic. The evolution in MPS results was consistent with the observed increase in the slope of the equilibrium m-H curves of the samples, as measured by VSM over the same range of fields probed in the MPS.[181] The maximum signal intensity was observed for NPs in the range of 20nm. The decrease of the signal in 22nm NPs can be described based on the larger size distribution (standard deviation, σ=0.373 calculated from Chantrell fitting) observed for the 22nm NPs, as shown in m-H graphs.[16] Also, as we will show later in Appendix A, this can be related to phase impurities and formation of un-desired Wustite during the synthesis of these larger core sizes.

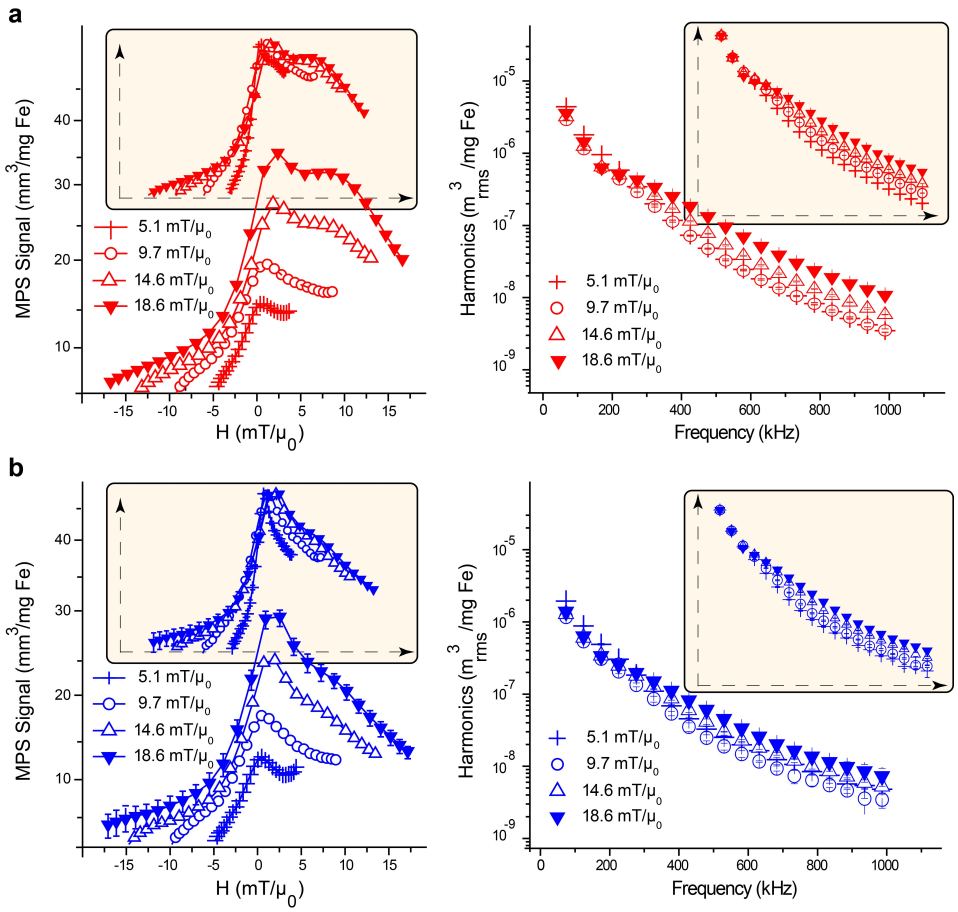

Fig. 3.7. Effect of the excitation field amplitude on dm/dH (left) and harmonics (right) spectra of the 22nm NPs in water (a) and agarose (b). Hysteretic reversal appeared to dominate at larger field amplitudes. As a result, as the field amplitude was increased, it reversed ever larger size fractions of the NPs in the sample, resulting in greater signal intensity, a shift in the dm/dH peak, and increased higher harmonics. This effect was observed both in water and in gel immobilized samples.

The equilibrium magnetization slopes (measured by VSM) are largest in 20 and 22nm NPs, accompanied by appearance of an open hysteresis loop. For the given VSM measurement time (~100s), this behavior is due to a superparamagnetic to ferromagnetic transition with increasing core size.[21] The transition could be further enhanced by the magnetic interactions between the nanoparticles when they are not coated with PMAO-PEG, which can lead to interparticle interactions that tend to align the particles into chains (Fig. 3.1(b)).[416] The open loop behavior observed for oleic acid coated particles

is not seen after coating of the NPs with the co-polymer. Similar evolution was observed in the MPS data of these samples, due to hysteretic reversal of these aggregates. Prior to coating with PMAO-PEG, the oleic acid coated NPs (core sizes~ 20 and 22nm) featured a narrow dm/dH centered at ~8 mT and flat harmonic spectra with high intensity, whereas PMAO-PEG coated particles showed a broader peak centered at 0 mT, and weaker harmonics. TOPO immobilized NPs typically showed the weakest MPS response. However, NPs smaller than 18nm did not show such dramatic signal variations before and after coating, either in their MPS or VSM measurements (Fig. 3.4). This is likely due to their smaller size; these NPs experience weaker interaction forces in comparison with 20 and 22nm NPs. However, compared with samples dispersed in chloroform, MPS signal intensity decreases after coating for all different sizes, due to the presence of the hydrodynamic layer around the NPs that stabilizes the particles and limits their interaction (also see Table 3.1).

The observed dependence in M(H) and MPS behavior on the suspending matrix could have several origins, including changes in the size distribution during phase transfer, clustering caused by inter-particle interactions, and the ability of the NPs to align their easy axes by rotation in liquid suspensions. For example, the dm/dH FWHM (insets of Figs. 3.4 and 3.5), decreases after transferring the as-synthesized NPs from chloroform to water, which can be clearly seen for 12, 16 and 18nm NPs. We interpret this peak narrowing phenomenon to a narrowing of the size distribution of the NPs during phase transfer to water, due to elimination of larger and smaller NPs by filtration and size exclusion purification after their coating with PMAO-PEG co-polymer. Also, again it is important to consider the potential for strong interaction between un-coated NPs in chloroform, where steric stabilization is poor and local aggregation can occur, specially when an external field is applied, such as during MPS measurements. For the NPs larger than 20nm, which are strongly interacting in chloroform, the dm/dH was fully changed after freezing the NPs motion in TOPO with maximum values shifted to zero field. The peaks in chloroform were sharp and appeared at larger field values, but after freezing in TOPO, they transformed to significantly broader peaks (Fig. 3.5). NPs frozen in TOPO

show the lowest signal intensities for all core sizes. Their equilibrium magnetization also shows a distinctive change that matches with the dm/dH data: when the NPs are allowed to align by rotation, such as in chloroform, a sharp transition is noted in the dm/dH, harmonic spectrum and m-H loop. Furthermore, chaining of the nanoparticles in chloroform may serve to enhance this effect. However, freezing the NPs in random orientations, such as by cooling a TOPO dispersion in the absence of an applied field, results in a change in saturation field and susceptibility in the equilibrium measurement that corresponds to a low intensity, broad dm/dH and low-intensity harmonics. This change could be due to alignment of the free NPs along their easy axis, compared to randomly immobilized NPs in TOPO and is in accordance with the Stoner-Wohlfarth model for magnetization reversal of single domain nanoparticles with different orientations with respect to the direction of the applied field.[417]

Unlike differences between chloroform and TOPO, immobilization of the aqueous NPs in agarose gel did not change the dm/dH peak width considerably (Figs. 3.4, 3.5, and 3.6 and Table 3.1). The observation of the same peak width in water and gel is indeed an interesting finding, regarding tracer design for tissue targeted MPI. However, this similarity was mainly observed in NPs smaller than 20nm. For the largest NPs with median size of 22nm, the full width at half maximum of the dm/dH in gel is smaller than in water. This might be due to clustering of these larger NPs during the phase transfer and their stronger magnetic interactions and alignments, when the field is applied, a phenomenon which is prohibited when their field induced movements are limited in nanoporous gel structure.[418] These clusters are larger than 100nm and form about 5 to 10 volume percentage of this sample, as shown by DLS data in Fig. 3.3(f). Also, free NPs in water can align with each other, when the magnetic field is applied and form clusters with large coercivities, acting like larger NPs. The hysteretic reversal occurs for these large size NPs at higher fields, resulting in a wider dm/dH peak and a small change in the slope of their harmonics spectra (Figs. 3.5 and 3.7). Also, the NPs dispersed in water show higher signal intensities in comparison with gelled samples. This could also be due to alignment of the free NPs and/or clusters in water, a phenomenon which does not

occur in gelled samples and as mentioned above, it can be described based on the Stoner-Wohlfarth model.[417]

Table 3.1. (a) Signal intensities (approximate peak values, unit: mm^3/ mg Fe) and (b) FWHM (unit: mT/μ_0) of the dm/dH of the nanoparticles with different core sizes (7, 12, 16, 18, 20 and 22nm) in different environments (water, agarose, chloroform and TOPO). The graphs are added for better visualization of the values (Continued in the next page).

(a)

Core Size (nm)	Water	Agarose	Chloroform	TOPO
7	NA	NA	NA	NA
12	5	3.1	5	2.9
16	16.5	11	17.5	7.7
18	19.5	15	22.5	6.5
20	25	17.5	45	17.5
22	28.5	20	42.5	14

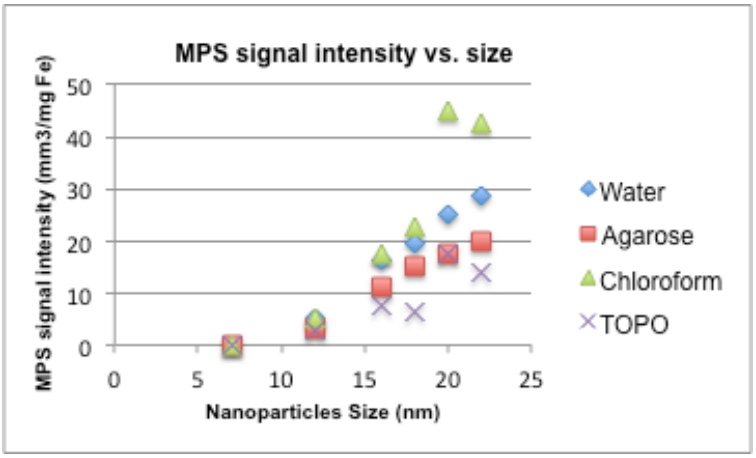

Table 3.1. Continued from previous page.

(b)

Core Size (nm)	Water	Agarose	Chloroform	TOPO
7	NA	NA	NA	NA
12	11	11.5	14.5	13
16	9	9	10	9.5
18	8.5	8.5	11	10.7
20	9.5	9.5	3	NA
22	13.5	10.5	3.5	13

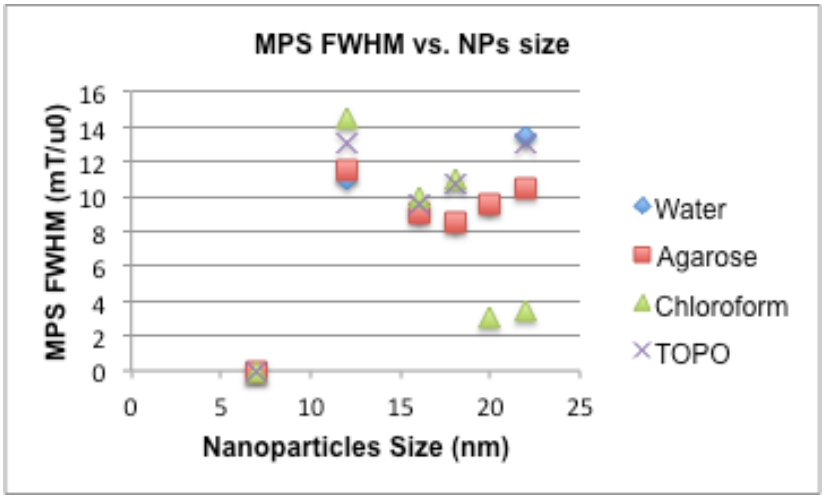

Considerably higher dm/dH signal intensities (~2.5x and 5x, respectively) were observed in our 16.5nm (σ=0.185) synthesized NPs, in comparison with two typical commercially available NPs, Resovist (median size of d_0=13.82nm and σ=0.49) and Feridex (d_0=7.6nm and σ=0.38, Fig. 3.6). Resovist has been extensively used as a gold standard for developing the MPI technique. However, increasing the magnetic core size to 20.16nm with narrow size distribution (σ=0.29), increased the signal intensity by a factor of five compared with 12nm NPs. This increase in signal can be related to the larger magnetic core size (Fig. 3.3) and lower σ values of our synthesized NPs. As it can be seen in their VSM data, low magnetization rates of these commercial NPs agree with

their weaker MPS signal. It is noteworthy that the MPS signal intensities of Resovist and Feridex are also very low after immobilization in agarose.

For many clinical applications of NPs, such as cell tracking and a wide range of tissue targeted imaging and related therapeutic approaches, it is necessary to quantify the internalized iron in tissues at very low concentrations without interference of iron-containing proteins (e.g., hemoglobin, transferrin, and ferritin) supplied by the blood.[346] This is more challenging for the organs with low level of NPs accumulation, such as kidney, brain and tumors. MPI signal is only sensitive to iron oxide NPs and there is no conflicting signal from the endogenous iron. Also, it is critical to see linearity in the variation of the MPS signal with iron concentration in the order of tens of micrograms per milliliter.[4, 346] Figs. 3.8(a) and (c) shows the harmonic spectra of these NPs at different concentrations. Note that our spectrometer is able to measure up to 39 harmonics.

Decreasing the concentration equally shifts all the harmonics in each spectrum to lower intensities. The inset shows the linear variation of the 3^{rd}, to 39^{th} harmonics of the NPs (d_0=22nm) down to very low iron concentrations (i.e. 15μg Fe.mL^{-1}). Also, Fig. 3.8(b) and (d) shows that the dm/dH peak width does not change with decreasing concentrations of the NPs. Again, the inset shows linear decrease of the dm/dH peak height with concentration. Larger error bars in the low-concentration dm/dH graphs and non-linearity of the 29^{th} and 39^{th} harmonics appear because the MPS signal for these samples is close to the background noise level of the spectrometer.

Generally, when NPs are expected to bind to cells during MPI imaging, it is necessary to consider how immobilization will affect their magnetic response. For applied fields at 25 kHz and field amplitudes greater than 5 m$T\mu_0^{-1}$, which have been introduced as a safe range for clinical applications,[15] the Brownian relaxation is much slower than the hysteretic reversal, which was observed to dominate. Synthesizing the data we have presented above, we can make some general remarks about optimizing tracers for MPI. We observed that signal intensity could be increased by increasing the

median core size (up to our 20 nm sample); increasing the field amplitude also enhanced the signal intensity when there was a distribution of sizes. However, resolution and

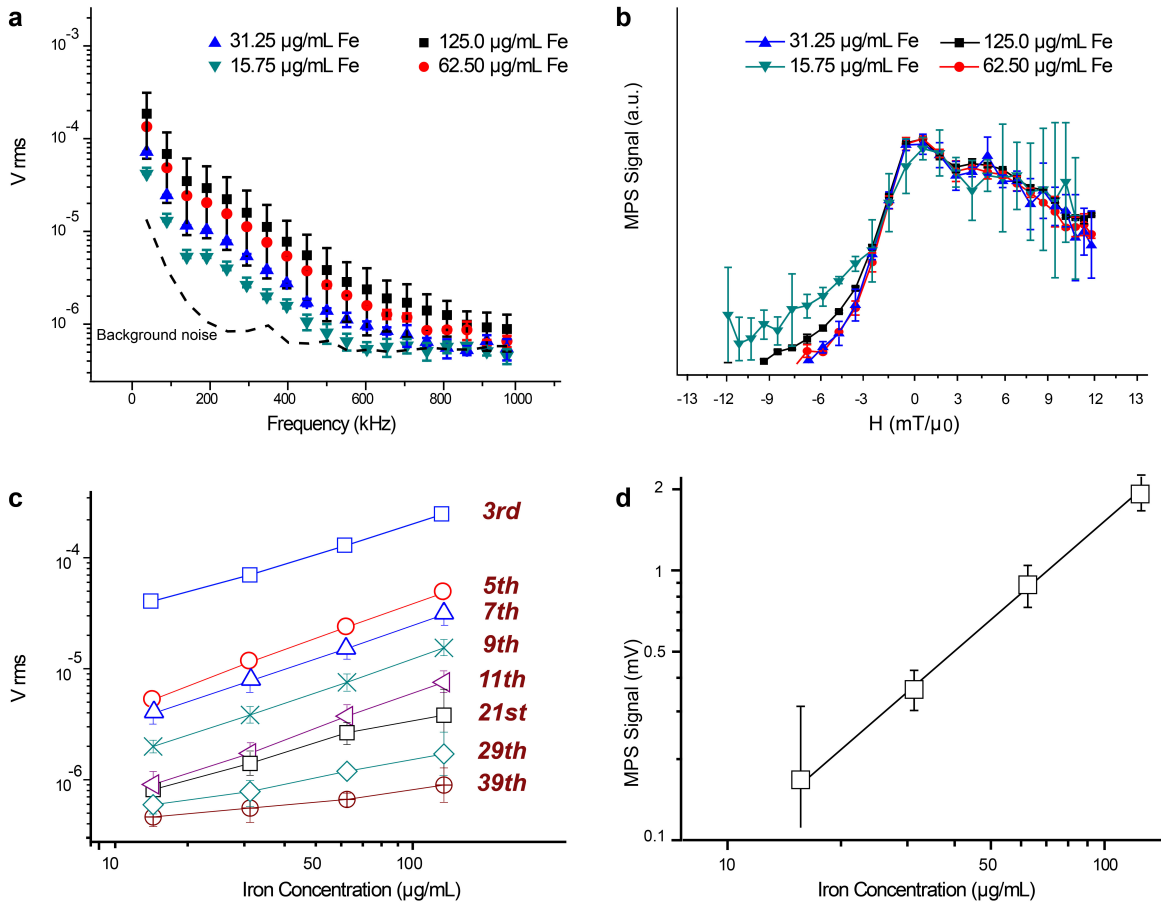

Fig. 3.8. Effect of concentration of 22 nm NPs in water on its harmonics spectra (a), and the spatial resolution, shown as the dm/dH graphs normalized to one (b). The harmonics intensity is decreasing linearly with decreasing the concentration (c). Non-linearity of the signals in 29th and 31st harmonics at low concentrations is due to interference of the system background noise. The spatial resolution does not change with dilution up to iron concentration of 15.725µg.mL^{-1}. The dm/dH intensity shows a linear variation with concentration (d). Note that the background noise curve shown in part (a) comes from several sources. There is thermal noise from the receive coil, which is a significant source. There is also noise coming from the transmit circuit, which includes harmonic noise from the power amplifier. There is also some noise from ambient sources. All of these contribute, though the first two are most significant.

intensity should both be improved by using monodisperse NPs with a uniform coercivity and a sharp switching field. Such a sample would also have the advantage that its performance would be invariant in water or in tissue. While making large, monodisperse samples presents a practical challenge, given the tendency for the nanoparticles to cluster due to strong interactions, it represents the best course for further improving MPI performance. In other words, highest MPI image quality is achievable through efficient surface functionalization of the larger (i.e. NPs with core sizes of ~20-27nm, as shown in Chapters 4 and 5 and Appendix A) and monodisperse NPs to avoid formation of aggregates during the NPs processing or applications.

3.1.9. Conclusions

NPs with approximate median core sizes of 7, 12, 16, 18, 20 and 22 nm and narrow polydispersity values were synthesized and successfully functionalized. We immobilized the NPs to study their MPI performance and found that signals obtained from smaller sizes of the NPs (~12 to 18nm) are less sensitive to their environment, while NPs larger than about 20nm that are best for MPI are highly sensitive to the surrounding media. To verify this crucial finding, the chloroform dispersed NPs were frozen in TOPO prior to phase transfer and the water dispersed NPs were immobilized in agarose gel after functionalization. Peak narrowing was observed when the NPs were transferred from chloroform to water due to their smaller size distribution after phase transfer. Open loop magnetization hysteresis was observed in hydrophobic NPs larger than 20nm, suggesting magnetic interaction of the NPs, which was fully suppressed after coating. The relaxation mechanism of the hydrophilic NPs was changed from Néel for smaller NPs to a combination of Néel and hysteretic reversal for NPs larger than 20nm. Immobilization in agarose, did not change the spatial resolution based on the FWHM of dm/dH and the slope of the harmonic spectra for NPs smaller than 20nm. For larger sizes (i.e. 22nm), hysteretic reversal of the large size fraction of the NPs, shifted the peak to larger fields, a phenomenon that was eliminated after preventing the NPs alignment in gel. This shows the key role of monodispersity of the synthesized NPs in order to get the

highest MPI signal, specially for larger sizes. Harmonics and dm/dH intensities varied linearly with concentration, while the dm/dH peak width remained constant, confirming consistent MPI performance of the synthesized tracers down to very low concentrations comparable to the usual ranges observed in targeted tissues. The results of the model designed here, help to improve the image quality in a broad range of tissue- or cell-targeted MPI applications in future.

3.2. Nanoparticles stability and consistency of their MPI signal quality in biological solutions

3.2.1. Introduction

The core and hydrodynamic size of the iron oxide nanoparticles determine the signal intensity and spatial resolution in MPI, whilst their monodispersity when preserved during the biomedical application, generates a consistently high quality MPI image.[7, 16, 392] Detachment of the coating molecules in the presence of strong ionic species in the biological media such as blood and adsorption of the proteins are two challenging phenomena resulting in instability of the NPs and the formation of aggregates.[21, 22] These large size aggregates have shorter blood circulation half-life and rapid clearance through the reticuloendothelial system (RES). Also, they have a larger coercivity, and respond by hysteretic reversal, requiring larger applied magnetic field amplitudes.[417] Therefore, when present in a sample, these aggregates decrease the signal intensity and spatial resolution in MPI.[406]

In this section, we present a silanization method for ligand exchange and subsequent conjugation of bis-amine polyethylene glycol (PEG) to the surface of the 18nm oleic acid coated NPs.[176, 400, 401, 419] Using this effective process to coat the synthesized NPs with amine terminated PEG molecules, we show by DLS that they are water-soluble with long-term stability in biological media such as phosphate buffered saline (PBS) and sodium bicarbonate buffers and Dulbecco's modified Eagle medium (DMEM) enriched with 10% fetal bovine serum (FBS). The MPS efficacy of the functionalized

nanoparticles was also monitored over time, and both signal intensity and resolution remained unchanged even after 7 days of incubation. This is attributed to the dominant contribution of the Néel relaxation mechanism of the monodisperse and highly stable nanoparticles, which was preserved through the incubation period. These results show that the NPs were individually coated without forming aggregates and remained highly stable in different biological media for more than a week maintaining their spatial resolution and signal intensity. The results of this study paved the way for future use of these highly stable NPs in various MPI related biomedical applications. For example, we will show in Chapter 4 that these stable amine-functionalized NPs can be effectively used for multimodal imaging (MPI/MRI/Fluorescent**)** with a long blood circulation time (i.e. ~25min) in mice.

3.2.2. Synthesis of highly stable amine-functionalized MPI tracers

The procedure used for synthesis and PEG coating of the NPs is shown in Table 3.2. Monodisperse iron oxide NPs were prepared, as discussed before in section 3.1.2. Briefly, iron oleate was synthesized and dissolved in 1-octadecene [398, 399] and then a mixture of iron oleate, oleic acid and 1-octadecene was refluxed at 320°C for 22h under inert argon atmosphere. The molar ratio of iron oleate to oleic acid was adjusted to 1:18. The core size of the synthesized NPs was ~18nm. To purify the as-synthesized NPs, we sonicated them in 40mL of a 1:1 (v/v) mixture of chloroform and methanol and precipitated them three times with a strong magnet. Purified NPs (~30mg) were dried in vacuum, redispersed in 35mL toluene by 15min sonication. NPs were functionalized with amine-terminated polyethylene glycol (PEG), by modification of the procedures described before.[176, 419] First, NPs were silanized by addition of 50µl of 3-(triethoxysilyl)propyl succinic anhydride (TSP) to the NPs and refluxing the mixture at 105°C for 12h under argon atmosphere (See Appendix D for details). NPs were then purified by addition of 50mL hexane and separated using a strong permanent magnet. Precipitated NPs were dispersed in 7mL tetrahydrofuran (THF). Dicyclohexylcarbodiimide (DCC, 80mg) and bis-amine PEG (170mg, MW 2kDa) were

added to the NPs and the mixture was sonicated at 50°C for about 20h. PEG coated NPs were separated by addition of excess hexane and using a strong magnet. Dried NPs were dispersed in 3mL sodium bicarbonate buffer (pH=8.5) and sonicated for 15min. Size exclusion purification (Sephacryl$_{TM}$ S-200 gel) was used to remove un-reacted PEG molecules.

We used ICP to determine the iron concentration at each step of the NPs preparation. For long-term stability tests, 50µL of the NPs were incubated in 1mL PBS and sodium bicarbonate buffers and DMEM cell culture media enriched with 10% FBS. DLS was used to monitor the variation of the average hydrodynamic size of the NPs in different media. TEM was used for morphological analysis of the NPs before and after the functionalization. For studying the room temperature magnetization (M vs. H) of the NPs, about 100µL of the liquid samples (100-200µg of NPs) were transferred to a polycarbonate capsule and analysis were performed using a room temperature vibrating sample magnetometer (VSM). Size of the NPs were calculated using Chantrell method, by fitting the resulted magnetization curves to the Langevin function.[404] We calculated the Brownian relaxation times (τ_B) of the NPs using equations (1) and (2) (section 3.1.5). MPS measurements and data analyses were performed as explained in section 3.1.6.

Table 3.2. Procedure used for synthesis of PEG coated NPs.

Step 1: Synthesis of the oleic acid coated NPs:

Iron Oleate + Oleic acid + 1-octadecene	Refluxing 320 °C, 22h	Oleic acid coated NPs (Hydrophobic)

Step 2: Silanization of the oleic acid coated NPs:

Oleic acid coated NPs + TSP	Refluxing 105 °C, 12h	Silanized NPs

Step 3: PEG coating of the silanized NPs:

Silanized NPs + DCC + NH_2-PEG-NH_2	Sonication 50 °C, 20h	PEG coated NPs (Hydrophilic)

3.2.3. Results and discussions

We used a ligand exchange approach to transfer the hydrophobic NPs to aqueous media. NPs were first modified with silane functionalized molecules, which introduces carboxyl groups to the surface of the NPs. DCC was then used to bond bis-amine PEG molecules to these carboxyl groups. Using SPDP assay,[420] the average number of active amine groups per NP was estimated to be about 102 (see Appendix H for detailed procedure). As shown in Fig. 3.9(a), the slope of the m-H curves did not change after coating of the NPs with PEG, showing that the median core size of the NPs did not change considerably during the process. This indicates that no aggregates or cross-linked NPs were formed through the coating reaction and it was confirmed by calculation of the average core sizes of the NPs before and after PEGylation, using the Chantrell fitting.[404] Note that the slight decrease of the magnetization slope after silanization is due to pre-silanization purification process that we used to remove the large aggregates that were formed during the high temperature synthesis of oleic acid coated NPs. The calculated median core size of the PEG coated NPs was 17.8nm, with a narrow standard deviation of 0.126. These values are 18.35nm and 0.225 before silanization and 18.06 and 0.04 after silanization. TEM image of the PEG-coated NPs shown in Fig. 3.9(b), clearly confirms our VSM-based size calculations. The PEG coating cannot be seen in TEM due to its very low contrast in comparison with the crystalline core. Also, it rapidly gets decomposed due to beam damage from the high energy electron beam (i.e. 200 KeV).

PEG-coated NPs had a very narrow hydrodynamic size distribution (Z-average of 112nm with polydispersity index of 0.189). Due to the electrostatic repulsions between NPs and steric hindrance provided by PEG molecules, NPs were very well stable in biological media, showing an almost constant hydrodynamic size, without formation of aggregates after a week (Fig. 3.9(c)).

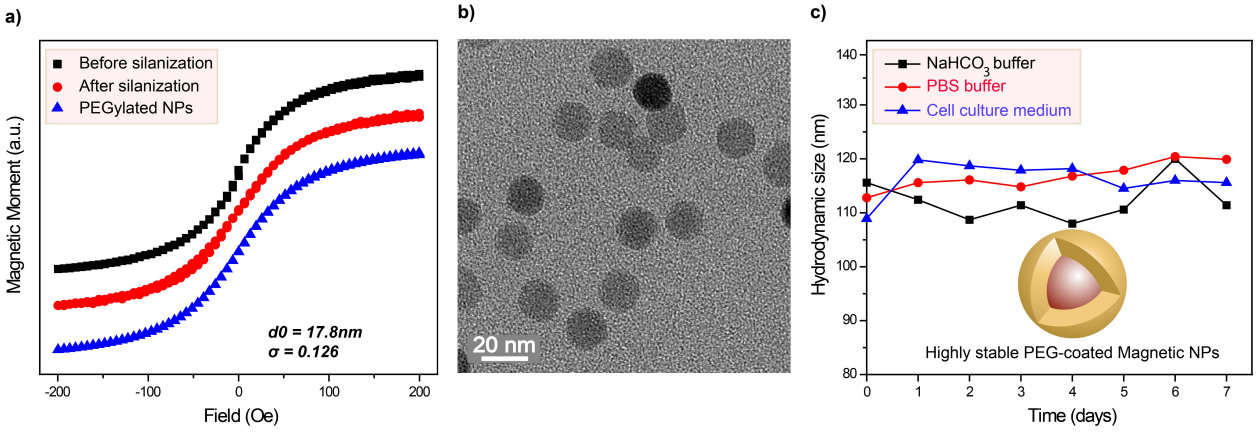

Fig. 3.9. (a) Normalized m-H curves of the nanoparticles before and after silanization, and after their coating with PEG molecules. The plots are shifted vertically for clarity. The median core size (d_0) and standard deviation (σ) of the PEG-coated NPs were calculated using Chantrell fitting.[404] (b) TEM image of the PEG-coated nanoparticles, showing results in accordance with our m-H size measurements. (c) Stability of the hydrodynamic size of the PEG-coated nanoparticles in different biological solutions as a function of incubation time. Stability plays an important role in long-term MPI performance of the NPs as shown by MPS data presented in Fig. 3.10.

The dm/dH and harmonic spectra of the NPs at each step of the procedure (Table 3.2) are shown in Fig. 3.10. Signal intensity (i.e. peak height or harmonic values) and spatial resolution of the NPs were enhanced after silanization (compare Figs. 3.10(a) and (b)). Also, the slope of the harmonics spectrum was less for silanized NPs, showing higher harmonic intensities for these particles. Note that higher harmonic intensities represent a higher MPI signal intensity in system matrix image re-construction approach. As mentioned earlier, these are due to elimination of the larger and smaller fractions of the as-synthesized NPs during the washing process that resulted in narrower size distribution of the NPs after silanization (σ=0.04) and is in agreement with the m-H curves (Fig. 3.9(a)).[406] This can be also correlated with the increased interaction of the NPs after replacement of the oleic acid with TSP molecules. After coating with PEG, the NPs showed a narrow core and hydrodynamic size distributions. These resulted in their high spatial resolution and signal intensity (Fig. 3.10(c)). The dm/dH peak and 3rd harmonic intensities of the PEG coated NPs were 18.31±0.03 mm^3/mg Fe and 14.91±0.02 V_{rms}/mg Fe, respectively, before starting the incubation. Also, the harmonics spectra of the NPs in

different solutions perfectly overlap with each other even up to 39th harmonic. Long-term, the NPs maintained their MPS performance in different biological media, even for up to a week of incubation (Figs. 3.10(d) and (e)). We have shown before that there are three possible mechanisms (i.e. Néel, Brownian and hysteretic reversal) for relaxation of the NPs in MPI.[13, 16, 392, 406] We used equations (1) and (2) to calculate the Néel and Brownian relaxation times (~2 and ~300 microseconds, respectively) and compared these values with field switching time in our MPS system (~40 microseconds) to investigate the relaxation mechanisms of the NPs. The time needed for Brownian relaxation was much higher than field reversal time for the frequency used in our MPS (25kHz). Therefore, there was no Brownian relaxation contribution in our MPS signals. Also, when hysteretic reversal dominates, the dm/dH peak occurs at a finite non-zero value that depends on the particle's anisotropy, so that the dm/dH is asymmetric about the origin.[406, 421] Therefore, symmetrical dm/dH peak at near zero field range confirms that Neel relaxation was the dominant mechanism, resulting in the consistent MPS performance of the PEG-coated NPs.[406]

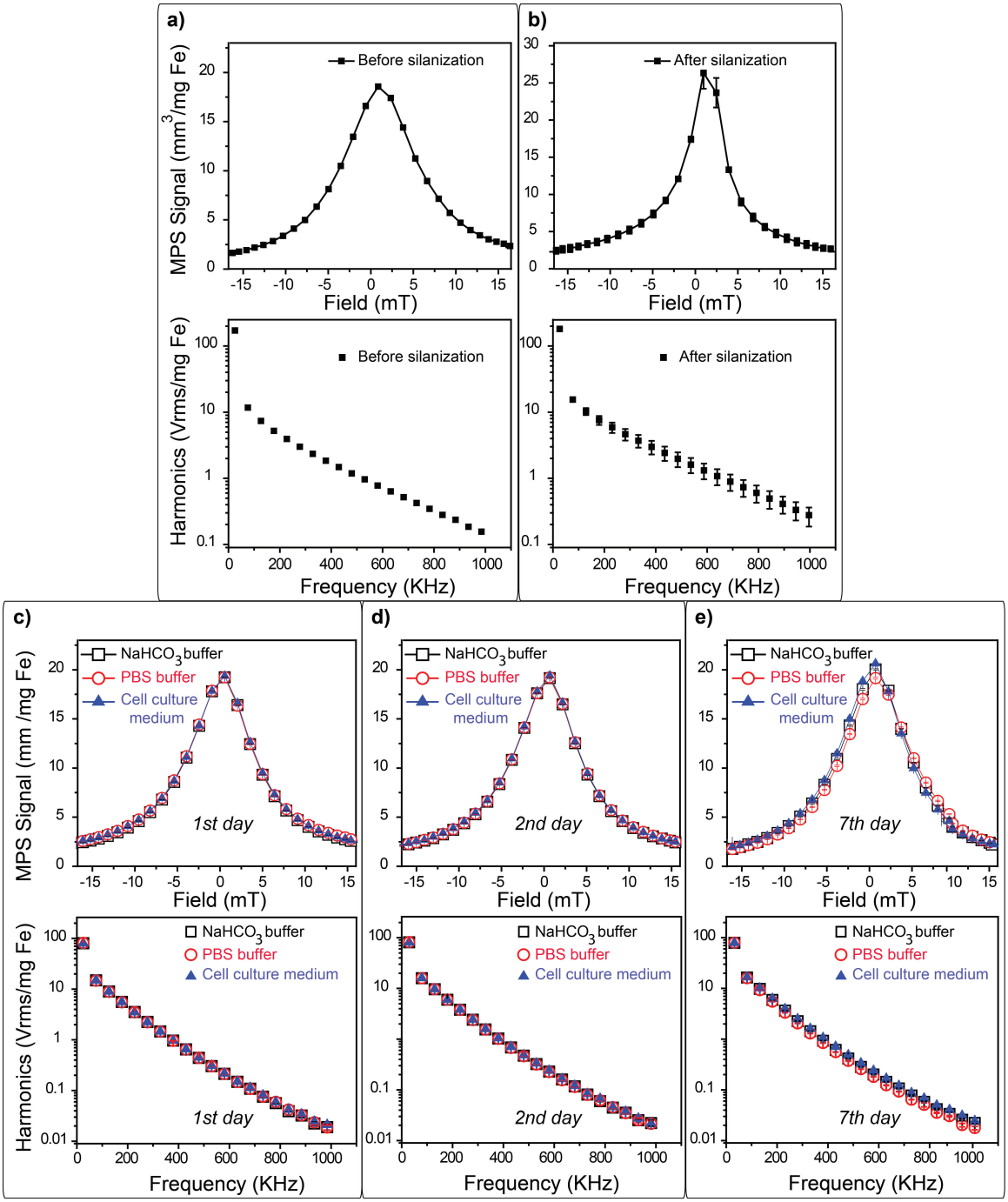

Fig. 3.10. dm/dH (top) and harmonics (bottom) diagrams of the nanoparticles before (a) and after silanization (b) and PEGylation (c). The PEG-coated NPs showed a consistent signal intensity and spatial resolution after incubation in sodium bicarbonate, PBS and cell culture (DMEM enriched with 10% FBS) media for 2 (d) and 7 days (e).

3.2.4. Conclusions

The nanoparticles reported in this study show consistent performance, without any agglomeration, suitable for practical MPI measurements related to future cardiovascular imaging, cancer diagnosis and stem cell tracking. In fact, size stability of these NPs in biological media is the crucial parameter required for these applications. As we will show later in Chapter 4, this also helps to improve the blood half-life of these nanoparticles. Furthermore, the presence of amine groups on the surface of the NPs provide abundant chemically active sites for conjugation of other molecules such as fluorescent Cy5.5 (see Chapter 4). High spatial resolution and signal intensity of these NPs, with the majority contribution from Néel relaxation, makes them promising candidates for a wide range of *in vitro* and *in vivo* MPI applications in the future.

3.3. Intracellular performance of tailored nanoparticle tracers in MPI

3.3.1. Introduction

Magnetic Particle Imaging (MPI) is a quantitative mass-sensitive, tracer-based imaging technique, with potential applications in various cellular imaging applications. As shown in Section 3.1 (Fig. 3.8), it has a high mass sensitivity – down to 15μg/mL – and its signal is linear with NPs concentration. Therefore MPI is a potentially useful technique for various in vivo cell tracking and tissue imaging applications. However, there is limited information available about the MPI performance of the NPs after their internalization into cells.

As discussed before, the spatial resolution of MPI, in the first approximation, improves by decreasing the full width at half maximum (FWHM) of the field-derivative of the magnetization, dm/dH, of the nanoparticle (NP) tracers. We showed in previous sections that the monodispersity, core size, and environment-dependent relaxation mechanism of the iron oxide nanoparticles determine the signal intensity and spatial resolution of the MPI images.[42] Therefore, considering these parameters is crucial for successful utilization of MPI for *in vivo* imaging of carcinoma tissues or tracking of

labeled cells in the future. The exact mechanisms for MPI performance of the NPs after cellular internalization are still unknown because of the possible intracellular degradation and aggregation of the NPs.

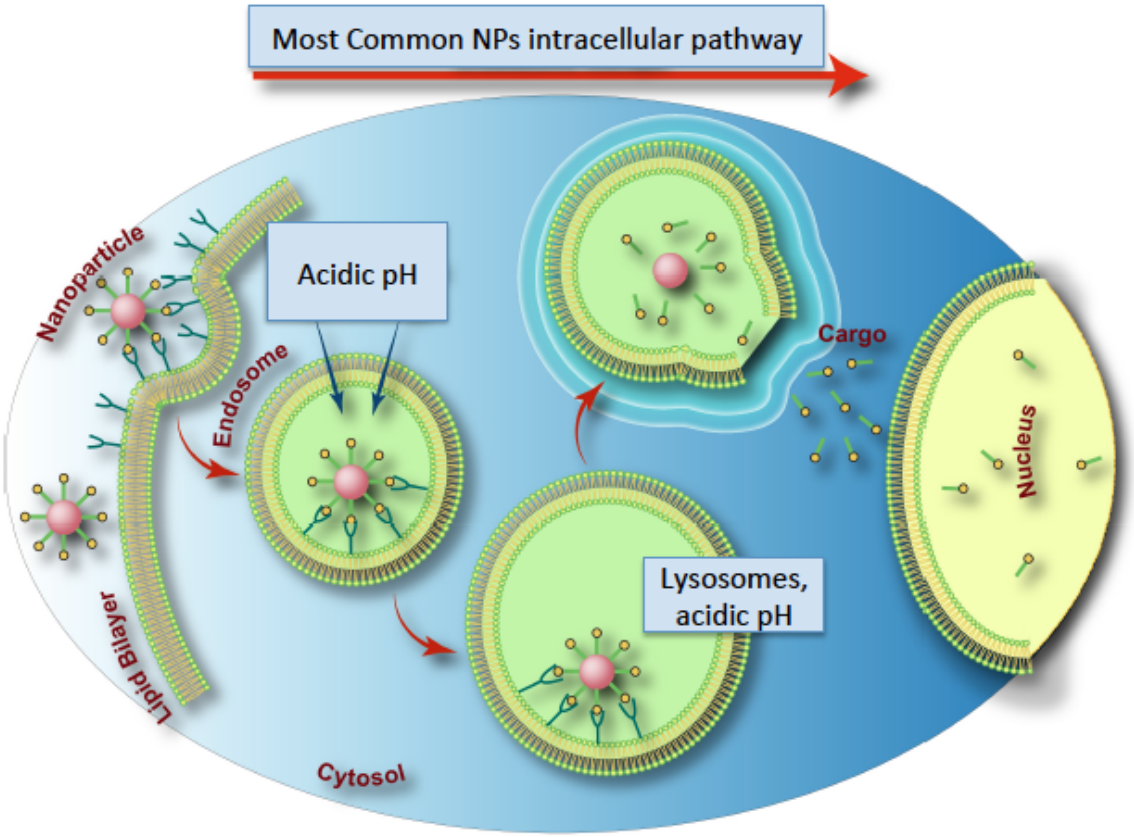

Fig. 3.11. The most common intracellular pathway of the MPI tracers. Lysosomes are the main organelles responsible for degradation of the NPs. Note that in this schematic picture, we only show one single nanoparticle in endosome and lysosome with emphasis on their possible pathways in the cells, for simplicity. In real situations, large number of the nanoparticles or their aggregates can get accumulated in one endosome or lysosome. NPs entered into acidic environment of lysosomes start to degrade. Degradation can happen for both coating materials and core iron oxide and its kinetics may vary with NPs size or type of the coating materials. Again, degradation of the core and coating molecules are not shown in this schematic for simplicity. Coating degradation has been conventionally used for drug delivery purposes (shown as cargo molecules). However, we believe when the coating molecules are detached from the surface of the nanoparticles due to degradation, nanoparticles aggregate and their MPI performance changes.

Following the analysis of the NPs performance in a tissue equivalent environment with a neutral pH (Sections 3-1 and 3-2),[42] in this section, we studied the long-term MPI performance of monodisperse PEG-coated NPs in a simulated lysosome solution.[201] Lysosomes are the main intracellular organelles, responsible for degradation of the NPs (Fig. 3.11).[105] The results of our study show that depending on the concentration of the NPs, the degradation alters the size of the NPs and can cause their partial aggregation. These structural changes of the NPs in such intracellular environments increase the FWHM of their d*m*/d*H* curves, which eventually results in lowering the resolution of the MPI images.

In this work, we incubated 30 to 150μg of the iron oxide NPs (core size: ~20.1nm and hydrodynamic size: ~82nm) in a lysosome-like acidic buffer (0.2mL, 20mM citric acid, pH 4.7) and investigated their changes by VSM, MPS, TEM and DLS. The FWHM of the d*m*/d*H* curves of the NPs increased with incubation time and buffer to NPs ratio, consistent with a decrease in the median core size of the NPs from ~20.1±0.98 to ~18.5±3.15nm and an increase in their hydrodynamic size from ~82nm to ~260nm. In fact, these smaller degraded NPs formed aggregates that responded to the applied field by hysteretic reversal at higher field values and increased the FWHM. The rate of core size decrease and aggregation were inversely proportional to the concentration of the incubated NPs, due to their slower biodegradation kinetics, suggesting that higher cellular internalization might preserve the spatial resolution of MPI in future cellular imaging applications. The results of this model experiment show that the MPI performance of the NPs in the acidic environments of the intracellular organelles (i.e. lysosomes and endosomes) can be highly dependent on their rate of internalization, residence time and degradation.

3.3.2. Incubation of NPs in simulated lysosome solution

PEG-coated NPs (core size: ~20.1nm and hydrodynamic size: ~82nm) were synthesized as described in section 3.2.2. To simulate the intracellular performance of the NPs, different amounts of the NPs (30, 50, 100 and 150μg) were dispersed in 0.2mL of 20mM

citric acid buffer with pH of 4.8.[201] The mixtures were then sealed and incubated at 37°C for up to 96 hours and the MPS performances of the NPs were monitored over the incubation period. The size variations of the incubated NPs were also verified by DLS, TEM and VSM analyses as described in sections 3.1.3, 3.1.5 and 3.1.6.

3.3.3. Results and discussions

Dynamic light scattering measurements showed that the PEG-coated NPs had a hydrodynamic size of about 82nm. We have shown before (section 3.2) that these NPs are highly stable in aqueous buffers (e.g. PBS) and biological media (e.g. cell culture media enriched with 10% fetal bovine serum) and show a consistent performance as efficient MPI tracers without notable change in their core and hydrodynamic sizes over a period of at least one week of incubation in these solutions.[17]

To simulate the MPI performance of these NPs after internalization into main cellular organelles (i.e. endosomes and lysosomes), we incubated 30µg of the NPs in 0.2mL of an acidic lysosome-like buffer solution[201] and determined their core and hydrodynamic size variations and MPS performance over a period of 4 days. TEM (Figs. 3.12(a) and (b)) and DLS (Fig. 3.14(b)) analysis showed that initially monodisperse NPs were partially

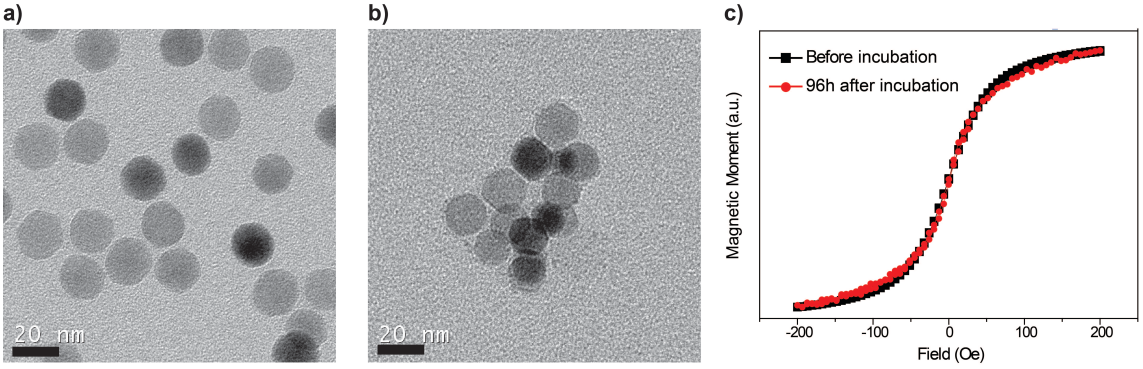

Fig. 3.12. TEM images of the PEG coated NPs before (a) and after (b) incubation (96 hours) in lysosome-like (pH=4.8) solution. Core sizes calculated by fitting the $m(H)$ plots of the NPs (c) to the Langevin function,[404] confirmed the size variations observed in TEM images . Here, 30µg of the NPs were incubated in 200µL of the acidic solution.

degraded after incubation and formed aggregates composed of these smaller size NPs. These aggregates can be potentially formed following detachment of the stabilizing PEG molecules from the surface of the degraded NPs. In agreement with the TEM observations, fitting of the VSM magnetization curves of these NPs to a Langevin function, showed that their median core size decreased from ~20.1±0.098 nm to ~18.5±3.15nm after incubation in acidic buffer for 96 hours (Figs. 3.12(c) and 3.14(b)). As shown in Fig. 3.12(c), the slope, *dm/dH*, of the *m*(*H*) curves of these smaller NPs was slightly less than the NPs prior to incubation. This degradation-dependent size decrease was slower when higher concentrations of the NPs (i.e. 50, 100 and 150μg) were incubated in the same amount of the buffer solution (Fig. 3.14(b)). Also, the larger core size standard deviations after incubation (Fig. 3.14(b)) show that the degradation phenomenon increased the core size polydispersity of the NPs. Considering the same amount of the acidic solution for all the incubation conditions, the slower degradation of higher concentration of the NPs can be correlated with their larger total surface area exposed to the degrading solution.[201, 422]

Spatial resolution of MPI images directly depends on the FWHM of the d*m*/d*H* curves of the NPs used as the contrast agent.[15] Using magnetic particles spectrometry (MPS), we have shown before that this FWHM parameter is highly dependent on the median core and hydrodynamic sizes and monodispersity of the NPs.[16, 42, 423] Therefore, partial dissolution and aggregation of the NPs in acidic buffer increases their FWHM (Figs. 3.13(a) to (d) and 3.14(a)), which results in poor resolution in MPI images. This FWHM increase can be attributed to the resemblance of these aggregates to NPs with larger core sizes and their forced hysteretic reversal at higher magnetic field values (>5mT).[42] Variation of the hydrodynamic sizes in Fig. 3.14(b) show that at lower concentration of the NPs (e.g. 30μg) higher percentage of these aggregates form during the incubation. These aggregates increase the average hydrodynamic size of the NPs and result in shifting the location of the MPS peak to higher field values (Fig. 3.13(a)) and formation of *m*(*H*) curves with larger coercivity as shown in Fig. 3.13(e) for the applied

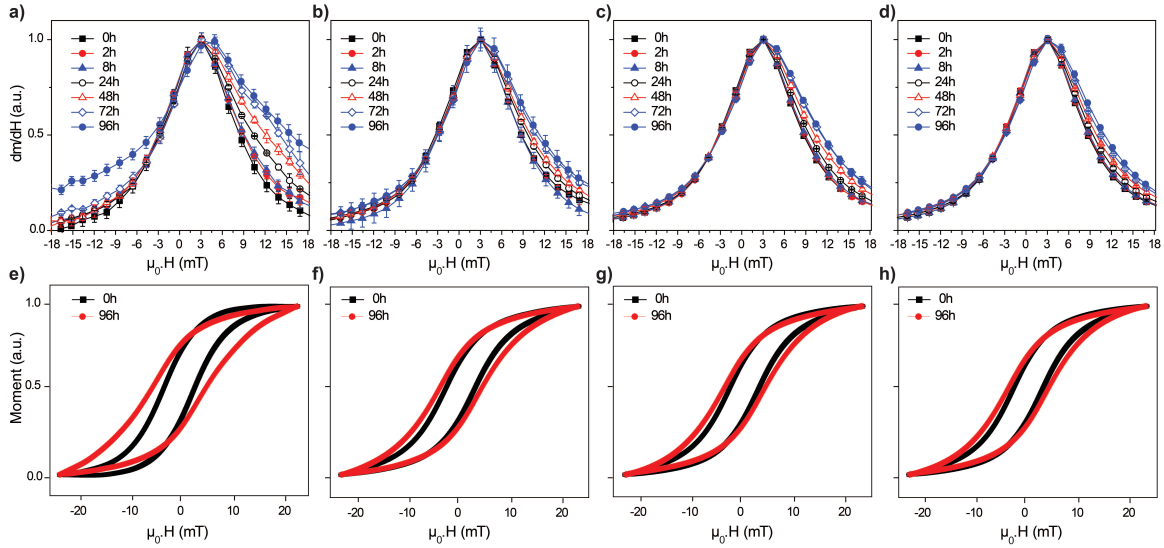

Fig. 3.13. The d*m*/d*H* plots (a–d), measured at 25 kHz in our Magnetic Particle Spectrometer,[18] were integrated to derive the corresponding AC hysteresis *m*(*H*) curves (e–h). Different amounts of NPs – 30 (a and e), 50 (b and f), 100 (c and g) and 150μg (d and h) – were incubated in lysosome-like buffer for 0-96 hrs.

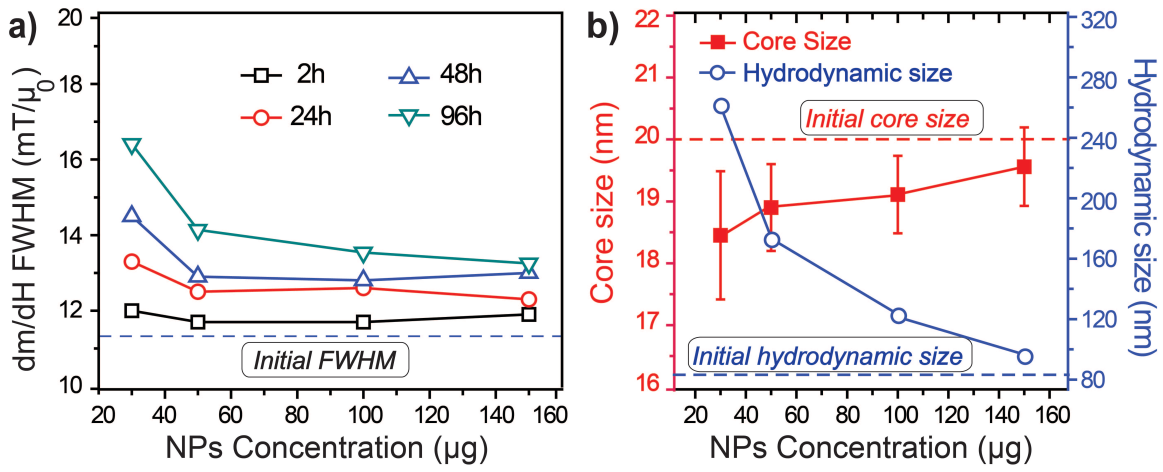

Fig. 3.14. (a) Change of the FWHM of d*m*/d*H* as a function of NPs concentration and incubation time at pH = 4.8. NPs concentrations were held constant during each incubation experiment. Note that the lines connecting different concentrations of NPs for the same incubation times are intended as guides to the eye. (b) Core and hydrodynamic size variation by concentration of the NPs incubated for 96h. The core sizes were calculated by fitting of the NPs *m*-*H* curves to the Langevin function and the hydrodynamic sizes were determined using dynamic light scattering.

field frequency (f_0=25kHz) used in our spectrometer. Similar to core size variation rates, this FWHM and coercivity increases were less for higher concentration of the incubated NPs (Figs. 3.13(a)-(f) and 3.14(a)). The details of the relaxation mechanisms of the monodisperse NPs in the presence of the applied AC magnetic field (25kHz) can be found in Section 3.1.

3.3.4. Conclusions

Future application of MPI for imaging of targeted tissues (such as cancers or atherosclerotic plaques) or magnetically labeled cells (such as stem cells[424, 425], macrophages or red blood cells[426]) depends on the consistent performance of the NPs after cellular internalization. Lysosomes, the most probable destination of the internalized NPs, are acidic (pH ~5.0) and this environment likely degrades the NPs in a short time. The spatial resolution in MPI is strongly correlated with the core size and polydispersity of the NPs. Therefore, this degradation phenomenon weakens the MPI performance of the NPs and special surface modification strategies should be developed to tune the cellular internalization rate, pathways and degradation rates of the NPs, based on the desired MPI application.

3.4. Chapter summary and future outlook

Our results in Section 3.1 show that the MPI signal is very sensitive to both NP size and environment. Our calculations show that Brownian rotational diffusion is slower than the applied field switching cycle and therefore it has considerably less influence on MPS signals (assuming non-interacting NPs in MPS magnetic field). dm/dH analyses show that Néel relaxation is the dominant mechanism determining MPI response in smaller NPs (d_0 < ~20nm). Larger NPs show hysteretic reversal when the applied field amplitude is large enough to overcome the coercivity. Linear variation of the MPS signal intensity with iron concentration but with uniform spatial resolution enable quantitative imaging for a range of applications, from high-concentration bolus chase imaging to low-concentration molecular imaging (while our instrument is noise-limited to ~milli-molar

iron concentrations, nano-molar sensitivity is expected for MPI, theoretically). These results show that MPI has the potential to be an effective imaging modality even when the NPs are immobilized in tissues (e.g. cancer targeting) and cells (e.g. stem cells) and pave the way for future application of our synthesized tracers for immobilized or in-vivo targeted MPI of tissues. We also, evaluated the MPI performance of the tracers in an acidic lysosome-like solution (Section 3.3), since lysosomes are one of the most common destinations for nanoparticles after their internalization into cells. Our results showed that the partial degradation of the nanoparticles in this acidic environment changes the MPI performance (e.g. dm/dH FWHM as a representative of spatial resolution). However, this phenomenon is dose-dependent and might be less when higher concentrations of the nanoparticles are internalized in lysosomes. We also, developed surface chemistry approaches to enhance the stability of our MPI tracers and functionalize them with amine groups (Section 3.2). In Chapter 4, we will use these highly stable and functionalized MPI tracers for multimodal MPI/MRI/NIRF imaging in mice.

Chapter 4.

IN VIVO MULTIMODAL MAGNETIC PARTICLE IMAGING (MPI) WITH TAILORED MAGNETO/OPTICAL CONTRAST AGENTS

4.1. Introduction

The theoretically predicted spatial resolution (sub-mm) and tracer mass sensitivity (~ nanograms) of MPI, position it as a versatile and competitive medical imaging technique in comparison with other established whole body imaging modalities such as MRI and PET.[1, 7] However, MPI is still at an early stage in its development. In order to expedite its clinical translation, further development in both imaging hardware and tracer optimization are required.[7, 18] For example, we have shown before that the nature (Néel or Brownian) and rate of magnetic relaxation of the NPs in response to the AC magnetic fields applied in MPI scanners play a significant role in determining the resolution and signal intensity in MPI.[19, 392, 427] These relaxation mechanisms depend on the core size, monodispersity and the molecular coatings of the NPs.[18, 42]

Following these initial findings, we reported a significant improvement in signal resolution and intensity using highly monodisperse NPs synthesized by a controlled thermal decomposition method, which were subsequently coated with a co-polymer of polyethylene glycol (PEG) and poly(maleic anhydride-alt-1-octadecene) (PMAO).[9, 10, 406] However, surface modification of these monodispersed MPI tracers is required to incorporate functionalities that enable a wide range of MPI image guided therapeutic applications.[17, 423] In particular, active surface functional groups such as amines (-NH_2), carboxyls (-COOH) or thiols (-SH) can be used for conjugation of various antibodies and peptides (*e.g.* for targeting cancer cells[97, 428]) cationic polymers (*e.g.* for improved stem cells labeling [429]) or labeling of the NPs with reporter molecules of other imaging modalities (*e.g.* fluorescent [430] or PET [153]). Additional functionalization of these NPs for other imaging modalities would also accelerate

screening of the MPI tracers based on their *in vitro* and *in vivo* performance in pre-clinical trials.

In section 3.2, we used a combination of ligand exchange and PEG conjugation to make amine functionalized PEG-coated monodisperse MPI tracers. Here, we conjugated two different types of poly-ethylene-glycols (NH_2-PEG-NH_2 and NH_2-PEG-FMOC) to monodisperse carboxylated 19.7nm NPs by amide bonding. Note that our later studies showed that nanoparticles core sizes in the range of 24-27nm are ideal for generating highest signal intensities and spatial resolution in MPI (See appendix A). However, at the time of these studies, we had repeatability challenges to synthesize nanoparticles with larger core sizes. Further, we conjugated Cy5.5 NIRF molecules to these functional groups and evaluated their *in vitro* and *in vivo* imaging efficiency as multimodal (MPI/MRI/NIRF) contrast agents. Labeling MPI tracers with NIRF molecules, which have a higher tissue penetration depth than other fluorescent molecules, [37, 292] provides details of their anatomical biodistribution and intracellular pathways that will enable future cellular MPI applications.[83, 327] Note that these amine functional groups can be also used for conjugation of cancer targeting biomolecules to NPs.

In addition, we show that implementation of a proper NPs surface functionalization approach can improve their multimodal imaging performance and prolong their blood half-lives. Bi-functional PEG (NH_2-PEG-NH_2) resulted in larger hydrodynamic size (~98nm vs. ~43nm for hetero-functional PEGs, NH_2-PEG-FMOC) of the tracers, due to interparticle crosslinking (see next sections). Formation of such clusters impacted the multimodal imaging performance and decreased the blood half-life of these tracers, which is critical for some applications such as cancer targeting that require longer plasma circulation times.[35] We also found that MPI signal intensity of the tracers in blood depends on their plasma clearance pharmacokinetics.

We also evaluated the biodistribution of these multimodal tracers in mice. Whole body mice MPI/MRI/NIRF imaging, showed primary distribution of NPs in liver and spleen. We used the T_2 MRI relaxivity of the NPs for quantitative assessment of the biodistribution of these NPs. Biodistribution of tracers and their clearance pathway was

further confirmed by MPI and NIRF signals from the excised organs, where the Cy5.5 labeling enabled detailed anatomical mapping of the tracers in tissue sections. Therefore, addition of other imaging modalities (*i.e.* NIRF and MRI) to optimized MPI tracers not only enhances their imaging functionality but also helps to monitor their *in vivo* biodistribution and clearance with anatomical sensitivity.

These multimodal MPI tracers, combining the strengths of each imaging modality (*e.g*. resolution, tracer sensitivity and clinical use feasibility) pave the way for various *in vitro* and *in vivo* MPI applications. Designing such multimodal MPI/MRI/NIRF imaging contrast agents should help open new areas for fluorescent or MRI assisted applications of MPI in molecular imaging, where MPI can not provide high resolution anatomical signals. MPI's clinical safety, cost effectiveness and imaging efficacy make it a promising tool for primary diagnosis of tumors, lesions or plaques. Addition of optical imaging modalities to MPI tracers further expands their scope of applications; for instance, optically labeled MPI tracers can be used as tumor or lesion paints, which can help delineate pre-operatively detected areas from the surrounding healthy tissues using portable fluorescent detectors.[431, 432] Thus, physicians in surgery rooms can safely remove only the affected areas. The pharmacokinetic and biodistribution results presented here will help expedite the development of a new generation of MPI tracers for a wide range of intracellular or tissue targeted MPI applications.

4.2. Synthesis of Cy5.5 labeled MPI tracers

Oleic acid coated NPs were synthesized as described before in section 3.1.2. Then, we silanized the NPs according to the procedure discussed in section 3.2.2. Silanized NPs were further conjugated with either bi-functional (NH_2-PEG-NH_2) or hetero-functional (NH_2-PEG-FMOC) PEG molecules (MW 5kDa, Laysan Bio, US) following modification of the method reported for conjugation of bis-amine PEG to carboxylated NPs described in section 3.2.2 (Fig. 4.1(a) and (b)).[17] Briefly, 170mg PEG was dissolved in 9mL THF and added to the NPs solution. Previous reports have shown that the succinic anhydride

group of TSP-coated NPs can hydrolyze and generate free carboxylic acid groups;[176] thus, 80mg of dicyclohexyl carbodiimide (DCC) coupling agent was added to facilitate

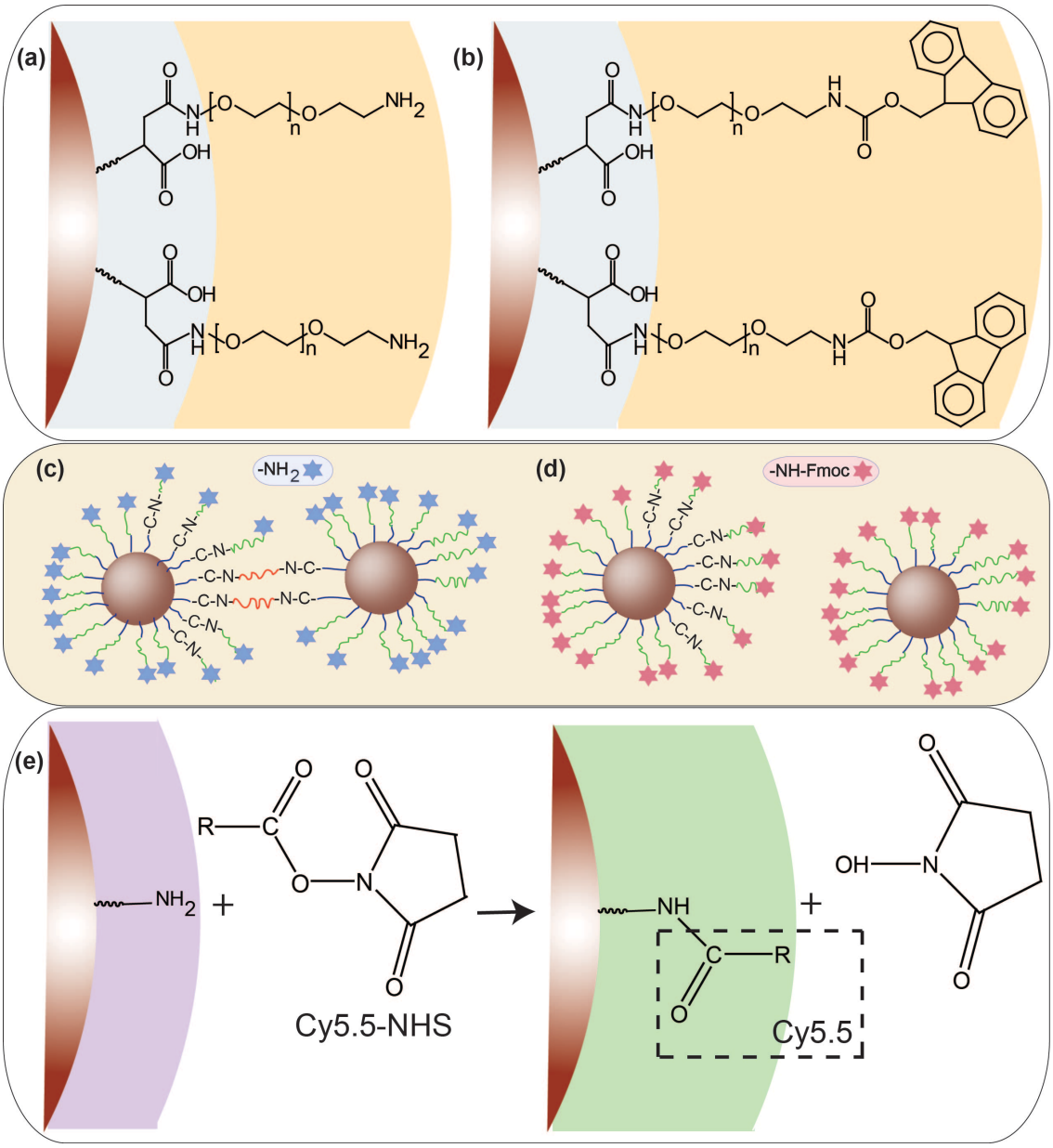

Fig. 4.1. Two different surface modifications of the NPs by formation of an amide bonding between the amine groups on the PEG backbone and carboxyl groups on the surface of the silanized NPs: (a) conjugation of the bi-functional (NH_2-PEG-NH_2) and (b) hetero-functional (NH_2-PEG-FMOC) PEG molecules. (c) Potential inter-particle bridging of some fraction of nanoparticles when bi-functional PEG is used for coating in comparison with (d) individually dispersed NPs modified with hetero-functional PEG. (e) Conjugation of amine-reactive Cy5.5 NHS ester to amine-functionalized NPs.

amide bond formation between the carboxylic acid-functionalized NPs and amine-terminated PEG molecules. The reaction vial was filled with argon, sealed and sonicated for 16h at 50°C. The PEG conjugated NPs were washed three times with excess hexane (50mL) and separated each time using a strong magnet. The final PEG-coated NPs were dried in vacuum and dispersed in 3mL sodium bicarbonate buffer (0.1M $NaHCO_3$, pH 8.2). A 20% solution of piperidine in N,N-dimethylformamide (DMF) solution was added to the NPs to release the FMOC protected amine groups on the surface of the NPs functionalized with hetero-functional PEG.[433] Size exclusion chromatography columns filled with s-200 Sephacryl^{TM} gel (GE Healthcare Life Sciences, US) were used as the final purification step using 1x PBS as the eluent. The average number of the active amine groups on the surface of NPs was determined using N-succinimidyl 3-(2-pyridyldithio)-propionate (SPDP) assay (see Appendix H).[114, 176]

Cy5.5 NHS ester (amine reactive, $C_{44}H_{46}CN_3O_4$) near infra-red fluorescence molecules (Lumiprobe, US) were conjugated to the amine groups of the NPs using the protocol recommended by the manufacturer (see Appendix I). The emission and excitation wavelengths of these NIRF molecules were 673 and 707nm, respectively, with a fluorescence quantum yield of 0.2. Briefly, 1mg of the dye was dissolved in fresh DMF and added to the degassed aqueous solutions of the NPs (5mg). The vials were wrapped with aluminum foil and shaken overnight. The un-reacted dye molecules were removed using S-200 columns.

4.3. Characterization of the NIRF labeled MPI tracers

We used ICP to determine the iron concentration in each NPs solution. DLS was used to measure the hydrodynamic size of the NPs. High Resolution TEM was used for analysis of the core size and morphology of the NPs. Using a room temperature VSM, we measured the magnetization, $m(H)$, behavior of the NPs. Further, using Chantrell fitting to the magnetization curves, we determined the median core size of a statistically-significant number (100μL, ~2.65mg Fe/mL) of the NPs to be about 19.7nm

(σ=0.27).[404] Weight losses of the samples were also studied after freeze-drying of the water-dispersed NPs using a thermo-gravimetric analysis system (TG, Perkin-Elmer, US). We also used a Bruker Vertex 70 Fourier transform infra-red (FTIR) spectrometer equipped with an attenuated total reflectance (ATR) unit for analysis of the surface coating of the freeze-dried NPs.

We used our home-built Magnetic Particle Spectrometer (MPS, f_0 = 25kHz and $\mu_0 H_{max}$ = 20mT) to estimate the MPI performance of the MNP tracers in real MPI scanners. The details of these MPS measurement parameters can be found in section 3.1.6. To measure the Cy5.5 fluorescence signal of the NPs, 50μL of the NPs with different concentrations were added to 96-well clear bottom plates and the plates were scanned using an Odyssey NIRF instrument (LI-COR, US), using the 700nm channel with excitation and emission wavelengths of 685 and 705nm.

4.4. Animal experiments

Female CD-1 mice (25-35g, 8 weeks old) were purchased from Charles River Laboratories and used for the *in vivo* studies. We used 36 mice for blood circulation studies and 9 mice for biodistribution studies. All the animal studies were reviewed and approved by the Institutional Animal Care and Use Committee (IACUC) of the University of Washington (protocol number 4282). All the animal study data are expressed as mean ± standard deviation (SD).

4.5. Pharmacokinetics studies

Anesthetized mice were injected with NPs (100μL, 2mg Fe/mL) through their tail veins. Blood samples were collected retro-orbitally at ~ 0 (immediately after injection), 5, 10, 15, 20, 30, 45 and 60 mins after injection. The blood samples were stored in anti-coagulant EDTA coated vials and then transferred into 100 μL polycarbonate capsules for VSM and MPS studies. Two samples were collected from each mouse, after which the animals were euthanized immediately. Three blood samples were prepared for each blood-draw time point. The VSM and MPS measurements were repeated three times for

each sample and the results were averaged. In most of the measurements the standard deviation values were very small and not observable on the presented graphs. The average saturation magnetization obtained from the VSM and the average signal intensity determined from the MPS measurements were compared with the standard calibration lines generated from the NPs prior to injection to assess the amount of the NPs in the blood after normalization to mouse weight (kg). The average amounts of the NPs in blood samples were plotted versus post-injection time and the blood circulation half-life was determined from the exponential decay curve generated for each type of NPs. The half-lives determined from VSM (static magnetic field) and MPS (AC magnetic field, f_0 = 25kHz) were compared to check the consistency of the results. Note that these magnetic measurements show the half-life of magnetic component of the nanoparticles (i.e. iron oxide core), and here we think, based on high stability of the nanoparticles, the half-life observed for the core and coating materials are the same and nanoparticles do not dis-integrate during the circulation in blood. Future radiolabeling experiments are required to determine the exact half-lives of each compartment of the nanoparticles (i.e. core and different coating molecules).

4.6. Blood phantoms imaging

For MPI imaging of the blood samples, 100μL of the blood was transferred into polycarbonate capsules and placed in the center of the centrifuge tubes as shown in Fig. 4.2. MPI images of the blood phantoms were acquired with the projection Field Free Line (FFL) MPI scanner at UC Berkeley [434, 435] operating with a magnetic field gradient strength of 2.4 T/m along *x*- and *z*-axes. The *y*-axis of the instrument, which corresponds to the direction of the FFL, has a significantly smaller magnetic field gradient strength of 0.08 T/m. The samples were translated along the *z*-axis of the imager using a single-axis translation stage (Velmex, US). Images of the blood phantoms were taken with a field of view (FOV) of 4 cm x 6 cm and acquisition time of 12 seconds. The maximum intensity of the images was then extracted for analysis.

For T_2-weighted MRI imaging, the blood samples were mixed (1:1 volume ratio) with 2wt.% solution of agarose in water and cooled down in the refrigerator to 4°C to solidify. Agarose is usually considered as a tissue equivalent material for similar MRI analyses. [402] We used a 14T (600MHz) vertical bore Magnetic Resonance Spectrometer (Bruker). T_2 weighted images of the blood samples were acquired by Bruker MSME T_2 protocol (12 echo times; TR/TE=4000/6.28...12x6.28). ImageJ and MATLAB software were used to generate the colorized R_2 images of the blood samples drawn at different times from their reciprocal T_2 images.

For NIRF imaging, 50µL of the blood drawn at different post-injection times were added to wells of a 96-well clear-bottom plate and the plate was then scanned on the Odyssey NIRF scanner similar to NPs measurements.

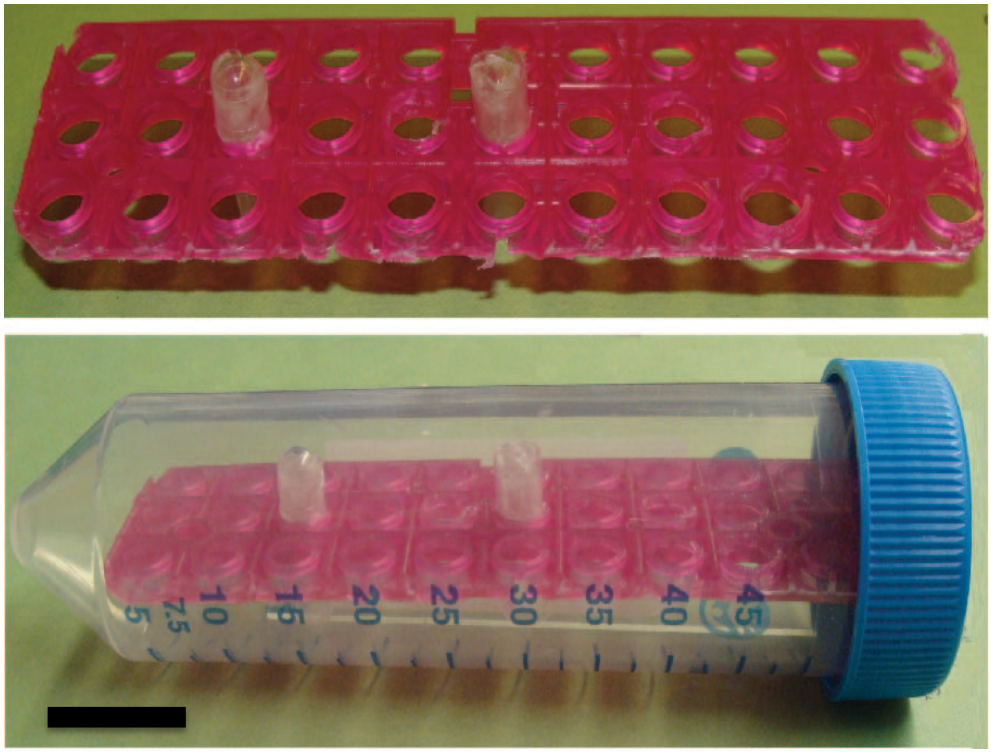

Fig. 4.2. Phantoms used for MPI imaging of the blood samples. The blood samples were transferred to 100µL polycarbonate capsules, which were then placed inside a 50mL polypropylene tube (scale bar~ 2cm).

4.7. Biodistribution studies

For biodistribution studies, mice were injected with 100μL, 1mg Fe/mL of the NPs. Three mice were used to test each type of NPs and the results were compared with control mice injected with sterile PBS (1x). Axial T_2–weighted MRI images (i.e. MRI images with T2 contrast) of the mice (25 axial slices of the abdominal region, each 1mm thick) were acquired before injection and 24 and 72 hours after injection of the NPs. Using ImageJ software we determined the change in R2 values (ΔR_2) in the liver, spleen and kidneys before and after injection of the NPs and calculated the amount of the NPs in each organ as follows [10]:

$$\Delta R_2 = r_2 * C \quad (1)$$

where, r_2 is the NPs T_2 relaxivity ($mMFe^{-1}.s^{-1}$) and C is the NPs concentration (mM Fe) in each organ. To determine the T_2 relaxivity of the NPs, we mixed (1:1 volume ratio) of various concentration of the NPs (0, 2.5, 5, 10, 20 and 40μg Fe/mL) with 2wt.% agarose gel. The R_2 images were generated using the same parameters described for blood phantoms. Relaxation times (r_2) of the NPs were determined using the slope of their linear plot of R_2 values versus iron concentration.[10, 356]

NIRF images of the mice and excised organs were acquired using the *in vivo* imaging system (IVIS, Caliper Life Sciences, US) equipped with the Living Image software package. Images were acquired using a high lamp level (excitation and emission wavelengths of 640 and 680 nm, respectively, exposure time of 1 second and f-step at f_4). MPI images of the sacrificed mice were acquired using the same scanner described for blood phantom imaging, with a FOV of 4 cm x 12 cm and acquisition time of 16 seconds. For *ex vivo* MPS analysis, organs sections with determined weights were placed inside the 0.5mL vials and analyzed using our home-built MPS with a drive frequency, f_0=25kHz. The resulting data were then normalized to tissue weight.

For histology analyses, we sacrificed the mice 72 hours after injection of the NPs and fixed the harvested organs in 10% formalin and then embedded them in paraffin. Tissue sections were then imaged following hematoxylin & eosin (H&E) and Prussian Blue (PB) staining. For ex-vivo NIRF imaging of the tissue sections, formalin fixed tissues were

placed into sucrose solution (30%) at 4°C until the tissues sank. Then, the tissues were transferred to optimum cutting temperature (OCT) compound and sectioned (12μm thickness) after freezing. The sections were then imaged using the Odyssey scanner, similar to the NPs and blood phantom analyses described above.

4.8. Results and discussions

4.8.1. Synthesis and evaluation of the multimodal MPI tracers

Structural, magnetic and MPS results of the two types of the NPs are summarized in Table 4.1. We have shown before that a well-controlled synthesis is required to synthesize monodisperse iron oxide NPs with enhanced performance as MPI tracers in comparison with other commercially available NPs such as Resovist and Feridex.[10, 21] Here, we used thermal decomposition of iron oleate in the presence of oleic acid to make highly monodisperse oleic acid capped NPs in organic solvents with the median core size of 19.7nm (standard deviation: 0.267). This core size was calculated using Chantrell fitting to the NPs magnetization curve and matched well with the TEM results (Fig. 4.3.a).[404] These NPs were carboxylated using a previously reported ligand exchange (or silanization) method.[17, 176, 419] Two PEG derivatives (bi-functional NH_2-PEG-NH_2 and hetero-functional NH_2-PEG-FMOC) with the same PEG to NPs molar ratios were conjugated to these NPs by the formation of an amide bond between the terminating amine groups (-NH_2) of the polymers and carboxyl groups (-COOH) on the surface of the silanized NPs (Fig. 4.1). FMOC protected amine groups were de-protected by addition of a 20% piperidine in DMF solution. Finally, amine-reactive Cy5.5 NHS ester NIRF molecules were conjugated to the amine-functionalized NPs (Fig. 4.1.e).

Table 4.1. Structural, magneto/optical and blood circulation characteristics of the two different NPs.

Coating	Size		MPS signal		Relaxivity [s^{-1}.mg Fe^{-1}][(a)]	NIRF [a.u.][(b)]	Half life [min]
	Core [nm] (σ)	Hydrodynamic [nm] (PDI)	Intensity [mv/mg Fe]	FWHM			
NH_2-PEG-NH_2	19.7 (0.27)	98 (0.29)	22	11.1	376.8±22	23	12-14
NH_2-PEG-FMOC		43 (0.18)	27	9.2	325.59±24	42	23-26

[(a)] MRI T_2 relaxivity of the NPs.
[(b)] NIRF signal intensity from 50μg of the NPs.

NPs functionalized with bi-functional PEG had a larger average hydrodynamic size (~98nm) in comparison with those functionalized with hetero-functional PEGs (~43nm) (Fig. 4.3.b). The bi-functional PEG molecules can further form amide bonds with the NPs carboxyl groups through both their terminating amine groups (Fig. 4.1.b). Therefore, some of these bi-functional PEG molecules can form clusters by bridging between the adjacent NPs and increase the average hydrodynamic size to ~98nm. The bridging keeps the NPs close to each other and shields a major part of the carboxyl groups on the surface of the NPs, making them inaccessible to other PEG molecules. Therefore, the average number of PEG molecules that could covalently bond with the NPs carboxyl groups decreased when bi-functional PEG was used compared to the hetero-functional PEG. This was confirmed by lower weight loss percentage of bi-functional PEG coated NPs (~25% less compared to those coated with hetero-functional PEG) due to thermal decomposition of the coating polymer in TG analyses (Figs. 4.3.c and d). Note that the oleic acid coated NPs showed only ~4% weight loss due to decomposition of the surface coating oleic acid molecules by increasing the temperature (Fig. 4.4). In order to prevent bridging between NPs, a hetero-functional PEG molecule with only one active amine group (the other amine was protected with a FMOC group) was used (Fig. 4.1.d). In comparison with the bi-functional PEG, the hetero-functional PEG resulted in a denser coating as confirmed in TG analysis (Fig. 4.3.d). ATR-IR spectroscopy of the freeze-dried samples (Fig. 4.5) showed characteristic peaks of PEG C-H stretch band (at ~2850

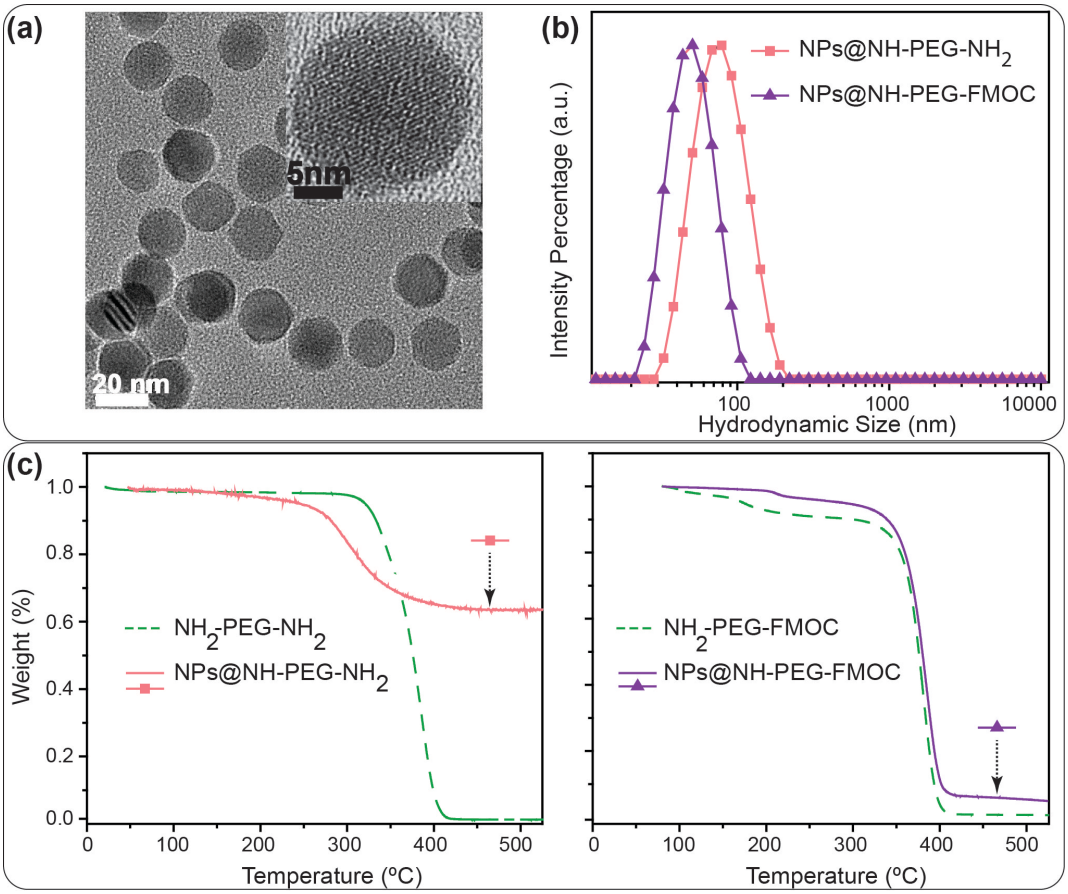

Fig. 4.3. (a) TEM image showing the core size distribution and morphology of the NPs. The inset HRTEM image shows the lattice fringes of a single nanoparticle. (b) DLS intensity data showing the hydrodynamic size distribution of the NPs functionalized with NH_2-PEG-NH_2 and NH_2-PEG-FMOC. (c) and (d) Thermogravimetric (TG) analysis data showing the weight percentage of the PEG molecules in each type of the NPs – notice the lower weight loss in NPs coated with bi-functional PEG (~70%) compared to heterofunctional PEG (~95%), suggesting a greater coating density with hetero-functional PEG. The dotted curves show the TG graphs of the pure polymers before their conjugation to the NPs; on the other hand, the TG graphs of the coated NPs represent the total weight loss due to decomposition of the conjugated polymers, silanization molecules (TSP) and any oleic acid residue on the surface of the NPs. Note that the same polymer to NPs molar ratio was used for both types of the NPs presented here. Square and triangle symbols are added to graphs in parts (c) and (d) to help recognizing the samples.

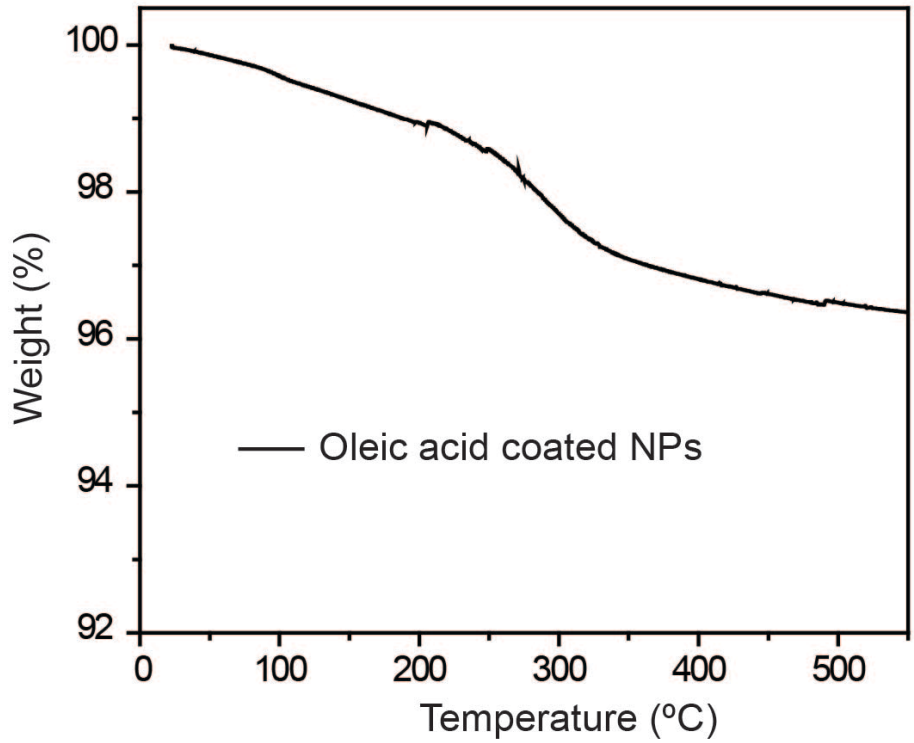

Fig. 4.4. Thermogravimetric (TG) analysis of the oleic acid coated NPs. The as-synthesized NPs were purified and dried in vacuum before this measurement. Compared to Fig. 4.3, this graph shows that oleic acid was only a small fraction of the NPs weight.

cm^{-1}) and different vibrational modes of PEG C-O-C bonds (at around 950, 1115, 1248, 1341 and 1462 cm^{-1}) in all samples.[48, 436] The bands at ~1646 and 1565 cm^{-1} showed the presence of primary amine groups or amides bands on the NPs surface, confirming the successful conjugation of PEG molecules to carboxyl groups of the silanized

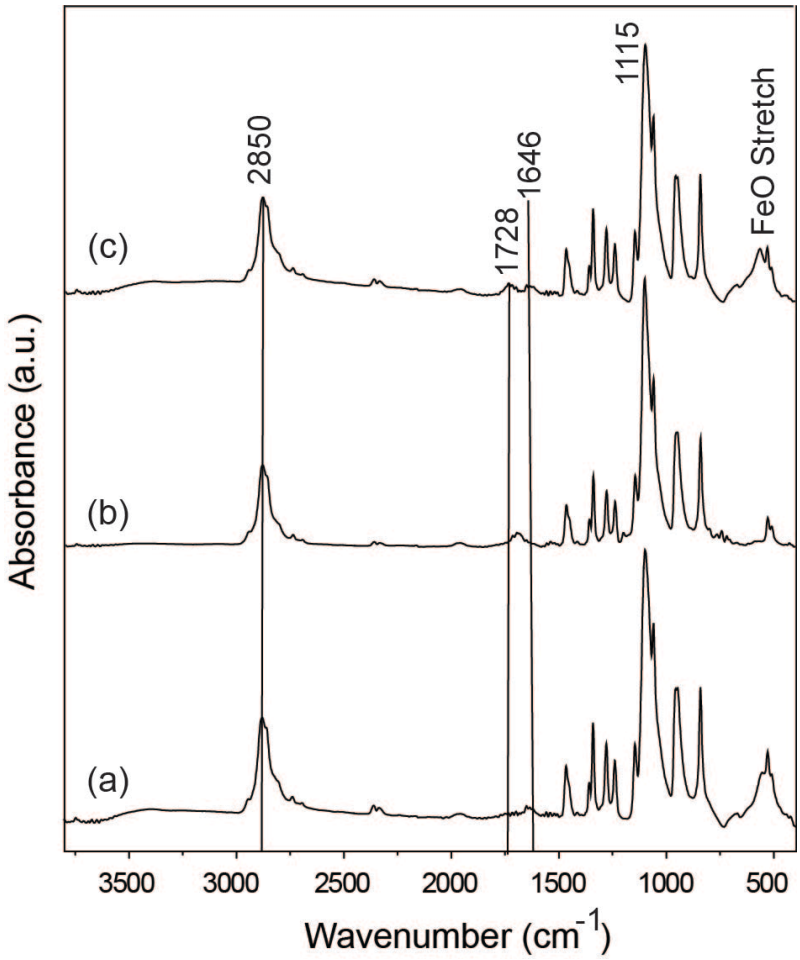

Fig. 4.5. ATR IR spectra of the NPs coated with (a) NH_2-PEG-NH_2 and (b) NH_2-PEG-FMOC. Part (C) shows the appearance of the amine characteristic peak at 1646 cm^{-1}, after releasing the FMOC-protected amine groups. The peak at 1728 cm^{-1} corresponds to presence of carboxyl groups on the surface of the NPs.

NPs resulted from our ligand exchange method.[176] These bands were more pronounced after releasing the FMOC-protected amine groups. Also, in previous reports, no characteristic peaks of the TSP anhydride rings were observed at around 1800-1850 cm^{-1}, showing that they were hydrolyzed and formed carboxyl groups (~1728 cm^{-1}) after silanization.[48, 176] Amine quantification using the SPDP assay further validated findings from TG and IR analyses – the average number of the active amine groups on the surface of the NPs was about 47% less (~97 for NH_2-PEG-NH_2 versus ~185 for de-protected NH_2-PEG-FMOC) when bi-functional PEG was used to functionalize the NPs.

The clusters formed due to the bi-functional PEG behaved similar to larger core sizes of iron oxide and respond to the applied AC magnetic field of the MPS system at higher field values (Fig. 4.6.a); consequently, the full width at half maximum of the field dependence of the differential susceptibility, d*m*/d*H*, increases slightly, confirming as an additional supportive evidence that some clusters formed in these samples (Fig. 4.6.b).[17, 42, 423] Note that d*m*/d*H* is the instrument-independent point spread function (PSF) in MPI, and is solely the contribution of the nonlinear particle response to the AC magnetic field. Therefore, the FWHM and peak height of the d*m*/d*H* curves obtained from MPS can be interpreted as the instrument-independent spatial resolution and signal intensity in ideal MPI images, respectively.[42] In a MPI scanner, a static field gradient (*dH/dx*) is superimposed with the AC magnetic field, and the system PSF is given by the product of *dm/dH* and *dH/dx*.[7, 15]

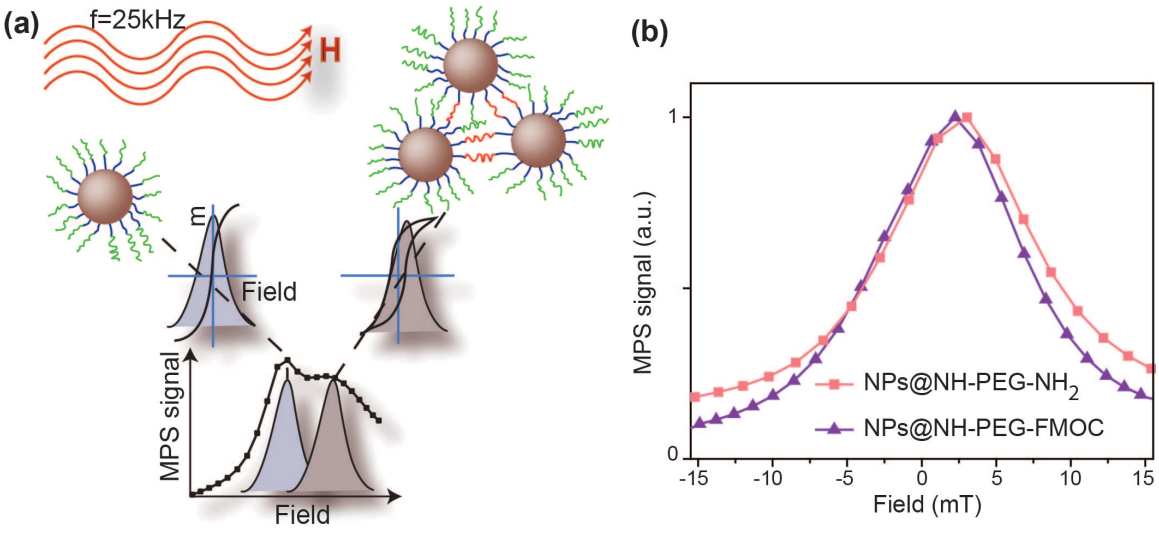

Fig 4.6. (a) Schematic showing the increase in FWHM of the d*m*/d*H* graphs due to partial cross-linking between the NPs when bi-functional PEG (NH_2-PEG-NH_2) was used for their surface modification. (b) MPS performance (d*m*/d*H*) of the NPs after conjugation of NH_2-PEG-NH_2 or NH_2-PEG-FMOC to their surface.

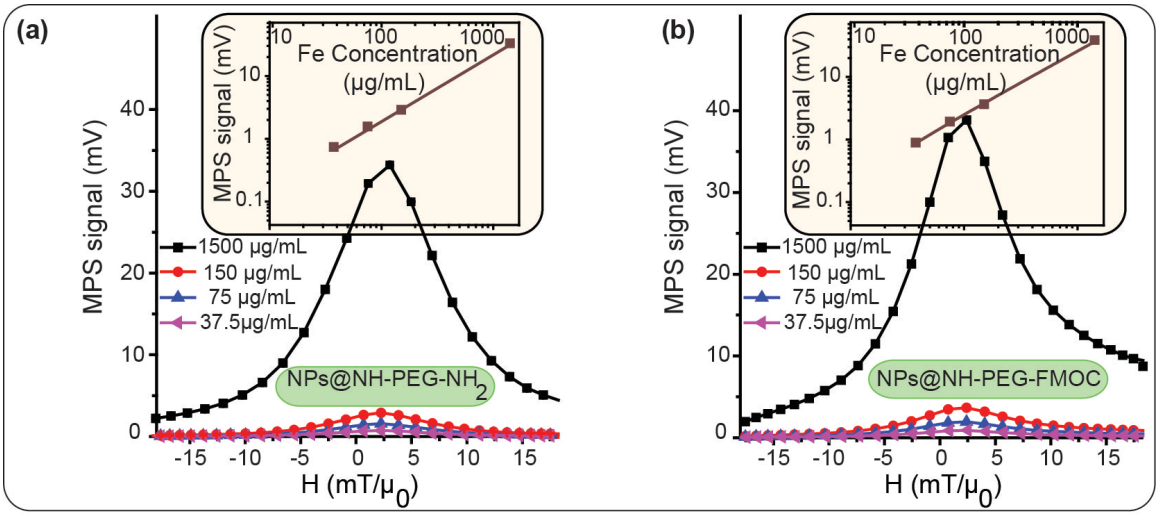

Fig. 4.7. MPS (d*m*/d*H*) graphs of the NPs as representatives of their MPI performance.

The linear dependence of the MPS signal intensity with concentration of the NPs helps determine the amount of the tracer accumulated in imaging volume (voxels) in different organs, such as liver, spleen and brain. In other imaging applications such as cancer imaging and atherosclerosis diagnosis, this linearity can be used to quantify the nanoparticles uptaken by tumors or aorta leasions. The MPS signal intensity (maximum of d*m*/d*H*) of the Cy5.5 labeled NPs discussed above showed a linear dependence with iron concentration, ranging from 37.5 to 1500μg/mL (Fig. 4.7). We have seen this linearity for various other MPI tracer formulations and one example is also shown in Figs. 3.5. This linearity of the MPI signal intensity measured with MPS, matches well with the linear variation of the NPs saturation magnetization (M_s) with iron concentration, measured with VSM (Fig. 4.10).

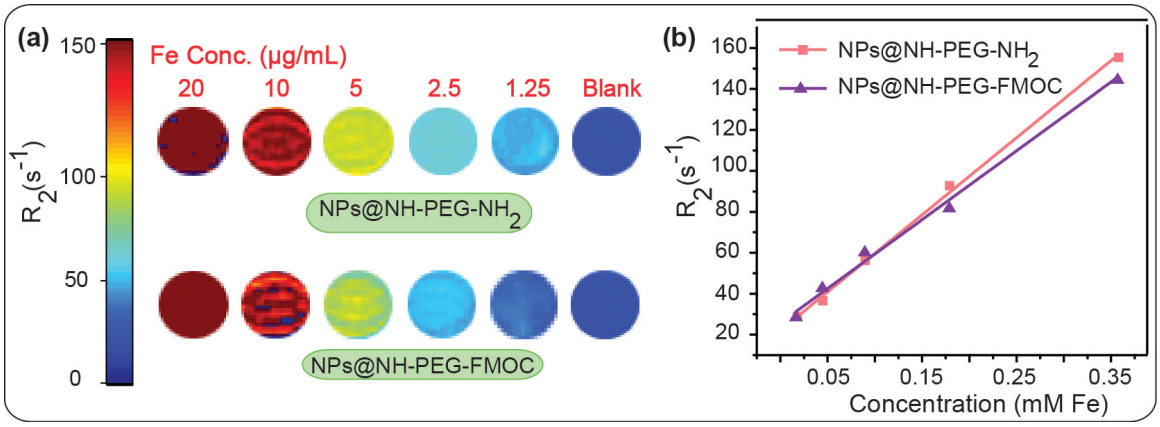

Fig. 4.8. (a) MRI R_2 maps and (d) T_2 relaxivity of the NPs, showing the performance of the nanoparticles as MRI contrast agents. These relaxivity values were calculated from the R_2 maps shown in part (a) and were later used for determination of the nanoparticles biodistribution in live mice.

When used as T_2 MRI contrast agents, the T_2 contrast generated by NPs dispersed in agarose gel phantoms also changed linearly with iron concentration. This MRI signal change linearity has been also used in various quantitative analyses of the nanoparticles in tissues and organs during the last two dcades. The colorized R_2 images (Fig. 4.8.a) were then generated from the reciprocal of these T_2-weighted MRI phantom images. The average R_2 values of the samples were plotted as a function of iron concentration in each sample (Fig. 4.8.b). The slope of this line is the T_2 relaxivity (r_2) of the NPs. The relaxivity (r_2) of the NPs coated with NH_2-PEG-NH_2 and NH_2-PEG-FMOC were calculated as 376.8±22 and 325.59±24 s^{-1}.mg Fe^{-1}, respectively. These are relatively high r_2 values compared to various values reported for iron oxide nanoparticles in literature. We believe this larger r_2 value is due to higher magnetization rate of the larger core sizes.

We also used an Odyssey NIRF scanner to determine the fluorescent signal of the NPs phantoms. Similar to MPI and MRI imaging modalities, the NIRF signal intensities of these fluorescently labeled NPs, decrease approximately linearly with dilution of the NPs concentration (Fig. 4.9). Note that the samples were transferred to wells of a 96-wells plate and inserted into an Odyssay scanner to measure the fluorescent signal. The signal at edges of the wells is slightly more than the central points, even though they represent the same sample. This is in fact an imaging artifact generated due to convex

interfaces between nanoparticles aqueous solutions and wells edges. The NIRF signal intensity was higher in NPs functionalized with hetero-functional PEG. This was due to presence of larger number of active amine groups on the surface of these NPs (~185 vs. 97), which increased the Cy5.5 labeling efficacy. Overall, Figs. 4.7, 4.8 and 4.9 show the efficiency of these nanoparticles as multimodal MPI/MRI and NIRF imaging contrast agents at different concentrations. The signal intensities in all these imaging modalities change linearly with NPs concentration, which is critical for determining the amount of the NPs in tissues.

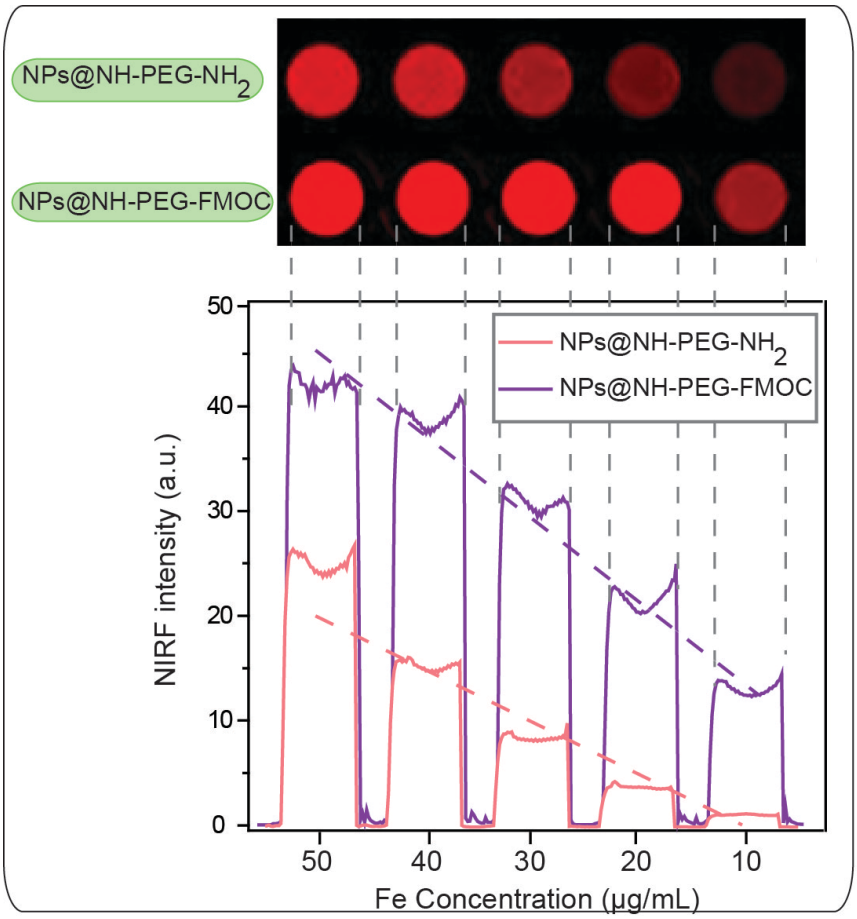

Fig. 4.9. (a) NIRF images of the NPs and (b) fluorescent signal intensities measured from each sample using and Odyssay scanner.

4.8.2. Pharamacokinetic studies

NPs tracers are often intravenously injected for various applications such as targeted imaging of the organs (*e.g.* cancers) [97, 437] and cardiovascular diseases.[438] The major part of the IV injected tracers gets rapidly eliminated from the blood stream by mononuclear phagocytizing macrophages in the mononuclear phagocytic system (also called reticuloendothelial system, RES).[147]

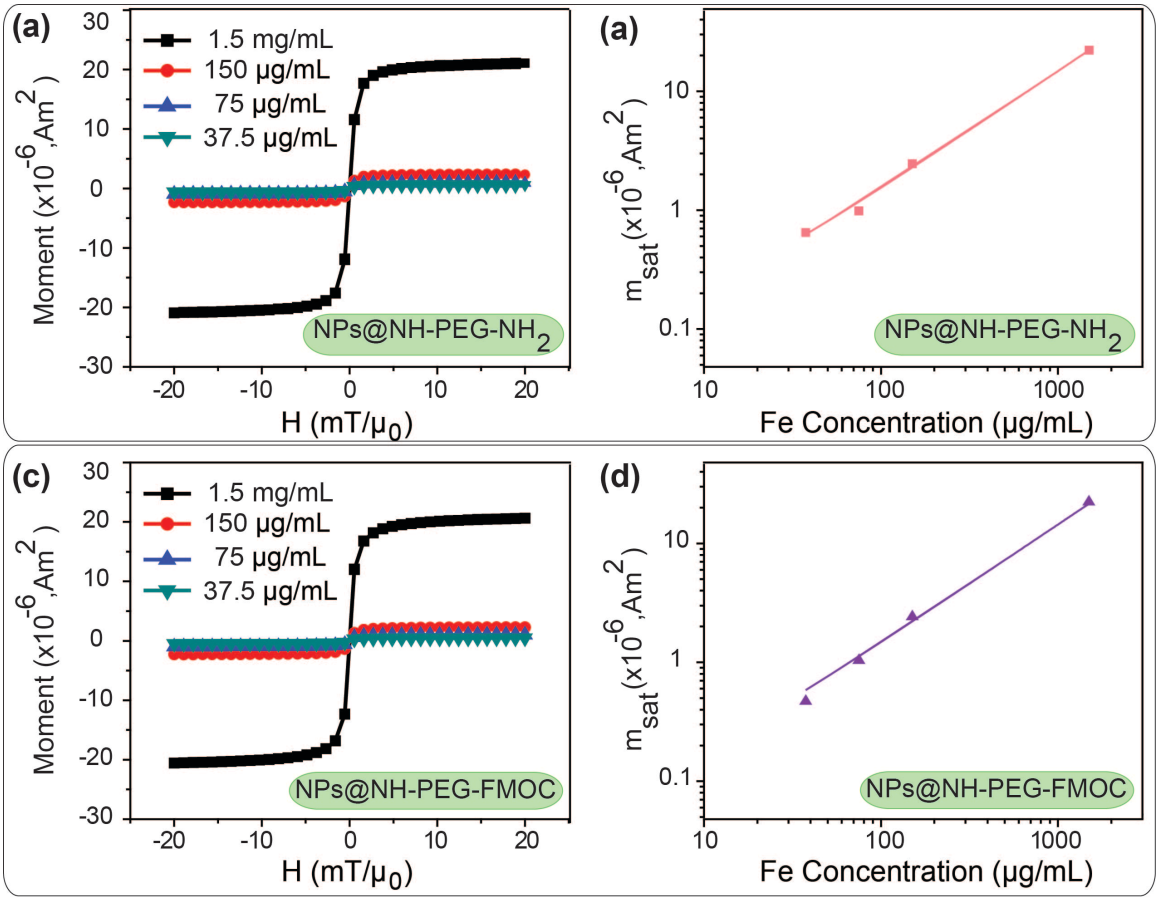

Fig. 4.10. Magnetization (*m-H*) graphs ((a) and (c)) and saturation magnetization (m_{sat}, (b) and (d)) of the NPs at different concentrations: (a) and (b) NH_2-PEG-NH_2 and (c) and (d) NH_2-PEG-FMOC. These graphs were used as standard references for determination of the NPs concentration in blood samples from their *m-H* diagrams (Fig. 4.12).

The pharmacokinetics of this phenomenon determines the blood circulation half-life of the NPs, which is a critical parameter defining the efficiency of the NPs to reach or reside in targeted organs or regions of the body.[34]

We injected the two types of the Cy5.5 labeled NPs into CD-1 female mice through tail veins (100μL, 2mg Fe/mL) and determined the NPs concentrations in the blood samples drawn retro-orbitally at different times post-injection (0 to 60 min). To find the half-lives, we measured the MPI signal intensity and saturation magnetization of the blood samples by MPS and VSM analyses, respectively (Fig. 4.11). These values were then compared with our MPS and VSM calibration lines generated using standards prepared from the original NPs (Figs. 4.7 and 4.10).[10] After normalizing to mice body weight (kg), we determined the half-lives of the NPs by fitting both MPS and VSM data to a first-order exponential decay model, assuming a one compartment structure for nanoparticles which do not dis-integrate during the circulation in blood. The NPs functionalized with bi-functional amine had a blood half-life of about 12 min, while NPs functionalized with heterogeneous PEG had a longer blood half-life of about 23-26 min (Fig. 4.12). This observed difference is attributed to the larger hydrodynamic size of the NPs coated with bi-functional PEG. NPs with larger hydrodynamic sizes have a considerably higher chance to get entrapped and taken up by macrophages in trabecular meshworks of the RES organs.[34, 147] Also, the half-lives determined from both MPS ($f_0 \sim$ 25kHz) and VSM techniques were consistent, suggesting that the circulating NPs were superparamagnetic without any aggregation, which would otherwise alter their responses to the applied magnetic fields.

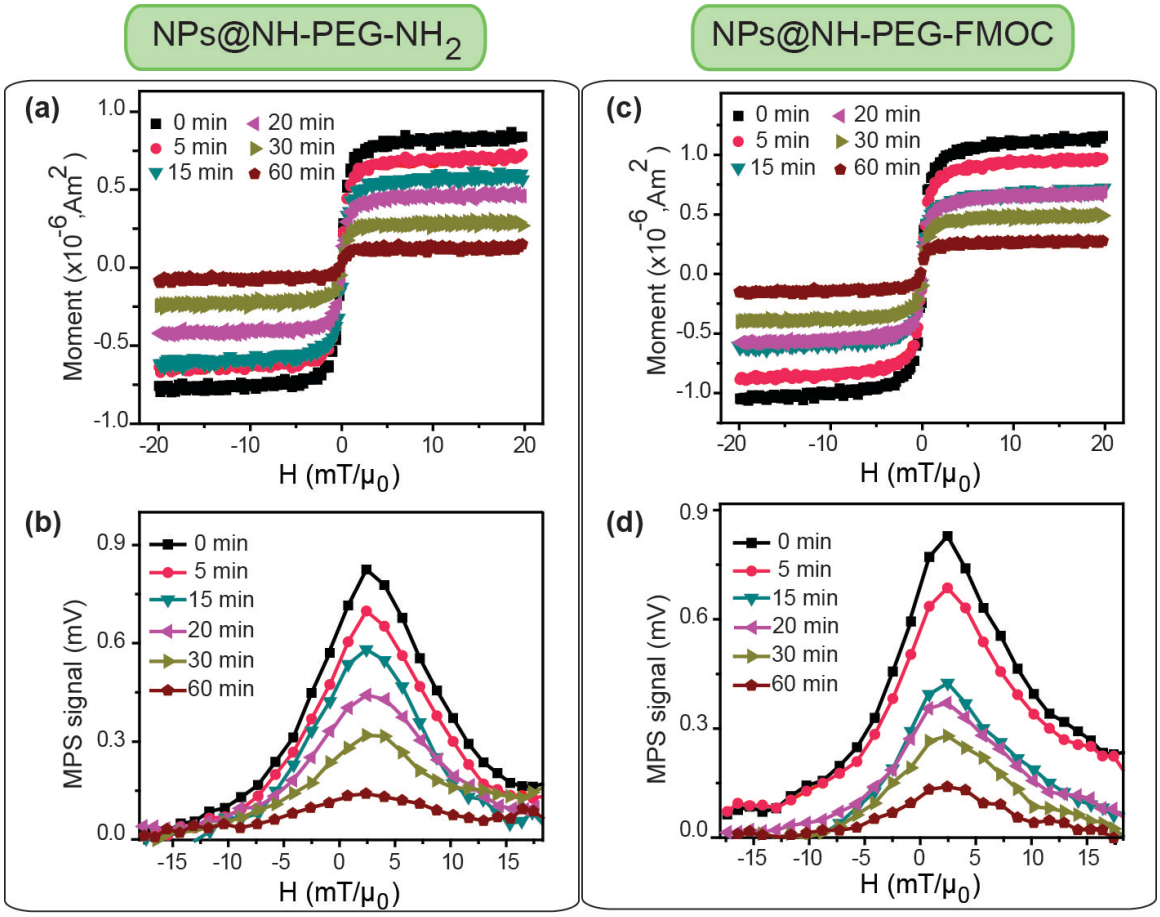

Fig. 4.11. *m-H* (a and c) and MPS d*m*/d*H* (b and d) graphs of the blood samples drawn retro-orbitally at different (0-60 min) post-injection times. Note that 0 min data correspond to a blood sample that was directly taken after NPs injection. (a) and (b) are the results of the blood analyses after injection of the NH_2-PEG-NH_2 modified NPs, and (c) and (d) show the same results for the NH_2-PEG-FMOC modified NPs. All the VSM and MPS measurements were repeated three times and average graphs with standard deviations are presented here.

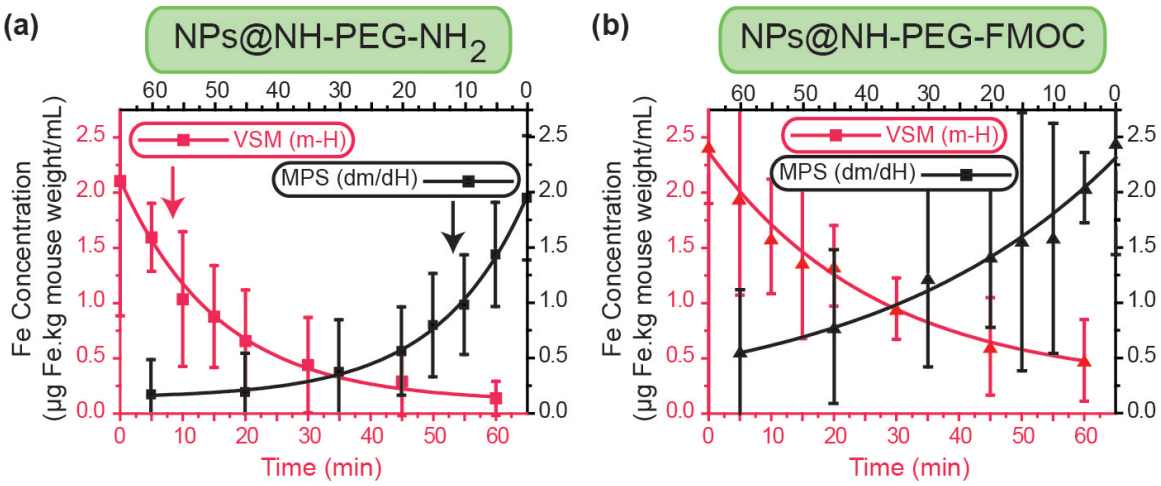

Fig. 4.12. Concentration of the NPs in blood samples calculated from *m-H* and d*m*/d*H* graphs shown in Fig. 4.9. Red and black color graphs in (c) and (f) show the blood half-lives of the NPs determined by VSM and MPS data, respectively. We used the standard lines generated by NPs before the injections (Figs. 4.7a and 4.8) to determine the blood half-lives of the NPs from these blood MPS and VSM data. NPs coated with hetero-functional PEG (NH_2-PEG-FMOC) showed a longer plasma circulation time (23-26 min) than NPs coated with bi-functional NH_2-PEG-NH_2 (12-14 min).

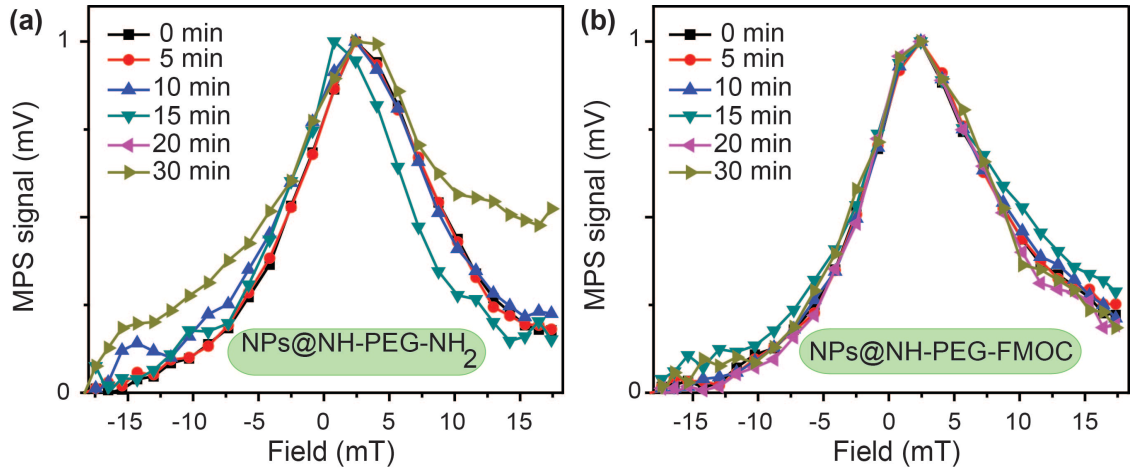

Fig. 4.13. Consistency of the FWHM of the MPS (dm/dH) graphs of the blood samples drawn retro-orbitally at different NPs post-injection times. The NPs were functionalized with (a) NH_2-PEG-NH_2 and (b) NH_2-PEG-FMOC.

When NPs are unstable and form aggregates, the resulting increase in their hydrodynamic size leads to a widening of the FWHM of their MPS signal (d*m*/d*H*) (Fig.

4.6).[9, 178, 354] We have shown earlier that our PEG functionalized NPs show a consistent hydrodynamic size and MPI performance over 7 days of incubation in different biological media such as PBS and DMEM cell culture media enriched with 10% fetal bovine serum (FBS).[17, 423] However, the incubation salt concentrations, pH values and temperature, even if controlled precisely, cannot usually replicate the stability of the NPs characteristics in the presence of different plasmatic proteins and body innate immune system. Therefore, in our pharmacokinetic studies, we also focused on monitoring the FWHM of the NPs in blood samples drawn at different times, in order to evaluate their *in vivo* blood stability. The FWHM of the d*m*/d*H* of all the NPs were unchanged during their circulation in blood (Fig. 4.13). This constant FWHM implies a stable spatial resolution when these NPs are used as MPI tracers, in a wide range of applications such as cardiovascular imaging or targeted cancer imaging. Generally, MPS measurements can uniquely show the aggregation state of the injected magnetic NPs in the blood at very low tracer concentrations, an important phenomenon that has not been detectable by other size measurement techniques such as dynamic light scattering or microscopy methods.

We prepared MPI, MRI and NIRF phantoms from these blood samples and studied the signal variations in each modality. Fig. 4.14.a shows the MPI images of the blood phantoms (also see Fig. 4.2). The MPI signal intensity decreased 20 min after the injection of the NPs, due to elimination of the NPs from the blood. The same trends were observed in MRI T_2-weighted and NIRF images (Fig. 4.14.b and c). The rate of decrease of signal intensity was faster for NPs coated with bi-functional PEG, which had a shorter half-life (Fig. 4.12) in all the three imaging modalities. Comparable trends were observed in all the imaging modalities.

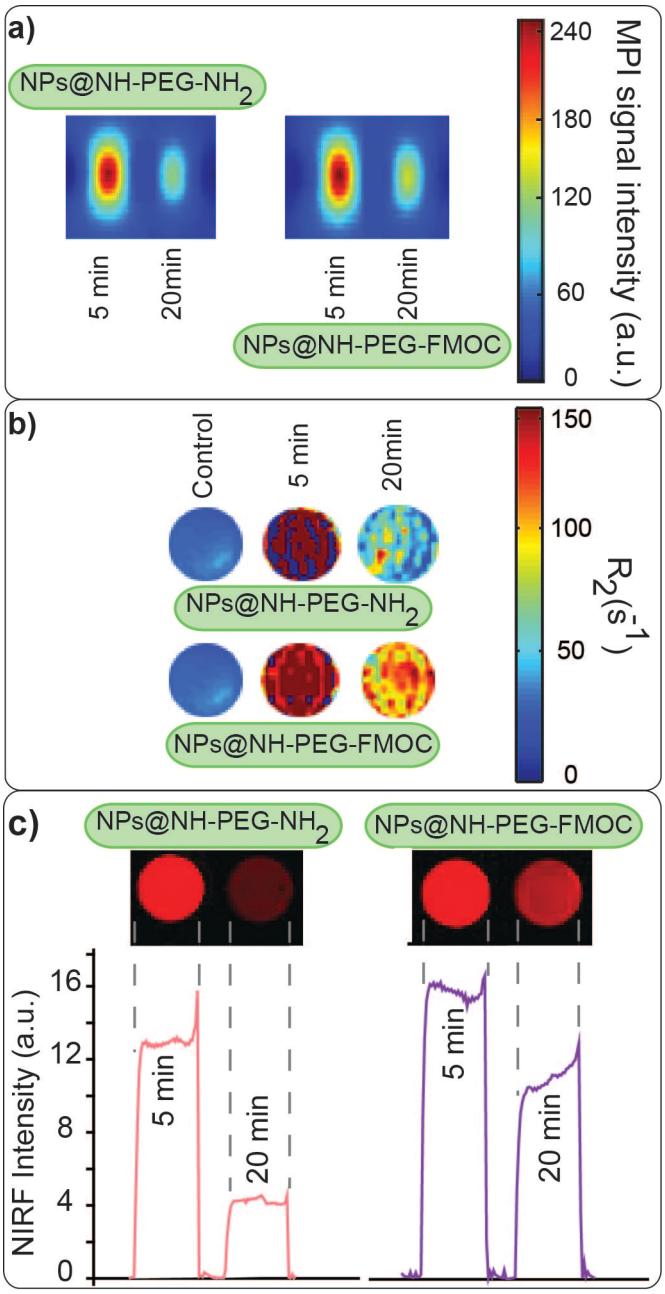

Fig. 4.14. Tri-modal imaging of the blood samples drawn after injection of NIRF labeled NPs functionalized with NH_2-PEG-NH_2 and NH_2-PEG-FMOC: (a) MPI, (b) MRI R_2 map and (c) NIRF images. No signal was observed in blood samples without any NPs. The signal intensity in all the three imaging modalities depends on the concentration and pharmacokinetic of the NPs in the blood plasma. NPs coated with NH_2-PEG-FMOC showed stronger post-injection signals in the blood in all these three imaging modalities.

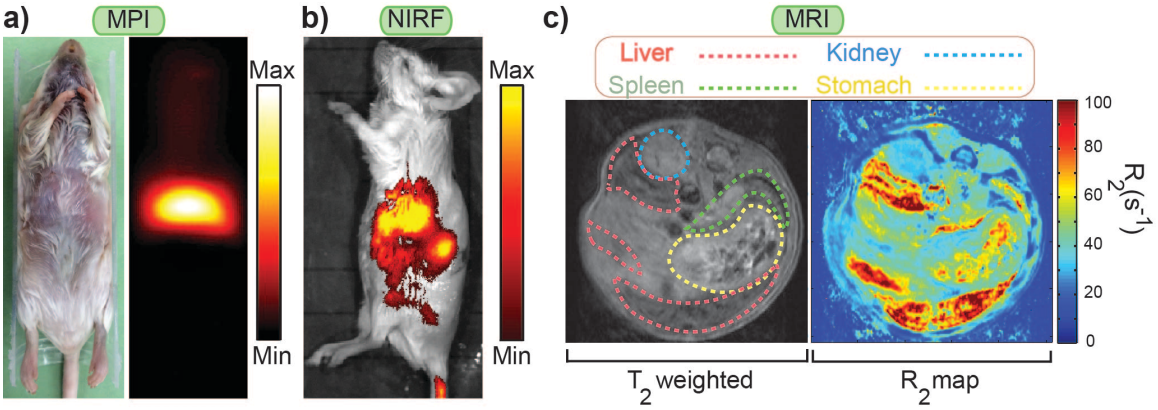

Fig. 4.15. Whole mouse body imaging 72 hours after injection of NPs functionalized with NH_2-PEG-FMOC: (a) colorized MPI (b) NIRF and (c) MRI T_2 weighted and colorized R_2 images. These three imaging modalities show that injected NPs were accumulated in the principal RES organs (*i.e*. liver and spleen). MPI generates a positive contrast image directly originated form the superparamagnetic NPs without any background noise from surrounding diamagnetic tissues. The NIRF image generated from the tissue penetrating signals of the Cy5.5 molecules and the negative contrast T_2-weighted MRI images confirm the MPI biodistribution observations. These complementary modalities can be used for more accurate targeted imaging of the organs (*e.g*. tumors) in future.

4.8.3. Biodistribution and toxicity studies

Fig. 4.15 shows the MPI image of a mouse 72 hours after injection of the NPs functionalized with NH_2-PEG-FMOC (100µL, 1mg Fe/mL), in comparison with its NIRF IVIS and T_2-weighted and colorized R2 MRI images. We show the rest of the data for these NPs because of their longer blood half-life and better imaging performance (Figs. 4.6 to 4.9 and 4.12). Note that in comparison with pharmacokinetic studies, we injected lower dosage of the NPs for biodistribution studies to avoid quenching of the T_2 MRI images of the liver and spleen due to presence of high concentration of NPs.[10] The images show that the NPs accumulated in liver and spleen. As described in details in section 2.2.1.2, this was because of the dominant role of the Kupffer cells in liver and splenic macrophages in spleen in recognizing and taking up the NPs.[147]

Cross-modal imaging functionality of these tracers enabled us to track their biodistribution and pharmacokinetic pathways by means of different techniques and protocols developed based on the strengths of each imaging modality. While each one of

these imaging tools can reveal specifically relevant information about the fate of the injected NPs, combination of all their complementary results helps to track them more precisely in the body and therefore ensure higher levels of safety evaluation. For example, here for quantitative biodistribution studies we used the relative change of the contrast and the rate of T_2 relaxivity decay in axial slices across the abdomen (Figs. 4.16a and b). We compared the change of relaxivity of different organs in T_2-weighted MRI images of the live mice before and after injection of the NPs, to calculate the amount of the NPs in each organ over this 72 hours post-injection time (Figs. 4.16a and 4.17). The NPs were mostly observed in liver and spleen.

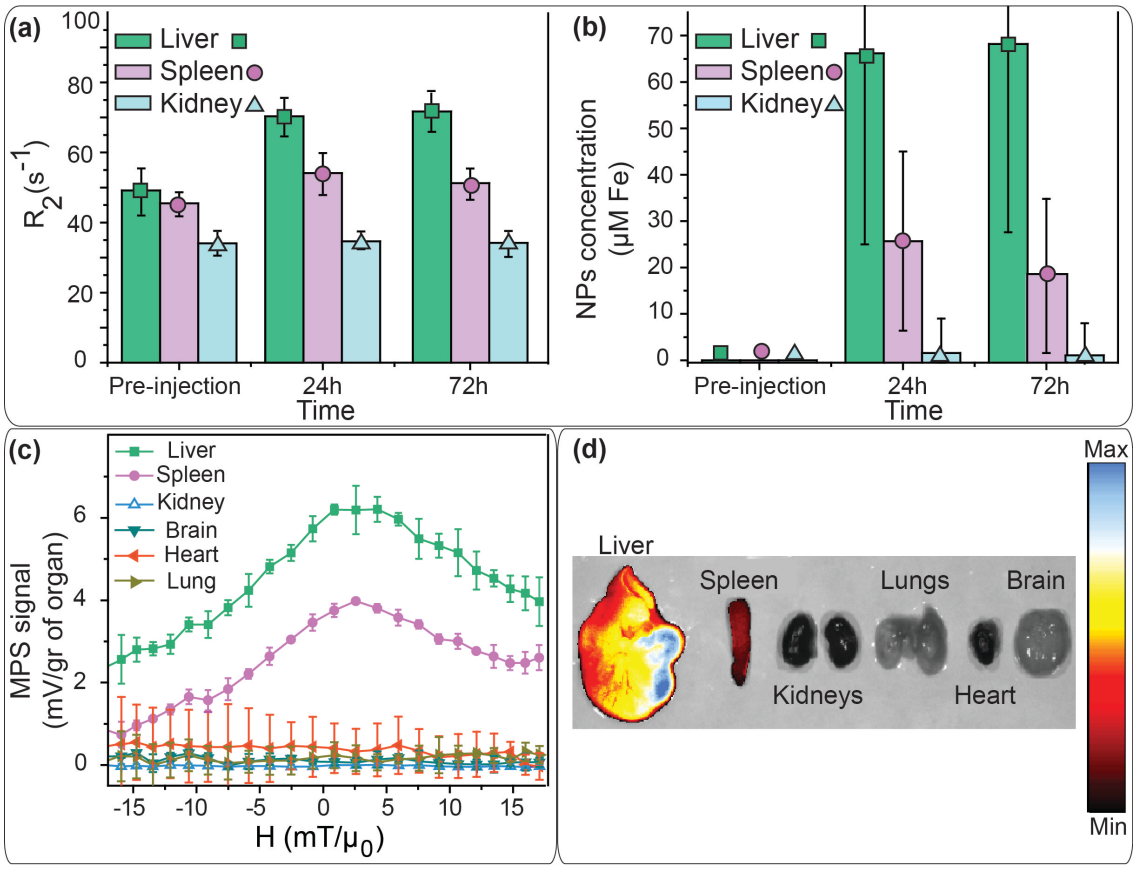

Fig. 4.16. (a) R_2 values calculated form the change of the T_2 contrast of the organs in live mice used for calculation of the concentration of the NPs functionalized with NH_2-PEG-FMOC in each organ (b). Note that the negligible signal observed for pre-injections mice in part (b) is due to presence of unavoidable tissue background signals in MRI. Biodistribution of these NPs determined by (c) MPS and (d) IVIS NIRF scanning of the excised organs of the mice sacrificed 72 hours after injection of the NPs. MPS, NIRF and MRI results show a similar mice biodistribution pattern for the injected NPs. A major part of the NPs were accumulated in liver. The remaining fraction of the NPs was detected in spleen, without any signal in kidney, brain, heart and lungs.

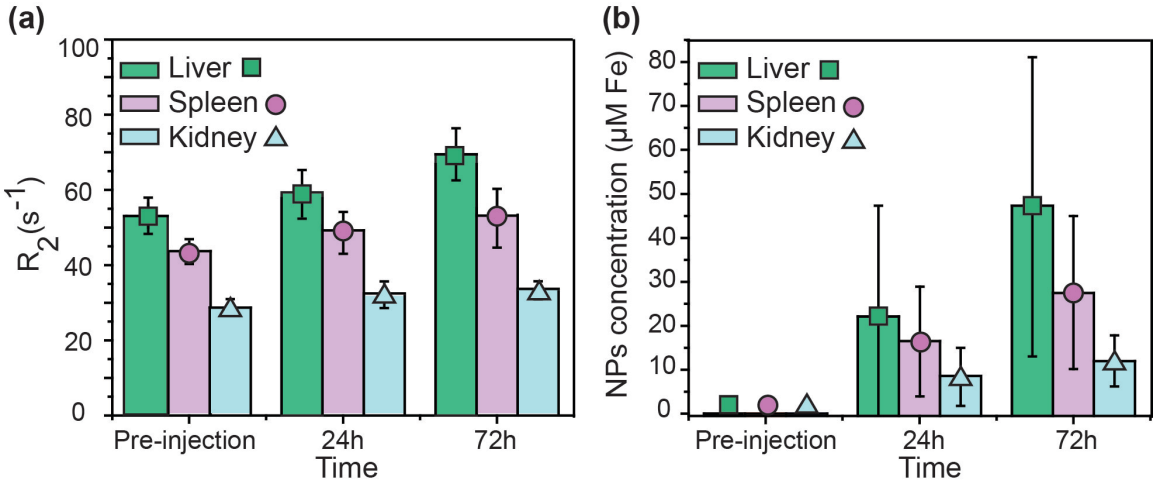

Fig. 4.17. (a) Average R_2 values of the live mice organs determined from the T_2 weighted MRI images obtained 72 hours after injection of the NPs functionalized with NH_2-PEG-NH_2, instead of NH_2-PEG-FMOC which is shown in Fig. 4.14.a and b. Again, R_2 values were used to calculate the NPs concentrations in each organ using equation 1.

The *ex vivo* MPS and NIRF IVIS analyses of the excised organs (Figs. 4.16.c and d) also confirmed the MRI biodistribution results. A high intensity NIRF signal was observed in the liver in comparison with the spleen. Other organs (kidneys, lung, heart and brain) did not show any fluorescent signal. These results were also confirmed when we used an Odyssey scanner to detect the fluorescent signal in 12μm sections of these organs. Our MPS system also did not detect any magnetic response from the excised lung, heart, brain and kidney. However, similar to other modalities, we observed a strong MPS signal generated from the liver and spleen. The NIRF and MPS signals from other excised organs were statistically indistinguishable from the background.

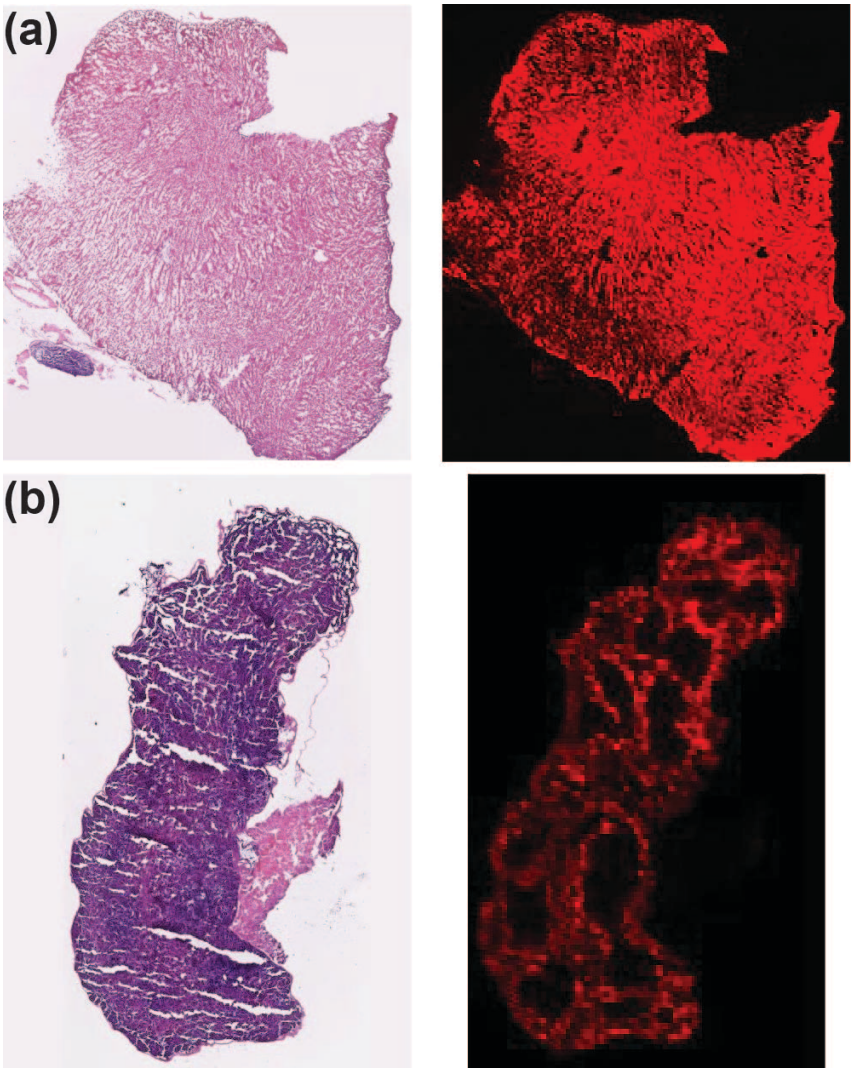

Fig. 4.18. Optical microscope images (left) of H & E stained liver (a) and spleen (b) sections (12μm thickness slices) in comparison with their NIRF images (right) obtained form an Odyssey fluorescence scanner. The NIRF images show that NPs were only entrapped in the red pulp and marginal zones of the spleen. An almost uniform distribution of the NPs was observed in liver.

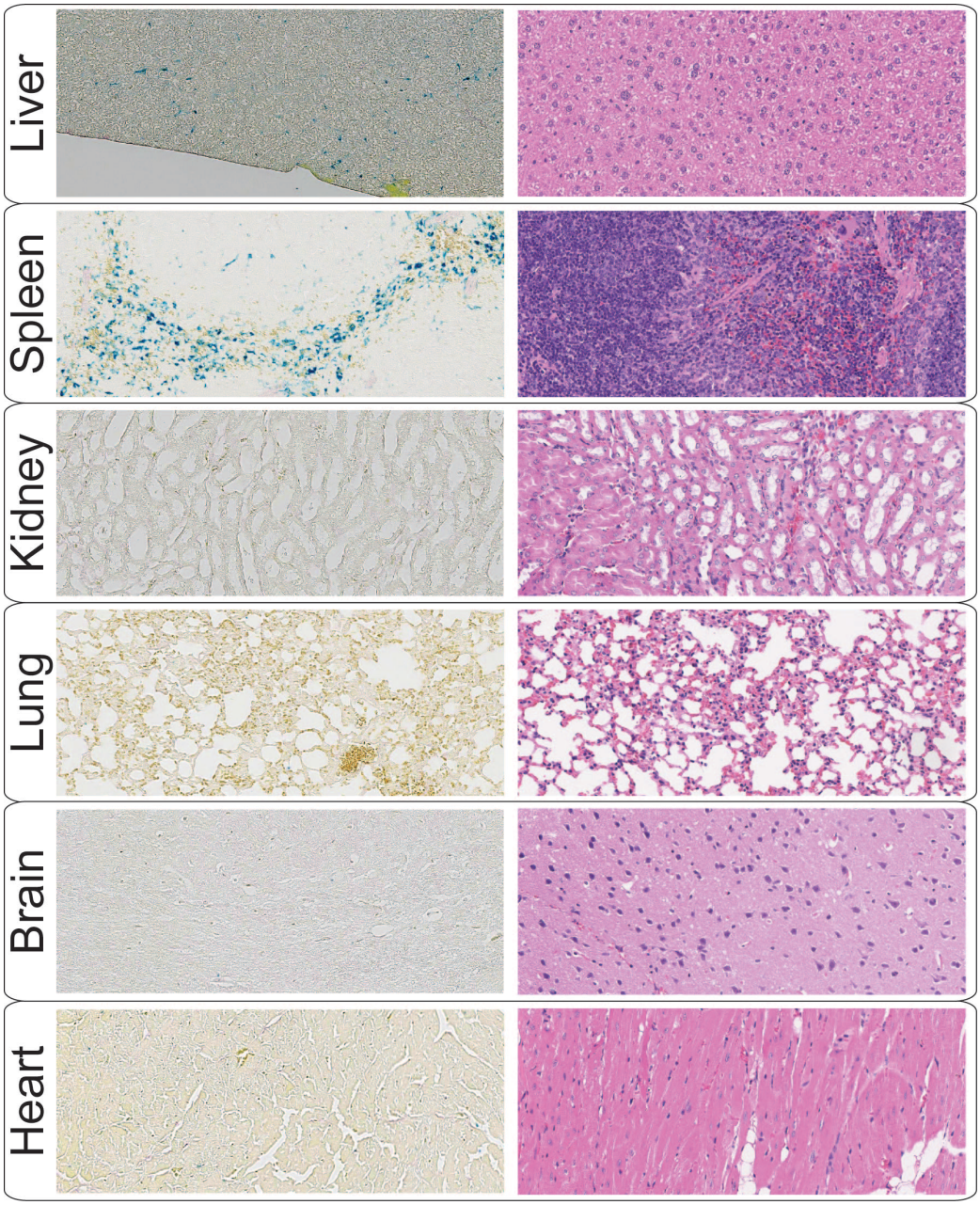

Fig. 4.19. Optical microscope images of the Prussian Blue (left) and H&E (right) stained tissue sections. The images were used for histological evaluation of the liver, spleen, kidney, heart, lung and brain 72 hours after injection of the NPs functionalized with NH_2-PEG-FMOC. Comparison of these Prussian Blues stained sections with PBS-injected control tissues (Fig. S8a) confirm the results of Fig. 6, showing that the NPs were mostly accumulated in RES organs (liver and spleen). The typical H&E images of the tissue sections show that the NPs did not cause any abnormal toxicity-related feature in these organs 72 hours after injection.

High magnification NIRF images of the 12µm cross-sections of the liver and spleen revealed more microstructural details of the NPs biodistribution in the liver and spleen

(Fig. 4.18). This NIRF slice-imaging assay delineates, with anatomic resolution, smaller areas in these organs with higher percentage of the NPs. Such information would be missed by other imaging methods that involve whole organ imaging or homogenization of the organs. Here, the NIRF images of the liver and spleen sections, obtained from the Odyssey scanner are compared with the optical microscope images of their H&E stained counterpart slices. As shown in Fig. 4.18.a, the NPs were almost homogeneously distributed in liver section. However, in the spleen, they were only observed in the red pulp and marginal zones, without any inter-diffusion into the white pulp regions (Fig. 4.18.b). The structure of the spleen is shown in Fig. 2.3 and the uptake mechanism of the nanoparticles by spleen is discussed in details in section 2.2.1.2. Such distribution is observed because spleen arteries direct the NPs and other blood components to regions where the resident splenic macrophages uptake NPs – red pulp and marginal zone. On the other hand, the white pulp is mainly composed of lymphatic tissue and does not show any uptake of NPs. These distribution patterns also confirm the high rate of the NPs uptake by macrophages in these RES organs.[83] The Prussian Blue (PB) stained histology results (Figs. 4.19 and 4.20.a) also show consistent biodistribution results, when compared with control PBS injected mice (Fig. 4.20.b).

No symptoms of NPs toxicity (e.g. weight loss and behavioral changes) were observed among the injected mice during this period. H&E stained tissue sections of the liver, spleen, kidneys, lungs, heart and brain were also reviewed to find any unusual microstructural feature due to injection of the NPs (Figs. 4.19 and 4.20.a). Despite the relatively high levels of the NPs in liver and spleen, no visible abnormalities were found in these organs, when compared with control mice organs. Overall, the preliminary toxicity evaluations show that the NPs were well tolerated by the rodents.

(a) Nanoparticles coated with NH_2-PEG-NH_2

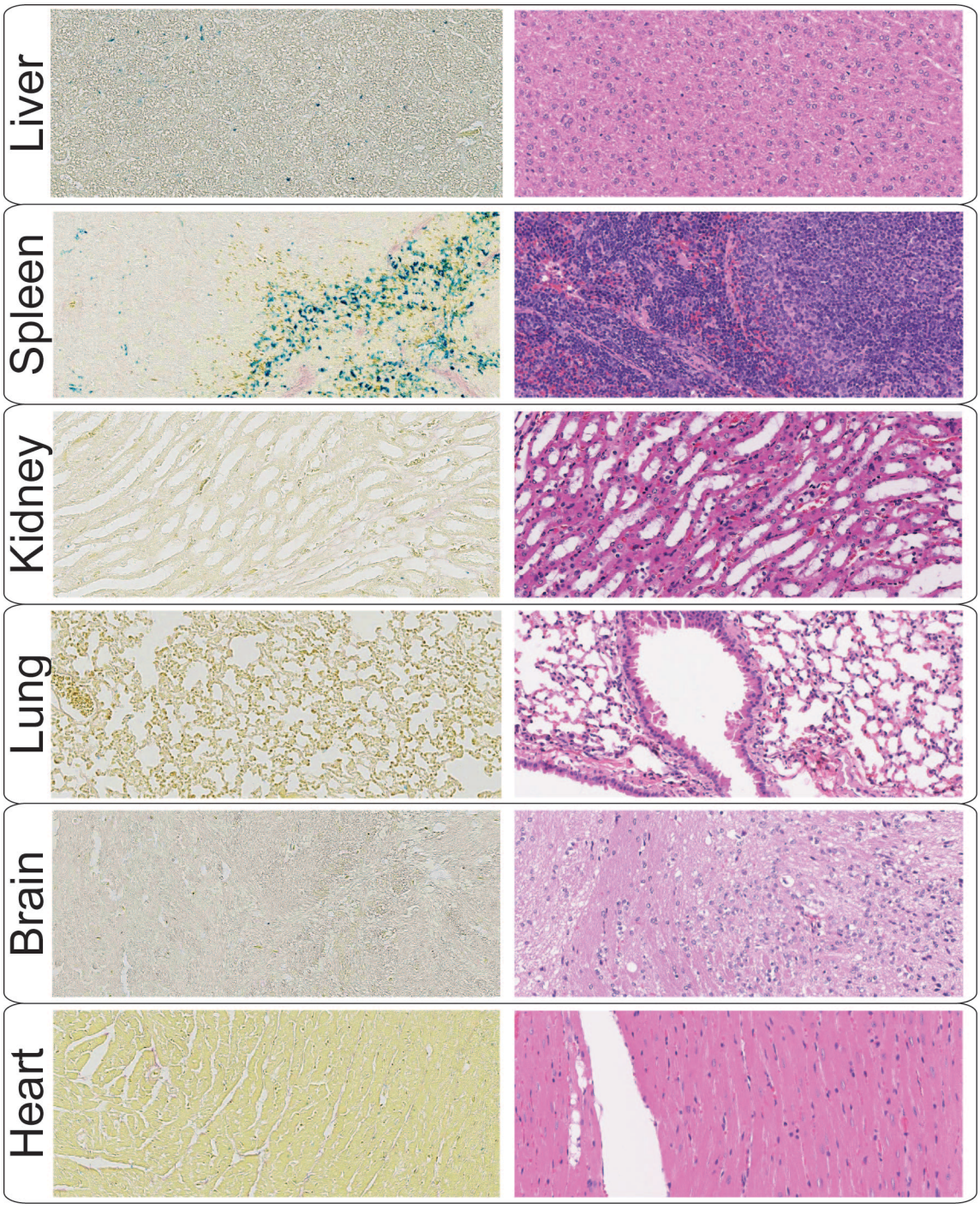

Fig. 4.20. Continued.

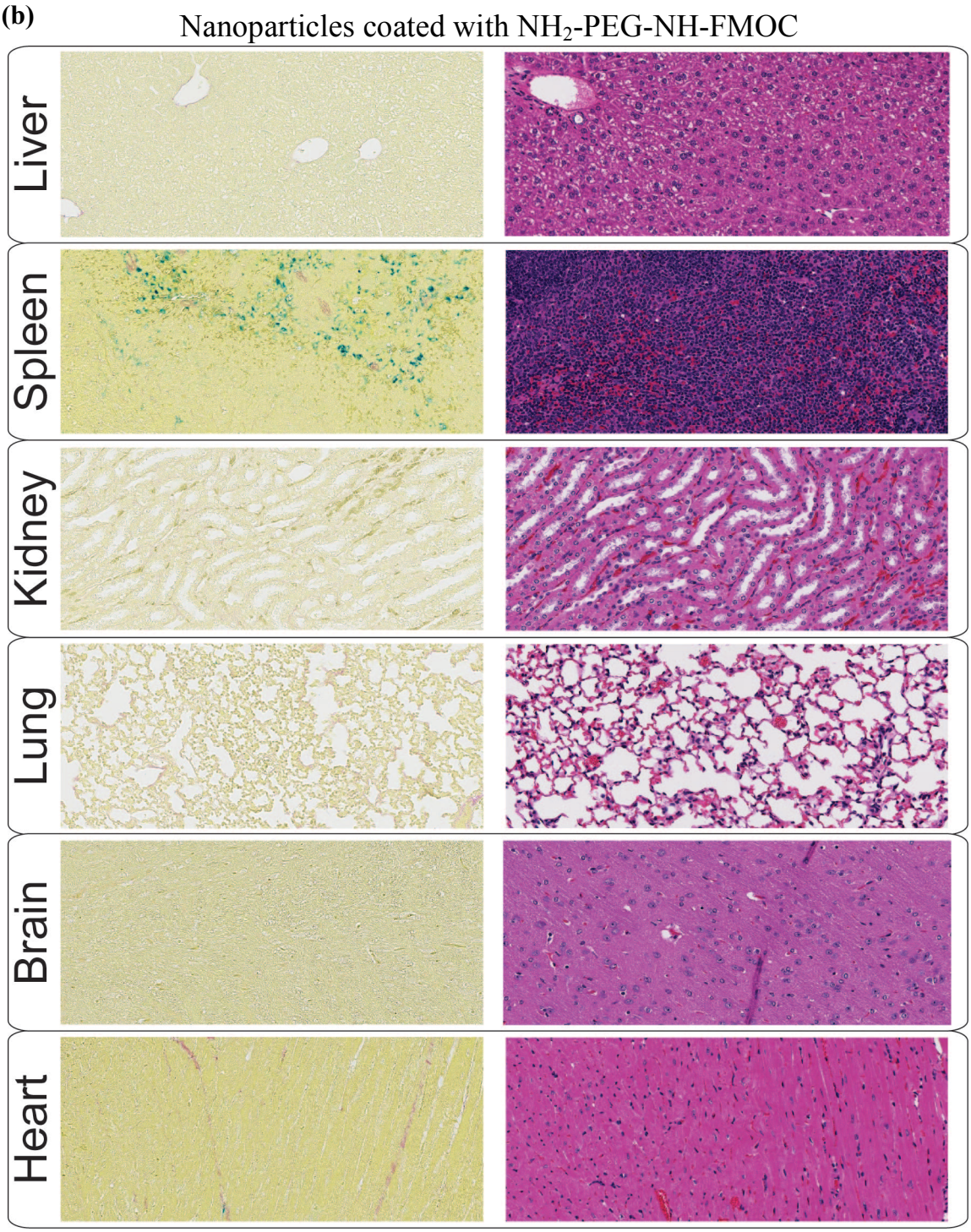

Fig. 4.20. Histology images of the Prussian Blue (left) and H&E (right) stained tissue sections prepared from the mice sacrificed 72 hours after injection of (a) NPs functionalized with NH_2-PEG-NH_2 and (b) PBS (1x, control mice). 20x magnification was used for all images.

4.9. Chapter summary and future outlook

The predicted high resolution and tracer mass sensitivity of MPI make it a potentially effective bio-imaging technique. However, enhancement of resolution and sensitivity in MPI demands synergistic efforts aimed at advancing both currently available scanners and NPs tracers as contrast agents. In the latter case, MPI signal intensity and spatial resolution are highly dependent on the size selectivity and monodispersity of the core and hydrodynamic sizes of NPs. Here, we used a controlled synthesis method to make highly monodispersed NPs (core size ~ 19.7nm) functionalized with amine groups. We showed that selection of a proper PEG derivative is necessary in order to make highly monodisperse nanoparticles. DLS, TG, magnetic measurements, and MPI measurements showed formation of clusters when bi-fucntional PEG was used for the phase transfer. Staining of the nanoparticles coating with heavy metals (such as uranium) and TEM analyses can be used for more accurate analyses of these clusters in future. We used these amine groups as conjugation sites for labeling of the NPs by Cy5.5 near infrared fluorescent molecules. Then, we explored the performance of these NPs as multimodal (MPI/MRI/NIRF) contrast agents. The combination of MPI, MRI and NIRF imaging modalities enabled us to monitor the biodistribution and pharmacokinetics of our MPI tracers with *anatomical precision*. MRI enabled quantitative mapping of NPs distributed in different organs after administration in mice. Tissue penetration and signal stability of the NIRF technique also provided more detailed anatomical information about the pathway of the MPI tracers in organs. For example, the high-resolution NIRF images of the spleen sections showed the NPs accumulation only in red pulp and marginal zones of the white pulp. Therefore, by using these novel types of the MPI tracers, the key pharmacokinetic and biodistribution information can be obtained from a reduced number of animal experiments by only a single MPI tracer administration. These improvements in MPI tracers design will expedite the development of future MPI applications in cancer targeting or stem cell-labeling and tracking. Also, we believe that using the methods reported here for nanoparticles with larger core sizes (i.e. 24-27nm, which were not available in our lab at the time of these studies due to synthesis challenges), helps to

improve the MPI signal intensity and spatial resolution of these multimodal tracers. However, clinical use feasibility and safety of the iron oxide nanoparticles becomes less certain with any additional surface modifications. Therefore, translation of these NPs to clinical applications will require careful toxicity studies.

Chapter 5.

EVALUATION OF MPI FOR ADVANCED *IN VIVO* APPLICATIONS

We discussed the size-dependent biodistribution and blood clearance pharmacokinetic of the nanoparticles in Chapters 2 and 4. Also, we showed that proper functionalization of the NPs enable us to control the size (Chapters 3 and 4) and presence of functional groups such as amines (-NH_2), carboxyls (-COOH), thiols (-SH) and maleimides on the surface of the NPs can be used for conjugation of other molecules such as near infra red fluorescent (NIRF) or targeting peptides. In this section, we evaluate MPI capability for targeted imaging of the tissues in animal models. We also provide preliminary data on radiolabeling of optimized tracers for multimodal MPI/SPECT/PET/C imaging. For targeted MPI studies, we use nude mice with brain cancer (C6) xenografts subcutaneously injected to their flanks. We label optimized MPI tracers with near infra red Cy5.5 and conjugate lactoferrin (a specific targeting molecules for targeting the glioma)[439] and evaluate the targeting ability of the NPs with and without using an external permanent magnet placed adjacent to the tumor xenograft. We use an IVIS system (animal whole body fluorescent imaging) to monitor the accumulation of the NPs in the tumors. Here, fluorescent signal analyses enable us to estimate the targeting efficiency of the tracers and select the animals with highest targeting efficiency for tissue harvesting and MPI evaluation by our magnetic particle spectrometer (MPS). The results of this study will provide fundamental knowledge about MPI feasibility for forthcoming tissue targeted imaging in animal models. In addition, SPECT and PET provide high tracer mass sensitivities and combining them with MPI enables us to study the biodistribution of the tracers more accurately. We hope these preliminary studies can expedite clinical translation of MPI for various cancer diagnosis or cardiovascular imaging applications in future.

5.1. Cancer targeted magnetic particle imaging (MPI)

In Chapter 4, we used healthy CD-1 mice to evaluate the blood circulation half-life and biodistribution of our iron oxide nanoparticles optimized for cardiovascular imaging (i.e. imaging of the blood flow in aorta after intravenous injection of the nanoparticles). Here, we study the cancer targeting ability of our functionalized MPI tracers in mice with tumors. We evaluate diffusion and binding of our magnetic nanoparticle tracer in the tumors through their leaky vasculatures, following tail vein injection of the nanoparticles. We conjugate a targeting peptide (lactoferrin) to the NPs for brain cancer targeting and compare the results with and without using a strong magnet adjacent to the tumors.

Here, we provide preliminary studies to gather critical proof-of-concept data necessary for future application of these magnetic nanoparticles as contrast agents for cancer imaging (or diagnosis) using MPI in combination with other imaging modalities such as fluorescent imaging, SPECT/PET/CT and MRI. Note that our nanoparticles are specifically optimized for MPI and there is currently no MPI cancer imaging report available in literature, due to novelty of this imaging technique. We believe MPI clinical safety, high resolution and tracer sensitivity makes it a suitable technique for future cancer imaging applications. For this study, we conjugate a specific targeting peptide (i.e. lactoferrin for brain cancer targeting) and use a strong magnet to enhance nanoparticles uptake by tumors. Also, we use PBS (1x) solution and NPs without lactoferrin as controls. Our hypothesis is that nanoparticles get accumulated in tumors based on three mechanisms: 1) magnetic targeting effect, 2) ligand assisted targeting, and 3) enhanced permeation and retention (EPR) effect. EPR is based on the diffusion of particles through the tumors leaky vasculatures (enhanced permeation) and subsequent accumulation in tumors (retention). All these three mechanisms depend on nanoparticles hydrodynamic size, surface coating and charge. For more details of these mechanisms please refer to Section 2.2.3. Note that our goal is to enhance the nanoparticles uptake by the tumors using a combination of these three parameters together and evaluate MPI for cancer

imaging. Determination of the exact role of each parameter on tumor uptake requires extensive studies with larger number of mice in future.

Here, we evaluate the accumulation of our tracers in tumors using NIRF imaging and magnetic particle spectroscopy (MPS). This pilot study enables us to assess capability of our tracers (already optimized for cardiovascular imaging using MPI) for detecting tumors, using MPI. Therefore, similar to our previous studies (Chapter 4), we use whole body NIRF imaging to determine the distribution of our tracers following a tail vein injection in mice with tumors and focus more on monitoring the signals (fluorescence and magnetic signals) from the tumor tissues. To do this, we label our NPs with a Cy5.5 near infrared fluorescent dye after conjugation of lactoferrin to their surface and then we track them using a near-infrared optical camera (IVIS), after their intravenous injections via the tail veins. Post-euthanasia, we will measure the amount of the nanoparticles accumulated in tumors using our magnetic particle spectrometer (MPS) for MPI assessments. The procedures for nanoparticles injection, animals anesthesia and euthanasia are based on our approved animal protocol # 4282-01 (similar to Chapter 4). The results of this proposed research will pave the ways to explore new nanomedicine strategies for cancer diagnosis and therapy in future, using clinically safe magnetic iron oxide nanoparticles and MPI.

5.1.1. Animal models

Nanoparticles biodistriibution and pharmacokinetics studies in normal CD-1 mice were discussed in Chapter 4. Here, we use athymic CD-1 nude mice (Charles river), since their genetically designed immune system deficiency, allows growth of tumors in their bodies. These are ideal mice for tumor xenograft studies. Subcutaneous injection of the tumor cells to generate xenograft models have been extensively used as a standard method for various cancer researches. To generate the tumor xenografts required for this investigation, we used subcutaneous injection of the rats C6 glioma cells (1,000,000 cells in 100μL of DMEM-10%FBS cell culture media and 100μL of Matrigel, Fig. 5.1) into mice (female, 8 weeks old) right side flanks. The tumor growth was monitored and

tracers were injected through the tail veins, when the tumor size reached to 10% of the body weight (after about 3-4 weeks[30]).

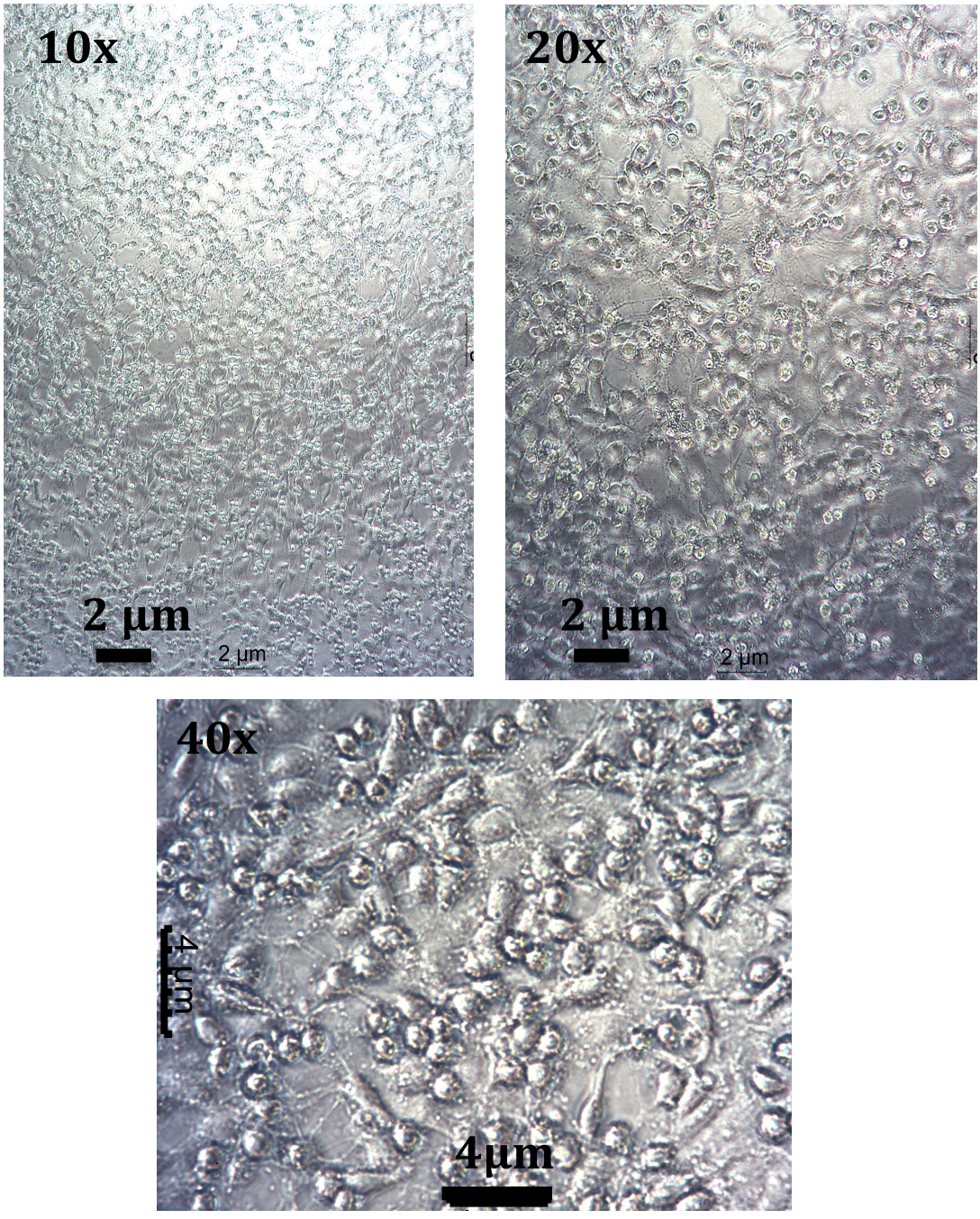

Fig. 5.1. Rats C6 glioma (brain cancer) cells injected subcutaneously to generate brain cancer xenografts in nude CD-1 mice.

To assure that the tumor sizes do not exceed 10% of the normal body weight, we used body condition scoring (BCS) twice a week following the criteria reported before.[440] To do this, mice should be picked up at the base of their tails and body conditions should be assessed by passing the finger over the pubic bones and the back. Then we assign a score ranging from 1 to 5 to each mouse based on their body conditions and our observations. Following is the criteria for scoring the mice:

Score 5: Obese mouse, where bones can not be felt by crossing the finger

Score 4: Well-fleshed mouse, which is not obese and fingers can barely touch the mouse bones

Score 3: Mouse with normal and optimal conditions

Score 2: Thin mouse with prominent bones

Score 1: All muscles are wasted with no traces of fats left in the body.

Animals should be used for nanoparticles injection and imaging experiments when their BCS numbers are in the range of more than 2. If animals gain or lose 10% of their body weight or have a score of 1-2, they should be euthanized based on protocols. In addition, subcutaneous tumor sizes were monitored by use of calipers once per week (Fig. 5.2). Also, if animals show symptoms of pain and distress during this perios, they should be euthanized.

Table 5.1. Animal model used for cancer targeted MPI studies.

Species	Strains	Sex	Ages	Size
Mouse	Nude CD-1 mice	Female	8-12 weeks	20-30gr

5.1.2. Nanoparticles

We used lactoferrin conjugated nanoparticles for targeting of the brain cancer xenografts. Oleic acid coated NPs with median core size of about 27nm were coated with a PMAO-PEG co-polymer, in which PEG molecules were functionalized with a maleimide group. Maleimides are highly reactive with thiols (-SH), which makes them a suitable platform for conjugation of various types of targeting peptides with thiol groups on their backbone structure. We used lactoferrin, since our recent in vitro studies showed that they can effectively target the C6 brain cancer cells, presenting a decent MPI signal after cellular internalization.[439] However, lactoferrin lacks any thiol group, but it has large number of amine groups on its backbone structure. Therefore, we used a simple thiolation procedure to transform some of these amine groups to thiols (Fig. 5.2).[30] For the thiolation, we dissolved 1 mg of lactoferrin in 1ml PBS. Then, 50µg of 2-iminothiolane (also called Traut's reagent) was added to the lactoferrin solution and purified using Amicon vials (MWCO 30kDa) and re-dispersion in the same amount of PBS. The thiolated lactoferrin was then added to the NPs solution, wrapped in aluminum foil and placed on a shaker at room temperature overnight. Then, the lactoferrin conjugated NPs were purified using PD-10 columns equilibrated with sodium bicarbonate (pH~8-8.5) buffer. 5mg of Cy5.5-NHS NIRF molecules were dissolved in 0.5mL of DMSO and then 100µL of this solution was added to each 1mg of lactoferrin conjugated NPs. The mixture was wrapped in aluminum foil and placed on a s shaker for 2 hours. Finally, the NPs were purified using Amicon centrifuge vials (MWCO 30kDa) to remove the un-reacted Cy5.5 molecules from the NPs solution and redispersed in PBS solution. DLS measurements showed that the final hydrodynamic size of the NPs was about 112nm. We also developed another batch of the NPs without any lactoferrin on their surface and used them as control samples to evaluate the effect of lactoferrin on targeting. To do this, we added 100mg NH_2-PEG-SH (3.4 kDa) to the NPs solution (1mg Fe), sonicated the mixture for 15 minutes to make sure all the polymer is dissolved and then wrapped it in Aluminum foil and placed it on a shaker overnight. Thiol groups of the PEG react with maleimide groups on the surface of the NPs and their other amine terminating tail can be

used for Cy5.5 conjugation. Finally, we purified these NPs and labeled them with Cy5.5 as described above. DLS measurements showed that the hydrodynamic size of these NPs was around 104nm.

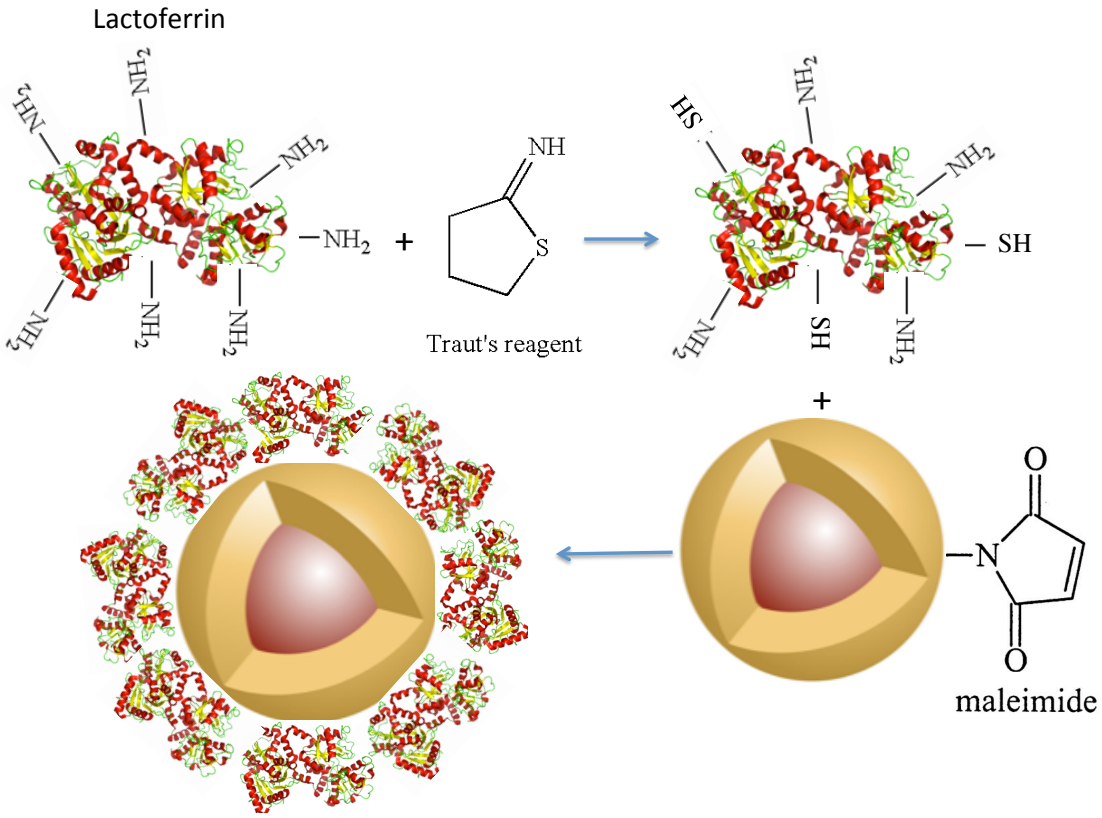

Fig. 5.2. Schematic showing the thiolation of lactoferrin and its conjugation to maleimide functionalized MPI tracers.

5.1.3. Biodistribution and tumor uptake studies

The outline of the procedures used for these animal studies is shown in Table 5.2. We monitored all these mice 2-3 times per week during these studies to check the specific behavioral and clinical signs and tumor growth. Mice were injected through the tail veins with 200 µL of 1 gFe/L iron oxide nanoparticle tracer solution. Before and during injections, mice were anesthetized with 2-3% isoflurane. Prior to injections, all agents

were filtered using 0.2-μm sterile nylon syringe filters to ensure sample sterility. Small magnetic discs (diamter~1cm, thickness~0.5cm) were placed on the skin adjacent to the tumors and fixed using sterile wound tapes, based on the results reported by Cole et al. [40]. We compared the targeting results with and without using an external magnet. As discussed in Chapter 2 (Section 2.2.3), using external magnets adjacent to tumors have been extensively used for enhancing the accumulation of the magnetic nanoparticles in tumors.

Before the injections and 1 and 2 hours post-injection, mice were monitored using an IVIS fluorescent imaging system to evaluate nanoparticles extravasation through the tumors leaky blood vessels and uptake in the tumor, clearance organs (such as liver, spleen, kidneys), lungs, brain and heart. Artificial tears ointment was used to prevent ocular drying that can cause blindness during prolonged anesthesia. The anesthesia parameters are listed in Table 5.3. During the nanoparticles injections and imaging steps, mice were maintained under 2-3% isoflurane anesthesia and immediately euthanized with isoflurane overdose following completion of the experiments. Cervical dislocation was performed as the secondary method for euthanasia. Then, the tumors were harvested for fluorescent imaging and MPS measurements.

Table 5.2. Outline of the procedures used for each mice during the tumor xenograft imaging experiments.

Species	Name of Procedures
Nude CD-1 Mice	Subcutaneous injection of the tumors, Tail vein injection of the nanoparticles, IVIS imaging, euthanasia.

Table 5.3. Anesthesia parameters and procedures used during these studies.

Mice with brain cancer xenografts:

Species	Anesthetic Agent	Dose (mg/kg or %)	Route	Procedures requiring anesthesia
Nude CD-1 mice	Isoflurane	2-3% in O_2 flowing at 1L/min	Gas via nose cone	Subcutaneous injection of the tumor cells, injection of the nanoparticles through tail veins

We used 3 mice for each condition to determine the targeting efficiency using whole body and xenograft IVIS imaging and MPS. There are various reports showing that using three mice for imaging studies is enough for getting reliable results with significant differences, at least for a preliminary and pilot nanoparticles biodistribution study similar to these experiments.[10, 30, 92, 114, 441, 442] We used fluorescent imaging (IVIS) and magnetic particles spectrometry (MPS) to determine the amount of the nanoparticles in tumors. Change of signal in MPS is highly sensitive to the concentration of these magnetic nanoparticles. Tissues fluorescent signal intensity is also highly dependent on the number of the fluorescent-tagged nanoparticles accumulated in them. These techniques have been effectively used for quantifying the nanoparticles in tissues and organs.[30, 92, 114, 441, 442] Therefore, based on these reports, we estimated that using n=3 for imaging is a reliable number for our pilot studies and we do not think increasing the number of mice was necessary at this stage.

5.1.4. Results and Discussions

We have developed a general PMAO-PEG coating platform for functionalizing the surfaces of our chemically synthesized iron-oxide nanoparticles[1] tailored for MPI.[2] We showed the potential of this coating platform for enhancing in vivo circulation time,[3] multimodal imaging,[4] and by conjugating lactoferrin, demonstrated their MPS efficacy in specific internalization of glioma cells in vitro.[5] Here, we demonstrate the

targeting efficiency of lactoferrin-Cy5.5 conjugated NPs in a rodent model with brain cancer xenografts, using in vivo near infra red fluorescent (NIRF) imaging (IVIS system) and ex vivo magnetic particle spectroscopy (MPS).

Iron oxide NPs with median core size of 27nm were synthesized, thiolated lactoferrin was conjugated to their PMAO-PEG coatings (Fig. 5.2.) and then purified using PD-10 columns. Cy5.5-NHS NIRF molecules were also conjugated to the lactoferrin molecules using methods reported earlier.[92, 439] In vivo evaluation of the NPs uptake in tumors, 1 and 2 hours after injection, was carried out using an IVIS system; then the animals were sacrificed and the magnetic and fluorescence signals of excised tumors were measured by IVIS and MPS (frequency~25 kHz). Mice were injected in four different groups with: (1) Lactoferrin-conjugated NPs and external magnet to enhance the targeting, (2) Lactoferrin without magnetic targeting, (3) NPs without lactoferrin on their surface to evaluate EPR perfusion, and (4) phosphate buffered solution (PBS) as a control.

Overall, our in vivo (Figs. 5.3, 5.4. 5.5 and 5.6) and ex vivo results (Fig. 5.7) showed that nanoparticles were accumulated in tumors based on three mechanisms: 1) enhanced permeation and retention (EPR) effect, based on the diffusion of particles through the tumors leaky vasculature (enhanced permeation) and subsequent accumulation in tumors (retention); 2) ligand (lactoferrin) assisted targeting and 3) magnetic targeting. Generally, these three mechanisms depend on nanoparticles hydrodynamic size, surface coating and charge.[6] In vivo NIRF imaging showed a very small uptake in the tumors due to the EPR effect (Fig. 5.6); however, the lactoferrin conjugated NPs were readily internalized into xenografts (Fig. 5.5), with further enhanced uptake when we placed a magnet adjacent to the tumors (Fig. 5.4).

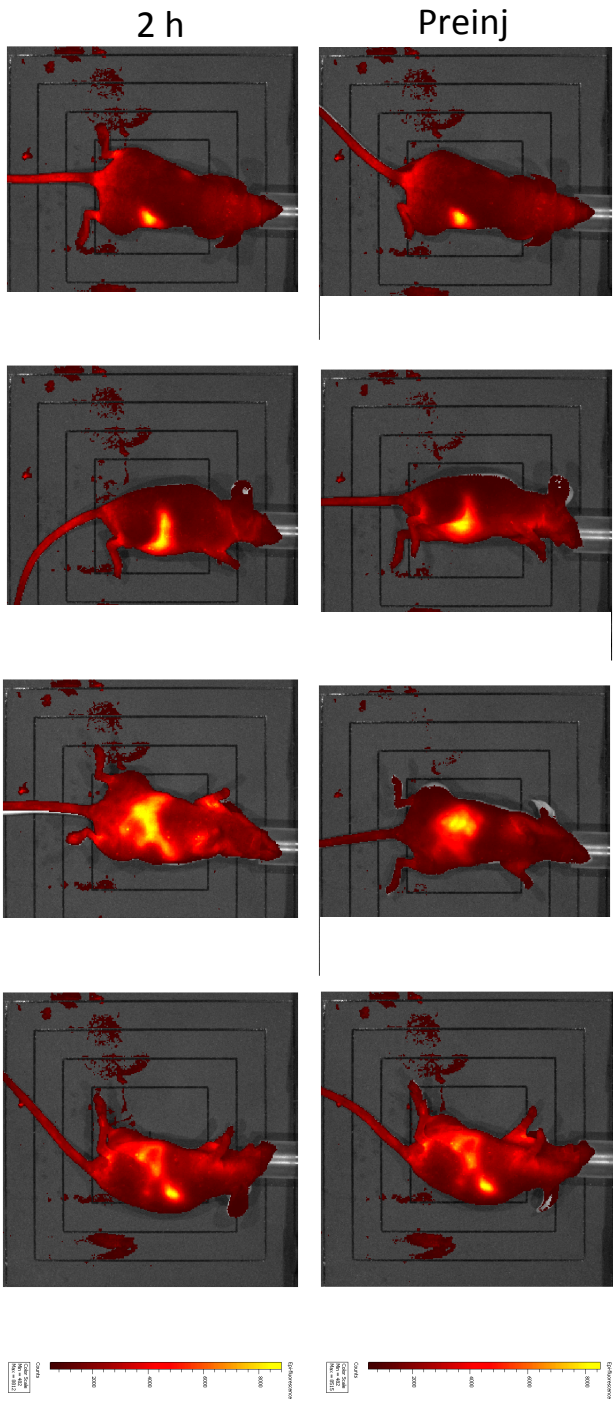

Fig. 5.3. Fluorescent images of a control mouse (anesthetized) with brain cancer xenograft, at different angles, before and 2 hours after injection of PBS. Note that the bright spots are related to innate autofluorescence of the mice and have a much weaker signal intensities compared with fluorescent signals observed in mice after injection of Cy5.5 labeled NPs, shown in Figures 5.4, 5.5 and 5.6.

Mouse 1

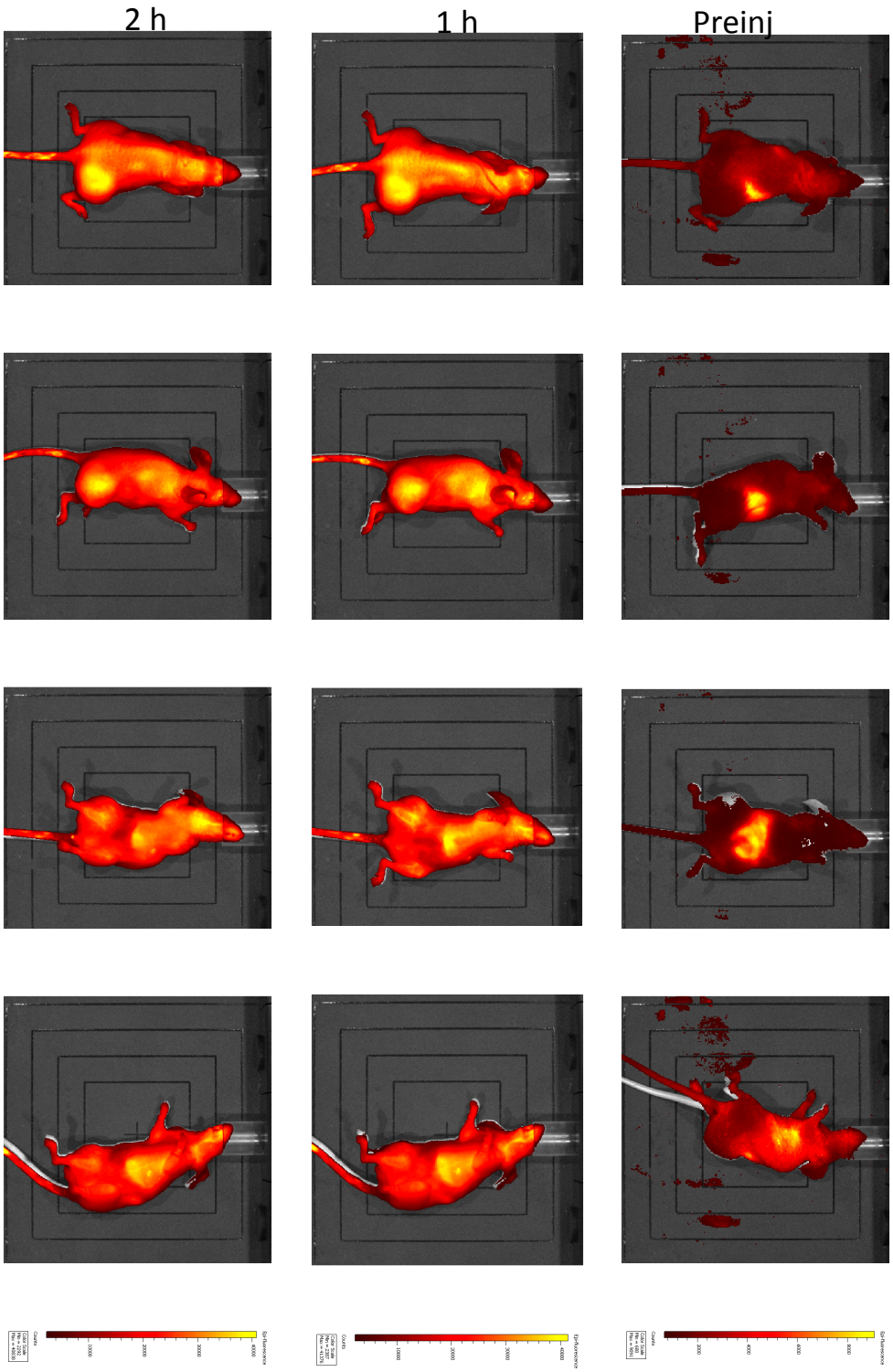

Fig. 5.4. Continued.

Mouse 2:

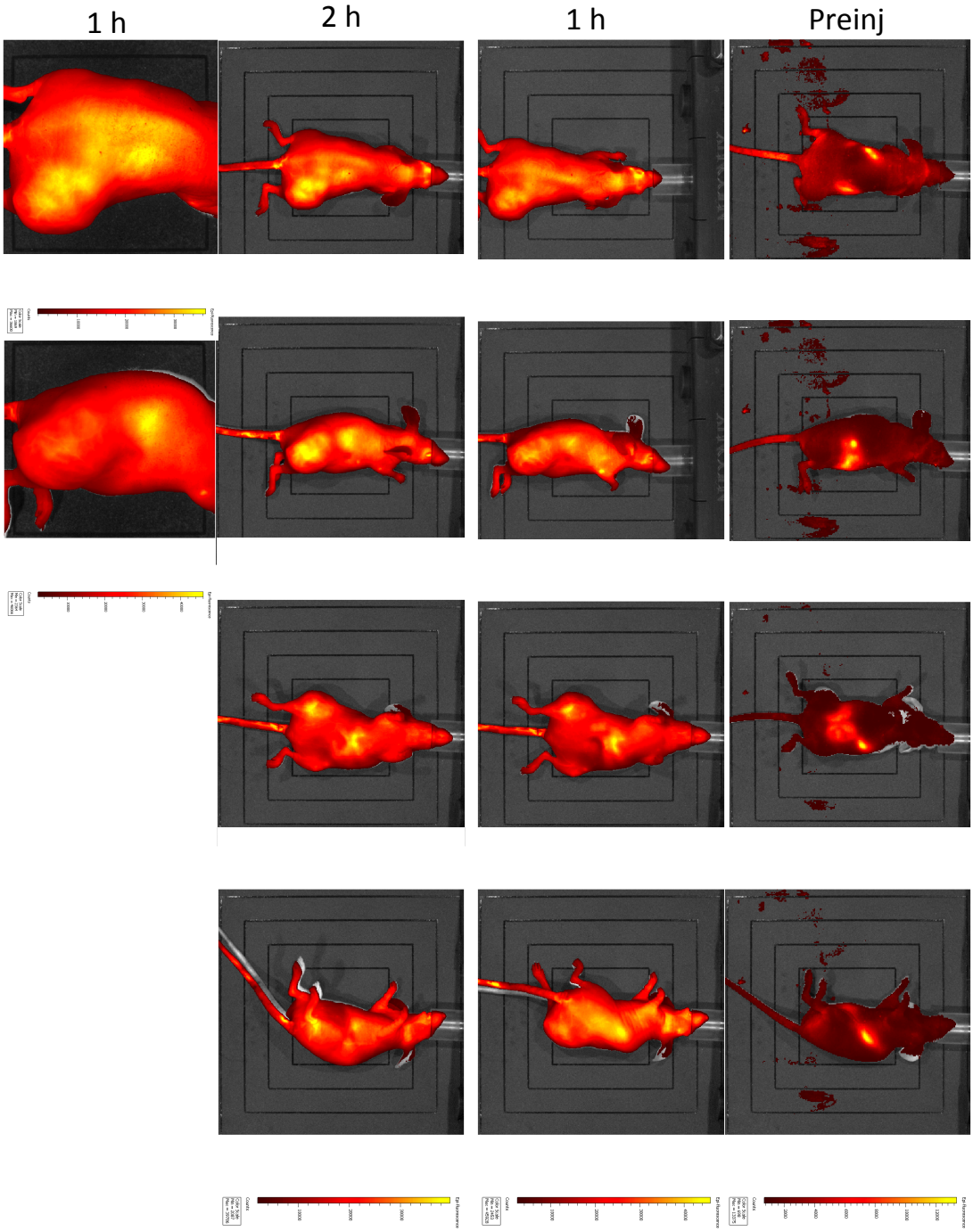

Fig. 5.4. Continued.

Mouse 3:

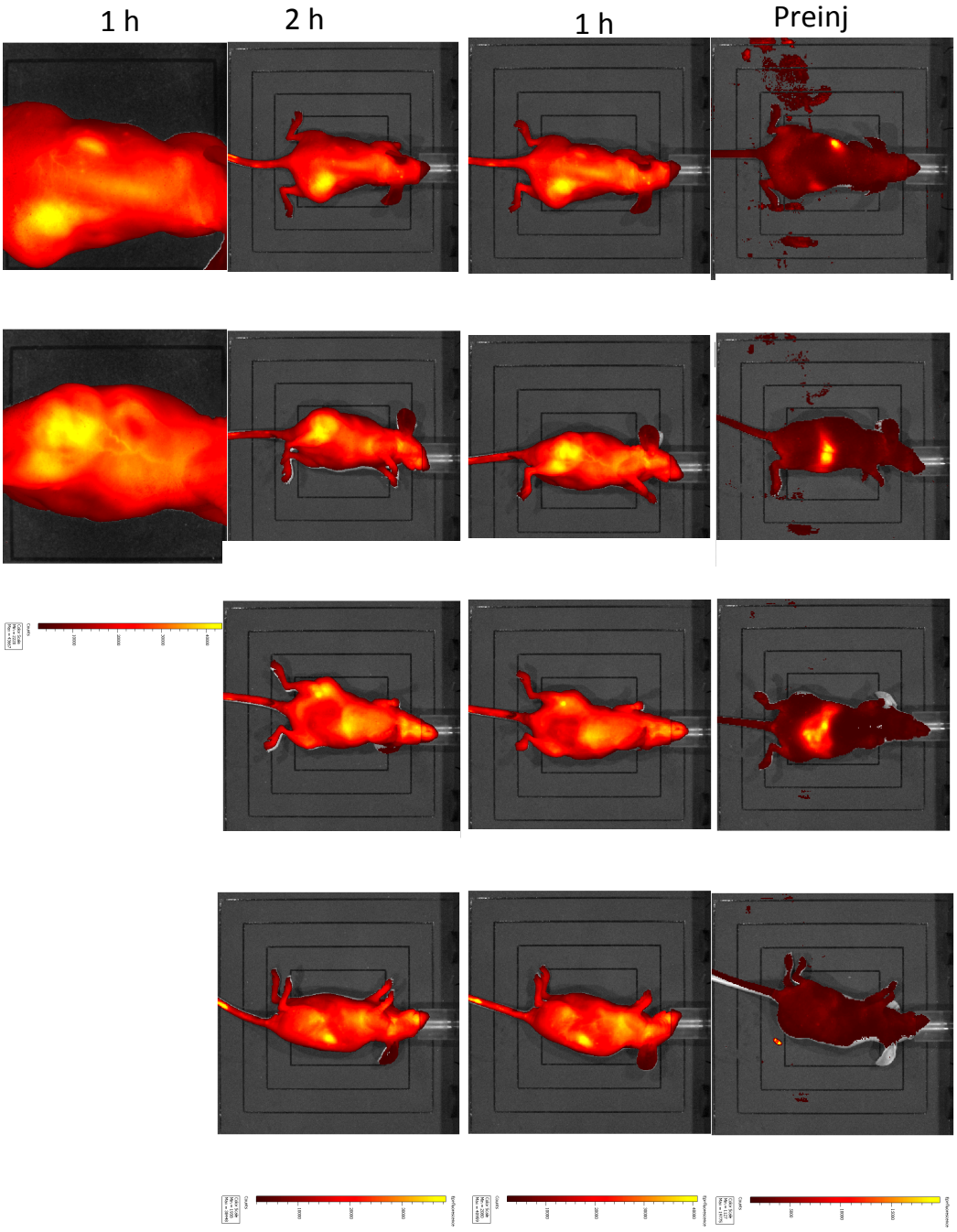

Fig. 5.4. IVIS image of the mice injected with Cy5.5-Lactoferrin conjugated NPs, with a magnet placed adjacent to the tumor xenograft on the right side flank.

Mouse 4:

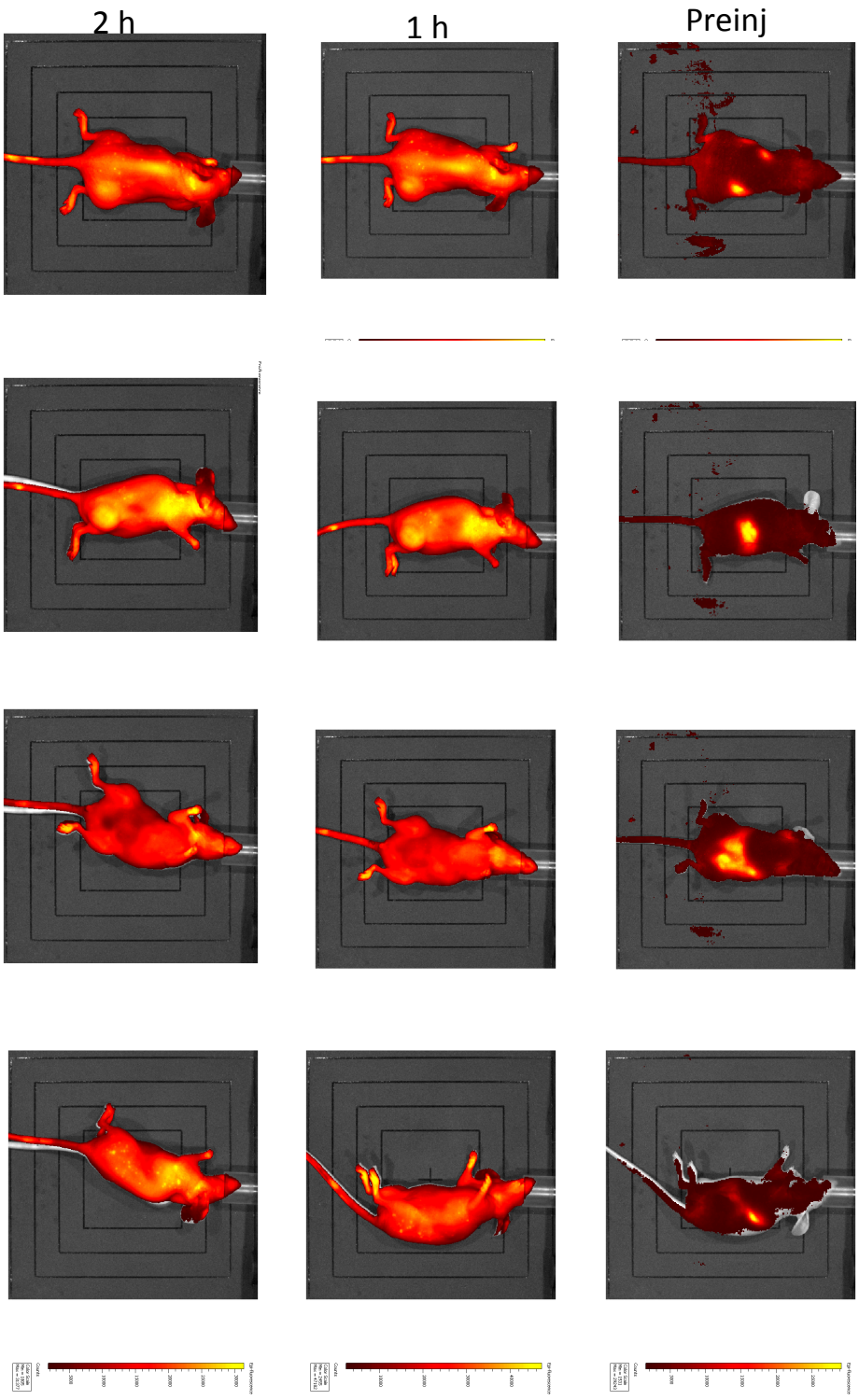

Fig. 5.5. Continued.

Mouse 5:

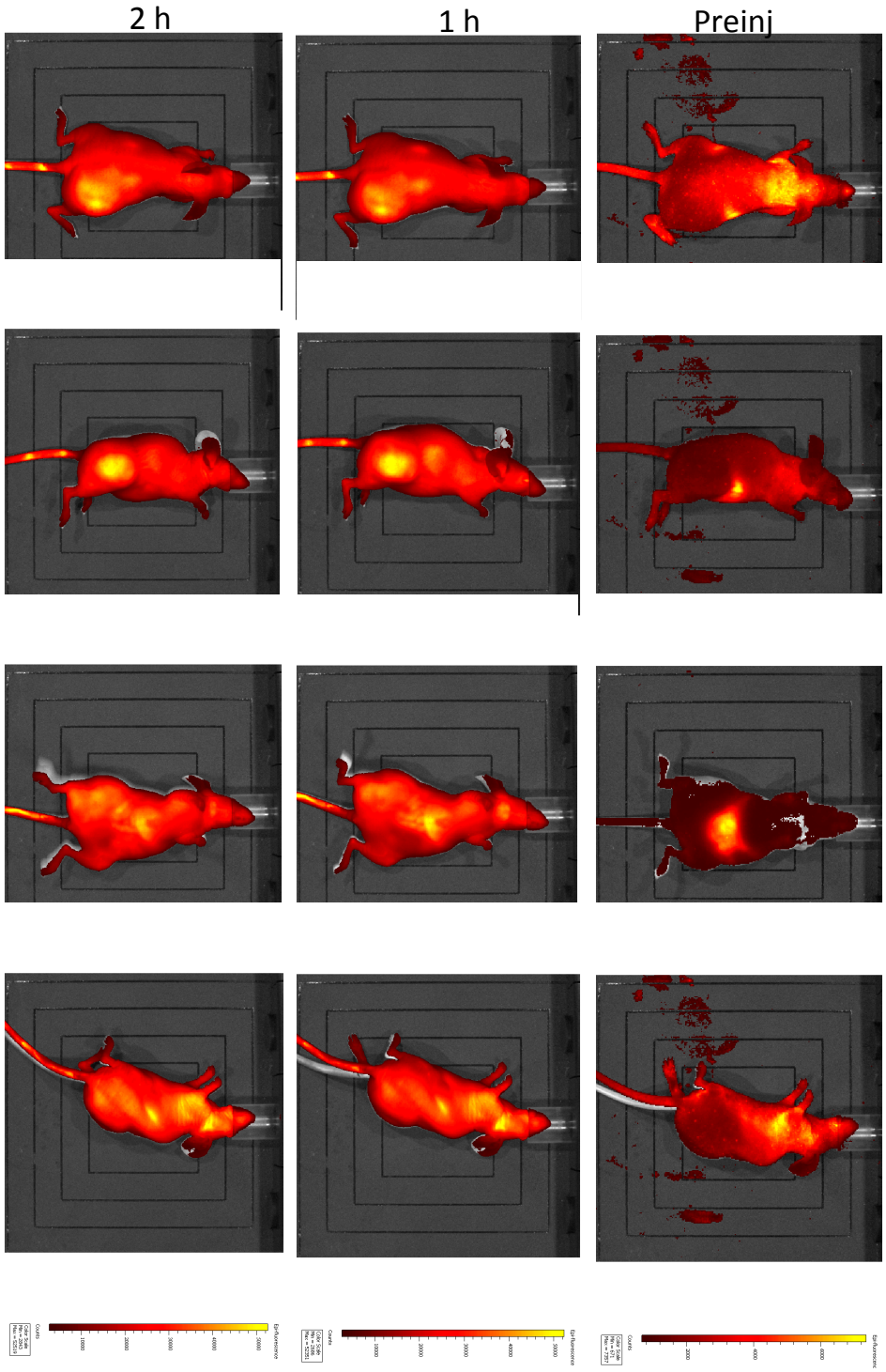

Fig. 5.5. Continued.

Mouse 6:

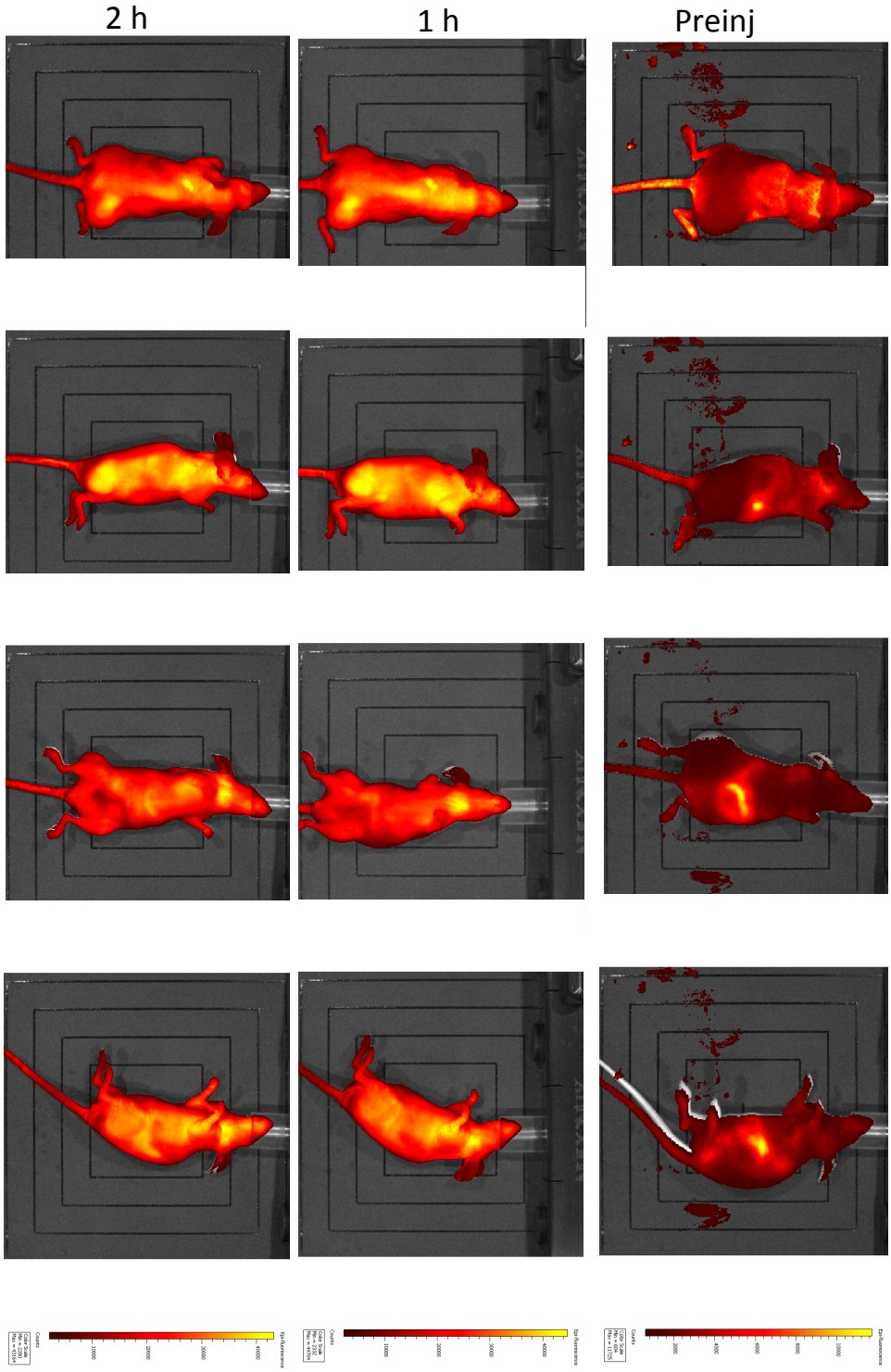

Fig. 5.5. IVIS image of the mice injected with Cy5.5-Lactoferrin conjugated NPs, without using magnetic targeting.

Mouse 7:

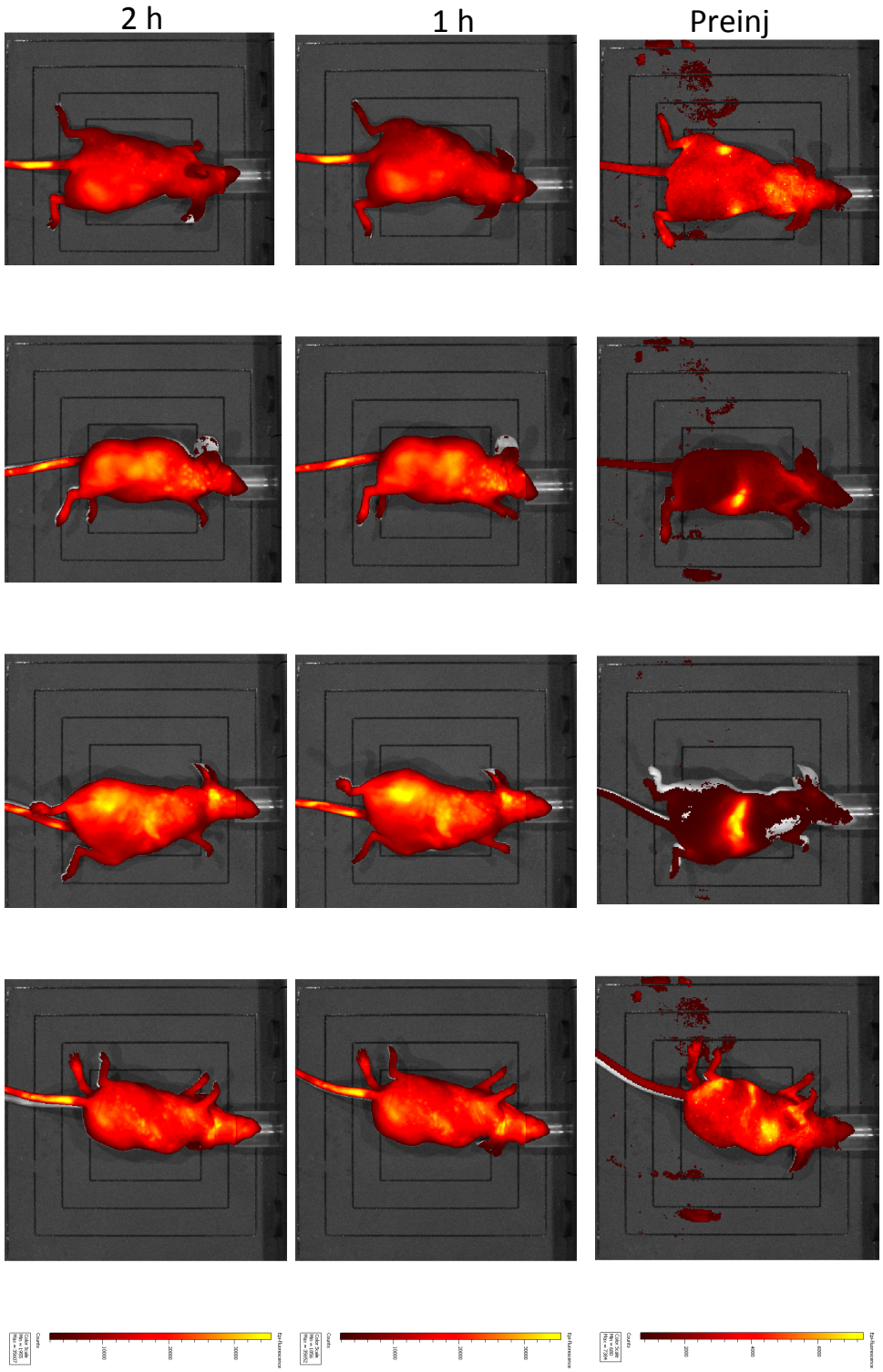

Fig. 5.6. Continued.

Mouse 8:

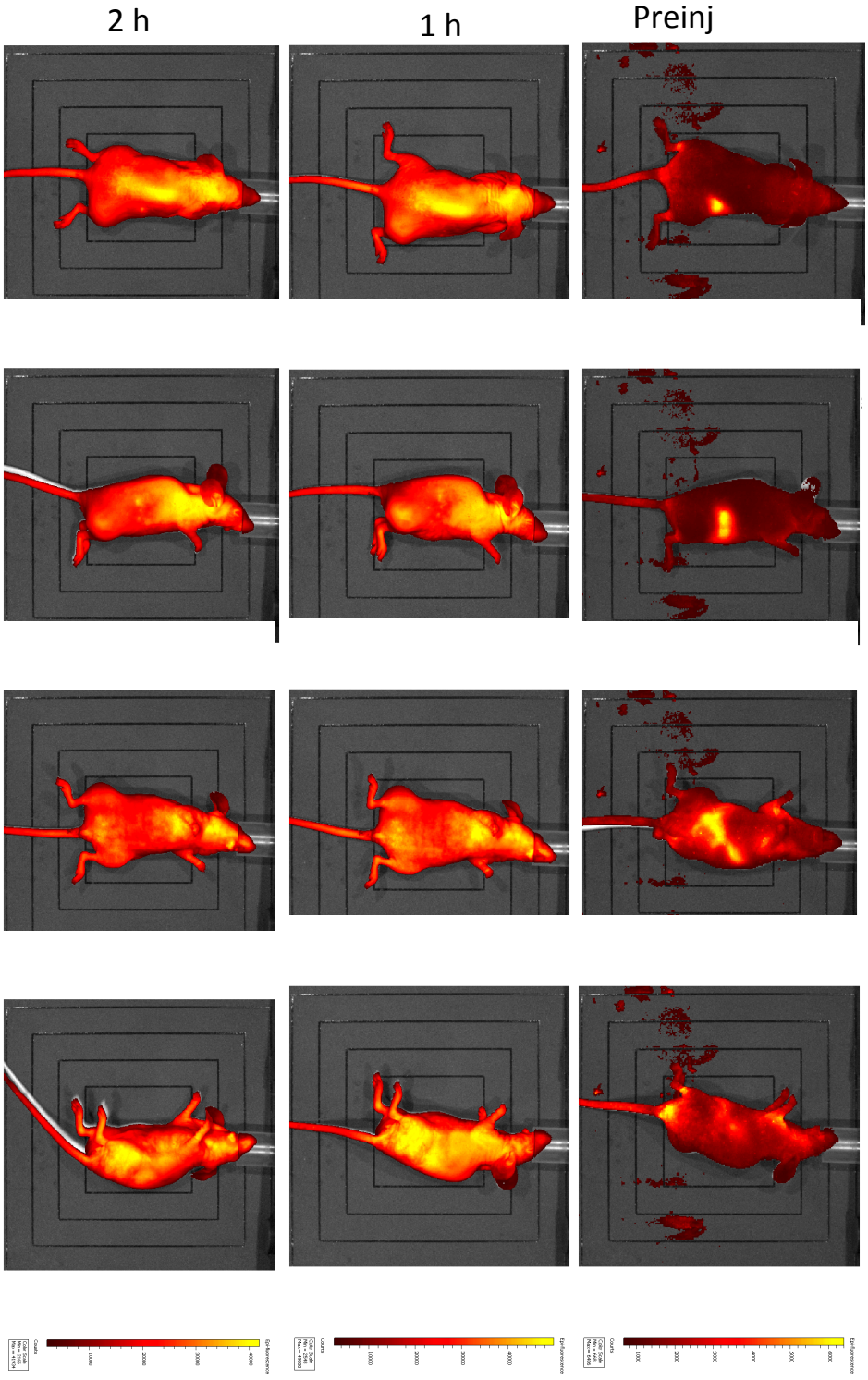

Fig. 5.6. Continued.

Mouse 9:

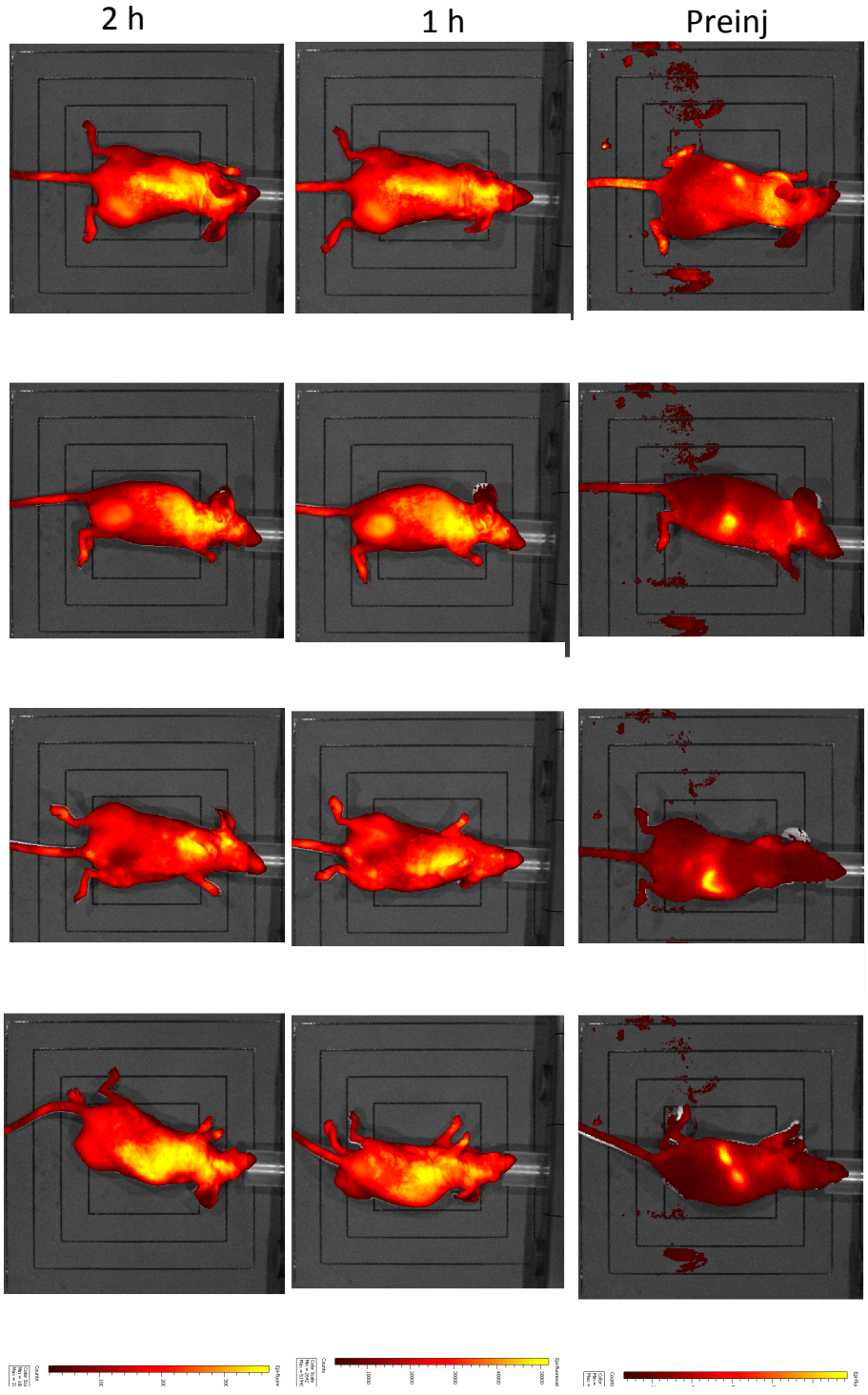

Fig. 5.6. IVIS image of the mice injected with Cy5.5-labeled NPs, without using lactoferrin and magnetic targeting.

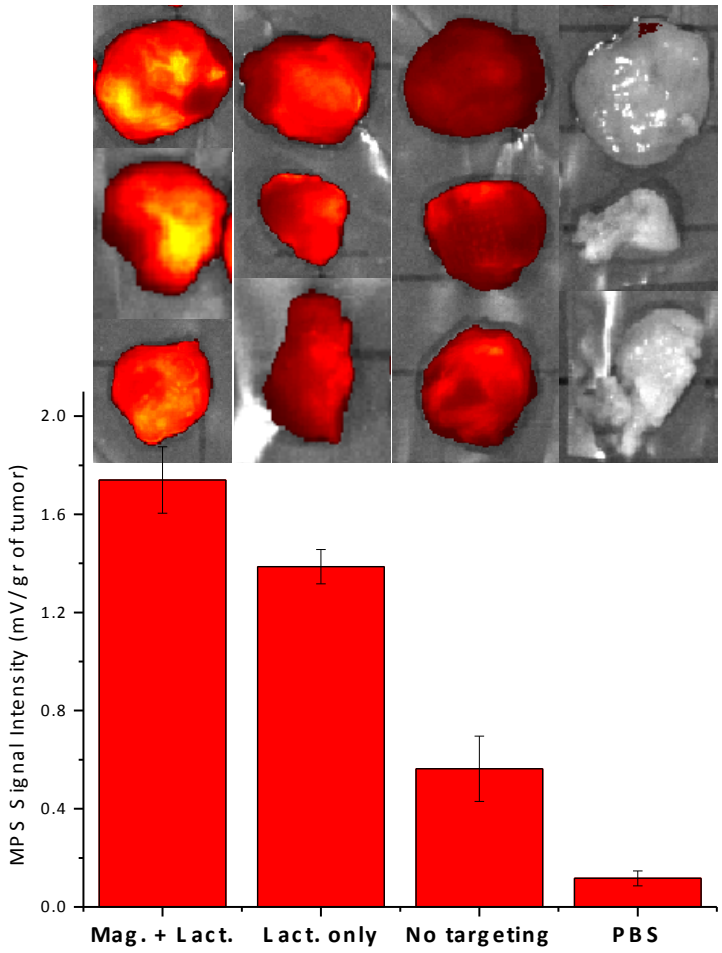

Fig. 5.7. NIRF (IVIS) images (top) and MPS signal intensity (per tumor mass) of the tumor xenografts excised from mice injected with Cy5.5-lactoferrin conjugated NPs, with and without using magnetic targeting, compared with Cy5.5-labeled NPs (without any lactoferrin and magnetic targeting) and PBS as controls. In IVIS images brightness is proportional to the uptake of the fluorescently labeled NPs.

NIRF images of the excised tumors (Fig. 5.7) showed that the tumor uptake, based on these mechanisms is cumulative, with the combination of magnetic and lactoferrin-assisted targeting showing the most increased uptake. These results were also confirmed by magnetic particle spectroscopy (MPS) analyses of the tumor tissues from the excised xenografts (Fig. 5.7).

5.2. Quantitative biodistribution studies of optimized MPI tracers radiolabeled for multimodal SPECT/CT imaging

Building on the robust PMAO-PEG co-polymer coating platform [1] for functionalizing our optimized MPI tracers [2], we radiolabeled them for SPECT/CT contrast to enable accurate determination of their biodistribution and pharmacokinetics. SPECT/CT imaging provide high tracer mass sensitivity, enabling accurate, quantitative estimation of NPs concentration in the main clearance organs (i.e., liver, spleen and kidneys, as discussed in Chapter 2).[443] This complements our earlier NIRF imaging of similar MPI tracers to determine their biodistribution with anatomical sensitivity (Chapter 4).[92]

5.2.1. NPs development and animal studies

Iron oxide NPs with median core size of 27 nm (Fig. 5.8), optimal for MPI, were synthesized and coated with PMAO in chloroform and transferred to water, showing a negative zeta potential (~-30 to -50 mV) due to presence of carboxyl groups on their surface. For details of PMAO coating and phase transfer of the NPs, please refer to Appendix F. Nanoparticles were coated by dispersing a dried mixture of nanoparticles and PMAO in 0.1M NaOH and sonicating for three hours. After sonication, aggregates were removed by permanent magnet and the remaining particles were centrifuged at 14,100 rcf for one hour. The supernatant was removed and enough 10mg PEI/ml in DI water was added to reach of a ratio of 10mgPEI/1mg nanoparticles. The mixture was purged with argon and sonicated for one hour. Centrifugation, PEI dispersion, and sonication were repeated once. Nanoparticles were purified by centrifugation and dispersed in PBS. NPs showed a hydrodynamic size of about 65nm (Fig. 5.9) and a positive zeta potential of ~+30 to +60mV (Figs. 5.10) due to presence of cationic PEI on their surface.

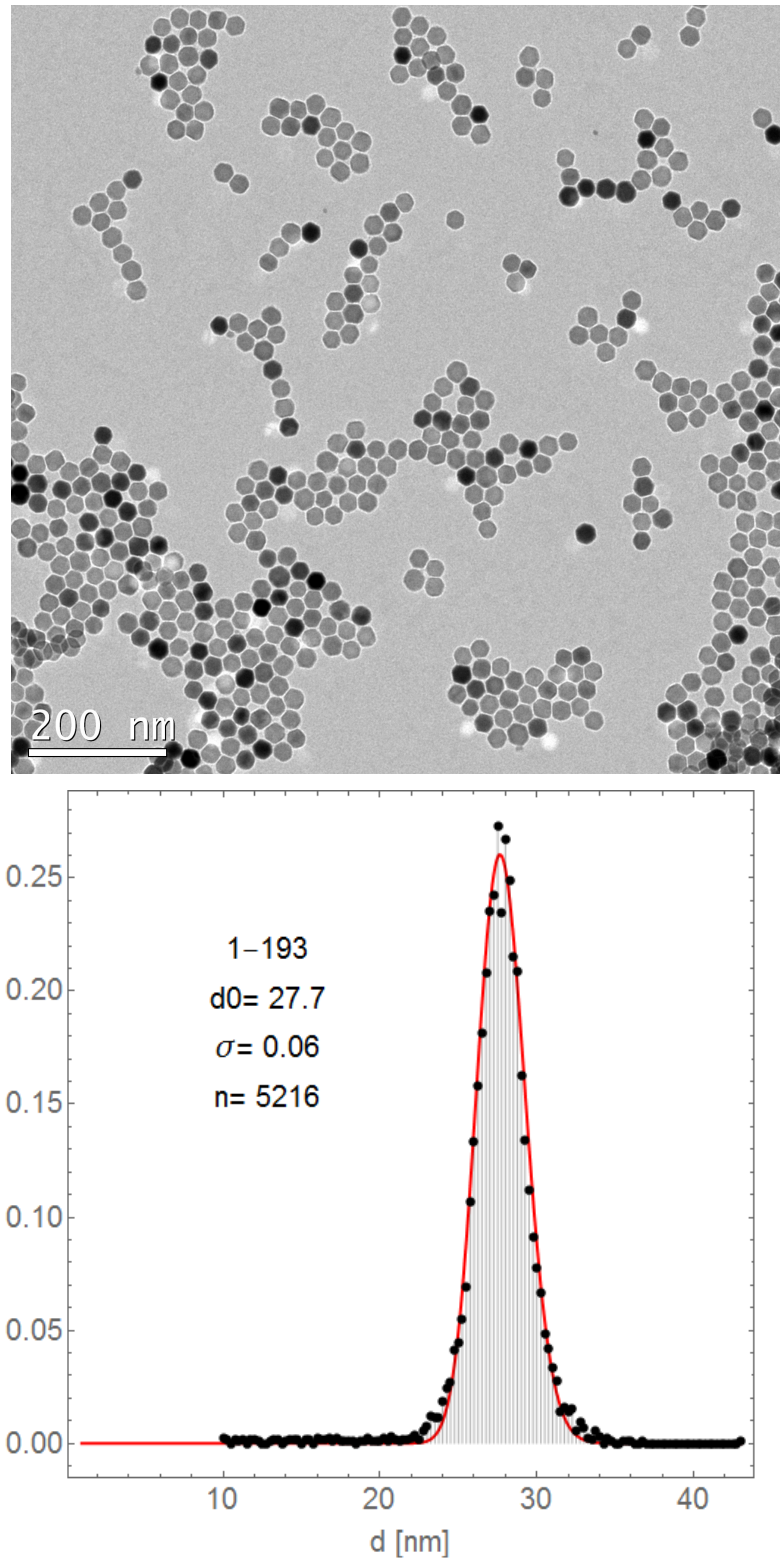

Fig. 5.8. TEM image and size distribution histogram of the NPs used for radiolabeling and biodistribution studies by SPECT/CT.

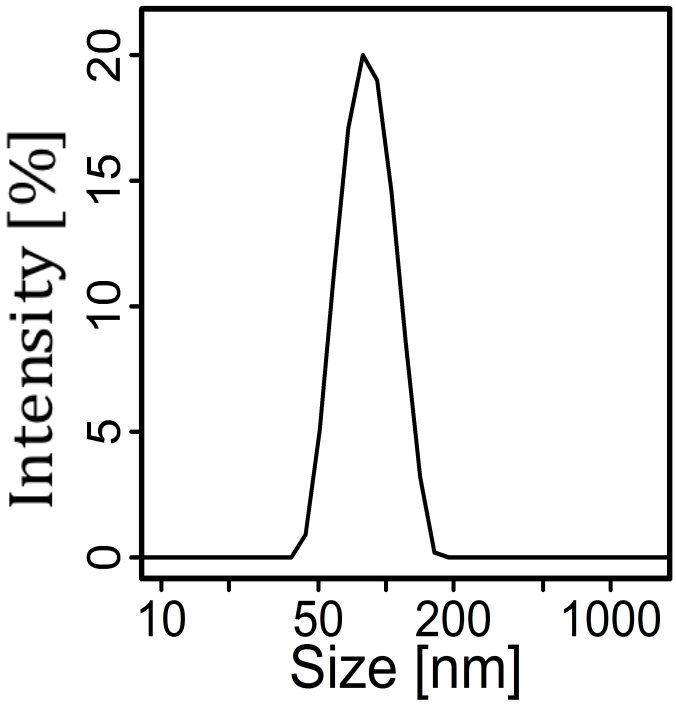

Fig. 5.9. Hydrodynamic size of the PEI coated NPs measured by DLS.

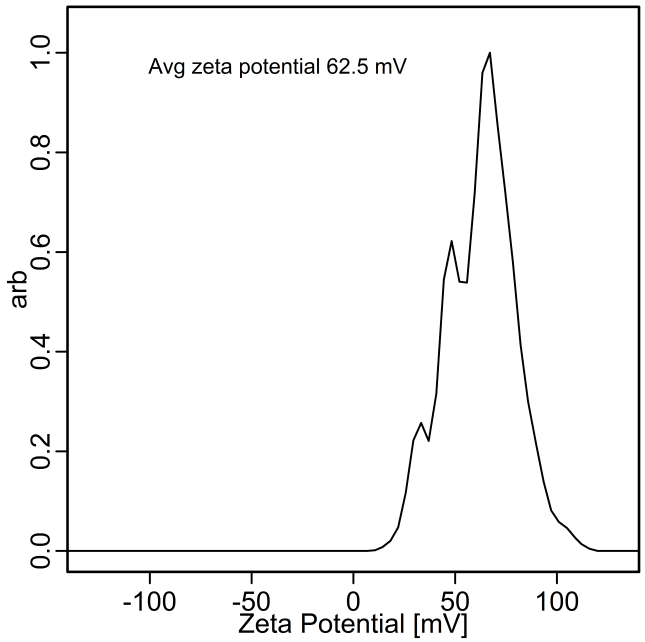

Fig. 5.10. Zeta potential of the PEI coated NPs showing a highly positive charge due to presence of cationic PEI on the surface of the NPs.

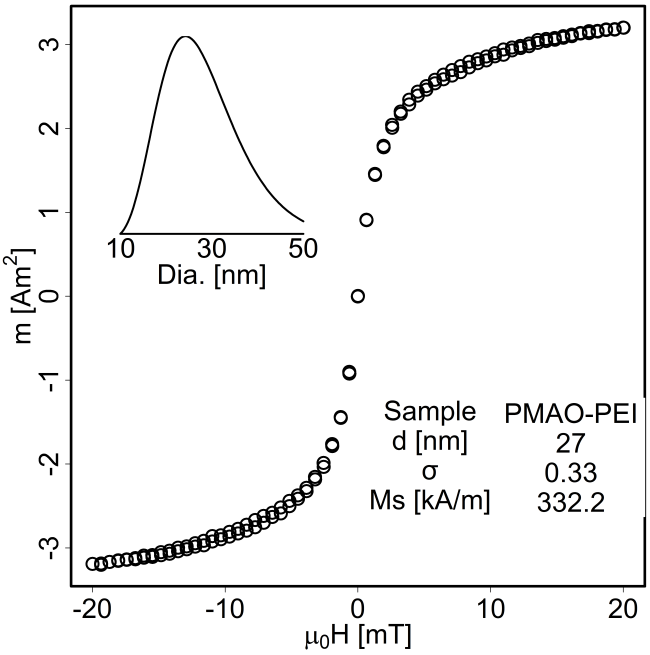

Fig. 5.11. m-H graph of the NPs. Size calculations using Chantrell fitting[404] showed a median core size of about 27nm, which matches with TEM images of these NPs.

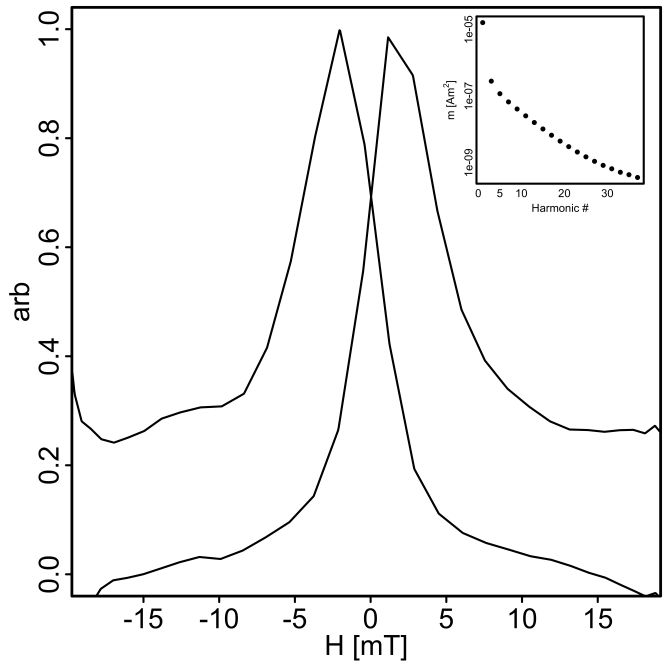

Fig. 5.12. MPS (dm/dH) graph of the NPs, showing a small FWHM, representative of a high spatial resolution in MPI.

For ligand modification and 67Ga-radiolabeling of these NPs with optimized magnetic properties and MPI performance (Figs. 5.11 and 5.12), the PEI coated particles were modified with the chelator p-SCN-bz-NOTA (Macrocyclics, USA) and then radiolabeled with Gallium-67 (^{67}Ga, $T_{1/2}$ = 78.3 h) (Fig. 5.13). For this purpose, 800 μL of the particles were diluted with $NaHCO_3$ (800 μl, 0.1 N) and incubated with 0.8 mg of *p*-SCN-bz-NOTA) solution at 19 °C overnight. The particles were concentrated using an Amicons (30 kDa MWCO), washed twice and re-suspended in 1 mL PBS. NOTA is now bound to the particles through a thiourea bond. Particles were radiolabeled by adding $^{67}GaCl_3$ (5.3 mCi) to the suspension and incubating at room temperature for 30 minutes with mixing, followed by Amicon concentration and washing twice with PBS (92% labeling efficiency). The radiolabeled particles were dispersed in PBS for the biodistribution studies. The hydrodynamic size and zeta potential of the labeled NPs are shown in Fig. 5.14.

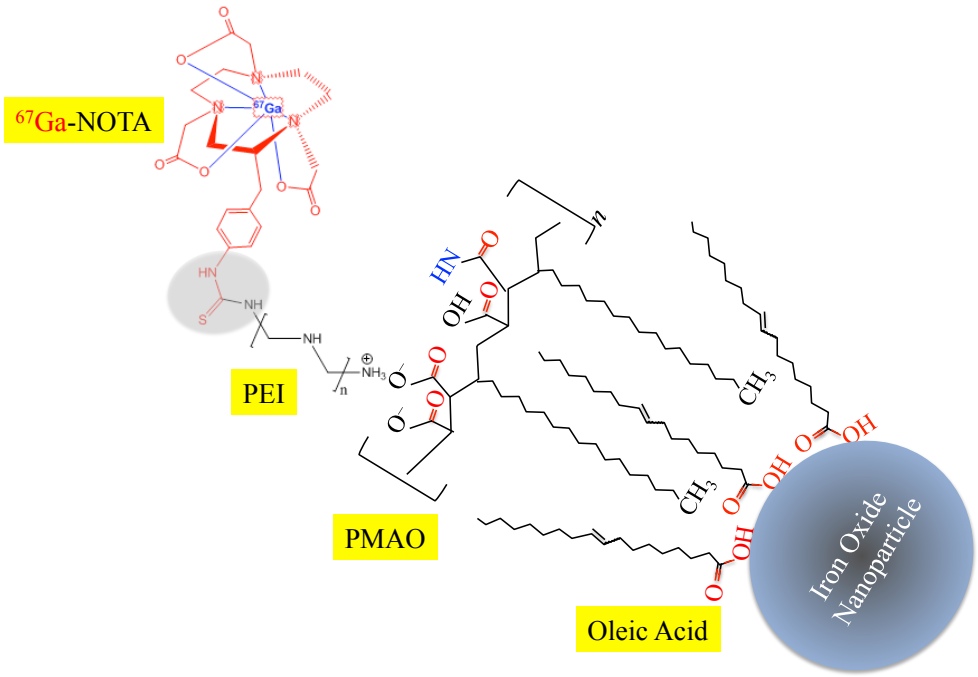

Fig. 5.13. Schematic showing the surface coating of the NPs with PMAO and PEI their radiolabeling with ^{67}Ga using NOTA chelator. We used a branched PEI. However, note that we show a linear PEI here to simplify the schematic, since NOTA conjugation and radiolabeling procedure are the same for both types of PEI (image courtesy of Prof. Kannan Krishnan).

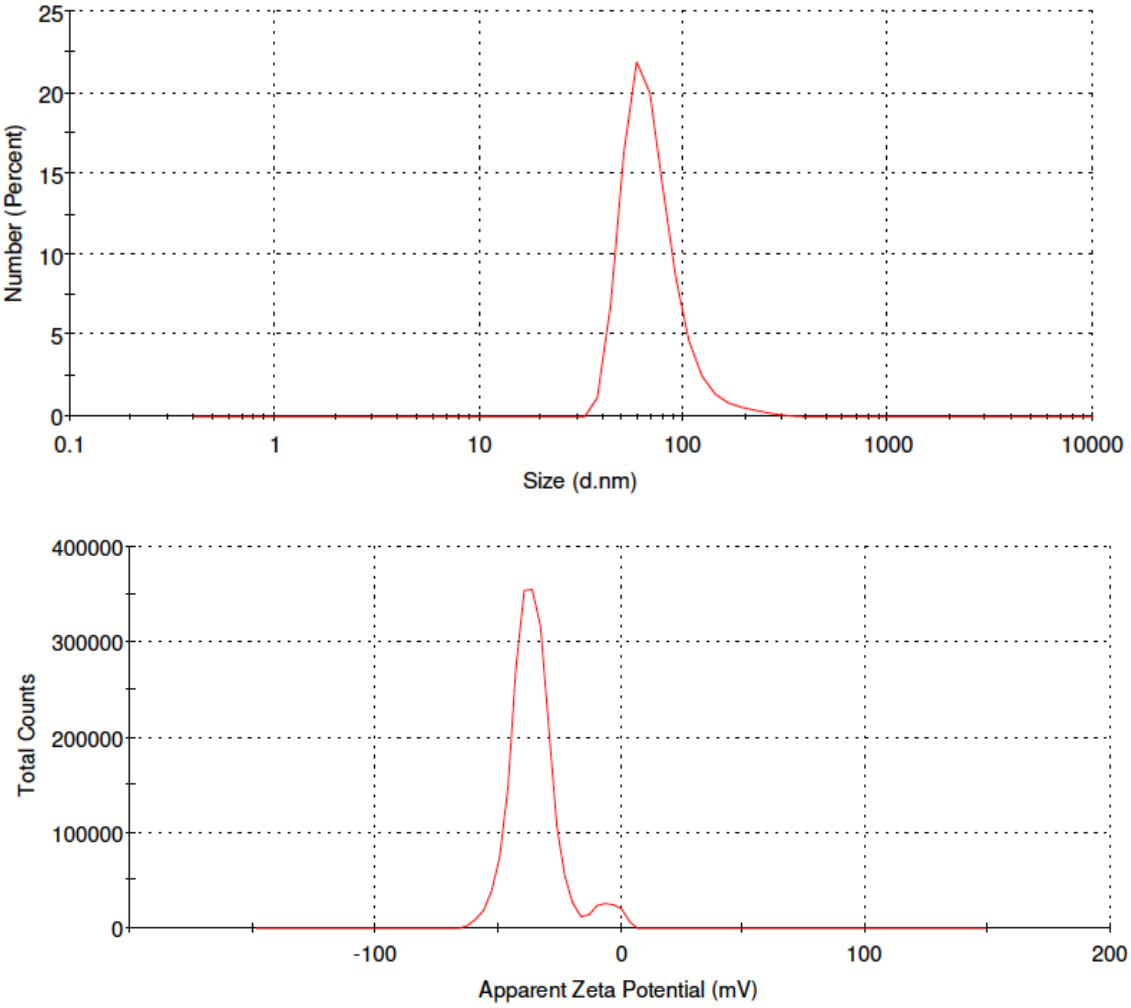

Fig. 5.14. Hydrodynamic size distribution and zeta potential of the radiolabelled NPs. Note to the negative zeta potential observed after conjugation of NOTA to PEI coated NPs, compared to the positive zeta potential of the PEI coated NPs shown in Fig. 5.10.

For biodistribution studies using SPECT/CT imaging, three female C57bl/6 mice (Charles River Laboratories ,Wilmington, MA) were injected via the tail veins with the tracers (120 μl, radiolabelled PEI-MNPs). The animals were scanned individually in a SPECT/CT (imaging protocol approved by the University of British Columbia Animal Care Committee according to guidelines set out by the Canadian Council on Animal Care) immediately and at 4 h post injection and sacrificed then (Fig. 5.15). Following each SPECT acquisition, a whole body CT scan was performed to obtain anatomical

information and both images were registered (Fig. 5.15). For quantitative analysis, SPECT data were reconstructed with ordered subset expectation maximization algorithm (OS-EM) using 6 iterations of 16 subsets and 0.4 mm^3 voxel size. All organs were then counted for radioactivity.

MPS analyses of the tracers showed an excellent dm/dH response with a narrow FWHM (Fig. 5.12), suitable for high resolutions MPI.[9] The branched PEI used in conjugation is a cationic polymer with abundant number of available amine groups, making it a suitable platform for radiolabeling with ^{67}Ga-NOTA (Fig. 5.13). SPECT/CT imaging (Fig. 5.15) and biodistribution studies (Fig. 5.16) confirmed that PEI-coated NPs were only accumulated in liver and spleen 4 h after injection, with almost no traces of NPs in kidneys, lungs and heart. Quantitative measurements of the radioactivity from all organs (Fig. 5.16) indicated the biodistribution to be predominantly in the liver (92±10% of the input dose) and spleen (5±1%) with trace distributions, within experimental error, in the brain and kidneys.

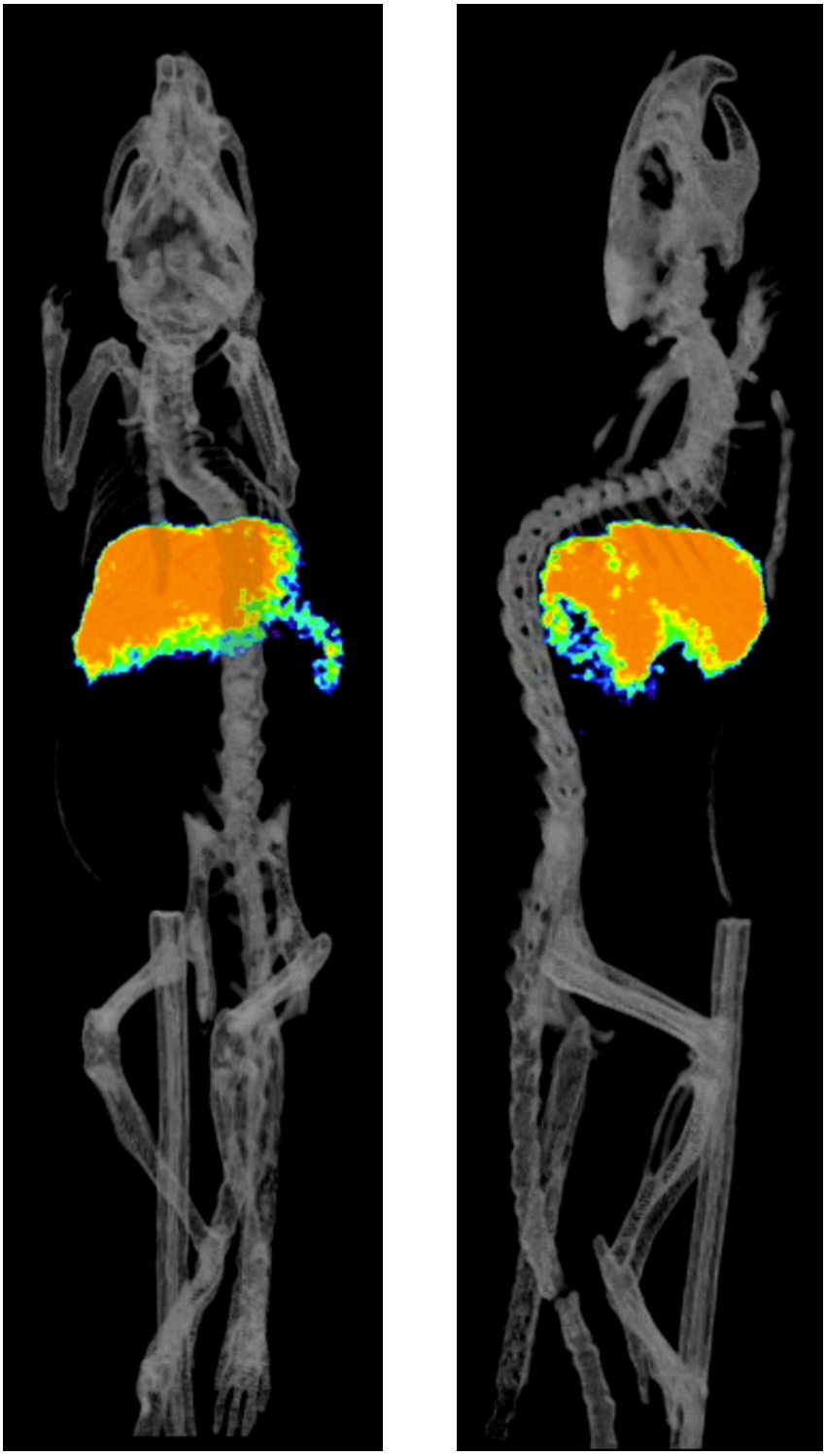

Fig. 5.15. Typical SPECT/CT image of a mouse showing the biodistribution of the ^{67}Ga-NOTA-labeled MPI tracers in mice, 4 h after tail vein injection. NPs were only accumulated in liver and spleen with no trace of NPs observed in kidneys or other organs.

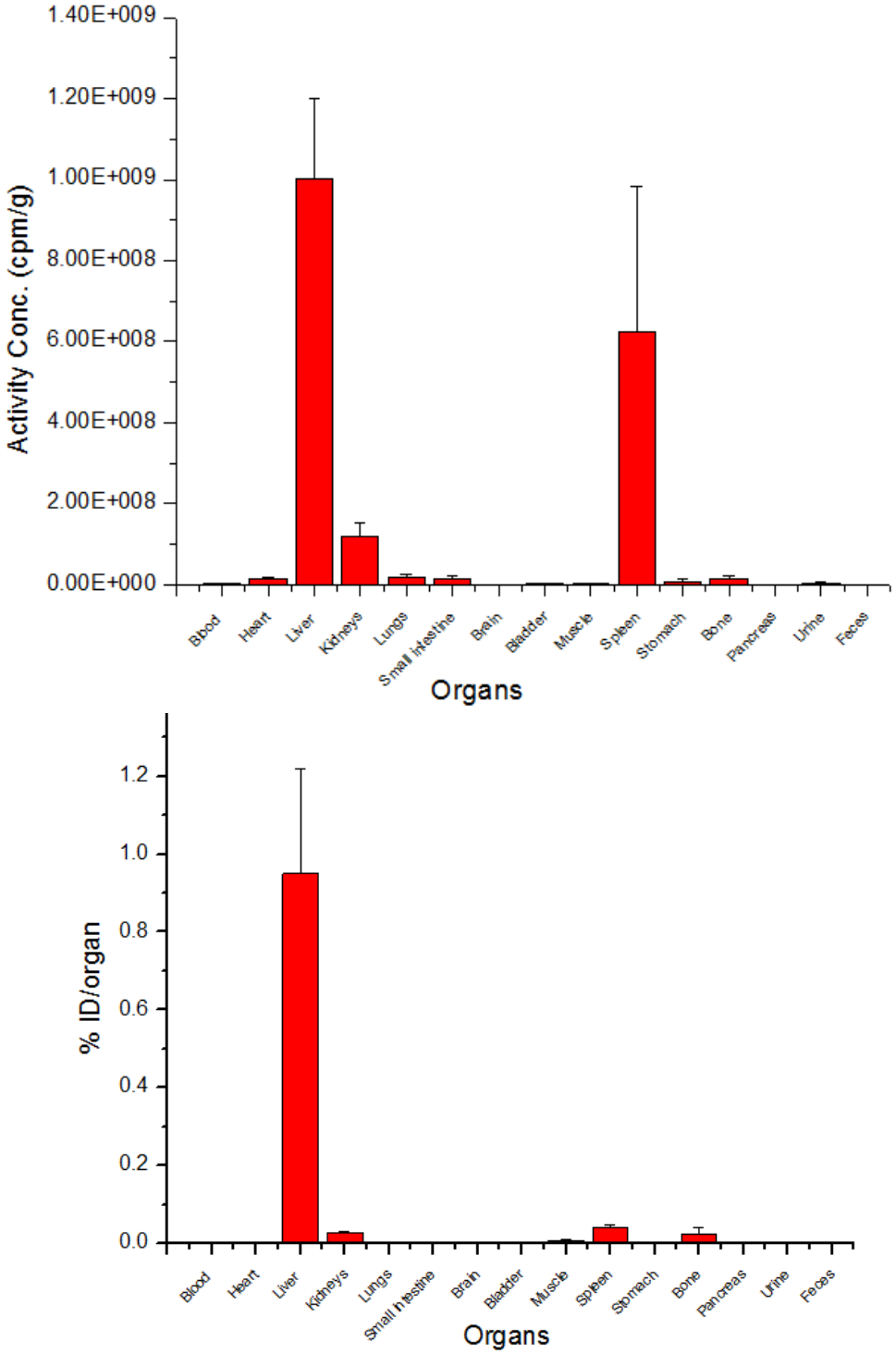

Fig. 5.16. Continued.

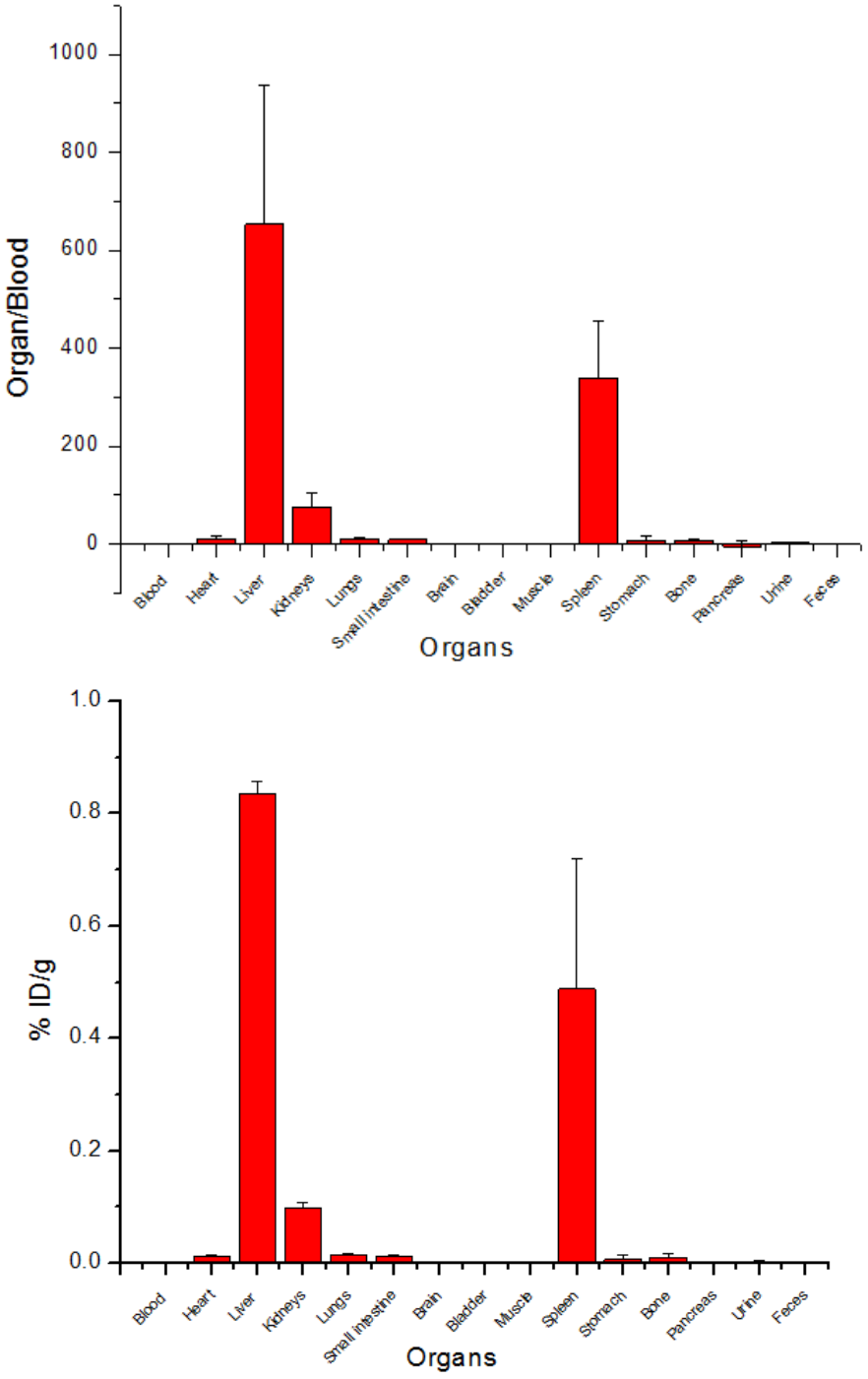

Fig. 5.16. Biodistribution of the ^{67}Ga-NOTA-labeled MPI tracers in mice, 4 h after tail vein injection. All graphs confirm that NPs were mainly accumulated in liver and spleen. The results are shown based on radiation activity observed in each organ, percentage of the injected NPs in each organ, percentage of the NPs in each organ divided by the dosage observed in the blood and percentage of the NPs per mass of each organ.

5.3. Conclusions and future outlook

Our functionalized platform, with glioma-targeting lactoferrin conjugated to the PMAO-PEG surface coatings of the optimized MPI tracers, enhanced uptake by tumors. As we were expecting, magnetic targeting further improved this phenomenon. High tracer mass sensitivity and fast image processing of NIRF, in combination with MPS analyses (as a first measure of the MPI performance of the NPs) enabled us to monitor the NPs uptake by tumors and do preliminary investigation of the feasibility of in vivo MPI cancer diagnosis. NPs uptake by the tumors can be improved by increasing blood circulation and decreasing hydrodynamic size.[6] Our results also show that improving tracer mass sensitivity is required for future applications of MPI in detecting solid tumors at early stages.

In addition, our radiolabeling studies show that amine functionalization of the PMAO coated MPI tracers with PEI, enables facile radiolabeling of ^{67}Ga-NOTA, using a thiourea bond, suitable for quantitative SPECT/CT imaging. Absence of radioactive tracers in the kidneys, 4 h post tail-vein injection, confirmed by the high tracer mass sensitivity of SPECT/CT imaging, is promising for the safe applications of these tracers for in vivo MPI imaging. The flexible PMAO-PEG platform further provides opportunities for various conjugation strategies, ideal for multimodal MPI/CT/NIRF/MRI/CT/SPECT imaging, and each one with distinct advantages.

Chapter 6.

CONCLUSIONS AND FUTURE DIRECTIONS

In this thesis, we used experimental models to simulate the extracellular and intracellular performance of the MPI tracers. We also functionalized the NPs and showed that these functional groups can be used for conjugation of contrast agents of other imaging modalities (such as near infra-red fluorescent microscopy). These functional groups can be also used for conjugation of targeting biomolecules (such as peptides and antibodies) for future cancer targeting and imaging applications. Functionalized NPs can be also used for chelating the radionuclides for multimodal MPI/PET imaging.

Similar to other imaging modalities, spatial resolution and signal intensity are the two major parameters that should be considered in order to generate decent MPI images. Following the results and discussions in previous sections, we know that the FWHM and peak height of the dm/dH curves generated from the NPs determine the quality of the images in MPI. Our animal studies showed that compared to pre-injection NPs, the FWHM was increased after internalization of the NPs in liver and spleen. This lowers the spatial resolution in MPI and decreases the efficiency of this technique for accurate location of targeted tissues (e.g. cancers or labeled stem cells). Future studies are required to investigate the correlation of the MPI image qualities (i.e. spatial resolution and signal intensity) with the intracellular status of the NPs and to find the optimum NPs characteristics in order to maintain their MPI performance efficiency after reaching to the cells and internalization. The surface characteristics, size and charge (i.e. zeta potential) of the NPs should be tuned to enhance their uptake by these cells. The optimum conditions (e.g. NPs incubation time and concentration and highest cell viability) should be found in order to have the highest MPI efficiency and consistency for imaging of these cells.

Cancer-targeting biomolecules (e.g. antibodies or targeting peptides) can be conjugated to the surface of the functionalized NPs reported in this thesis for cancer targeted MPI. However, to achieve this, it is important to preserve the MPI performance of the NPs after these conjugations and control the hydrodynamic size of the final NPs in order to have longest possible circulation time in the blood and higher accumulation of the NPs in cancer tissues. Using MPS measurements, the variation of the FWHM of the dm/dH curves obtained from the cells should be monitored, based on the intracellular location of the NPs and their possible aggregations or degradations in cells. Linearity of the MPI signal intensity and consistency of the resolution should be also studied for different concentration of the NPs in the cells.

For MPI evaluation of the macrophages or stem cells labeled with NPs, the number of uptaken NPs per cell is important in order to get a high intensity signal, specially after differentiation of the stem cells. Differentiation and proliferation of the cells may decrease the number of the NPs per cell and result in weaker MPI signal over incubation time. This can be a challenge for all *in vivo* applications of the MPI for stem cells or macrophage tracking. Therefore, it is necessary to monitor the variation of the MPI signal of the labeled cells by time to see the effects of these biological phenomena on the MPI signal. Combining the results of this study with the toxicity results, will help to find the optimum dosage of the NPs required for each labeling. Note that stability of the hydrodynamic size of the optimized NPs and consistency of the MPI signal of the NPs in cell culture medium are crucial factors for accurate analysis of these results.

The reviews, procedures, results and discussions provided in this thesis were published or used partially for publication of the following references:

1. **H. Arami**, R. M. Ferguson, A. P. Khandhar, K. M. Krishnan, "*Size-dependent Ferrohydrodynamic Relaxometry of Magnetic Particle Imaging Tracers in Different Environments",* **Medical Physics**, 40 (2013) 071904. **(Chapter 3)**

2. **H. Arami**, K. M. Krishnan, "*Highly Stable Amine Functionalized Iron Oxide Nanoparticles Designed for Magnetic Particle Imaging (MPI)*", **IEEE Transactions on Magnetics**, 49 (2013) 3500-3503. **(Chapter 3)**

3. **H. Arami**, K. M. Krishnan, "*Intracellular Performance of Tailored Nanoparticle Tracers in Magnetic Particle Imaging*", **Journal of Applied Physics**, 115 (2014) 17B306. **(Chapter 3)**

4. **H. Arami**, A. Khandhar, D. Liggitt, K. M. Krishnan "*In Vivo Delivery, Pharmacokinetics, Biodistribution and Toxicity of Iron Oxide Nanoparticles*", **Chemical Society Reviews**, 44 (2015) 8576-8607. **(Chapter 2)**

5. A. Tomitaka, **H. Arami**, S. Ghandi, K. M. Krishnan, "*Lactoferrin Conjugated Iron Oxide Nanoparticles for Targeting Brain Glioma Cells in Magnetic Particle Imaging*", **Nanoscale**, 7 (2015) 16890-16898. **(Chapters 4 and 5 and Appendix I)**

6. **H. Arami**, A. P. Khandhar, A. Tomitaka, P. W. Goodwill, E. Yu, S. M. Conolly, K. M. Krishnan, "*In vivo Multimodal Magnetic Particle Imaging (MPI) with Tailored Magneto/Optical Contrast Agents*", **Biomaterials**, 52 (2015) 251-261. **(Chapter 4)**

7. R. Hufschmid, **H. Arami**, M. Ferguson, M. Gonzales, E. Teeman, L. N. Brush, N. D. Browning, K. M. Krishnan "*Synthesis of superparamagnetic iron oxide nanoparticles by three organic phase thermal decomposition approaches*", **Nanoscale**, 7 (2015) 11142-11154. **(Chapter 5 and Appendices A, C and E)**

8. R. M. Ferguson, A. P. Khandhar, S. J. Kemp, **H. Arami**, E. U. Saritas, L. R. Croft, J. Konkle, P. W. Goodwill, A. Halkola, J. Rahmer, J. Borgert, S. M. Conolly, K. M. Krishnan, "*Magnetic Particle Imaging with Safe, Tailored Iron Oxide Nanoparticle*

Tracers", **IEEE Transactions on Medical Imaging,** 34 (2015) 1077-1084. **(Appendix A)**

9. A. P. Khandhar, R. M. Ferguson, **H. Arami**, K. M. Krishnan, "*In-vivo Characterization of Magnetic Nanoparticle Tracers Using Magnetic Particle Spectrometry*", **Biomaterials**, 34 (2013) 3837-3845. **(Chapter 4)**

10. S. Ghandi, **H. Arami**, K. M. Krishnan, "*Magnetic Relaxation of Iron Oxide Nanoparticles for Detection of Cancer Specific Proteases*", **Proceeding of National Academy of Science**, Submitted. **(Appendices C2 and F)**

11. A. Khandhar, R. M. Ferguson, **H. Arami**, S. J. Kemp, K. M. Krishnan, "*Tuning Surface Coatings of Optimized Magnetite Nanoparticle Tracers for In-vivo Magnetic Particle Imaging*", **IEEE Transactions on Magnetics**, 51 (2015) 1-4. **(Chapter 4)**

12. R. M. Ferguson, A. P. Khandhar, **H. Arami**, L. Hua, O. Hovorka, K. M. Krishnan, "*Tailoring the Magnetic and Pharmacokinetic Properties of Iron Oxide MPI Tracers*", **Biomedical Engineering**, 58 (2013) 493-507. **(Chapters 1 and 2)**

13. M. Gould, R. Barnour, N. Thomas, **H. Arami**, K. M. Krishnan, K. M. Fu, "*Room-temperature Detection of a Single 19nm Super-paramagnetic Nanoparticles with an Imaging Magnetometer*", **Applied Physics Letters**, 105 (2014) 072406.

14. F. Ludwig, H. Remmer, C. Kuhlmann, T. Wawrzik, **H. Arami**, R. M. Ferguson, K. M. Krishnan, "*Magnetic Properties of Single Core Magnetite Tracers Optimized for Magnetic Particle Imaging",* **Journal of Magnetism and Magnetic Materials,** 360 (2014) 169-173.

15. T. Wang, F. M. Kievit, O. Veiseh, **H. Arami**, Z. Stephen, C. Fang, Y. Liu, R. G. Ellenbogen, M. Zhang, "*Targeted Cell Uptake of a Non-internalizing Antibody through Conjugation to Iron Oxide Nanoparticles in Primary Central Nervous System Lymphoma*", **World Neurosurgery**, 80 (2013) 134-141.

16. F. M. Kievit, Z. Stephen, O. Veiseh, **H. Arami**, T. Wang, J. Park, V. Phan-Lai, M. L. Disis, M. Zhang, "*Targeting of Primary Breast Cancers and Metastases in a Transgenic Mouse Model Using Rationally Designed Multifunctional SPIONs*", **ACS Nano**, 6 (2012) 2591-2601.

17. O. Veiseh, F. M. Kievit, H. Mok, J. Ayesh, C. Clark, C. Fang, M. Leung, **H. Arami**, J. O. Park, M. Zhang, "*Cell Transcytosing Poly-arginine Coated Magnetic Nanovector for Safe and Effective siRNA Delivery*", **Biomaterials,** 32 (2011) 5717-5725.

18. **H. Arami**, Z. Stephen, M. Zhang, "*Chitosan Coated Iron Oxide Nanoparticles for Molecular Imaging and Drug Delivery*", **Advances in Polymer Science,** 243 (2011) 163-184.

19. L. R. Croft, P. W. Goodwill, J. J. Konkle, **H. Arami**, D. A. Price, A. X. Li, E. U. Saritas, S. M. Conolly, "*Low Drive Field Amplitude for Improved Image Resolution in Magnetic Particle Imaging*", **Medical Physics**, In press.

20. J.W.M. Bulte, H. Boeve, K.M. Krishnan, **H. Arami**, P. Walczak, B. Gleich, J. Borgert, J. Rahmer, "Non-Invasive Hot Spot Imaging of Transplanted Stem Cells using Magnetic Particle Imaging", **Tomography**, In press.

Appendices

A. Synthesis of 25nm magnetite nanoparticles as efficient magnetic particle imaging tracers optimized by tuning their size-dependent crystalline structure

A.1. Introduction

As we discussed before, in the *x-space* approach to image reconstruction in MPI, the point spread function (PSF) is a good measure of the signal intensity and spatial resolution of the images.[15] Here, the PSF is the product of the magnetic field gradient (dH/dx, where x is the position of the point source in imaging volume) and dm/dH.[42, 407] Typically, dH/dx is a constant parameter for a given MPI scanner, and dm/dH is an intrinsic property of the NPs; the latter is highly dependent on magnetization and relaxation dynamics of the NPs (*i.e.* size, monodispersity and excitation time).[10, 15, 42, 423] The full width at half maximum (FWHM) and peak height of dm/dH , measured in a MPS, can predict the spatial resolution and signal intensity in *x-space* MPI image processing. Smaller FWHM and larger peak height of dm/dH, correspond to improved spatial resolution and signal intensity, respectively.[18]

We have shown that increasing the core size of the highly monodisperse NPs to about 25-27nm (close to the superparamagnetic to ferromagnetic transition at a 100s measurement time) can significantly improve the spatial resolution and NPs mass sensitivity in MPI, compared to commercially available tracers such as Resovist.[9] This is because of the high saturation magnetization rate of these NPs at field points of magnetization reversal. Preparation of monodisperse NPs with tailored size is possible through thermal decomposition of the organometallic iron precursors (*e.g.* iron oleate, FeOOH or iron pentacarbonyl) in the presence of surfactants (*e.g.* oleic acid and oleyl amine). In fact, controlling the NPs nucleation time as an entirely separate step (*i.e.* burst of nucleation) followed by uniform growth of the nuclei is crucial to synthesize such monodisperse NPs by this method. This is in contrast to the simultaneous nucleation and growth phenomena happening continuously during the preparation of NPs by co-

precipitation of iron ferric and ferrous ions in alkaline solutions, which usually results in formation of highly polydisperse iron oxide nanoparticles (e.g. Resovist and Feridex).[22] In thermal decomposition synthesis, assuming a constant reaction volume, increasing the molar ratio of oleic acid surfactant to iron oleate precursor to an optimum value results in NPs with larger median core sizes.[42] However, presence of larger amounts of oleic acid required for synthesis of 25-27nm NPs has some drawbacks. Condensation and refluxing of the oleic acid create extensive turbulence (bumping) in the system, increasing NPs polydispersity. Also decomposition of oleic acid and its reaction components at high synthesis temperatures (*i.e.* 320ºC) generates carbon monoxide in the system that changes the crystalline structure, composition and phase purity of the NPs by reducing magnetite or maghemite to Wüstite .[444, 445] Wüstite is a magnetically weak phase of iron oxide that dramatically decreases the magnetization rate of the NPs resulting in poor MPS performance, and to prevent its formation, control of the oxidation levels in the synthesis systems is desirable.

Here, two separate batches of monodisperse NPs (d_C~25-27nm) were prepared using exactly identical synthesis parameters, but with significantly different crystalline structures and magnetic properties, caused by a small change in their synthesis atmosphere. First, we synthesized these NPs using thermal decomposition of iron oleate in the presence of oleic acid at 320ºC. Then, these two groups of the NPs were coated with poly(maleic anhydride-alt-1-octadecene) (PMAO) and polyethylene glycol (PEG) polymers, to make them fully soluble in aqueous solutions. High resolution TEM (HRTEM) and scanning TEM (STEM) characterization showed that the reaction produced Wüstite NPs coated with a thin layer of magnetite (i.e. a Wüstite[FeO]/ magnetite[Fe_3O_4] core/shell structure) when the system was purged with argon and fully sealed. On the other hand, when enough air was accessible into the synthesis system through the condensers, single crystalline magnetite NPs with considerably enhanced MPS performance were formed. Such dual-phase crystal structure resulted in poor MPS performance by increasing the FWHM of the dm/dH signal. Introducing controlled amounts of air in the synthesis reaction, however, formed single crystalline magnetite

structures with significantly improved MPI signals (narrower FWHM and higher intensity). We demonstrate that phase purity is as important as NP core size (d_C~25-27nm) to improve MPS performance, and generate high quality MPI images.

A.2. Large scale synthesis of 25nm NPs as efficient MPI tracers

Monodisperse hydrophobic NPs (d_C ~25-27nm) were synthesized by modification of a method reported before for synthesis of NPs with smaller core sizes (d_C < 22nm).[42, 46, 327] Note that the synthesis parameters were optimized for much larger scale synthesis with an approximate yield of about one gram of dried and purified NPs. Briefly, 9 mmol (8.1 gr) iron oleate and 99 mmol (27.96 gr) oleic acid were dissolved in 45 gr of 1-octadecene solvent and heated at 320°C for 24 hours. Two separate batches of NPs were prepared under inert argon atmosphere and in the presence of air, partially accessible to the system through open condenser exhaust tubing. Iron oxide nanocubes were also prepared in the presence of sodium oleate by adjustment of a previously reported approach.[446] Briefly, 3.1 gr iron oleate, 0.285 gr sodium oleate and 1 gr oleic acid were mixed with 30 gr squalene as the solvent and heated at 175°C for 2h under argon atmosphere, followed by heating at 320°C (heating rate of 20°C/min) for another 1h.

As-synthesized NPs were dispersed in 20mL mixture of chloroform and methanol (50-50 vol.%) by sonication (~3min) and then separated by a strong magnet. This step was repeated four times and the purified NPs (~10mg) were redispersed in 5mL chloroform, by 30min sonication. 500mg poly(maleic anhydride-alt-1-octadecene) (PMAO, Mn =30,000-50,000 kDa, dissolved in 5ml chloroform) was added to the NPs and sonication was continued for 1h. Then 660mg polyethylene glycol (mPEG-NH_2, MW 20kDa) was dissolved in 5mL chloroform and was added to PMAO coated NPs and sonication was continued for another 16h. Rotary evaporation was used to remove chloroform and then, 5mL Tris-acetate-EDTA (TAE, 1x) was added to the dried NPs, followed by 1h sonication to redisperse the NPs. The water dispersed PEG coated NPs were purified by repeating centrifugation (14000rpm, 45min) and redispersion in the same amount of dionized water for three times.

Transmission electron microscopy (TEM, FEI TecnaiTM G2 F20, 200 KeV), equipped with a Gatan CCD camera was used to analyze size and morphology of the synthesized NPs. STEM was performed on a Cs-corrected FEI Titan scanning/transmission electron microscope (S/TEM) operated at 300kV with a high-angle annular dark field (HAADF) detector. Magnetization behavior (*m*-*H*) of the NPs (~150μg of NPs solution in 100μL polycarbonate capsules) were studied using a vibrating sample magnetometer (VSM). Dynamic light scattering (DLS) was used to measure the hydrodynamic size of the PEG coated NPs. We also used our magnetic particle spectrometer (MPS) with a sinusoidal excitation field of 18.6m$T\mu_0^{-1}$ (peak-peak, f_0=25kHz) to evaluate the performance (d*m*/d*H*) of the synthesized NPs.[16, 42] The data processing method for calculating d*m*/d*H* graphs from the induced voltage in receiving coils of the MPS was reported earlier in section 3.1.6.[42] All d*m*/d*H* plots obtained from MPS were normalized to one in order to compare their FWHM, which is a good indicator, to first order, of the potential spatial resolution in an MPI scanner.

A.3. Results and Discussions

The signal in MPI is directly originated from superparamagnetic iron oxide nanoparticles (NPs) and therefore it is highly dependent on field dependent magnetization rate of the NPs.[18] We have shown before that increasing the core size (d_C) of the superparamagnetic NPs, increases the spatial resolution and signal intensity due to their much faster magnetization rates (d*m*/d*H*) caused by the AC field in MPI scanners.[9] In *x-space* MPI image reconstruction method, these image quality improvements are represented by narrower full width at half maximum (FWHM) and larger peak heights of the d*m*/d*H* graphs, as measured by a magnetic particle spectrometer (MPS).[7, 11, 42]
Synthesis of the different sizes of monodisperse hydrophobic NPs with narrow size distributions is achievable by controlled thermal decomposition of iron precursors in the presence of proper ratios of the stabilizing surfactants (*e.g.* oleic acid and oleyl amine) and solvents (*e.g.* 1-octadecene, octadecane, docosane and eicosane).[16, 42] However, our investigations showed that, compared to synthesis of the smaller sizes (i.e. d_C <

22nm), further adjustment of the synthesis parameters are required when larger core sizes (*e.g*. d_C ~ 25-27nm) of the NPs are desired. The size, monodispersity, crystalline structure and composition of larger NPs changes considerably with minor changes in reactants stirring rates, synthesis temperature, reaction volume, type of the solvents and synthesis atmosphere. In this study, we modified a previously reported method for large scale synthesis of 25-27nm monodisperse oleic acid coated NPs (~ one gram of the dried and purified NPs). While all the other synthesis parameters were exactly the same, the synthesis atmosphere can dramatically change the crystalline structure and therefore the magnetic properties and MPS performance of these NPs. To investigate this, we synthesized two separate batches of NPs using the same synthesis parameters and changed the reaction atmosphere to control the oxidation level of the NPs. One reaction was performed when the synthesis flask was fully purged with argon and the other reaction was done in the presence of partial air accessible to the synthesis flask through the condensers. The preliminary TEM images showed almost similar core sizes and morphologies, however, more accurate HRTEM, electron diffraction pattern and HAADF STEM analyses showed fundamental structural differences on the atomic scale (Fig. A1) that were further confirmed by VSM (*m*-*H*) and MPS (d*m*/d*H*) measurements (Fig. A2).

TEM and HAADF STEM images in Figs. A1(a) and (b), show that a core/shell structure was formed when the reaction was fully protected by inert argon gas. HRTEM analyses of the lattice fringes (Fig. A1(c)) showed an inter-planar (*d*-spacing) of 0.214nm, which matches well with the {200} crystallographic planes of Wüstite (FeO). This dual-phase structure generated Moiré patterns in HRTEM images. However, when oxygen was partially accessible to the reaction system, single crystalline NPs were formed (Figs. A1 (d) and (e)). The d-spacing of 0.792nm from the HRTEM images of these NPs corresponds to {111} planes in magnetite (Fe_3O_4). Electron diffraction patterns obtained from a selected area of these two samples also showed characteristic peaks related to FeO/Fe_3O_4 and pure Fe_3O_4, confirming the lattice fringe analyses results (Fig. A1(f)). It is known that the decomposition of oleic acid and its reaction by-products followed by their

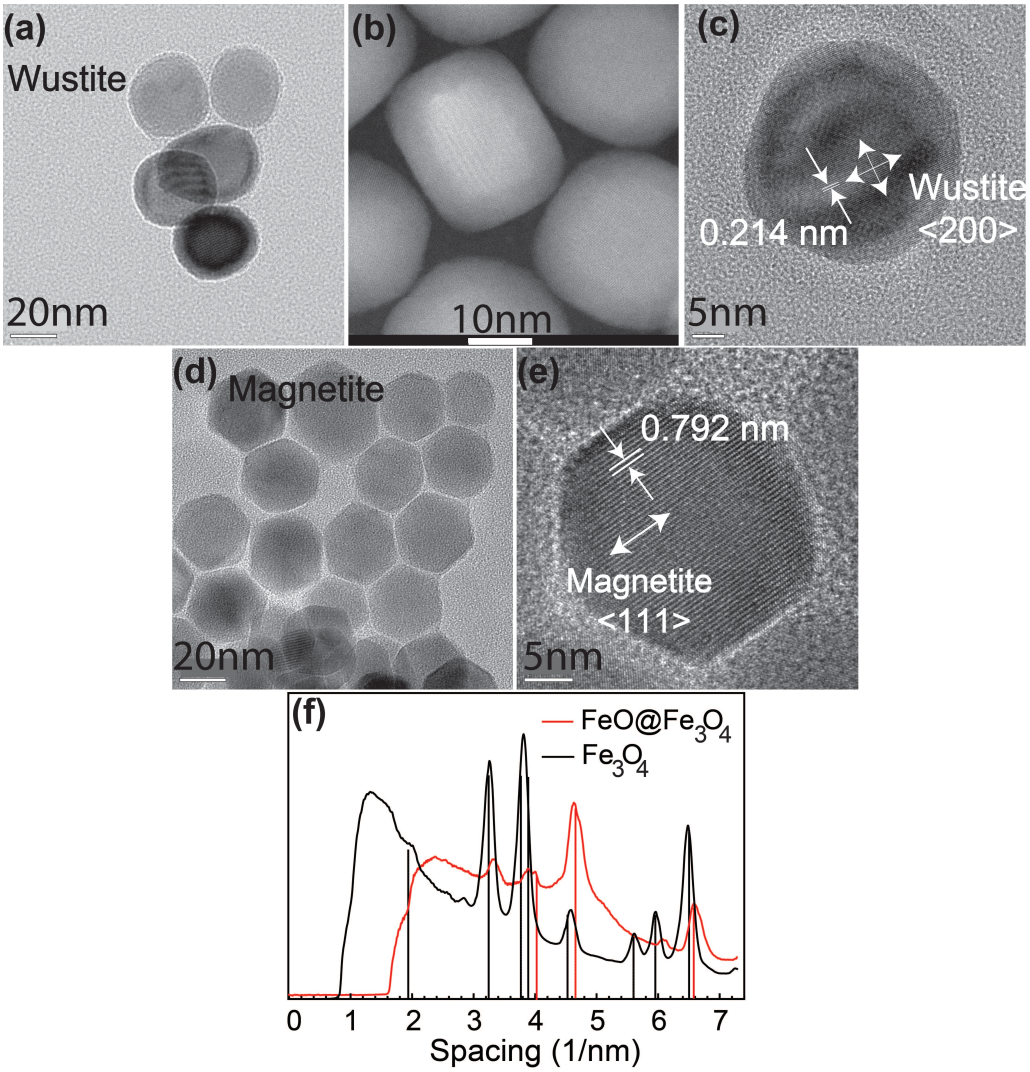

Fig. A1. HRTEM ((a) and (c)) and HAADF STEM (b) images showing Wüstite/magnetite core/shell formed due to reductive role of carbon monoxide during the synthesis; (d) and (e) HRTEM images of pure magnetite formed when partial oxygen was available in reaction flask; (f) electron diffraction patterns of these two types of NPs showing the characteristic peaks of Wüstite and magnetite.

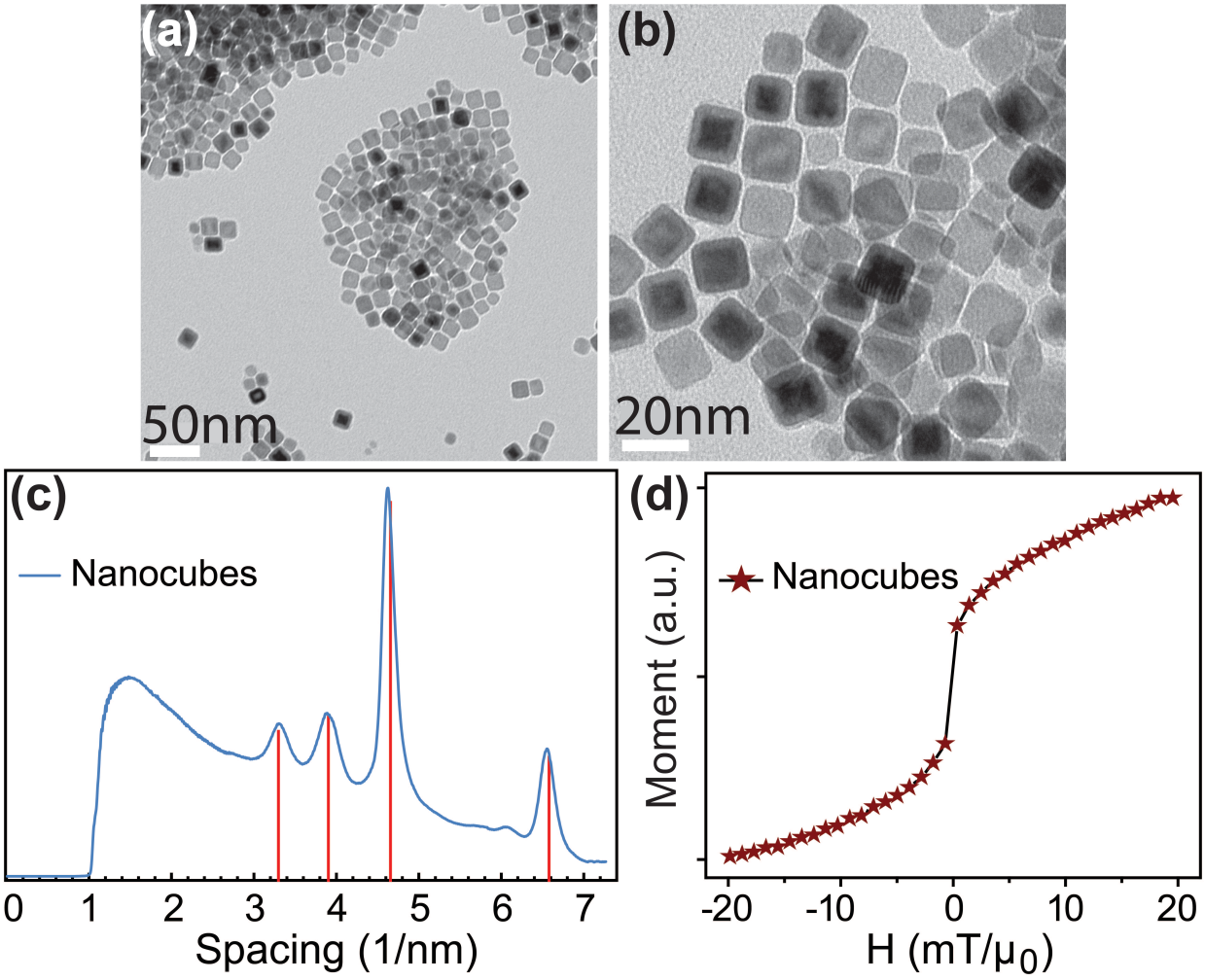

Fig. A2. TEM images ((a) and (b)) and electron diffraction pattern (c) of the nanocubes showing their core/shell Wüstite/magnetite nanostructures; Compared to apparent sizes in TEM images, a smaller core size of ~13.4nm was calculated using Chantrell fitting[404] to the VSM *m-H* plot of the nanocubes (d), due to presence of magnetically weak Wüstite as their main crystallographic phase.

condensation and vigorous bumping and turbulence in reaction system results in formation of excessive amounts of carbon monoxide (CO) in reaction flask.[447] This carbon monoxide reduces magnetite (Fe_3O_4) to Wüstite (FeO) and transforms to carbon dioxide (CO_2), a more thermodynamically stable state in the system.[444] Therefore, when the reaction system was fully purged and sealed with argon, this carbon monoxide resulted in a FeO/Fe_3O_4 core/shell structure. However, when oxygen was partially available, the magnetite reduction to Wüstite was prevented and single crystalline Fe_3O_4

NPs were obtained. This process was confirmed by introducing a strong reducing agent (sodium) into the system for synthesis of iron oxide nanocubes by a previously reported procedure, where it helps further to reduce Fe_3O_4 to FeO even at smaller oleic acid to iron oleate ratio, forming the same Wüstite/magnetite core/shell structure for smaller NPs sizes (Fig. A2).[445]

Other approaches such as post synthesis oxidation at mild temperatures in air,[448] or by an oxidizing agent (trimethylamine N-oxide),[449] followed by annealing at higher temperatures have been also used for transforming Wüstite to magnetite or maghemite NPs. Note that Wüstite is metastable at room temperature and tends to transform to zero iron (Fe), assuming that all kinetically favorable parameters (time and energy) are provided for diffusion of oxygen toward the surface of the NPs. This results in formation of Fe_3O_4 shell around the Wüstite core, based on the Kirkendal mechanism (preferred outward elemental diffusion in NPs systems).[450] Fe_3O_4 may also form on the surface of Wüstite during the growth stage, which happens after burst of nucleating by heating the reaction at 320°C for 24 hours. Also, a part of this Fe_3O_4 shell may be due to surface oxidation in ambient temperature when samples are exposed to air.

Wüstite is a magnetically weak phase, which dramatically changes the MPS performance of the NPs by increasing the FWHM (*i.e.* losing resolution in MPS, Fig. A3(a)). On the other hand, magnetite NPs showed a very narrow dm/dH peak, with a FWHM of about 60% of the Resovist (commercially provided iron oxide NPs). Note that hydrodynamic sizes and polydispersity indexes of the NPs measured by DLS method were almost identical (dH ~ 55-65nm, PDI ~ 0.2-0.25). Such variations in MPS dm/dH response were also confirmed by comparing the near zero field slopes of the m-H graphs and magnetization rates of these two types of NPs (Fig. A3(b)). Single crystalline magnetite NPs were rapidly magnetized and reached their saturation magnetization at much smaller field values, compared to FeO/Fe_3O_4 core/shell structures, a phenomenon which resulted in their significantly improved MPS performance (better FWHM of the PSF). Finally,

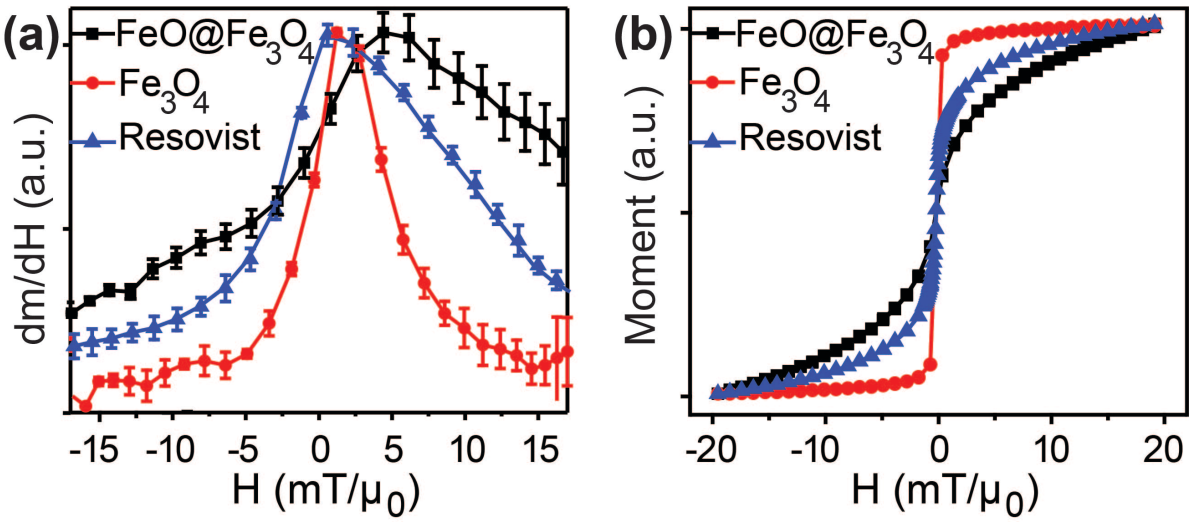

Fig. A3. Measures d*m*/d*H* in the MPS (a), and *m*-*H* plots obtained by VSM (b), showing narrower FWHM (higher MPI resolution) and faster saturation magnetization for single crystalline magnetite NPs (d_C~25nm) in comparison with Wüstite/magnetite core/shell NPs and a commercially provided tracer, Resovist®.

Chantrell fitting of *m*(*H*) curves to determine NPs core size based on their magnetization rates,[404] showed that in contrast to their apparent similar TEM sizes, the core size, d_C~12nm, for core/shell NPs, due to presence of the magnetically weak Wüstite core. The d_C calculated for the single crystalline magnetite NPs was ~25nm, matching well with their TEM images.

A.4. Conclusions

Increasing the core size of the highly monodisperse NPs to about 25-27nm can significantly improve the resolution and signal intensity in MPS. However, the MPS performance of these NPs depends on their crystalline structure and oxidation state; in other words, their phase purity. Formation of carbon monoxide due to decomposition of the oleic acid and other reactants during the synthesis reduces magnetite (Fe_3O_4) or maghemite (Fe_2O_3) to Wüstite (FeO), which is a magnetically weak phase of iron oxide with a poor MPS performance. When oxygen is partially accessible into the reaction system, pure magnetite NPs form due to an *in situ* oxidation. The FWHM of d*m*/d*H* of these single crystalline magnetite NPs was significantly smaller than commercially

available NPs such as Resovist, which is a substantial improvement toward MPI applications targeting sub-mm resolutions in the future.

B. Preparing samples for nanoparticles characterizations

Dynamic light scattering (DLS) and Zeta potential measurements:

DLS and Zeta potential measurements help to determine the hydrodynamic size and surface charge of the nanoparticles. Add 0.7-1mL DIW to a cuvette. Add about 30-50 µL of the NPs to the water and disperse them by several times pipetting. Insert the cuvette into DLS sample holder and run the measurement using DLS software. For Zeta potential measurements, make the sample similar to DLS samples, then use a needle to inject the solution into a zeta potential cuvette. Make sure there is no bubble left in cuvette.

Inductively coupled plasma (ICP):

ICP is used to determine the iron concentration (or nanoparticles concentration) in each sample. For Water dispersed samples, transfer 10 µL of NPs solution to a 15mL centrifuge tube. Add 100 µL concentrated HCl solution. Vortex and make sure all the NPs are dissolved. A yellow color solution will form when all the NPs are digested by acid. Now, increase the volume to 5mL by adding DIW. The sample is ready for ICP measurements. For oleic acid coated NPs in organic solvents such as chloroform and hexane, sonicate the solution and transfer 10 µL of the NPs solution to a vial. Keep the vial at room temperature to evaporate all the solvents. Then add 100 µL HCl and follow the procedure as described above for water dispersed samples.

Important safety note: Concentrated HCl is a very strong acid. Open the acid bottle only inside the fume hood and use lab coats, goggles and special gloves.

Vibrating sample magnetometer (VSM):

VSM is used for determination of magnetization of the NPs. It can be also used to estimate the median core size of the NPs using Chantrell fitting.[404] To run VSM, transfer 100 µL of the NPs in aqueous solutions to polycarbonate capsules and fix the

capsule in a straw using double-side tape. Then attach the straw to VSM sample holder and run the measurement. For samples in organic solvents use 200 μL gelatin capsules.

Transmission electron microscope (TEM):

TEM is used for determination of the size, morphology and crystalline phase of the NPs. To make TEM samples, first purify the oleic acid coated NPs, as described in Appendix D, Step 1. Then disperse the purified NPs in toluene, depending on the amount of the nanoparticles. A very pale color solution is best for TEM, which can be easily obtained by adjusting the NPs concentration and amount of the toluene. Sonicate the NPs solution for 15-30min. Clean a glass slide using chloroform and methanol. Cut a small piece of filter paper and place it on the glass slide. Place the TEM grid on the filter paper and add 7 μL of the NPs solution on the grid and let it dry. Sometimes, you can repeat adding NPs several times to ensure having higher concentration of the NPs on the grids, specially desired for electron diffraction and crystallographic phase analysis. For water dispersed samples, add 7 μL of the NPs solution to the grid and let it dry in oven at 50 °C.

Note: Grid type: Carbon Film only on 200 mesh, Copper, Ted Pella, current product No.# 01840-F)

Magnetic Particle Spcetrometer (MPS):

MPS is a quick test, helpful to estimate the MPI performance of the NPs. Transfer 200 μL of the NPs solution to 0.5mL centrifuge tubes and run MPS measurements.

C. Procedures for synthesis of oleic acid coated NPs

C.1. Using iron oleate as the iron precursor

Step 1: Synthesis of iron oleate

Dissolve 40 mmol of iron chloride (10.8 gr, $FeCl_3 \cdot 6H_2O$) in a mixture of 80mL methanol, 60mL DIW and 140mL hexane, in a three-necks flask. To do this, first dissolve iron chloride in methanol and then add water and hexane. Note that this generates some heat that may cause boiling of the methanol. It is better to add iron chloride powder to methanol slowly. Make sure iron chloride gets fully dissolved. An orange color solution forms. Then, add 36.5gr sodium oleate (120 mmol). Seal the reaction flask using rubber septums and purge the system with argon. Start heating the mixture by a slow heating ramp of 1°C/min. Set the temperature to 57°C and keep the mixture stirring and refluxing for four hours. Use a separatory funnel to separate organic layer containing iron oleate from the heavier water phase. Remove the water layer and then add equal volume of DIW. Shake it well and again keep it to separate the aqueous and organic layers. Repeat this for 2-3 times. Note that presence of sodium impurities may result in change of NPs morphology. Add about 5 grams of sodium sulfate to the hexane-iron oleate solution to remove any remaining water from the solution. Use rotary evaporator to remove all hexane from the system. A viscous dark brownish solution will be left, which is iron oleate usable for synthesis of the NPs.

Step 2: Synthesis of oleic acid coated NPs

Dissolve 9 mmol (8.1 gr) iron oleate and 99 mmol (27.96 gr) oleic acid in 45 gr of 1-octadecene solvent in a 250mL three-necks flask. Use a magnet bar for stirring the solution. Make sure the magnet bar is in the center of the flask. Wrap the reaction flask with aluminum foil to ensure a uniform temperature distribution in solution. Purge the system with argon. Increase the temperature to 120°C using a heating ramp of 3°C/min. Keep at this temperature for 1h, while there is a slow argon flow. This helps to remove residua water and other organic impurities from the system. Then start heating to 320°C using a heating ramp of 5°C/min. Keep the reaction running at this temperature for 24

hours. Note that these parameters are set to synthesize NPs with median core sizes ranging from 23-27nm. To make smaller core sizes, smaller iron oleate to oleic acid ratios should be used (such as ~1:9 for 18nm NPs or ~1:7.5 for 16nm NPs and etc.). Also, note that stirring rate used for this protocol is 450rpm. We have seen than using larger stirring rates decreases the size of the NPs. As mentioned in Appendix A, magnetite phase purity and formation of Wustite are challenges for synthesis of larger core sizes. Wustite forms due to formation of carbon monoxide. Post-oxidation steps can help to transform this wustite phase to magnetite and enhance the MPI performance of the NPs. To oxidize the NPs, decrease the temperature of the as-synthesized NPs solution to 150-250 °C/min, when the septums are removed and the solution surface is exposed to air. Depending on the size and the amount of impurities in each batch, keep heating the solution for 12-24h. Also, a flow of Argon-1% oxygen can help to oxidize the NPs. To do this, insert a needle into the reaction flask and keep the gas flow at 320 °C for 8-12 hours depending on the size of the NPs. Note that exceeding the amount of oxidation results in formation of hematite which is not desired for MPI applications due to its weak magnetic properties.

C.2. Using Iron oxyhydroxide as the iron precursor

The synthesis set up is very similar to Appendix C.1. The only difference is using FeOOH instead of iron oleate. Using FeOOH makes the synthesis procedure faster, compared with synthesis of nanoparticles from iron oleate, which requires an additional step to synthesize and purify iron oleate. The NPs synthesis mechanisms are almost the same as iron oleate method, since iron oleate forms as an intermediate phase when FeOOH is used for synthesis of NPs.

To do this synthesis dissolve 0.356gr FeOOH and 18.81gr oleic acid in 50mL 1-octadecene. Use iron oxyhydroxide (Iron(III) oxide - hydrated, Sigma-Aldrich, presumably goethite: α-FeOOH) and grind it using a mortar and pestle first. Changing the oleic acid to FeOOH ratios to 1:15, 1:16, 1:16.6, 1:18 and 1:20 results in synthesis of nanoparticles with median core sizes of about 15, 22, and 25-27nm, as shown in Fig. C.2.1. Do the refluxing reaction in a 250 mL three-neck round bottom flask. Purge the reaction flask with argon and heat the system to 120°C for approximately one hour. Then, increase the temperature to 320°C at 15°C/min and hold the reaction stirring (450rpm) at this temperature for 24 hours.

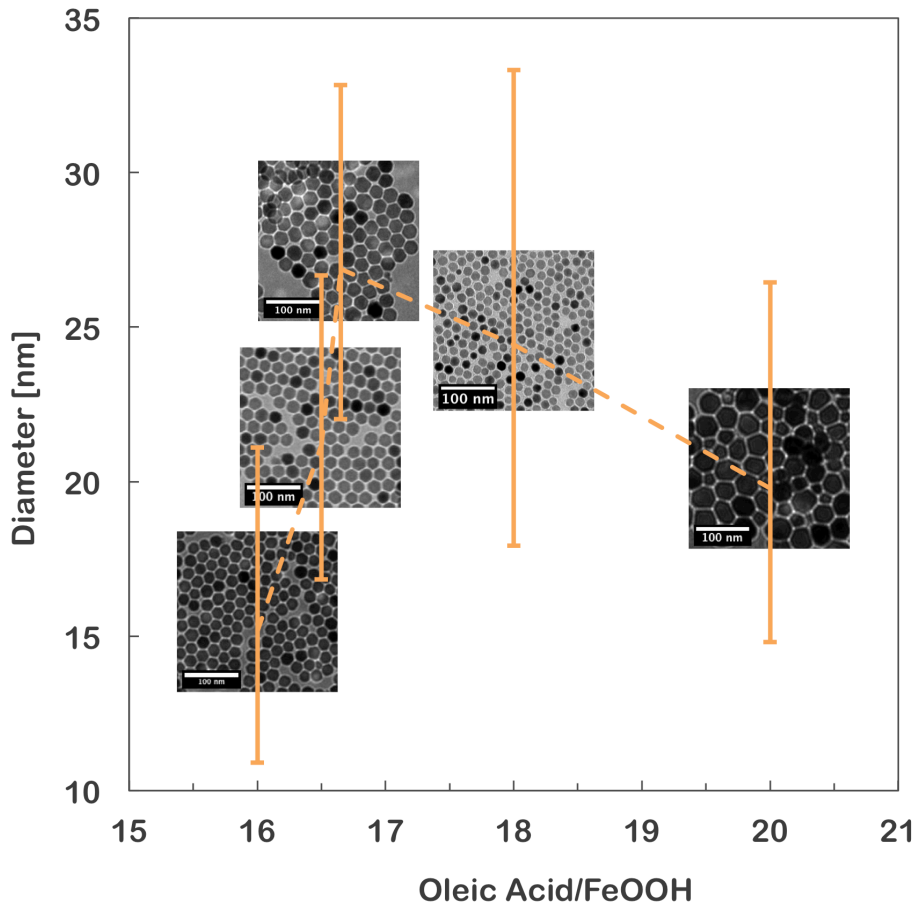

Fig. C.2.1. Particle size versus oleic acid:FeOOH ratio for iron oxide nanoparticles produced by thermal decomposition of iron oxyhydroxide.

D. Procedure for nanoparticles silanization and PEG conjugation

List of Materials:

Oleic acid coated Fe_3O_4 Nanoparticles, 3-(triethoxysilyl)propyl succinic anhydride (TSP), Toluene, Hexane, THF: tetrahydrofuran, NH_2-PEG-NH_2 (2 or 5kDa), dicyclohexylcarbodiimide (DCC), Sodium borate buffer (25mM, pH 8.5)

Procedure:

Step 1: Purification of the as-synthesized oleic acid coated nanoparticles

1. Transfer about 30mg of the as-synthesized NPs to three 40ml vials, about 10mg in each vial
2. Add 20mL of a methanol-chloroform mixture (40-60%) to the NPs, sonicate for 1 min to disperse the NPs and put the vial on a magnet to precipitate the NPs.
3. Repeat this step 3-4 times using a 50-50% methanol-chloroform mixture, until the supernatant gets clear.
4. Add about 13.3mL toluene to each vial and sonicate for about 15min to disperse the NPs.
5. Transfer all the NPs to one 40mL vial.
6. Aggregated NPs can be removed by centrifuge before starting the silanization.
7. Run ICP to know the exact concentration of the NPs before silanization.

Step 2: Silanization of the purified oleic acid coated NPs

1. Transfer the NPs solution to a 125mL flask. Purge the flask with Argon. Both mechanical stirrer or magnetic stirrer with a magnet bar can be used for stirring the solution. It is recommended to use mechanical stirrer for larger core sizes.
2. Increase the temperature to 80 °C, and add 50-100µL TSP (depending on the NPs size) to NPs by injection, using a needle and 1mL syringe.
3. Increase the temperature to 100-105 °C and run the reaction for 8 hours.

Step 3: Conjugation of NH_2-PEG-NH_2 to silanized NPs

Note: The same procedure can be used for conjugation of other PEG derivatives, such as mPEG-NH_2 and NH_2-PEG-FMOC and NH_2-PEG-SH.

1. Purify the silanized NPs by adding 90mL hexane and placing them flask on a strong magnet. Repeat this 3 times.
2. Dry the NPs (remove all hexane residues) by argon flow and then 30min vacuuming.
3. Disperse the NPs in ~7mL THF and sonicate for 15min. Usually the NPs should be well dispersed in THF.
4. Dissolve 170mg of PEG in 11mL THF. Use a 20ml glass vial and sonication. Make sure the polymer is fully dissolved. Larger molecular weights require longer sonication to dissolve.

Note: Thaw the PEG first before opening the vial and after using it, purge it with argon and store at -20°C.

5. Dissolve 80mg DCC in 320 µL THF.
6. Add DCC and PEG solutions to NPs solutions in the 125mL one-neck flask. Seal the flask using a rubber septum and zip-tie and purge the flask with argon for about 10min.
7. Sonicate the mixture for 16h.
8. Open the flask inside the fume hood and fill it with hexane and put it on a permanent magnet to precipitate the NPs.
9. Remove the supernatant and add 90mL hexane and repeat this purification step 2-3 times.
10. Finally remove all hexanes and dry the NPs using argon flow and then vacuuming for about 30-60min.

Note: Make sure all the hexane is removed. Otherwise, there will be issues for dispersing the NPs in aqueous phase (next steps).

11. Add 3-4mL of sodium bicarbonate buffer to dried NPs and sonicate them for 30-60min, depending on the batch.

12. Collect the NPs and transfer them to 1.5 centrifuge tubes.
13. Centrifuge at 5000 rcf for 15-30min (depending on the batch) to remove the aggregates. Collect the supernatant.
14. Filter the supernatant using 0.2 μL cellulose acetate filters and a 10mL syringe.
15. Prepare a PD-10 column packed with S-200 resin, equilibrated with sodium bicarbonate buffer.
16. Purify the NPs using the PD-10 columns.
17. Run DLS, Zeta potential, VSM, MPS and ICP to characterize the NPs.

E. Procedure for coating of nanoparticles with PMAO-PEG co-polymer

18. Choose a sample and follow standard purification procedure for 2 ml of sample.
    a. Be sure to weigh vial used for purification with or without cap.
8. After the last wash, close cap, puncture the cap with 2-3 16G needles and place vial in vacuum chamber for ~20-30 mins.
    a. Keep chamber on vacuum constantly in order to remove air and dry particles.
9. Once dried, remove vial and weigh in order to find mass of particles.
10. Disperse dried particles in chloroform (4ml chloroform for every 10 mg of particles).
    a. Sonicate for ~1hr. or until particles are fully dispersed in chloroform.
11. Weigh out 300 mg PMAO-PEG (at room temperature) for every 4 ml chloroform used in step 4. Measure identical amount of chloroform as used in step 4 in separate vial and dissolve PMAO-PEG into this vial.
12. Pipet PMAO-PEG chloroform solution into vial of particles. Sonicate combined solution for ~1 hr.
13. Add small magnetic stir bar to vial and place on magnetic stir plate overnight (~12 hrs.) at a speed ~8000 rpm.
    a. If particles are aggregating on magnet bar, additional PMAO-PEG may be needed
14. Remove magnet bar and transfer solution to 100 ml round bottom flask.
15. Rotovap at 33°C and 70 rpm for 90 minutes or until all chloroform is evaporated from particles (particles should be dried to the side of the flask).
16. Add 5ml TAE (10x) buffer to particles in flask. Sonicate for ~1hr.
17. Divide solution into 1.5 ml plastic vials and centrifuge
    a. Centrifuge at 8000 rcf for 1hr.

b. After centrifuging, collect and save supernatant and dispose of precipitates.
c. Filter particles through 200K filter using 5ml syringe to remove unbound PMAO-PEG.
d. Additional centrifuging time depends on particular particle batch. Centrifuge until DLS particle size is ~70nm and curve is monodispersed.
e. Before each additional centrifuging, sonicate and vortex 1.5 ml plastic vials with supernatant to fully disperse particles.

18. Once desired particle size is obtained, filter particles through PD-10 column.
19. If needed, concentrate particles using a 0.2 μm filter of cellulose acetate to desired concentration.
20. Run MPS and VSM.

F. Procedure for coating of the nanoparticles with PMAO and their functionalization with carboxyl groups

----------Purification of the NPs----------

1. Weigh out vial with or without cap but take note and keep same for future measurements.
2. Use glass pipet and take 2-3 aliquots of sample into weighed glass vial. Write down the NPs batch number/label.
3. Begin purification procedure
    a. Add a 1:2 ratio of Hexane and Ethyl Acetate to NPs (5 mL to 10 mL), sonicate for ~5-10 mins, then place the vials on magnet.
        i. **If solution isn't separating well after ~10 mins, add a variable volume of ethanol. When a milky white shade is seen near surface of solution then enough has been added. Amount of ethanol required to reach color is dependent on total volume in vial. Resonicate for 5-10 mins and place on magnet.**
    b. Discard supernatant after separation and add a 1:1 ratio of Hexane and Ethyl Acetate again (10mL to 10 mL), sonicate for ~10-20 mins, then place on magnet. Discard supernatant after separation.
    c. Repeat this procedure 2-3 more times using 1:1 ratio of Hexane and Acetone. More or less runs dependent on how well sample is separating and getting purified.
4. After final purification and discarding of supernatant, puncture cap of vial with 1-2, 16 gauge needles (purple color) and place in vacuum chamber of glove box for ~30mins/until dry.
5. Weigh dried out NP filled vials in same fashion as in step 1.
6. Calculate mass of NPs in vial and add chloroform in this way:

$$\frac{5\ mg\ NP}{2.5\ mL\ Chl} = \frac{found\ NP\ mass}{calculated\ vol\ Chl}$$

7. Sonicate to disperse NPs.
8. Note: when weighing out masses of NPs, be sure to have batches that add up to 10mg ±2mg. Otherwise, purify batches to get to such an amount as process currently doesn't have adequate repeatability in scales larger than 10 ± 2 mg of NP.

----------PMAO coating of the NPs----------

1. Now that you have the weight of the NPs, add PMAO to a new vial in a ratio of 50:1, PMAO to NP. Then add chloroform to this vial in a 1:100, chloroform to PMAO ratio. As an example, for 5 mg of NPs add ~250 mg PMAO dissolved in 2.5 mL Chloroform.
    a. Sonicate vial until PMAO is fully dissolved which will take anywhere from 10-30 mins. Observe solution to be sure so you don't wait too long.
2. Pour or pipet fully dissolved PMAO solution to vial containing dispersed NPs.
3. Sonicate the combined solution for an hour at ~55°C.
4. After sonication, use funnel and transfer solution to 250 mL round bottom flask. Again be sure that NP mass is around 10mg in your round bottom flask.
5. Place flask in rotary evaporator set to 40°C and 150 rpm. If water bath is above 40^{O}C it may be better, unknown at this point.
6. After 30-60mins have elapsed and all solution is evaporated and particles coating flask seem dry, use fume hood vacuum pump on the flask to ensure complete evaporation. Pump for ~1 hr.

----------NaOH----------

1. Create a 0.1M NaOH solution.
2. Use following ratio to determine amount of NaOH solution to add:
   $$\frac{1.67\ mg\ NP}{5\ mL\ NaOH} = \frac{total\ mass\ NP}{calculated\ vol\ NaOH}$$
3. Add the calculated amount of NaOH solution to round bottom flask containing dried NPs.
4. Sonicate this solution at ~57°C for 2-3 hours. For the initial time attempt to dislodge all dried, coated particles from flask wall. Once, dislodged leave in sonicator for remaining time.
5. After sonication, solution should be relatively clear. If solution is cloudy with a slightly milk colored layer then chloroform is still present and the batch is no good.
6. Take DLS and MPS to check quality of particles.

----------Final: purification of the functionalized NPs----------

1. Divide solution into 1.5 mL snap cap vials and centrifuge solution at 14.1 rcf for approximately 2-3 hours.
   a. Note that it may not take nearly as long. Check every 30-40 minutes.
2. Once supernatant is fully transparent remove vials and discard supernatant while retaining particles.
3. Add 0.5 mL deionized DIW to each vial, vortex and sonicate for 30 seconds to 1 minute to disperse particles then repeat this process for a total of 3 times.
4. After final centrifugation, disperse particles in 1 mL DIW and gather all solutions in a 40 mL glass vial and sonicate at 50-57°C the combined solution for 1 hour.
5. Filter the particles through 0.2 μm filter of cellulose acetate then run through PD-10.

    a. Medium for PD-10 filtration is DIW. Add ~40mL DIW to each column and let it pass through the column. Then add 2mL of nanoparticles solution and wait until all the nanoparticles solution enters the column. Then add another 40mL DIW and collect the nanoparticles droplets at the bottom. Finally add another 40mL of DIW to rinse the column and then close its top and bottom and keep it for next uses. Use new columns after 3-4 times of using them.

6. Gather eluted solution (nanoparticles) and run DLS. If DLS shows no aggregates then stop reading. The process is finished. If not, (most likely) then continue to step 7.
7. Divide solution amongst 1.5 mL vials. Centrifuge vials in 5-minute intervals at 3.0 rcf.
    a. When supernatant appears to be a copper to pale copper color then stop centrifuging, collect supernatant, and run DLS.
    b. If DLS shows aggregates in solution, then recentrifuge and test again until aggregates are no longer present.
8. Run MPS, Zeta Pot, and VSM once completely finished.

G. Effect of PEG molecular weight on MPS performance of the 25nm NPs

Samples Description:

Samples shown in Figures G.1, G.2, G.3 and G.4 were made by first coating the NPs (core size ~ 25-27nm) with PMAO (Appendix F) and then conjugating mPEG-NH_2 (MWs ranging from 3 to 40kDa) to the carboxyl groups of PMAO in chloroform. Note that we did not use NaOH to open the anhydride rings of the PMAO, since anhydride rings can react with primary amine groups in organic phases such as chloroform.[48] All these samples showed a negative surface charge after phase transfer to water. The sample shown in Figure G.5 was made by direct using of PMAO-PEG (20kDa) co-polymer using our conventional phase transfer method (Appendix E). Our zeta potential measurements showed that these NPs had a neutral charge on their surface.

As-synthesized NPs were purified and then coated with PMAO as the first step. For each 5mg of the dried and purified NPs, we used 250mg PMAO powder. We did the coating in chloroform (~1ml chloroform per 10mg of dried NPs). Then, PMAO coated NPs were purified and for each 5mg of the original NPs, 333mg of the mPEG-NH_2 was added to PMAO-coated NPs dispersed in chloroform (~1mL). The mixture was sonicated at room temperature for 16 hours. At the end the chloroform phase was evaporated using a rotary evaporator and dried NPs were dispersed in water. The un-reacted PEG molecules were purified by centrifuge and filtering (0.2μm Nylon syringe filters).

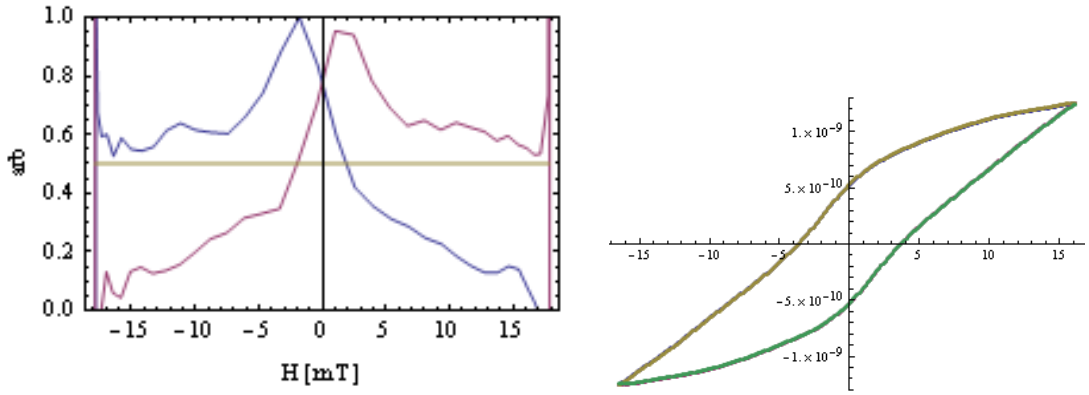

Fig. G1. MPS dm/dH graph (left) and m-H graph (right, generated by integration of the dm/dH graph) of the NPs after conjugation of mPEG-NH_2 with molecular weight of 3kDa to PMAO coated NPs and their transfer to water. The dm/dH graph is normalized to one. The hydrodynamic size and zeta potential of these NPs were 80-100nm and -30mV, respectively.

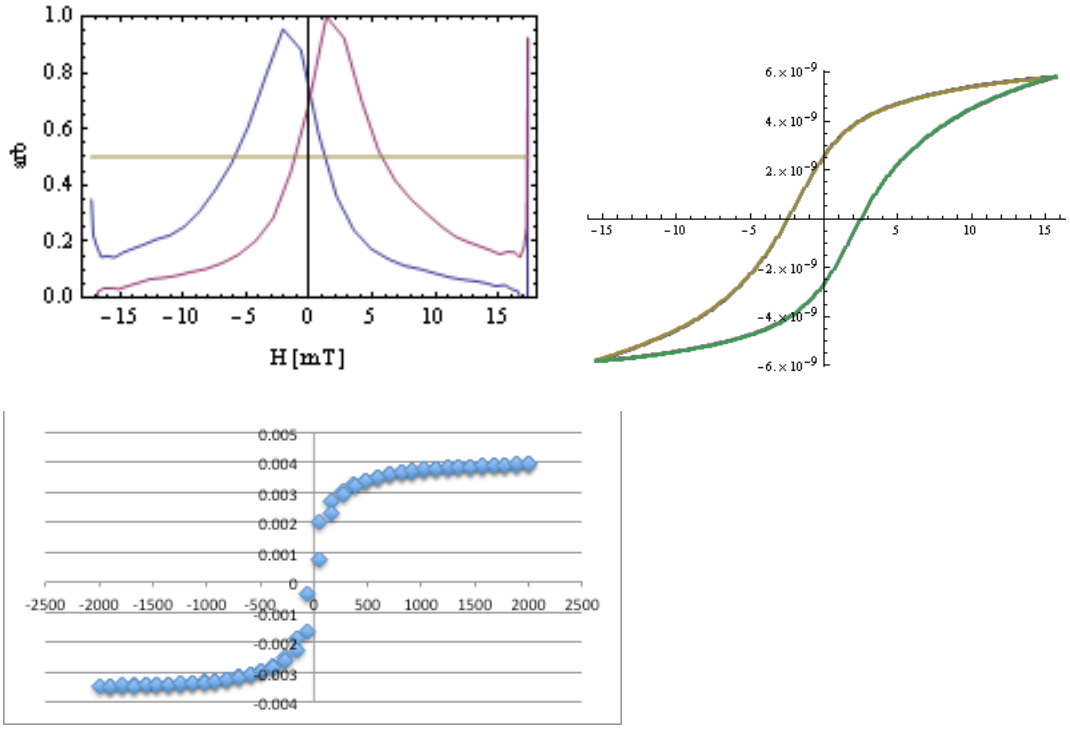

Fig. G2. MPS dm/dH graph (left) and m-H graph (right, generated by integration of the dm/dH graph) of the NPs after conjugation of mPEG-NH_2 (MW~ 20kDa) to PMAO coated NPs and their transfer to water. The dm/dH graph is normalized to one. m-H graph (dotted graph) of the NPs measured by VSM is also shown for comparison. The hydrodynamic size and zeta potential of these NPs were 69nm and -37.5mV, respectively.

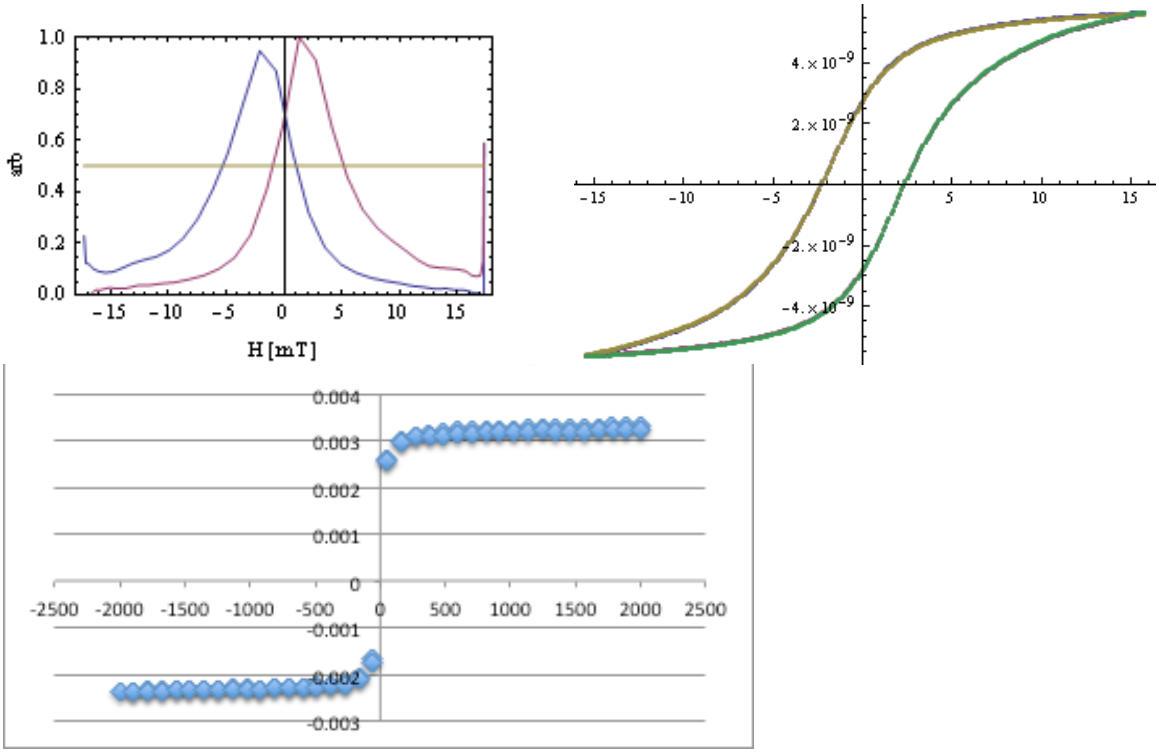

Fig. G3. MPS dm/dH graph (left) and m-H graph (right, generated by integration of the dm/dH graph) of the NPs after conjugation of mPEG-NH_2 (MW~ 30kDa) to PMAO coated NPs and their transfer to water. The dm/dH graph is normalized to one. m-H graph (dotted graph) of the NPs measured by VSM is also shown for comparison. The hydrodynamic size and zeta potential of these NPs were 47nm and -48.7mV, respectively.

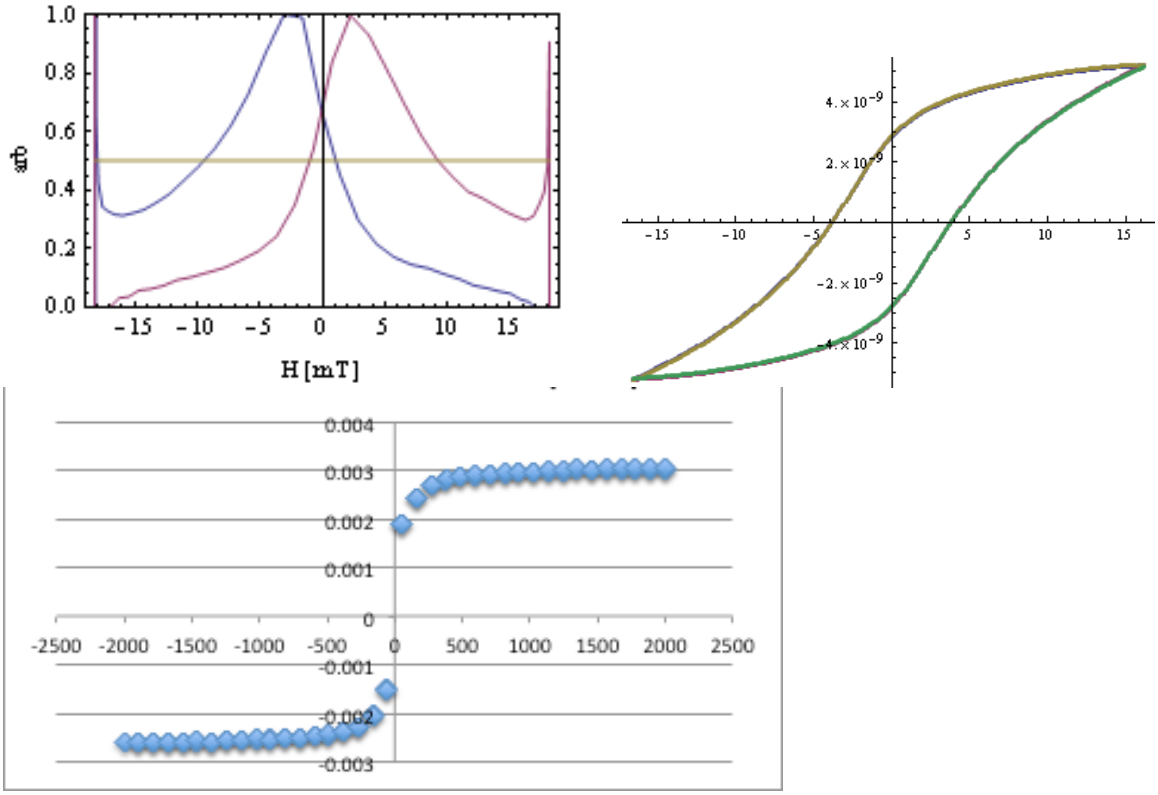

Fig. G4. MPS dm/dH graph (left) and m-H graph (right, generated by integration of the dm/dH graph) of the NPs after conjugation of mPEG-NH_2 (MW~ 40kDa) to PMAO coated NPs and their transfer to water. The dm/dH graph is normalized to one. m-H graph (dotted graph) of the NPs measured by VSM is also shown for comparison. The hydrodynamic size and zeta potential of these NPs were 70nm and -45mV, respectively.

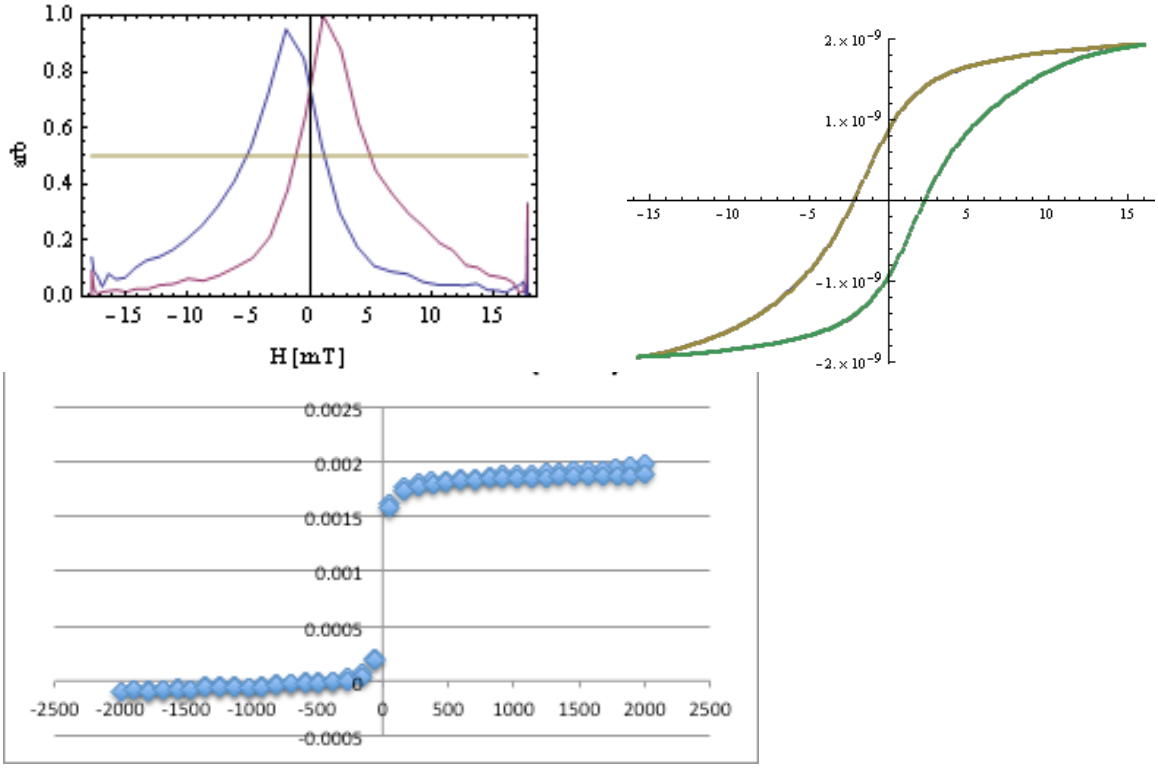

Fig. G5. MPS dm/dH graph (left) and m-H graph (right, generated by integration of the dm/dH graph) of the NPs after their coating with a co-polymer of PMAO-PEG (20kDa) are shown here for comparison with two-steps conjugation results shown in previous figures. The dm/dH graph is normalized to one. m-H graph (dotted graph) of the NPs measured by VSM is also shown. The hydrodynamic size and zeta potential of these NPs were 70-80nm and -3mV, respectively.

PEG Molecular Weight (kDa)	Hydrodynamic size (nm)	Zeta Potential (mV)	Calculated VSM core size (nm)	MPS FWHM (20mT, 25KHz)
3	80-110	-	-	very large
20	69	-37.5	-	~7
30	47	-48.7	23.1	~7
40	70	-45	19.92	~11
PMAO-PEG Co-polymer (20kDa)	70-80	Neutral	22.2nm	~7

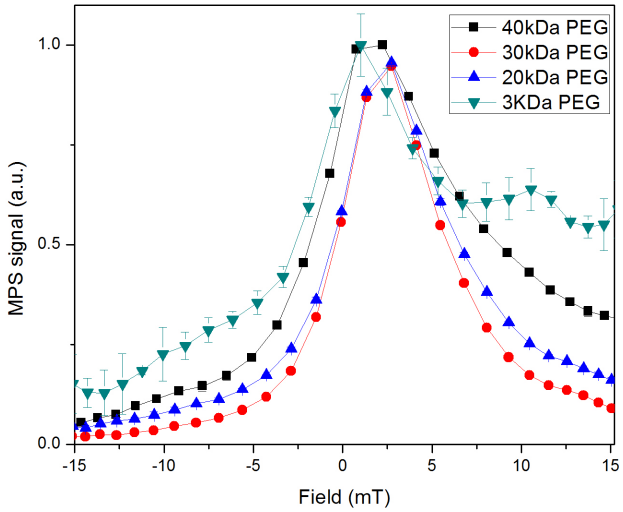

Fig. G6. Summary of the results shown in previous figures. Table shows the molecular weight and coating type of the NPs, their hydrodynamic sizes, zeta potentials, core sizes calculated from their VSM graphs and FWHM of their dm/dH graphs. Note that the NPs coated with 3kDa PEG were not stable and therefore, we were not able to measure their hydrodynamic size and zeta potential values. The lower graph shows the dm/dH graphs of all these NPs formulations after normalization to one.

20 and 30KDa PEGs seem to give the narrowest MPS signal, which means highest spatial resolutions. The data for 20 and 30KDa PEG are almost similar, however, 20KDa PEG is more cost-effective and dissolves in solvents easier. Smaller molecular weights of PEG are not effectively stabilizing the NPs in the presence of field during the MPS or MPI measurements, resulting in aggregations during the measurements and generating poor MPS signal. 40KDa PEG on the other hand results in increasing the FWHM of the MPS graphs, possibly due to its effects of relaxation mechanism (Neel or Brownian) of the NPs during the MPS and MPI measurements.

H. Quantification of the accessible primary amine groups on the surface of the iron oxide nanoparticles (SPDP assay)

List of Materials:

Amine-functionalized Fe_3O_4 Nanoparticles, Boric Acid Buffer (0.1 M, pH = 7.4), De-ionized Water, Dimethyl Sulfoxide (DMSO), Sodium Bicarbonate Buffer (0.1 M, pH = 8.5), N-Succinimidyl 3-(2-pyridyldithio)propionate (SPDP), Tris-(Carboxyethyl)phosphine hydrochloride (TCEP)

Procedure:

1- Adjust the concentration of the NPs to ~2.85mg Fe/mL. Total amount of the iron needed for this assay is ~2mg Fe.
2- Dissolve ~4.3 mg SPDP in 150 µL anhydrous DMSO (B).
3- Add the SPDP solution to nanoparticles solution using a pipette.
4- Shake the mixture at room temperature for about 2h.
5- During this time prepare a PD-10 column equilibrated with boric acid buffer.
6- Purify the nanoparticles-SPDP mixture using PD-10 columns.
7- Make an ICP sample. Iron concentration will be needed for later calculations.
8- In a separate vial dissolve ~72mg TCEP in 0.5mL boric acid buffer. Make sure it is fully dissolved.
9- Add 125 µL of TCEP solution to 1.125mL of purified SPDP-functionalized nanoparticles solution.
10- Let this mixture shaking for 30min.
11- Keep a part of this TCEP solution as blank sample, which will be needed later during this assay.
12- Transfer 0.5mL of the nanoparticles-TCEP mixture to an amicon centrifugal vial (MWCO 100kDa) and centrifuge this at 10,000 for about 10min. This will separate pyridine-2-thione (P2T).
13- Add 0.4mL of the boric acid buffer to 0.4mL of the P2T solution and vortex.

14- Measure the UV-vis absorbance spectra.

15- Record the absorbance at 343 and 415nm.

16- Use this equation to calculate the correct absorbance at 343nm:

$$\Delta A_{343} = 2 \times (A_{343} - A_{415})$$

17- Calculate the P2T concentration using 8080cm^{-1}, as the extinction co-efficient.

18- Comparing this with blank sample, calculate the amount of nmol amine groups per milligram of the nanoparticles. Note that iron concentration should be calculated using the ICP results.

19- Now, knowing the nanoparticles diameter and using density of bulk magnetite, calculate the average number of amine groups per nanoparticle.

I. Conjugation of Cy5.5-NHS NIRF molecules to amine functionalized NPs

1- Dissolve ~1mg of Cy5.5 in 1 mL dimethyl sulphoxide (DMSO) or dimethylformamide (DMF). A blue color solution forms.
2- Add the dye solution to the degassed aqueous solutions of the NPs (5mg).
3- Wrap the vials with aluminum foil and shake them at room temperature overnight.
4- Purify the labeled NPs using PD-10 columns to remove the un-reacted dye molecules.

J. Culture of the cells

Note: cell culture medium is DMEM or EMEM enriched with 10% FBS. This can be different for each cell line and the following procedure is the general protocol.

1- Thaw the cells using water bath.
2- Add 5mL cell culture medium to a 15mL centrifuge tube.
3- Using a pipette, transfer the cells solution to this centrifuge tube.
4- Centrifuge at 1000 rpm for 5 min to precipitate the cells.
5- Remove the supernatant and add 5 mL cell culture medium and pipette several times to disperse the cells (solution A).
6- Add 10mL cell culture medium to a 75mL Corning flask.
7- Add 1mL of the solution A to this flask. Pipette up and down several times to disperse the cells. Shake the flask to distribute the cells and gently place the flask inside the incubator.
8- Check the cells using the optical microscope before and after incubation.
9- Check the cells growth and confluency 1-3 days after incubation.
10- Depending on the number of the cells, change the media every 3-5 days. Check the color of the media and cells and do this when needed.
11- Remove the old cell culture medium and discard it.
12- Gently add 10ml PBS to flask and shake it slowly and then remove the PBS using pipettes.
13- Add fresh cell culture medium, check the cells using optical microscope and incubate the cells.

References

[1] B. Gleich, J. Weizenecker, Tomographic imaging using the nonlinear response of magnetic particles, Nature, 435 (2005) 1214-1217.

[2] B. Gleich, J. Weizenecker, J. Borgert, Experimental results on fast 2D-encoded magnetic particle imaging, Physics in Medicine and Biology, 53 (2008) N81-N84.

[3] J. Park, A. Estrada, J.A. Schwartz, P. Diagaradjane, S. Krishnan, A.K. Dunn, J.W. Tunnell, Intra-Organ Biodistribution of Gold Nanoparticles Using Intrinsic Two-Photon-Induced Photoluminescence, Lasers in Surgery and Medicine, 42 (2010) 630-639.

[4] J.W.M. Bulte, P. Walczak, B. Gleich, J. Weizenecker, D.E. Markov, H.C.J. Aerts, H. Boeve, J. Borgert, M. Kuhn, MPI cell tracking: what can we learn from MRI?, Proc. Soc. Photo. Opt. Instrum. Eng., 7965 (2011) 79650Z.

[5] S.M.C. Berman, P. Walczak, J.W.M. Bulte, Tracking stem cells using magnetic nanoparticles, Wiley Interdisciplinary Reviews-Nanomedicine and Nanobiotechnology, 3 (2011) 343-355.

[6] J. Weizenecker, B. Gleich, J. Rahmer, H. Dahnke, J. Borgert, Three-dimensional real-time in vivo magnetic particle imaging, Physics in Medicine and Biology, 54 (2009) L1-L10.

[7] P.W. Goodwill, E.U. Saritas, L.R. Croft, T.N. Kim, K.M. Krishnan, D.V. Schaffer, S.M. Conolly, X-Space MPI: Magnetic Nanoparticles for Safe Medical Imaging, Advanced Materials, 24 (2012) 3870-3877.

[8] P. Goodwill, M. Ferguson, E. Yu, B. Zheng, K. Lu, A. Khandhar, S. Kemp, K. Krishnan, S. Conolly, In vivo perfusion imaging using magnetic particle imaging, Journal of NeuroInterventional Surgery, 7 (2015) A105-A105.

[9] R.M. Ferguson, A.P. Khandhar, S.J. Kemp, H. Arami, E.U. Saritas, L.R. Croft, J. Konkle, P.W. Goodwill, A. Halkola, J. Rahmer, J. Borgert, S.M. Conolly, K.M. Krishnan, Magnetic Particle Imaging With Tailored Iron Oxide Nanoparticle Tracers, IEEE Transactions on Medical Imaging, 34 (2015) 1077-1084.

[10] A.P. Khandhar, R.M. Ferguson, H. Arami, K.M. Krishnan, Monodisperse magnetite nanoparticle tracers for in vivo magnetic particle imaging, Biomaterials, 34 (2013) 3837-3845.

[11] P.W. Goodwill, S.M. Conolly, Multidimensional X-Space Magnetic Particle Imaging, IEEE Transactions on Medical Imaging, 30 (2011) 1581-1590.

[12] R.M. Ferguson, Tracer design for Magnetic Particle Imaging: modeling, synthesis, and experimental optimization of biocompatible iron oxide nanoparticles, in: Materials Science and Engineering, University of Washington, Seattle, 2011.

[13] R.M. Ferguson, K.R. Minard, K.M. Krishnan, Optimization of nanoparticle core size for magnetic particle imaging, Journal of Magnetism and Magnetic Materials, 321 (2009) 1548-1551.

[14] J. Rahmer, J. Weizenecker, B. Gleich, J. Borgert, Signal encoding in magnetic particle imaging: properties of the system function, BMC Medical Imaging, 9 (2009) 1-21.

[15] P.W. Goodwill, S.M. Conolly, The X-Space Formulation of the Magnetic Particle Imaging Process: 1-D Signal, Resolution, Bandwidth, SNR, SAR, and Magnetostimulation, IEEE Transactions on Medical Imaging, 29 (2010) 1851-1859.

[16] R.M. Ferguson, A.P. Khandhar, K.M. Krishnan, Tracer design for magnetic particle imaging, Journal of Applied Physics, 111 (2012) 07B318.

[17] H. Arami, K.M. Krishnan, Highly Stable Amine Functionalized Iron Oxide Nanoparticles Designed for Magnetic Particle Imaging (MPI), IEEE Transactions on Magnetics, 49 (2013).

[18] R.M. Ferguson, A. Khandhar, H. Arami, L. Hua, O. Hovorka, K.M. Krishnan, Tailoring the magnetic and pharmacokinetic properties of iron oxide MPI tracers, Biomedical Engineering (Biomedizinische Technik), (2013) 1-15.

[19] P.W. Goodwill, A. Tamrazian, L.R. Croft, C.D. Lu, E.M. Johnson, R. Pidaparthi, R.M. Ferguson, A.P. Khandhar, K.M. Krishnan, S.M. Conolly, Ferrohydrodynamic relaxometry for magnetic particle imaging, Applied Physics Letters, 98 (2011) 262502.

[20] S. Biederer, T.F. Sattel, T. Knopp, M. Erbe, K. Lüdtke-Buzug, F.M. Vogt, J. Barkhausen, T.M. Buzug, A spectrometer to measure the usability of nanoparticles for magnetic particle imaging, in: T.M. Buzug, J. Borgert, T. Knopp, S. Biederer, T.F. Sattel, M. Erbe, K. Lüdtke-Buzug (Eds.) Magnetic Particle Imaging, World Scientific, Germany, 2010, pp. 66–72.

[21] K.M. Krishnan, Biomedical Nanomagnetics: A Spin Through Possibilities in Imaging, Diagnostics, and Therapy, IEEE Transactions on Magnetics, 46 (2010) 2523-2558.

[22] H. Arami, Z. Stephen, O. Veiseh, M. Zhang, Chitosan-Coated Iron Oxide Nanoparticles for Molecular Imaging and Drug Delivery, Advances in Polymer Science, 243 (2011) 163-184.

[23] A. Singh, T. Patel, J. Hertel, M. Bernardo, A. Kausz, L. Brenner, Safety of Ferumoxytol in Patients With Anemia and CKD, American Journal of Kidney Diseases, 52 (2008) 907-915.

[24] M. Gonzales, L.M. Mitsumori, J.V. Kushleika, M.E. Rosenfeld, K.M. Krishnan, Cytotoxicity of iron oxide nanoparticles made from the thermal decomposition of organometallics and aqueous phase transfer with Pluronic F127, Contrast Media & Molecular Imaging, 5 (2010) 286-293.

[25] M. Mahmoudi, H. Hofmann, B. Rothen-Rutishauser, A. Petri-Fink, Assessing the In Vitro and In Vivo Toxicity of Superparamagnetic Iron Oxide Nanoparticles, Chemical Reviews, 112 (2011) 2323-2338.

[26] I.A. Zaliznyak, Spin Structures and Spin Wave Excitations, in: Handbook of Magnetism and Advanced Magnetic Materials, Wiley, 2007.

[27] K.M. Krishnan, A.B. Pakhomov, Y. Bao, P. Blomqvist, Y. Chun, M. Gonzales, K. Griffin, X. Ji, B.K. Roberts, Nanomagnetism and spin electronics: materials, microstructure and novel properties, Journal of Materials Science, 41 (2006) 793-815.

[28] J.E. Rosen, L. Chan, D.B. Shieh, F.X. Gu, Iron oxide nanoparticles for targeted cancer imaging and diagnostics, Nanomedicine-Nanotechnology Biology and Medicine, 8 (2012) 275-290.

[29] M.A. McAteer, A.M. Akhtar, C. von zur Muhlen, R.P. Choudhury, An approach to molecular imaging of atherosclerosis, thrombosis, and vascular inflammation using microparticles of iron oxide, Atherosclerosis, 209 (2010) 18-27.

[30] F.M. Kievit, O. Veiseh, N. Bhattarai, C. Fang, J.W. Gunn, D. Lee, R.G. Ellenbogen, J.M. Olson, M.Q. Zhang, PEI-PEG-Chitosan-Copolymer-Coated Iron Oxide Nanoparticles for Safe Gene Delivery: Synthesis, Complexation, and Transfection, Advanced Functional Materials, 19 (2009) 2244-2251.

[31] H.Y. Xu, Z.P. Aguilar, L. Yang, M. Kuang, H.W. Duan, Y.H. Xiong, H. Wei, A. Wang, Antibody conjugated magnetic iron oxide nanoparticles for cancer cell separation in fresh whole blood, Biomaterials, 32 (2011) 9758-9765.

[32] M. Lu, M.H. Cohen, D. Rieves, R. Pazdur, FDA report: Ferumoxytol for intravenous iron therapy in adult patients with chronic kidney disease, American Journal of Hematology, 85 (2010) 315-319.

[33] N. Khlebtsov, L. Dykman, Biodistribution and toxicity of engineered gold nanoparticles: a review of in vitro and in vivo studies, Chemical Society Reviews, 40 (2011) 1647-1671.

[34] A. Albanese, P.S. Tang, W.C.W. Chan, The Effect of Nanoparticle Size, Shape, and Surface Chemistry on Biological Systems, Annual Review of Biomedical Engineering, 14 (2012) 1-16.

[35] O. Veiseh, J.W. Gunn, M. Zhang, Design and fabrication of magnetic nanoparticles for targeted drug delivery and imaging, Adv Drug Deliv Rev, 62 (2010) 284-304.

[36] K.E. Sapsford, W.R. Algar, L. Berti, K.B. Gemmill, B.J. Casey, E. Oh, M.H. Stewart, I.L. Medintz, Functionalizing Nanoparticles with Biological Molecules: Developing Chemistries that Facilitate Nanotechnology, Chemical Reviews, 113 (2013) 1904-2074.

[37] F.M. Kievit, M.Q. Zhang, Surface Engineering of Iron Oxide Nanoparticies for Targeted Cancer Therapy, Accounts of Chemical Research, 44 (2011) 853-862.

[38] S. Laurent, J.L. Bridot, L.V. Elst, R.N. Muller, Magnetic iron oxide nanoparticles for biomedical applications, Future Medicinal Chemistry, 2 (2010) 427-449.

[39] C. Tassa, S.Y. Shaw, R. Weissleder, Dextran-Coated Iron Oxide Nanoparticles: A Versatile Platform for Targeted Molecular Imaging, Molecular Diagnostics, and Therapy, Accounts of Chemical Research, 44 (2011) 842-852.

[40] A.J. Cole, A.E. David, J.X. Wang, C.J. Galban, H.L. Hill, V.C. Yang, Polyethylene glycol modified, cross-linked starch-coated iron oxide nanoparticles for enhanced magnetic tumor targeting, Biomaterials, 32 (2011) 2183-2193.

[41] M. Auerbach, J.A. Pappadakis, H. Bahrain, S.A. Auerbach, H. Ballard, N.V. Dahl, Safety and efficacy of rapidly administered (one hour) one gram of low molecular weight iron dextran (INFeD) for the treatment of iron deficient anemia, American Journal of Hematology, 86 (2011) 860-862.

[42] H. Arami, R.M. Ferguson, A.P. Khandhar, K.M. Krishnan, Size-dependent ferrohydrodynamic relaxometry of magnetic particle imaging tracers in different environments, Medical Physics, 40 (2013).

[43] B.H. Kim, N. Lee, H. Kim, K. An, Y.I. Park, Y. Choi, K. Shin, Y. Lee, S.G. Kwon, H.B. Na, J.-G. Park, T.-Y. Ahn, Y.-W. Kim, W.K. Moon, S.H. Choi, T. Hyeon, Large-Scale Synthesis of Uniform and Extremely Small-Sized Iron Oxide Nanoparticles for High-Resolution T1 Magnetic Resonance Imaging Contrast Agents, Journal Of The American Chemical Society, 133 (2011) 12624-12631.

[44] M. Gould, R.J. Barbour, N. Thomas, H. Arami, K.M. Krishnan, K.-M.C. Fu, Room-temperature detection of a single 19 nm super-paramagnetic nanoparticle with an imaging magnetometer, Applied Physics Letters, 105 (2014).

[45] R. Hufschmid, H. Arami, R.M. Ferguson, M. Gonzales, E. Teeman, L.N. Brush, N.D. Browning, K.M. Krishnan, Synthesis of phase-pure and monodisperse iron oxide nanoparticles by thermal decomposition, Nanoscale, 7 (2015) 11142-11154.

[46] J. Park, K.J. An, Y.S. Hwang, J.G. Park, H.J. Noh, J.Y. Kim, J.H. Park, N.M. Hwang, T. Hyeon, Ultra-large-scale syntheses of monodisperse nanocrystals, Nature Materials, 3 (2004) 891-895.

[47] W.W. Yu, J.C. Falkner, C.T. Yavuz, V.L. Colvin, Synthesis of monodisperse iron oxide nanocrystals by thermal decomposition of iron carboxylate salts, Chemical Communications, (2004) 2306-2307.

[48] W.W. Yu, E. Chang, C.M. Sayes, R. Drezek, V.L. Colvin, Aqueous dispersion of monodisperse magnetic iron oxide nanocrystals through phase transfer, Nanotechnology, 17 (2006) 4483-4487.

[49] R. Weissleder, G. Elizondo, J. Wittenberg, C.A. Rabito, H.H. Bengele, L. Josephson, Ultrasmall superparamagnetic iron-oxide- Characterization of a new class of contrast agents for MR imaging, Radiology, 175 (1990) 489-493.

[50] C. Chambon, O. Clement, A. Leblanche, E. Schoumanclaeys, G. Frija, Superparamagnetic iron-oxides as positive MR contrast agents- In vitro and in vivo evidence, Magnetic Resonance Imaging, 11 (1993) 509-519.

[51] E.X. Wu, H.Y. Tang, J.H. Jensen, Applications of ultrasmall superparamagnetic iron oxide contrast agents in the MR study of animal models, NMR in Biomedicine, 17 (2004) 478-483.

[52] M.E. Kooi, V.C. Cappendijk, K. Cleutjens, A.G.H. Kessels, P. Kitslaar, M. Borgers, P.M. Frederik, M. Daemen, J.M.A. van Engelshoven, Accumulation of ultrasmall superparamagnetic particles of iron oxide in human atherosclerotic plaques can be detected by in vivo magnetic resonance imaging, Circulation, 107 (2003) 2453-2458.

[53] M. Beaumont, B. Lemasson, R. Farion, C. Segebarth, C. Remy, E.L. Barbier, Characterization of tumor angiogenesis in rat brain using iron-based vessel size index MRI in combination with gadolinium-based dynamic contrast-enhanced MRI, Journal of Cerebral Blood Flow and Metabolism, 29 (2009) 1714-1726.

[54] N. Beckmann, C. Cannet, A.L. Babin, F.X. Ble, S. Zurbruegg, R. Kneuer, V. Dousset, In vivo visualization of macrophage infiltration and activity in inflammation using magnetic resonance imaging, Wiley Interdisciplinary Reviews-Nanomedicine and Nanobiotechnology, 1 (2009) 272-298.

[55] R. Weissleder, A. Bogdanov, E.A. Neuwelt, M. Papisov, Long-circulating iron-oxides for MR-imaging, Advanced Drug Delivery Reviews, 16 (1995) 321-334.

[56] K. Lee, C. Cheong, K.S. Hong, E.K. Koh, M. Kim, H.S. Shin, Y.N. Kim, S.H. Lee, Blood Half-Life Study of Magnetic Fluorescent Silica Nanoparticles by Using MR T2

Relaxation Measurement: Long Circulating SPIO, Journal of the Korean Physical Society, 53 (2008) 2535-2539.

[57] H.W. Yang, M.Y. Hua, H.L. Liu, C.Y. Huang, R.Y. Tsai, Y.J. Lu, J.Y. Chen, H.J. Tang, H.Y. Hsien, Y.S. Chang, T.C. Yen, P.Y. Chen, K.C. Wei, Self-protecting core-shell magnetic nanoparticles for targeted, traceable, long half-life delivery of BCNU to gliomas, Biomaterials, 32 (2011) 6523-6532.

[58] M. Taupitz, S. Wagner, J. Schnorr, I. Kravec, H. Pilgrimm, H. Bergmann-Fritsch, B. Hamm, Phase I clinical evaluation of citrate-coated monocrystalline very small superparamagnetic iron oxide particles as a new contrast medium for magnetic resonance imaging, Investigative Radiology, 39 (2004) 394-405.

[59] S.J. McLachlan, M.R. Morris, M.A. Lucas, R.A. Fisco, M.N. Eakins, D.R. Fowler, R.B. Scheetz, A.Y. Olukotun, PHASE-I CLINICAL-EVALUATION OF A NEW IRON-OXIDE MR CONTRAST AGENT, Jmri-Journal of Magnetic Resonance Imaging, 4 (1994) 301-307.

[60] C.D. Constantinides, J. Rogers, D.A. Herzka, F.E. Boada, D. Bolar, D. Kraitchman, J. Gillen, P.A. Bottomley, Superparamagnetic iron oxide MION as a contrast agent for sodium MRI in myocardial infarction, Magnetic Resonance in Medicine, 46 (2001) 1164-1168.

[61] F.Q. Zhao, M. Williams, X. Meng, D.C. Welsh, A. Coimbra, E.D. Crown, J.J. Cook, M.O. Urban, R. Hargreaves, D.S. Williams, BOLD and blood volume-weighted fMRI of rat lumbar spinal cord during non-noxious and noxious electrical hindpaw stimulation, Neuroimage, 40 (2008) 133-147.

[62] M. Sigovan, L. Boussel, A. Sulaiman, D. Sappey-Marinier, H. Alsaid, C. Desbleds-Mansard, D. Ibarrola, D. Gamondes, C. Corot, E. Lancelot, J.S. Raynaud, V. Vives, C. Lacledere, X. Violas, P.C. Douek, E. Canet-Soulas, Rapid-Clearance Iron Nanoparticles for Inflammation Imaging of Atherosclerotic Plaque: Initial Experience in Animal Model, Radiology, 252 (2009) 401-409.

[63] M. Sigovan, A. Bessaad, H. Alsaid, E. Lancelot, C. Corot, B. Neyran, N. Provost, Z. Majd, M. Breisse, E. Canet-Soulas, Assessment of Age Modulated Vascular Inflammation in ApoE(-/-) Mice by USPIO-Enhanced Magnetic Resonance Imaging, Investigative Radiology, 45 (2010) 702-707.

[64] R. Sigal, T. Vogl, J. Casselman, G. Moulin, F. Veillon, R. Hermans, F. Dubrulle, J. Viala, J. Bosq, M. Mack, M. Depondt, C. Mattelaer, P. Petit, P. Champsaur, S. Reihm, Y. Dadashitazehozi, T. de Jaegere, G. Marchal, D. Chevalier, L. Lemaitre, C. Kubiak, R. Helmberger, P. Halimi, Lymph node metastases from head and neck squamous cell carcinoma: MR imaging with ultrasmall superparamagnetic iron oxide particles (Sinerem MR) - results of a phase-III multicenter clinical trial, European Radiology, 12 (2002) 1104-1113.

[65] H.H. Bengele, S. Palmacci, J. Rogers, C.W. Jung, J. Crenshaw, L. Josephson, BIODISTRIBUTION OF AN ULTRASMALL SUPERPARAMAGNETIC IRON-OXIDE COLLOID, BMS-180549, BY DIFFERENT ROUTES OF ADMINISTRATION, Magnetic Resonance Imaging, 12 (1994) 433-442.

[66] O. Clément, N. Siauve, C.A. Cuénod, G. Frija, Liver imaging with ferumoxides (Feridex): fundamentals, controversies, and practical aspects, Topics in Magnetic Resonance Imaging, 9 (1998) 167-182.

[67] K.C. Briley-Saebo, V. Mani, F. Hyafil, J.-C. Cornily, Z.A. Fayad, Fractionated Feridex and positive contrast: In vivo MR imaging of atherosclerosis, Magnetic Resonance in Medicine, 59 (2008) 721-730.

[68] D. Simberg, J.H. Park, P.P. Karmali, W.M. Zhang, S. Merkulov, K. McCrae, S.N. Bhatia, M. Sailor, E. Ruoslahti, Differential proteomics analysis of the surface heterogeneity of dextran iron oxide nanoparticles and the implications for their in vivo clearance, Biomaterials, 30 (2009) 3926-3933.

[69] C. Chapon, F. Franconi, L. Lemaire, L. Marescaux, P. Legras, J.P. Saint-Andre, B. Denizot, J.J. Le Jeune, High field magnetic resonance imaging evaluation of superparamagnetic iron oxide nanoparticles in a permanent rat myocardial infarction, Investigative Radiology, 38 (2003) 141-146.

[70] V. Rousseau, D. Pouliquen, F. Darcel, P. Jallet, J.J. Le Jeune, NMR investigation of experimental chemical induced brain tumors in rats, potential of a superparamagnetic contrast agent (MD3) to improve diagnosis, Magnetic Resonance Materials in Physics Biology and Medicine, 6 (1998) 13-21.

[71] B.B. Frericks, F. Wacker, C. Loddenkemper, S. Valdeig, B. Hotz, K.J. Wolf, B. Misselwitz, A. Kuhl, J.C. Hoffmann, Magnetic Resonance Imaging of Experimental Inflammatory Bowel Disease Quantitative and Qualitative Analyses With Histopathologic Correlation in a Rat Model Using the Ultrasmall Iron Oxide SHU 555 C, Investigative Radiology, 44 (2009) 23-30.

[72] G.H. Simon, J. von Vopelius-Feldt, Y.J. Fu, J. Schlegel, G. Pinotek, M.F. Wendland, M.H. Chen, H.E. Daldrup-Link, Ultrasmall supraparamagnetic iron oxide-enhanced magnetic resonance imaging of antigen-induced arthritis - A comparative study

between SHUSSSC, ferumoxtran-10, and ferumoxytol, Investigative Radiology, 41 (2006) 45-51.

[73] K. Lind, M. Kresse, N.P. Debus, R.H. Muller, A novel formulation for superparamagnetic iron oxide (SPIO) particles enhancing MR lymphography: Comparison of physicochemical properties and the in vivo behaviour, Journal of Drug Targeting, 10 (2002) 221-230.

[74] S.A. Schmitz, S.E. Coupland, R. Gust, S. Winterhalter, S. Wagner, M. Kresse, W. Semmler, K.J. Wolf, Superparamagnetic iron oxide-enhanced MRI of atherosclerotic plaques in Watanabe hereditable hyperlipidemic rabbits, Investigative Radiology, 35 (2000) 460-471.

[75] W. Li, S. Tutton, A.T. Vu, L. Pierchala, B.S.Y. Li, J.M. Lewis, P.V. Prasad, R.R. Edelman, First-pass contrast-enhanced magnetic resonance angiography in humans using ferumoxytol, a novel ultrasmall superparamagnetic iron oxide (USPIO)-based blood pool agent, Journal of Magnetic Resonance Imaging, 21 (2005) 46-52.

[76] B. Tomanek, U. Iqbal, B. Blasiak, A. Abulrob, H. Albaghdadi, J.R. Matyas, D. Ponjevic, G.R. Sutherland, Evaluation of brain tumor vessels specific contrast agents for glioblastoma imaging, Neuro-Oncology, 14 (2012) 53-63.

[77] J.-H. Park, G. von Maltzahn, L. Zhang, A.M. Derfus, D. Simberg, T.J. Harris, E. Ruoslahti, S.N. Bhatia, M.J. Sailor, Systematic Surface Engineering of Magnetic Nanoworms for in vivo Tumor Targeting, Small, 5 (2009) 694-700.

[78] J. Hamzah, V.R. Kotamraju, J.W. Seo, L. Agemy, V. Fogal, L.M. Mahakian, D. Peters, L. Roth, M.K.J. Gagnon, K.W. Ferrara, E. Ruoslahti, Specific penetration and accumulation of a homing peptide within atherosclerotic plaques of apolipoprotein

E-deficient mice, Proceedings of the National Academy of Sciences of the United States of America, 108 (2011) 7154-7159.

[79] G. Wang, S. Inturi, N.J. Serkova, S. Merkulov, K. McCrae, S.E. Russek, N.K. Banda, D. Simberg, High-Relaxivity Superparamagnetic Iron Oxide Nanoworms with Decreased Immune Recognition and Long-Circulating Properties, Acs Nano, 8 (2014) 12437-12449.

[80] C. Nolte-Ernsting, G. Adam, A. Bucker, S. Berges, A. Bjornerud, R.W. Gunther, Abdominal MR angiography performed using blood pool contrast agents: Comparison of a new superparamagnetic iron oxide nanoparticle and a linear gadolinium polymer, American Journal of Roentgenology, 171 (1998) 107-113.

[81] R. Bachmann, R. Conrad, B. Kreft, O. Luzar, W. Block, S. Flacke, D. Pauleit, F. Traber, J. Gieseke, K. Saebo, H. Schild, Evaluation of a new ultrasmall superparamagnetic iron oxide contrast agent Clariscan (R), (NC100150) for MRI of renal perfusion: Experimental study in an animal model, Journal of Magnetic Resonance Imaging, 16 (2002) 190-195.

[82] D. Weishaupt, P.R. Hilfiker, M. Schmidt, J.F. Debatin, Pulmonary hemorrhage: Imaging with a new magnetic resonance blood pool agent in conjunction with breathheld three-dimensional magnetic resonance angiography, Cardiovascular and Interventional Radiology, 22 (1999) 321-325.

[83] M.J.-E. Lee, O. Veiseh, N. Bhattarai, C. Sun, S.J. Hansen, S. Ditzler, S. Knoblaugh, D. Lee, R. Ellenbogen, M. Zhang, J.M. Olson, Rapid Pharmacokinetic and Biodistribution Studies Using Cholorotoxin-Conjugated Iron Oxide Nanoparticles: A Novel Non-Radioactive Method, Plos One, 5 (2010).

[84] K.L. Hultman, A.J. Raffo, A.L. Grzenda, P.E. Harris, T.R. Brown, S. O'Brien, Magnetic resonance imaging of major histocompatibility class II expression in the renal medulla using immunotargeted superparamagnetic iron oxide nanoparticles, Acs Nano, 2 (2008) 477-484.

[85] K.C. Briley-Saebo, Y.S. Cho, P.X. Shaw, S.K. Ryu, V. Mani, S. Dickson, E. Izadmehr, S. Green, Z.A. Fayad, S. Tsimikas, Targeted Iron Oxide Particles for In Vivo Magnetic Resonance Detection of Atherosclerotic Lesions With Antibodies Directed to Oxidation-Specific Epitopes, Journal of the American College of Cardiology, 57 (2011) 337-347.

[86] S. Wagner, J. Schnorr, H. Pilgrimm, B. Hamm, M. Taupitz, Monomer-coated very small superparamagnetic iron oxide particles as contrast medium for magnetic resonance imaging - Preclinical in vivo characterization, Investigative Radiology, 37 (2002) 167-177.

[87] J. Schnorr, M. Taupitz, S. Wagner, H. Pilgrimm, J. Hansel, B. Hamm, Age-related blood half-life of particulate contrast material: Experimental results with a USPIO in rats, Journal of Magnetic Resonance Imaging, 12 (2000) 740-744.

[88] P.Y. Brillet, F. Gazeau, A. Luciani, B. Bessoud, C.A. Cuenod, N. Siauve, J.N. Pons, J. Poupon, O. Clement, Evaluation of tumoral enhancement by superparamagnetic iron oxide particles: comparative studies with ferumoxtran and anionic iron oxide nanoparticles, European Radiology, 15 (2005) 1369-1377.

[89] A. Ruiz, Y. Hernandez, C. Cabal, E. Gonzalez, S. Veintemillas-Verdaguer, E. Martinez, M.P. Morales, Biodistribution and pharmacokinetics of uniform magnetite nanoparticles chemically modified with polyethylene glycol, Nanoscale, 5 (2013) 11400-11408.

[90] A.P. Khandhar, R.M. Ferguson, H. Arami, S.J. Kemp, K.M. Krishnan, Tuning Surface Coatings of Optimized Magnetite Nanoparticle Tracers for In Vivo Magnetic Particle Imaging, IEEE Transactions on Magnetics, 51 (2015) 1-4.

[91] A.P. Khandhar, S.J. Kemp, R.M. Ferguson, K.M. Krishnan, Tunable in vivo circulation characteristics of PEGylated MPI tracers, in: 5th International Workshop on Magnetic Particle Imaging (IWMPI), IEEE, Turkey, Istanbul, 2015 pp. 1-1.

[92] H. Arami, A.P. Khandhar, A. Tomitaka, E. Yu, P.W. Goodwill, S.M. Conolly, K.M. Krishnan, In vivo multimodal magnetic particle imaging (MPI) with tailored magneto/optical contrast agents, Biomaterials, 52 (2015) 251-261.

[93] B. Moffat, G.R. Reddy, P. McConville, D.E. Hall, T.L. Chenevert, R.R. Kopelman, R. Weissleder, A. Rehemtulla, B.D. Ross, A novel polyacrylamide magnetic nanoparticle contrast agent for molecular imaging using MRI, Molecular Imaging, 2 (2003) 324-332.

[94] Y. Yang, Y. Yang, N. Yanasak, A. Schumacher, T.C.C. Hu, Temporal and Noninvasive Monitoring of Inflammatory-Cell Infiltration to Myocardial Infarction Sites Using Micrometer-Sized Iron Oxide Particles, Magnetic Resonance in Medicine, 63 (2010) 33-40.

[95] Y.D. Yang, J.M. Liu, Y.H. Yang, S.H. Cho, T.C.C. Hu, Assessment of Cell Infiltration in Myocardial Infarction: A Dose-Dependent Study Using Micrometer-Sized Iron Oxide Particles, Magnetic Resonance in Medicine, 66 (2011) 1353-1361.

[96] H. Xu, L. Cheng, C. Wang, X. Ma, Y. Li, Z. Liu, Polymer encapsulated upconversion nanoparticle/iron oxide nanocomposites for multimodal imaging and magnetic targeted drug delivery, Biomaterials, 32 (2011) 9364-9373.

[97] F.M. Kievit, Z.R. Stephen, O. Veiseh, H. Arami, T.Z. Wang, V.P. Lai, J.O. Park, R.G. Ellenbogen, M.L. Disis, M.Q. Zhang, Targeting of Primary Breast Cancers and Metastases in a Transgenic Mouse Model Using Rationally Designed Multifunctional SPIONs, Acs Nano, 6 (2012) 2591-2601.

[98] M. Ferrari, Cancer nanotechnology: Opportunities and challenges, Nature Reviews Cancer, 5 (2005) 161-171.

[99] D. Peer, J.M. Karp, S. Hong, O.C. FaroKhzad, R. Margalit, R. Langer, Nanocarriers as an emerging platform for cancer therapy, Nature Nanotechnology, 2 (2007) 751-760.

[100] M.P. Melancon, W. Lu, C. Li, Gold-Based Magneto/Optical Nanostructures: Challenges for In Vivo Applications in Cancer Diagnostics and Therapy, MRS Bulletin, 34 (2009) 415-421.

[101] I. Singh, Textbook of Human Histology, Jaypee Brothers Publishers, New Delhi, India, 2006.

[102] P.J. Murray, T.A. Wynn, Protective and pathogenic functions of macrophage subsets, Nature Reviews Immunology, 11 (2011) 723-737.

[103] K. Saijo, C.K. Glass, Microglial cell origin and phenotypes in health and disease, Nature Reviews Immunology, 11 (2011) 775-787.

[104] C. Shi, E.G. Pamer, Monocyte recruitment during infection and inflammation, Nature Reviews Immunology, 11 (2011) 762-774.

[105] M. Levy, N. Luciani, D. Alloyeau, D. Elgrabli, V. Deveaux, C. Pechoux, S. Chat, G. Wang, N. Vats, F. Gendron, C. Factor, S. Lotersztajn, A. Luciani, C. Wilhelm, F. Gazeau, Long term in vivo biotransformation of iron oxide nanoparticles, Biomaterials, 32 (2011) 3988-3999.

[106] J.V. Jokerst, T. Lobovkina, R.N. Zare, S.S. Gambhir, Nanoparticle PEGylation for imaging and therapy, Nanomedicine, 6 (2011) 715-728.

[107] A.J. Cole, A.E. David, J.X. Wang, C.J. Galban, V.C. Yang, Magnetic brain tumor targeting and biodistribution of long-circulating PEG-modified, cross-linked starch-coated iron oxide nanoparticles, Biomaterials, 32 (2011) 6291-6301.

[108] A. Beduneau, Z. Ma, C.B. Grotepas, A. Kabanov, B.E. Rabinow, N. Gong, R.L. Mosley, H. Dou, M.D. Boska, H.E. Gendelman, Facilitated Monocyte-Macrophage Uptake and Tissue Distribution of Superparmagnetic Iron-Oxide Nanoparticles, Plos One, 4 (2009).

[109] S.W. Jones, R.A. Roberts, G.R. Robbins, J.L. Perry, M.P. Kai, K. Chen, T. Bo, M.E. Napier, J.P.Y. Ting, J.M. DeSimone, J.E. Bear, Nanoparticle clearance is governed by Th1/Th2 immunity and strain background, Journal of Clinical Investigation, 123 (2013) 3061-3073.

[110] B.R. Smith, E.E.B. Ghosn, H. Rallapalli, J.A. Prescher, T. Larson, L.A. Herzenberg, S.S. Gambhir, Selective uptake of single-walled carbon nanotubes by circulating monocytes for enhanced tumour delivery, Nature Nanotechnology, 9 (2014) 481-+.

[111] D. Simberg, T. Duza, J.-H. Park, M. Essler, J. Pilch, L. Zhang, A.M. Derfus, M. Yang, R.M. Hoffman, S. Bhatia, M.J. Sailor, E. Ruoslahti, Biomimetic amplification of nanoparticle homing to tumors., Proceedings of the National Academy of Sciences of the United States of America, 104 (2007) 932-936.

[112] C. Wang, X.Q. Sun, L. Cheng, S.N. Yin, G.B. Yang, Y.G. Li, Z. Liu, Multifunctional Theranostic Red Blood Cells For Magnetic-Field-Enhanced in vivo Combination Therapy of Cancer, Advanced Materials, 26 (2014) 4794-+.

[113] V.I. Shubayev, T.R. Pisanic, II, S. Jin, Magnetic nanoparticles for theragnostics, Advanced Drug Delivery Reviews, 61 (2009) 467-477.

[114] O. Veiseh, C. Sun, C. Fang, N. Bhattarai, J. Gunn, F. Kievit, K. Du, B. Pullar, D. Lee, R.G. Ellenbogen, J. Olson, M. Zhang, Specific Targeting of Brain Tumors with an Optical/Magnetic Resonance Imaging Nanoprobe across the Blood-Brain Barrier, Cancer Research, 69 (2009) 6200-6207.

[115] R.A.M. Heesakkers, G.J. Jager, A.M. Hovels, B. de Hoop, H.C.M. van den Bosch, F. Raat, J.A. Witjes, P.F.A. Mulders, C.H. van der Kaa, J.O. Barentsz, Prostate Cancer: Detection of Lymph Node Metastases Outside the Routine Surgical Area with Ferumoxtran-10-enhanced MR Imaging, Radiology, 251 (2009) 408-414.

[116] G. Nakai, M. Matsuki, T. Harada, N. Tanigawa, T. Yamada, J. Barentsz, Y. Narumi, Evaluation of Axillary Lymph Nodes by Diffusion-Weighted MRI Using Ultrasmall Superparamagnetic Iron Oxide in Patients With Breast Cancer: Initial Clinical Experience, Journal of Magnetic Resonance Imaging, 34 (2011) 557-562.

[117] A. Yilmaz, S. Rosch, H. Yildiz, S. Klumpp, U. Sechtem, First Multiparametric Cardiovascular Magnetic Resonance Study Using Ultrasmall Superparamagnetic Iron

Oxide Nanoparticles in a Patient With Acute Myocardial Infarction New Vistas for the Clinical Application of Ultrasmall Superparamagnetic Iron Oxide, Circulation, 126 (2012) 1932-1934.

[118] D. Qiu, G. Zaharchuk, T. Christen, W.W. Ni, M.E. Moseley, Contrast-enhanced functional blood volume imaging (CE-fBVI): Enhanced sensitivity for brain activation in humans using the ultrasmall superparamagnetic iron oxide agent ferumoxytol, Neuroimage, 62 (2012) 1726-1731.

[119] C. Kleinschnitz, T. Bendszus, M. Frank, T. Solymosi, K.V. Toyka, G. Stoll, In vivo monitoring of macrophage infiltration in experimental ischemic brain lesions by magnetic resonance imaging, Journal of Cerebral Blood Flow and Metabolism, 23 (2003) 1356-1361.

[120] M.S.A. Deloire, T. Touil, B. Brochet, V. Dousset, J.M. Caille, K.G. Petry, Macrophage brain infiltration in experimental autoimmune encephalomyelitis is not completely compromised by suppressed T-cell invasion: in vivo magnetic resonance imaging illustration in effective anti-VLA-4 antibody treatment, Multiple Sclerosis, 10 (2004) 540-548.

[121] S. Valable, E.L. Barbier, M. Bemaudin, S. Roussel, C. Segebarth, E. Petit, C. Remy, In vivo MRI tracking of exogenous monocytes/macrophages targeting brain tumors in a rat model of glioma, Neuroimage, 40 (2008) 973-983.

[122] E. Penno, C. Johnsson, L. Johansson, H. Ahlstrom, Macrophage uptake of ultra-small iron oxide particles for magnetic resonance imaging in experimental acute cardiac transplant rejection, Acta Radiologica, 47 (2006) 264-271.

[123] A. Nchimi, O. Defawe, D. Brisbois, T.K.Y. Broussaud, J.-O. Defraigne, P. Magotteaux, B. Massart, J.-M. Serfaty, X. Houard, J.-B. Michel, N. Sakalihasan, MR Imaging of Iron Phagocytosis in Intraluminal Thrombi of Abdominal Aortic Aneurysms in Humans, Radiology, 254 (2010) 973-981.

[124] N. Beckmann, C. Cannet, S. Zurbruegg, R. Haberthur, J. Li, C. Pally, C. Bruns, Macrophage infiltration detected at MR imaging in rat kidney allografts: Early marker of chronic rejection?, Radiology, 240 (2006) 717-724.

[125] Y. Lee, J.W. Ryu, H. Chang, J.Y. Sohn, K.W. Lee, C.W. Woo, H.J. Kang, S.Y. Jeong, E.K. Choi, J.S. Lee, In Vivo MR Evaluation of the Effect of the CCR2 Antagonist on Macrophage Migration, Magnetic Resonance in Medicine, 64 (2010) 72-79.

[126] X. Chen, R. Wong, I. Khalidov, A.Y. Wang, J. Leelawattanachai, Y. Wang, M.M. Jin, Inflamed leukocyte-mimetic nanoparticles for molecular imaging of inflammation, Biomaterials, 32 (2011) 7651-7661.

[127] F. Braet, E. Wisse, Structural and functional aspects of liver sinusoidal endothelial cell fenestrae: a review, Comparative Hepatology, 1 (2002) 1.

[128] H. Sarin, Physiologic upper limits of pore size of different blood capillary types and another perspective on the dual pore theory of microvascular permeability, Journal of Angiogenesis Research, 2 (2010) 1-19.

[129] M. Saito, T. Matsuura, K. Nagatsuma, K. Tanaka, H. Maehashi, K. Shimizu, Y. Hataba, F. Kato, I. Kashimori, H. Tajiri, F. Braet, The functional interrelationship between gap junctions and fenestrae in endothelial cells of the liver organoid, Journal of Membrane Biology, 217 (2007) 115-121.

[130] R. Gref, Y. Minamitake, M.T. Peracchia, V. Trubetskoy, V. Torchilin, R. Langer, BIODEGRADABLE LONG-CIRCULATING POLYMERIC NANOSPHERES, Science, 263 (1994) 1600-1603.

[131] J. Huang, L. Bu, J. Xie, K. Chen, Z. Cheng, X. Li, X. Chen, Effects of Nanoparticle Size on Cellular Uptake and Liver MRI with Polyvinylpyrrolidone-Coated Iron Oxide Nanoparticles, Acs Nano, 4 (2010) 7151-7160.

[132] J.T. Ferrucci, D.D. Stark, IRON-OXIDE ENHANCED MR-IMAGING OF THE LIVER AND SPLEEN - REVIEW OF THE 1ST-5 YEARS, American Journal of Roentgenology, 155 (1990) 943-950.

[133] D.P. Cormode, G.O. Skajaa, A. Delshad, N. Parker, P.A. Jarzyna, C. Calcagno, M.W. Galper, T. Skajaa, K.C. Briley-Saebo, H.M. Bell, R.E. Gordon, Z.A. Fayad, S.L.C. Woo, W.J.M. Mulder, A Versatile and Tunable Coating Strategy Allows Control of Nanocrystal Delivery to Cell Types in the Liver, Bioconjugate Chemistry, 22 (2011) 353-361.

[134] L. Gu, R.H. Fang, M.J. Sailor, J.-H. Park, In Vivo Clearance and Toxicity of Monodisperse Iron Oxide Nanocrystals, Acs Nano, 6 (2012) 4947-4954.

[135] T. Seested, R.S. Appa, E.I. Christensen, Y.A. Ioannou, T.N. Krogh, D.M. Karpf, H.M. Nielsen, In vivo clearance and metabolism of recombinant activated factor VII (rFVIIa) and its complexes with plasma protease inhibitors in the liver, Thrombosis Research, 127 (2011) 356-362.

[136] S.-J. Cheong, C.-M. Lee, S.-L. Kim, H.-J. Jeong, E.-M. Kim, E.-H. Park, D.W. Kim, S.T. Lim, M.-H. Sohn, Superparamagnetic iron oxide nanoparticles-loaded chitosan-

linoleic acid nanoparticles as an effective hepatocyte-targeted gene delivery system, International Journal of Pharmaceutics, 372 (2009) 169-176.

[137] C.-M. Lee, H.-J. Jeong, E.-M. Kim, D.W. Kim, S.T. Lim, H.T. Kim, I.-K. Park, Y.Y. Jeong, J.W. Kim, M.-H. Sohn, Superparamagnetic Iron Oxide Nanoparticles as a Dual Imaging Probe for Targeting Hepatocytes In Vivo, Magnetic Resonance in Medicine, 62 (2009) 1440-1446.

[138] B.E. Van Beers, C. Sempoux, R. Materne, M. Delos, A.M. Smith, Biodistribution of ultrasmall iron oxide particles in the rat liver, Journal of Magnetic Resonance Imaging, 13 (2001) 594-599.

[139] A.C. Guyton, J.E. Hall, Textbook of Medical Physiology, 12th ed., Elsevier, PA, USA, 2011.

[140] C.-C. Huang, C.-Y. Tsai, H.-S. Sheu, K.-Y. Chuang, C.-H. Su, U.S. Jeng, F.-Y. Cheng, C.-H. Su, H.-Y. Lei, C.-S. Yeh, Enhancing Transversal Relaxation for Magnetite Nanoparticles in MR Imaging Using Gd3+-Chelated Mesoporous Silica Shells, Acs Nano, 5 (2011) 3905-3916.

[141] M. Demoy, J.P. Andreux, C. Weingarten, B. Gouritin, V. Guilloux, P. Couvreur, Spleen capture of nanoparticles: Influence of animal species and surface characteristics, Pharmaceutical Research, 16 (1999) 37-41.

[142] S. Pillai, A. Cariappa, The follicular versus marginal zone B lymphocyte cell fate decision, Nature Reviews Immunology, 9 (2009) 767-777.

[143] M.G. Harisinghani, J. Barentsz, P.F. Hahn, W.M. Deserno, S. Tabatabaei, C.H. van de Kaa, J. de la Rosette, R. Weissleder, Noninvasive detection of clinically occult

lymph-node metastases in prostate cancer, New England Journal of Medicine, 348 (2003) 2491-U2495.

[144] V.-Q. Hieu, M.-K. Yoo, H.-J. Jeong, H.-J. Lee, M. Muthiah, J.H. Rhee, J.-H. Lee, C.-S. Cho, Y.Y. Jeong, I.-K. Park, Targeted delivery of mannan-coated superparamagnetic iron oxide nanoparticles to antigen-presenting cells for magnetic resonance-based diagnosis of metastatic lymph nodes in vivo, Acta Biomaterialia, 7 (2011) 3935-3945.

[145] C. Corot, P. Robert, J.-M. Idee, M. Port, Recent advances in iron oxide nanocrystal technology for medical imaging, Advanced Drug Delivery Reviews, 58 (2006) 1471-1504.

[146] F. Alexis, E. Pridgen, L.K. Molnar, O.C. Farokhzad, Factors affecting the clearance and biodistribution of polymeric nanoparticles, Molecular Pharmaceutics, 5 (2008) 505-515.

[147] J.P.M. Almeida, A.L. Chen, A. Foster, R. Drezek, In vivo biodistribution of nanoparticles, Nanomedicine, 6 (2011) 815-835.

[148] S.C. Satchell, F. Braet, Glomerular endothelial cell fenestrations: an integral component of the glomerular filtration barrier, American Journal of Physiology-Renal Physiology, 296 (2009) F947-F956.

[149] J.E. Zuckerman, C.H.J. Choi, H. Han, M.E. Davis, Polycation-siRNA nanoparticles can disassemble at the kidney glomerular basement membrane, Proceedings of the National Academy of Sciences of the United States of America, 109 (2012) 3137-3142.

[150] A.B. Fogo, V. Kon, The glomerulus - a view from the inside - the endothelial cell, International Journal of Biochemistry & Cell Biology, 42 (2010) 1388-1397.

[151] T. Skotland, T.-G. Iversen, K. Sandvig, New metal-based nanoparticles for intravenous use: requirements for clinical success with focus on medical imaging, Nanomedicine-Nanotechnology Biology and Medicine, 6 (2010) 730-737.

[152] G. Lamanna, M. Kueny-Stotz, H. Mamlouk-Chaouachi, C. Ghobril, B. Basly, A. Bertin, I. Miladi, C. Billotey, G. Pourroy, S. Begin-Colin, D. Felder-Flesch, Dendronized iron oxide nanoparticles for multimodal imaging, Biomaterials, 32 (2011) 8562-8573.

[153] C. Glaus, R. Rossin, M.J. Welch, G. Bao, In Vivo Evaluation of Cu-64-Labeled Magnetic Nanoparticles as a Dual-Modality PET/MR Imaging Agent, Bioconjugate Chemistry, 21 (2010) 715-722.

[154] K. Chen, J. Xie, H. Xu, D. Behera, M.H. Michalski, S. Biswal, A. Wang, X. Chen, Triblock copolymer coated iron oxide nanoparticle conjugate for tumor integrin targeting, Biomaterials, 30 (2009) 6912-6919.

[155] N. Arsalani, H. Fattahi, S. Laurent, C. Burtea, L. Vander Elst, R.N. Muller, Polyglycerol-grafted superparamagnetic iron oxide nanoparticles: highly efficient MRI contrast agent for liver and kidney imaging and potential scaffold for cellular and molecular imaging, Contrast Media & Molecular Imaging, 7 (2012) 185-194.

[156] Y.F. Tan, P. Chandrasekharan, D. Maity, C.X. Yong, K.-H. Chuang, Y. Zhao, S. Wang, J. Ding, S.-S. Feng, Multimodal tumor imaging by iron oxides and quantum dots formulated in poly (lactic acid)-D-alpha-tocopheryl polyethylene glycol 1000 succinate nanoparticles, Biomaterials, 32 (2011) 2969-2978.

[157] S. Abe, I. Kida, M. Esaki, T. Akasaka, M. Uo, T. Hosono, Y. Sato, B. Jeyadevan, Y. Kuboki, M. Morita, K. Tohji, F. Watari, Biodistribution imaging of magnetic particles in mice: X-ray scanning analytical microscopy and magnetic resonance imaging, Bio-Medical Materials and Engineering, 19 (2009) 213-220.

[158] L. Yang, H. Mao, Z. Cao, Y.A. Wang, X. Peng, X. Wang, H.K. Sajja, L. Wang, H. Duan, C. Ni, C.A. Staley, W.C. Wood, X. Gao, S. Nie, Molecular Imaging of Pancreatic Cancer in an Animal Model Using Targeted Multifunctional Nanoparticles, Gastroenterology, 136 (2009) 1514-1525.

[159] L. Yang, H. Kuang, W. Zhang, Z.P. Aguilar, Y. Xiong, W. Lai, H. Xu, H. Wei, Size dependent biodistribution and toxicokinetics of iron oxide magnetic nanoparticles in mice, Nanoscale, 7 (2015) 625-636.

[160] M. Varna, P. Ratajczak, I. Ferreira, C. Leboeuf, G. Bousquet, A. Janin, In Vivo Distribution of Inorganic Nanoparticles in Preclinical Models, Journal of Biomaterials and Nanobiotechnology, 3 (2012) 269-279.

[161] Z. Lin, N.A. Monteiro-Riviere, J.E. Riviere, Pharmacokinetics of metallic nanoparticles, Wiley Interdisciplinary Reviews-Nanomedicine and Nanobiotechnology, 7 (2015) 189-217.

[162] F. Roohi, J. Lohrke, A. Ide, G. Schuetz, K. Dassler, Studying the effect of particle size and coating type on the blood kinetics of superparamagnetic iron oxide nanoparticles, International Journal of Nanomedicine, 7 (2012) 4447-4458.

[163] Y.X.J. Wang, S.M. Hussain, G.P. Krestin, Superparamagnetic iron oxide contrast agents: physicochemical characteristics and applications in MR imaging, European Radiology, 11 (2001) 2319-2331.

[164] A.K. Gupta, S. Wells, Surface-modified superparamagnetic nanoparticles for drug delivery: Preparation, characterization, and cytotoxicity studies, IEEE Transactions on Nanobioscience, 3 (2004) 66-73.

[165] Y. Chen, B.-A. Chen, Application and development of magnetic iron-oxide nanoparticles in tumor -targeted therapy, Chinese Journal of Cancer, 29 (2010) 118-122.

[166] A. Kunzmann, B. Andersson, T. Thurnherr, H. Krug, A. Scheynius, B. Fadeel, Toxicology of engineered nanomaterials: Focus on biocompatibility, biodistribution and biodegradation, Biochimica Et Biophysica Acta-General Subjects, 1810 (2011) 361-373.

[167] G. Fleige, F. Seeberger, D. Laux, M. Kresse, M. Taupitz, H. Pilgrimm, C. Zimmer, In vitro characterization of two different ultrasmall iron oxide particles for magnetic resonance cell tracking, Investigative Radiology, 37 (2002) 482-488.

[168] H. Arami, A. Khandhar, D. Liggitt, K.M. Krishnan, In vivo delivery, pharmacokinetics, biodistribution and toxicity of iron oxide nanoparticles, Chemical Society Reviews, 44 (2015) 8576-8607.

[169] A.P. Khandhar, Biomedical imaging and therapy with physically and physiologically tailored magnetic nanoparticles, in: Materials Science and Engineering, University of Washington, University of Washington, 2013.

[170] M. Longmire, P.L. Choyke, H. Kobayashi, Clearance properties of nano-sized particles and molecules as imaging agents: considerations and caveats, Nanomedicine, 3 (2008) 703-717.

[171] S.H. Choi, W.K. Moon, J.H. Hong, K.R. Son, N. Cho, B.J. Kwon, J.J. Lee, J.K. Chung, H.S. Min, S.H. Park, Lymph node metastasis: Ultrasmall superparamagnetic iron oxide-enhanced MR imaging versus PET/CT in a rabbit model, Radiology, 242 (2007) 137-143.

[172] B.B. Pultrum, E.J. van der Jagt, H.L. van Westreenen, H.M. van Dullemen, P. Kappert, H. Groen, J. Sietsma, M. Oudkerk, J.T.M. Plukker, G.M. van Dam, Detection of lymph node metastases with ultrasmall superparamagnetic iron oxide (USPIO)-enhanced magnetic resonance imaging in oesophageal cancer: a feasibility study, Cancer Imaging, 9 (2009) 19-28.

[173] O. Veiseh, C. Sun, C. Fang, N. Bhattarai, J. Gunn, F. Kievit, K. Du, B. Pullar, D. Lee, R.G. Ellenbogen, J. Olson, M. Zhang, Specific targeting of brain tumors with an optical/magnetic resonance imaging nanoprobe across the blood-brain barrier, Cancer Res, 69 (2009) 6200-6207.

[174] A. Iannone, R.L. Magin, T. Walczak, M. Federico, H.M. Swartz, A. Tomasi, V. Vannini, BLOOD CLEARANCE OF DEXTRAN MAGNETITE PARTICLES DETERMINED BY A NONINVASIVE INVIVO ESR METHOD, Magnetic Resonance in Medicine, 22 (1991) 435-442.

[175] M. Di Marco, C. Sadun, M. Port, I. Guilbert, P. Couvreur, C. Dubernet, Physicochemical characterization of ultrasmall superparamagnetic iron oxide particles (USPIO) for biomedical application as MRI contrast agents, International Journal of Nanomedicine, 2 (2007) 609-622.

[176] C. Fang, N. Bhattarai, C. Sun, M.Q. Zhang, Functionalized Nanoparticles with Long-Term Stability in Biological Media, Small, 5 (2009) 1637-1641.

[177] X.-H. Peng, X. Qian, H. Mao, A.Y. Wang, Z. Chen, S. Nie, D.M. Shin, Targeted magnetic iron oxide nanoparticles for tumor imaging and therapy, International Journal of Nanomedicine, 3 (2008) 311-321.

[178] H. Arami, K.M. Krishnan, Highly Stable Amine Functionalized Iron Oxide Nanoparticles Designed for Magnetic Particle Imaging (MPI), IEEE Transactions on Magnetics, 49 (2013) 3500-3503.

[179] D.L.J. Thorek, A. Tsourkas, Size, charge and concentration dependent uptake of iron oxide particles by non-phagocytic cells, Biomaterials, 29 (2008) 3583-3590.

[180] C. Boyer, M.R. Whittaker, V. Bulmus, J.Q. Liu, T.P. Davis, The design and utility of polymer-stabilized iron-oxide nanoparticles for nanomedicine applications, Nature Publishing Group Asia Materials, 2 (2010) 23-30.

[181] S. Tong, S. Hou, Z. Zheng, J. Zhou, G. Bao, Coating Optimization of Superparamagnetic Iron Oxide Nanoparticles for High T(2) Relaxivity, Nano Letters, 10 (2010) 4607-4613.

[182] S. Lou, J.-y. Ye, K.-q. Li, A. Wu, A gold nanoparticle-based immunochromatographic assay: The influence of nanoparticulate size, Analyst, 137 (2012) 1174-1181.

[183] Y. Geng, P. Dalhaimer, S.S. Cai, R. Tsai, M. Tewari, T. Minko, D.E. Discher, Shape effects of filaments versus spherical particles in flow and drug delivery, Nature Nanotechnology, 2 (2007) 249-255.

[184] Z. Liu, W. Cai, L. He, N. Nakayama, K. Chen, X. Sun, X. Chen, H. Dai, In vivo biodistribution and highly efficient tumour targeting of carbon nanotubes in mice, Nature Nanotechnology, 2 (2006) 47-52.

[185] Arnida, M.M. Janat-Amsbury, A. Ray, C.M. Peterson, H. Ghandehari, Geometry and surface characteristics of gold nanoparticles influence their biodistribution and uptake by macrophages, European Journal of Pharmaceutics and Biopharmaceutics, 77 (2011) 417-423.

[186] R.A. Petros, J.M. DeSimone, Strategies in the design of nanoparticles for therapeutic applications, Nature Reviews Drug Discovery, 9 (2010) 615-627.

[187] J.H. Park, G. von Maltzahn, L.L. Zhang, M.P. Schwartz, E. Ruoslahti, S.N. Bhatia, M.J. Sailor, Magnetic iron oxide nanoworms for tumor targeting and imaging, Advanced Materials, 20 (2008) 1630-+.

[188] L. Zhan, G. Yanxia, Z. Xiaoyong, Q. Wei, F. Qiaohui, L. Yan, J. Zongxian, W. Jianjun, T. Yuqin, D. Xiaojiang, W. Wangsuo, Biodistribution of co-exposure to multi-walled carbon nanotubes and graphene oxide nanoplatelets radiotracers, Journal of Nanoparticle Research, 13 (2010) 2939-2947.

[189] S.-T. Yang, J. Luo, Q. Zhou, H. Wang, Pharmacokinetics, metabolism and toxicity of carbon nanotubes for biomedical purposes., Theranostics, 2 (2012) 271-282.

[190] Y. Akiyama, T. Mori, Y. Katayama, T. Niidome, Conversion of rod-shaped gold nanoparticles to spherical forms and their effect on biodistribution in tumor-bearing mice., Nanoscale Research Letters, 7 (2012) 565.

[191] H. Wu, G. Liu, Y. Zhuang, D. Wu, H. Zhang, H. Yang, H. Hu, S. Yang, The behavior after intravenous injection in mice of multiwalled carbon nanotube/Fe3O4 hybrid MRI contrast agents, Biomaterials, 32 (2011) 4867-4876.

[192] F. Erogbogbo, K.T. Yong, R. Hu, W.C. Law, H. Ding, C.W. Chang, P.N. Prasad, M.T. Swihart, Biocompatible Magnetofluorescent Probes: Luminescent Silicon Quantum Dots Coupled with Superparamagnetic Iron(III) Oxide, Acs Nano, 4 (2010) 5131-5138.

[193] M.P. Melancon, W. Lu, M. Zhong, M. Zhou, G. Liang, A.M. Elliott, J.D. Hazle, J.N. Myers, C. Li, R.J. Stafford, Targeted multifunctional gold-based nanoshells for magnetic resonance-guided laser ablation of head and neck cancer, Biomaterials, 32 (2011) 7600-7608.

[194] H. Yang, Y. Zhuang, Y. Sun, A. Dai, X. Shi, D. Wu, F. Li, H. Hu, S. Yang, Targeted dual-contrast T-1- and T-2-weighted magnetic resonance imaging of tumors using multifunctional gadolinium-labeled superparamagnetic iron oxide nanoparticles, Biomaterials, 32 (2011) 4584-4593.

[195] J. Xie, F. Zhang, M. Aronova, L. Zhu, X. Lin, Q. Quan, G. Liu, G. Zhang, K.-Y. Choi, K. Kim, X. Sun, S. Lee, S. Sun, R. Leapman, X. Chen, Manipulating the Power of an Additional Phase: A Flower-like Au-Fe3O4 Optical Nanosensor for Imaging Protease Expressions In vivo, Acs Nano, 5 (2011) 3043-3051.

[196] M.P. Melancon, A. Elliott, X. Ji, A. Shetty, Z. Yang, M. Tian, B. Taylor, R.J. Stafford, C. Li, Theranostics With Multifunctional Magnetic Gold Nanoshells Photothermal Therapy and T2* Magnetic Resonance Imaging, Investigative Radiology, 46 (2011) 132-140.

[197] T. Liu, S.X. Shi, C. Liang, S.D. Shen, L. Cheng, C. Wang, X.J. Song, S. Goel, T.E. Barnhart, W.B. Cai, Z. Liu, Iron Oxide Decorated MoS2 Nanosheets with Double PEGylation for Chelator-Free Radio labeling and Multimodal Imaging Guided Photothermal Therapy, Acs Nano, 9 (2015) 950-960.

[198] X.X. He, F.Y. Liu, L. Liu, T.C. Duan, H.M. Zhang, Z.X. Wanq, Lectin-Conjugated Fe2O3@Au Core@Shell Nanoparticles as Dual Mode Contrast Agents for in Vivo Detection of Tumor, Molecular Pharmaceutics, 11 (2014) 738-745.

[199] Y. Liu, T.C. Hughes, B.W. Muir, L.J. Waddington, T.R. Gengenbach, C.D. Easton, T.M. Hinton, B.A. Moffat, X. Hao, J. Qiu, Water-dispersible magnetic carbon nanotubes as T-2-weighted MRI contrast agents, Biomaterials, 35 (2014) 378-386.

[200] J.L. Campbell, J. Arora, S.F. Cowell, A. Garg, P. Eu, S.K. Bhargava, V. Bansal, Quasi-Cubic Magnetite/Silica Core-Shell Nanoparticles as Enhanced MRI Contrast Agents for Cancer Imaging, Plos One, 6 (2011).

[201] L. Lartigue, D. Alloyeau, J. Kolosnjaj-Tabi, Y. Javed, P. Guardia, A. Riedinger, C. Pechoux, T. Pellegrino, C. Wilhelm, F. Gazeaut, Biodegradation of Iron Oxide Nanocubes: High-Resolution In Situ Monitoring, Acs Nano, 7 (2013) 3939-3952.

[202] G. Sinigaglia, M. Magro, G. Miotto, S. Cardillo, E. Agostinelli, R. Zboril, E. Bidollari, F. Vianello, Catalytically active bovine serum amine oxidase bound to

fluorescent and magnetically drivable nanoparticles, International Journal of Nanomedicine, 7 (2012) 2249-2259.

[203] R. Venerando, G. Miotto, M. Magro, M. Dallan, D. Baratella, E. Bonaiuto, R. Zboril, F. Vianello, Magnetic Nanoparticles with Covalently Bound Self-Assembled Protein Corona for Advanced Biomedical Applications, Journal of Physical Chemistry C, 117 (2013) 20320-20331.

[204] M. Magro, R. Campos, D. Baratella, G. Lima, K. Hola, C. Divoky, R. Stollberger, O. Malina, C. Aparicio, G. Zoppellaro, R. Zboril, F. Vianello, A Magnetically Drivable Nanovehicle for Curcumin with Antioxidant Capacity and MRI Relaxation Properties, Chemistry-a European Journal, 20 (2014) 11913-11920.

[205] J. Skopalik, K. Polakova, M. Havrdova, I. Justan, M. Magro, D. Milde, L. Knopfova, J. Smarda, H. Polakova, E. Gabrielova, F. Vianello, J. Michalek, R. Zboril, Mesenchymal stromal cell labeling by new uncoated superparamagnetic maghemite nanoparticles in comparison with commercial Resovist - an initial in vitro study, International Journal of Nanomedicine, 9 (2014) 5355-5372.

[206] Q. Quan, J. Xie, H. Gao, M. Yang, F. Zhang, G. Liu, X. Lin, A. Wang, H.S. Eden, S. Lee, G. Zhang, X. Chen, HSA Coated Iron Oxide Nanoparticles as Drug Delivery Vehicles for Cancer Therapy, Molecular Pharmaceutics, 8 (2011) 1669-1676.

[207] Q. Tong, H. Li, W. Li, H. Chen, X. Shu, X. Lu, G. Wang, In Vitro and In Vivo Anti-Tumor Effects of Gemcitabine Loaded with a New Drug Delivery System, Journal of Nanoscience and Nanotechnology, 11 (2011) 3651-3658.

[208] S. Garcia-Jimeno, E. Escribano, J. Queralt, J. Estelrich, Magnetoliposomes prepared by reverse-phase followed by sequential extrusion: Characterization and

possibilities in the treatment of inflammation, International Journal of Pharmaceutics, 405 (2011) 181-187.

[209] A.S. Karakoti, S. Das, S. Thevuthasan, S. Seal, PEGylated Inorganic Nanoparticles, Angewandte Chemie International Edition, (2011) n/a-n/a.

[210] T.Y. Liu, K.H. Liu, D.M. Liu, S.Y. Chen, I.W. Chen, Temperature-Sensitive Nanocapsules for Controlled Drug Release Caused by Magnetically Triggered Structural Disruption, Advanced Functional Materials, 19 (2009) 616-623.

[211] S. Purushotham, P.E.J. Chang, H. Rumpel, I.H.C. Kee, R.T.H. Ng, P.K.H. Chow, C.K. Tan, R.V. Ramanujan, Thermoresponsive core-shell magnetic nanoparticles for combined modalities of cancer therapy, Nanotechnology, 20 (2009).

[212] Y.X. Zhao, C.L. Wang, L. Wang, Q. Yang, W.Y. Tang, Z.N. She, Y.H. Deng, A frustrating problem: Accelerated blood clearance of PEGylated solid lipid nanoparticles following subcutaneous injection in rats, European Journal of Pharmaceutics and Biopharmaceutics, 81 (2012) 506-513.

[213] H. Xu, K.Q. Wang, Y.H. Deng, D.W. Chen, Effects of cleavable PEG-cholesterol derivatives on the accelerated blood clearance of PEGylated liposomes, Biomaterials, 31 (2010) 4757-4763.

[214] T. Ishida, H. Kiwada, Accelerated blood clearance (ABC) phenomenon upon repeated injection of PEGylated liposomes, International Journal of Pharmaceutics, 354 (2008) 56-62.

[215] T. Ishihara, M. Takeda, H. Sakamoto, A. Kimoto, C. Kobayashi, N. Takasaki, K. Yuki, K.I. Tanaka, M. Takenaga, R. Igarashi, T. Maeda, N. Yamakawa, Y. Okamoto, M.

Otsuka, T. Ishida, H. Kiwada, Y. Mizushima, T. Mizushima, Accelerated Blood Clearance Phenomenon Upon Repeated Injection of PEG-modified PLA-nanoparticles, Pharmaceutical Research, 26 (2009) 2270-2279.

[216] E. Hara, A. Makino, K. Kurihara, F. Yamamoto, E. Ozeki, S. Kimura, Pharmacokinetic change of nanoparticulate formulation "Lactosome" on multiple administrations, International Immunopharmacology, 14 (2012) 261-266.

[217] T. Suzuki, M. Ichihara, K. Hyodo, E. Yamamoto, T. Ishida, H. Kiwada, H. Ishihara, H. Kikuchi, Accelerated blood clearance of PEGylated liposomes containing doxorubicin upon repeated administration to dogs, International Journal of Pharmaceutics, 436 (2012) 636-643.

[218] H. Wei, N. Insin, J. Lee, H.-S. Han, J.M. Cordero, W. Liu, M.G. Bawendi, Compact Zwitterion-Coated Iron Oxide Nanoparticles for Biological Applications, Nano Letters, 12 (2012) 22-25.

[219] A.J. Keefe, S. Jiang, Poly(zwitterionic)protein conjugates offer increased stability without sacrificing binding affinity or bioactivity, Nat Chem, 4 (2012) 59-63.

[220] Y. Zhang, J.-Y. Liu, S. Ma, Y.-J. Zhang, X. Zhao, X.-D. Zhang, Z.-D. Zhang, Synthesis of PVP-coated ultra-small Fe3O4 nanoparticles as a MRI contrast agent, Journal of Materials Science-Materials in Medicine, 21 (2010) 1205-1210.

[221] K. Knop, R. Hoogenboom, D. Fischer, U.S. Schubert, Poly(ethylene glycol) in Drug Delivery: Pros and Cons as Well as Potential Alternatives, Angewandte Chemie-International Edition, 49 (2010) 6288-6308.

[222] R.R. Arvizo, O.R. Miranda, D.F. Moyano, C.A. Walden, K. Giri, R. Bhattacharya, J.D. Robertson, V.M. Rotello, J.M. Reid, P. Mukherjee, Modulating Pharmacokinetics, Tumor Uptake and Biodistribution by Engineered Nanoparticles, Plos One, 6 (2011).

[223] Q. Yang, S.W. Jones, C.L. Parker, W.C. Zamboni, J.E. Bear, S.K. Lai, Evading Immune Cell Uptake and Clearance Requires PEG Grafting at Densities Substantially Exceeding the Minimum for Brush Conformation, Molecular Pharmaceutics, 11 (2014) 1250-1258.

[224] S.M. Moghimi, J. Szebeni, Stealth liposomes and long circulating nanoparticles: critical issues in pharmacokinetics, opsonization and protein-binding properties, Progress in Lipid Research, 42 (2003) 463-478.

[225] K. Ujiie, N. Kanayama, K. Asai, M. Kishimoto, Y. Ohara, Y. Akashi, K. Yamada, S. Hashimoto, T. Oda, N. Ohkohchi, H. Yanagihara, E. Kita, M. Yamaguchi, H. Fujii, Y. Nagasaki, Preparation of highly dispersible and tumor-accumulative, iron oxide nanoparticles Multi-point anchoring of PEG-b-poly(4-vinylbenzylphosphonate) improves performance significantly, Colloids and Surfaces B-Biointerfaces, 88 (2011) 771-778.

[226] C. Passirani, J.-P. Benoit, Biomaterials for Delivery and Target- ing of Proteins and Nucleic Acids, CRC Press, Boca Raton, Florida 2005.

[227] W.D. Callister, D.G. Rethwisch, Fundamentals of Materials Science and Engineering, Wiley, Hoboken, New Jersy, 2011.

[228] K. Kunal, C.G. Robertson, S. Pawlus, S.F. Hahn, A.P. Sokolov, Role of chemical structure in fragility of polymers: A qualitative picture, Macromolecules, 41 (2008) 7232-7238.

[229] H. Chen, L. Wang, J. Yeh, X. Wu, Z. Cao, Y.A. Wang, M. Zhang, L. Yang, H. Mao, Reducing non-specific binding and uptake of nanoparticles and improving cell targeting with an antifouling PEO-b-P gamma MPS copolymer coating, Biomaterials, 31 (2010) 5397-5407.

[230] P.P. Karmali, Y. Chao, J.H. Park, M.J. Sailor, E. Ruoslahti, S.C. Esener, D. Simberg, Different Effect of Hydrogelation on Antifouling and Circulation Properties of Dextran-Iron Oxide Nanoparticles, Molecular Pharmaceutics, 9 (2012) 539-545.

[231] M.F. Bellin, C. Roy, K. Kinkel, D. Thoumas, S. Zaim, D. Vanel, C. Tuchmann, F. Richard, D. Jacqmin, A. Delcourt, E. Challier, T. Lebret, P. Cluzel, Lymph node metastases: Safety and effectiveness of MR imaging with ultrasmall superparamagnetic iron oxide particles - Initial clinical experience, Radiology, 207 (1998) 799-808.

[232] L. Josephson, C.H. Tung, A. Moore, R. Weissleder, High-efficiency intracellular magnetic labeling with novel superparamagnetic-tat peptide conjugates, Bioconjugate Chemistry, 10 (1999) 186-191.

[233] M. Mahmoudi, S. Sheibani, A.S. Milani, F. Rezaee, M. Gauberti, R. Dinarvand, H. Vali, Crucial role of the protein corona for the specific targeting of nanoparticles, Nanomedicine, 10 (2015) 215-226.

[234] T.L. Doane, C.H. Chuang, R.J. Hill, C. Burda, Nanoparticle zeta-Potentials, Accounts of Chemical Research, 45 (2012) 317-326.

[235] J.C. Berg, An Introduction to Interfaces and Colloids, World Scientific Publishing Co., Singapore, 2010.

[236] N.B. Shah, G.M. Vercellotti, J.G. White, A. Fegan, C.R. Wagner, J.C. Bischof, Blood-Nanoparticle Interactions and in Vivo Biodistribution: Impact of Surface PEG and Ligand Properties, Molecular Pharmaceutics, 9 (2012) 2146-2155.

[237] C. Sun, J.S.H. Lee, M. Zhang, Magnetic nanoparticles in MR imaging and drug delivery, Advanced Drug Delivery Reviews, 60 (2008) 1252.

[238] L. Maurizi, A.L. Papa, L. Dumont, F. Bouyer, P. Walker, D. Vandroux, N. Millot, Influence of Surface Charge and Polymer Coating on Internalization and Biodistribution of Polyethylene Glycol-Modified Iron Oxide Nanoparticles, Journal of Biomedical Nanotechnology, 11 (2015) 126-136.

[239] B. Chertok, A.E. David, V.C. Yang, Polyethyleneimine-modified iron oxide nanoparticles for brain tumor drug delivery using magnetic targeting and intra-carotid administration, Biomaterials, 31 (2010) 6317-6324.

[240] U. Sakulkhu, M. Mahmoudi, L. Maurizi, J. Salaklang, H. Hofmann, Protein Corona Composition of Superparamagnetic Iron Oxide Nanoparticles with Various Physico-Chemical Properties and Coatings, Scientific Reports, 4 (2014).

[241] C. Schweiger, R. Hartmann, F. Zhang, W.J. Parak, T.H. Kissel, P. Rivera Gil, Quantification of the internalization patterns of superparamagnetic iron oxide nanoparticles with opposite charge, Journal of Nanobiotechnology, 10 (2012).

[242] S. Metz, G. Bonaterra, M. Rudelius, M. Settles, E.J. Rummeny, H.E. Daldrup-Link, Capacity of human monocytes to phagocytose approved iron oxide MR contrast agents in vitro, European Radiology, 14 (2004) 1851-1858.

[243] D.E. Owens, N.A. Peppas, Opsonization, biodistribution, and pharmacokinetics of polymeric nanoparticles, International Journal of Pharmaceutics, 307 (2006) 93-102.

[244] S. Nagayama, K. Ogawara, Y. Fukuoka, K. Higaki, T. Kimura, Time-dependent changes in opsonin amount associated on nanoparticles alter their hepatic uptake characteristics, International Journal of Pharmaceutics, 342 (2007) 215-221.

[245] P. Aggarwal, J.B. Hall, C.B. McLeland, M.A. Dobrovolskaia, S.E. McNeil, Nanoparticle interaction with plasma proteins as it relates to particle biodistribution, biocompatibility and therapeutic efficacy, Advanced Drug Delivery Reviews, 61 (2009) 428-437.

[246] U. Sakulkhu, M. Mahmoudi, L. Maurizi, G. Coullerez, M. Hofmann-Amtenbrink, M. Vries, M. Motazacker, F. Rezaee, H. Hofmann, Significance of surface charge and shell material of superparamagnetic iron oxide nanoparticle (SPION) based core/shell nanoparticles on the composition of the protein corona, Biomaterials Science, 3 (2015) 265-278.

[247] M. Mahmoudi, V. Serpooshan, Large Protein Absorptions from Small Changes on the Surface of Nanoparticles, Journal of Physical Chemistry C, 115 (2011) 18275-18283.

[248] M. Mahmoudi, I. Lynch, M.R. Ejtehadi, M.P. Monopoli, F.B. Bombelli, S. Laurent, Protein-Nanoparticle Interactions: Opportunities and Challenges, Chemical Reviews, 111 (2011) 5610-5637.

[249] A.M.W. Reed, S.J. Metallo, Oriented Protein Adsorption to Gold Nanoparticles through a Genetically Encodable Binding Motif, Langmuir, 26 (2010) 18945-18950.

[250] P.P. Karmali, D. Simberg, Interactions of nanoparticles with plasma proteins: implication on clearance and toxicity of drug delivery systems, Expert Opinion on Drug Delivery, 8 (2011) 343-357.

[251] H.H.P. Yiu, Engineering the multifunctional surface on magnetic nanoparticles for targeted biomedical applications: a chemical approach, Nanomedicine, 6 (2011) 1429-1446.

[252] I.T. Lucas, S. Durand-Vidal, E. Dubois, J. Chevalet, P. Turq, Surface charge density of maghemite nanoparticles: Role of electrostatics in the proton exchange, Journal of Physical Chemistry C, 111 (2007) 18568-18576.

[253] G.W. Simmons, B.C. Beard, CHARACTERIZATION OF ACID-BASE PROPERTIES OF THE HYDRATED OXIDES ON IRON AND TITANIUM METAL-SURFACES, Journal of Physical Chemistry, 91 (1987) 1143-1148.

[254] S. Wildermuth, B. Dubno, J. Romanowski, A. Borseth, A. Annweiler, J.F. Debatin, Open-label, phase l trial of a new blood pool contrast agent (NC100150) in 12 healthy volunteers: Safety and vas- cular imaging characteristics, in: Sixth Annual Scientific Meeting of the International Society of Magnetic Resonance in Medicine (ISMRM), Sidney, 1998.

[255] H. Jackson, O. Muhammad, H. Daneshvar, J. Nelms, A. Popescu, M.A. Vogelbaum, M. Bruchez, S.A. Toms, Quantum dots are phagocytized by macrophages and co-localize with experimental glioma, Journal of Neuro-Oncology, 87 (2008) 243-243.

[256] V. Dousset, C. Gomez, K.G. Petry, C. Delalande, J.-M. Caille, Dose and scanning delay using USPIO for central nervous system macrophage imaging, Magnetic Resonance Materials in Physics Biology and Medicine, 8 (1999) 185-189.

[257] M.M. Bailey, C.J. Berkland, Nanoparticle Formulations in Pulmonary Drug Delivery, Medicinal Research Reviews, 29 (2009) 196-212.

[258] A.A. Faraj, A.P. Shaik, A.S. Shaik, Effect of surface coating on the biocompatibility and in vivo MRI detection of iron oxide nanoparticles after intrapulmonary administration, Nanotoxicology, Early Oline (2014) 1-10.

[259] A.R. Martin, R.B. Thompson, W.H. Finlay, MRI Measurement of Regional Lung Deposition in Mice Exposed Nose-Only to Nebulized Superparamagnetic Iron Oxide Nanoparticles, Journal of Aerosol Medicine and Pulmonary Drug Delivery, 21 (2008) 335-341.

[260] A. Al Faraj, G. Lacroix, H. Alsaid, D. Elgrabi, V. Stupar, F. Robidel, S. Gaillard, E. Canet-Soulas, Y. Cremillieux, Longitudinal He-3 and proton imaging of magnetite biodistribution in a rat model of instilled nanoparticles, Magnetic Resonance in Medicine, 59 (2008) 1298-1303.

[261] W.S. Cho, M.J. Cho, S.R. Kim, M. Choi, J.Y. Lee, B.S. Han, S.N. Park, M.K. Yu, S. Jon, J. Jeong, Pulmonary toxicity and kinetic study of Cy5.5-conjugated superparamagnetic iron oxide nanoparticles by optical imaging, Toxicology and Applied Pharmacology, 239 (2009) 106-115.

[262] J.L. Turi, F.M. Yang, M.D. Garrick, C.A. Piantadosi, A.J. Ghio, The iron cycle and oxidative stress in the lung, Free Radical Biology and Medicine, 36 (2004) 850-857.

[263] E.A. Heilig, K.J. Thompson, R.M. Molina, A.R. Ivanov, J.D. Brain, M. Wessling-Resnick, Manganese and iron transport across pulmonary epithelium, American Journal of Physiology-Lung Cellular and Molecular Physiology, 290 (2006) L1247-L1259.

[264] C.R.A. Valois, J.M. Braz, E.S. Nunes, M.A.R. Vinolo, E.C.D. Lima, R. Curi, W.M. Kuebler, R.B. Azevedo, The effect of DMSA-functionalized magnetic nanoparticles on transendothelial migration of monocytes in the murine lung via a beta(2) integrin-dependent pathway, Biomaterials, 31 (2010) 366-374.

[265] F.W. Merkus, M.P.v.d. Berg, Can nasal drug delivery bypass the blood-brain barrier?: questioning the direct transport theory, Drugs in R&D, 8 (2007) 133-144.

[266] B. Wang, W.Y. Feng, M. Wang, J.W. Shi, F. Zhang, H. Ouyang, Y.L. Zhao, Z.F. Chai, Y.Y. Huang, Y.N. Xie, H.F. Wang, J. Wang, Transport of intranasally instilled fine Fe2O3 particles into the brain: Micro-distribution, chemical states, and histopathological observation, Biological Trace Element Research, 118 (2007) 233-243.

[267] D.B. Rao, B.A. Wong, B.E. McManus, A.M. McElveen, A.R. James, D.C. Dorman, Inhaled iron, unlike manganese, is not transported to the rat brain via the olfactory pathway, Toxicology and Applied Pharmacology, 193 (2003) 116-126.

[268] J.T. Kwon, S.K. Hwang, H. Jin, D.S. Kim, A. Mina-Tehrani, H.J. Yoon, M. Chop, T.J. Yoon, D.Y. Han, Y.W. Kang, B.I. Yoon, J.K. Lee, M.H. Cho, Body distribution of inhaled fluorescent magnetic nanoparticles in the mice, Journal of Occupational Health, 50 (2008) 1-6.

[269] J.T. Kwon, D.S. Kim, A. Minai-Tehrani, S.K. Hwang, S.H. Chang, E.S. Lee, C.X. Xu, H.T. Lim, J.E. Kim, B.I. Yoon, G.H. An, K.H. Lee, J.K. Lee, M.H. Cho, Inhaled Fluorescent Magnetic Nanoparticles Induced Extramedullary Hematopoiesis in the Spleen of Mice, Journal of Occupational Health, 51 (2009) 423-431.

[270] C. Geraldes, S. Laurent, Classification and basic properties of contrast agents for magnetic resonance imaging, Contrast Media & Molecular Imaging, 4 (2009) 1-23.

[271] P.F. Hahn, D.D. Stark, J.M. Lewis, S. Saini, G. Elizondo, R. Weissleder, C.J. Fretz, J.T. Ferrucci, 1ST CLINICAL-TRIAL OF A NEW SUPERPARAMAGNETIC IRON-OXIDE FOR USE AS AN ORAL GASTROINTESTINAL CONTRAST AGENT IN MR IMAGING, Radiology, 175 (1990) 695-700.

[272] R.C.H. Heusler, E. Wight, B. Marincek, ORAL SUPERPARAMAGNETIC CONTRAST AGENT (FERUMOXSIL) - TOLERANCE AND EFFICACY IN MR-IMAGING OF GYNECOLOGIC DISEASES, Jmri-Journal of Magnetic Resonance Imaging, 5 (1995) 385-391.

[273] J.J. Cheng, B.A. Teply, S.Y. Jeong, C.H. Yim, D. Ho, I. Sherifi, S. Jon, O.C. Farokhzad, A. Khademhosseini, R.S. Langer, Magnetically responsive polymeric microparticles for oral delivery of protein drugs, Pharmaceutical Research, 23 (2006) 557-564.

[274] M. Goldberg, I. Gomez-Orellana, Challenges for the oral delivery of macromolecules, Nature Reviews Drug Discovery, 2 (2003) 289-295.

[275] H.D. Singh, S. Roychowdhury, P. Verma, V. Bhandari, A review on recent advances of enteric coating IOSR Journal of Pharmacy, 2 (2012) 5-11.

[276] J. Huang, Q. Shu, L.Y. Wang, H. Wu, A.Y. Wang, H. Mao, Layer-by-layer assembled milk protein coated magnetic nanoparticle enabled oral drug delivery with high stability in stomach and enzyme-responsive release in small intestine, Biomaterials, 39 (2015) 105-113.

[277] J.T. Sockolosky, M.R. Tiffany, F.C. Szoka, Engineering neonatal Fc receptor-mediated recycling and transcytosis in recombinant proteins by short terminal peptide extensions, Proceedings of the National Academy of Sciences of the United States of America, 109 (2012) 16095-16100.

[278] C.A. Smith, C.A. Simpson, G. Kim, C.J. Carter, D.L. Feldheim, Gastrointestinal Bioavailability of 2.0 nm Diameter Gold Nanoparticles, Acs Nano, 7 (2013) 3991-3996.

[279] J.R. Kanwar, K. Roy, R.K. Kanwar, Chimeric aptamers in cancer cell-targeted drug delivery, Critical Reviews in Biochemistry and Molecular Biology, 46 (2011) 459-477.

[280] K. Tsuchiya, N. Nitta, A. Sonoda, A. Nitta-Seko, S. Ohta, H. Otani, M. Takahashi, K. Murata, K. Murase, S. Nohara, K. Mukaisho, Histological study of the biodynamics of iron oxide nanoparticles with different diameters, International Journal of Nanomedicine, 6 (2011) 1-8.

[281] J.S. Kim, T.J. Yoon, B.G. Kim, S.J. Park, H.W. Kim, K.H. Lee, S.B. Park, J.K. Lee, M.H. Cho, Toxicity and tissue distribution of magnetic nanoparticles in mice, Toxicological Sciences, 89 (2006) 338-347.

[282] W.W. Wu, B.A. Chen, J.A. Cheng, J. Wang, W.L. Xu, L.J. Liu, G.H. Xia, H.L. Wei, X.M. Wang, M.M. Yang, L.Y. Yang, Y. Zhang, C.L. Xu, J.Y. Li, Biocompatibility of Fe3O4/DNR magnetic nanoparticles in the treatment of hematologic malignancies, International Journal of Nanomedicine, 5 (2010) 1079-1084.

[283] H.B. Raju, Y. Hu, K.R. Padgett, J.E. Rodriguez, J.L. Goldberg, Investigation of nanoparticles using magnetic resonance imaging after intravitreal injection, Clinical and Experimental Ophthalmology, 40 (2012) 100-107.

[284] J. Harrison, C.A. Bartlett, G. Cowin, P.K. Nicholls, C.W. Evans, T.D. Clemons, B. Zdyrko, I.A. Luzinov, A.R. Harvey, K.S. Iyer, S.A. Dunlop, M. Fitzgerald, In vivo Imaging and Biodistribution of Multimodal Polymeric Nanoparticles Delivered to the Optic Nerve, Small, 8 (2012) 1579-1589.

[285] F. Gardikiotis, C. Peptu, M. Popa, D. Costin, Nanoparticles biodistribution in the eye, Oftalmologia, 55 (2011) 92-96.

[286] K. Pusic, Z. Aguilar, J. McLoughlin, S. Kobuch, H. Xu, M. Tsang, A. Wang, G. Hui, Iron oxide nanoparticles as a clinically acceptable delivery platform for a recombinant blood-stage human malaria vaccine, Faseb Journal, 27 (2013) 1153-1166.

[287] L. Johnson, S.E. Pinder, M. Douek, Deposition of superparamagnetic iron-oxide nanoparticles in axillary sentinel lymph nodes following subcutaneous injection, Histopathology, 62 (2013) 481-486.

[288] D.J. Grootendorst, J. Jose, R.M. Fratila, M. Visscher, A.H. Velders, B. Ten Haken, T.G. Van Leeuwen, W. Steenbergen, S. Manohar, T.J.M. Ruers, Evaluation of superparamagnetic iron oxide nanoparticles (Endorem (R)) as a photoacoustic

contrast agent for intra-operative nodal staging, Contrast Media & Molecular Imaging, 8 (2013) 83-91.

[289] Z.R. Stephen, F.M. Kievit, O. Veiseh, P.A. Chiarelli, C. Fang, K. Wang, S.J. Hatzinger, R.G. Ellenbogen, J.R. Silber, M.Q. Zhang, Redox-Responsive Magnetic Nanoparticle for Targeted Convection-Enhanced Delivery of O-6-Benzylguanine to Brain Tumors, Acs Nano, 8 (2014) 10383-10395.

[290] E. Corem-Salkmon, Z. Ram, D. Daniels, B. Perlstein, D. Last, S. Salomon, G. Tamar, R. Shneor, D. Guez, S. Margel, Y. Mardor, Convection-enhanced delivery of methotrexate-loaded maghemite nanoparticles, International Journal of Nanomedicine, 6 (2011) 1595-1602.

[291] G. De Rosa, G. Salzano, M. Caraglia, A. Abbruzzese, Nanotechnologies: A Strategy to Overcome Blood-Brain Barrier, Current Drug Metabolism, 13 (2012) 61-69.

[292] S.L. Raut, B. Kirthivasan, M.M. Bommana, E. Squillante, M. Sadoqi, The formulation, characterization and in vivo evaluation of a magnetic carrier for brain delivery of NIR dye, Nanotechnology, 21 (2010).

[293] E.A. Rozhkova, Nanoscale Materials for Tackling Brain Cancer: Recent Progress and Outlook, Advanced Materials, 23 (2011) H136-H150.

[294] R. Chen, G. Romero, M.G. Christiansen, A. Mohr, P. Anikeeva, Wireless magnetothermal deep brain stimulation, Science, 347 (2015) 1477-1480.

[295] R.D.O. Engberink, E.L.A. Blezer, C.D. Dijkstra, S.M.A. van der Pol, A. van der Toorn, H.E. de Vries, Dynamics and fate of USPIO in the central nervous system in

experimental autoimmune encephalomyelitis, NMR in Biomedicine, 23 (2010) 1087-1096.

[296] C. Petters, E. Irrsack, M. Koch, R. Dringen, Uptake and Metabolism of Iron Oxide Nanoparticles in Brain Cells, Neurochemical Research, 39 (2014) 1648-1660.

[297] C.L. Stanfield, W.J. Germann, Principles of Human Physiology, 3rd edition ed., Pearson Education Inc., San Francisco, 2008.

[298] K. Cho, X. Wang, S. Nie, Z. Chen, D.M. Shin, Therapeutic Nanoparticles for Drug Delivery in Cancer, Clinical Cancer Research, 14 (2008) 1310.

[299] H. Sarin, A.S. Kanevsky, H.T. Wu, A.A. Sousa, C.M. Wilson, M.A. Aronova, G.L. Griffiths, R.D. Leapman, H.Q. Vo, Physiologic upper limit of pore size in the blood-tumor barrier of malignant solid tumors, Journal of Translational Medicine, 7 (2009).

[300] Z. Poon, J.B. Lee, S.W. Morton, P.T. Hammond, Controlling in Vivo Stability and Biodistribution in Electrostatically Assembled Nanoparticles for Systemic Delivery, Nano Letters, 11 (2011) 2096-2103.

[301] R.K. Jain, T. Stylianopoulos, Delivering nanomedicine to solid tumors, Nature Reviews Clinical Oncology, 7 (2010) 653-664.

[302] R. Ranganathan, S. Madanmohan, A. Kesavan, G. Baskar, Y.R. Krishnamoorthy, R. Santosham, D. Ponraju, S.K. Rayala, G. Venkatraman, Nanomedicine: towards development of patient-friendly drug-delivery systems for oncological applications, International Journal of Nanomedicine, 7 (2012) 1043-1060.

[303] E. Gultepe, F.J. Reynoso, A. Jhaveri, P. Kulkarni, D. Nagesha, C. Ferris, M. Harisinghani, R.B. Campbell, S. Sridhar, Monitoring of magnetic targeting to tumor vasculature through MRI and biodistribution, Nanomedicine, 5 (2010) 1173-1182.

[304] S.D. Perrault, C. Walkey, T. Jennings, H.C. Fischer, W.C.W. Chan, Mediating Tumor Targeting Efficiency of Nanoparticles Through Design, Nano Letters, 9 (2009) 1909-1915.

[305] M. Yu, J. Zheng, Clearance Pathways and Tumor Targeting of Imaging Nanoparticles, ACS Nano, 9 (2015) 6655-6674.

[306] L. Agemy, K.N. Sugahara, V.R. Kotamraju, K. Gujraty, O.M. Girard, Y. Kono, R.F. Mattrey, J.-H. Park, M.J. Sailor, A.I. Jimenez, C. Cativiela, D. Zanuy, F.J. Sayago, C. Aleman, R. Nussinov, E. Ruoslahti, Nanoparticle-induced vascular blockade in human prostate cancer, Blood, 116 (2010) 2847-2856.

[307] F. Yamashita, M. Hashida, Pharmacokinetic considerations for targeted drug delivery, Advanced Drug Delivery Reviews, 65 (2013) 139-147.

[308] C. Plank, NANOMEDICINE Silence the target, Nature Nanotechnology, 4 (2009) 544-545.

[309] M.L.M. Pisciotti, E. Lima, M.V. Mansilla, V.E. Tognoli, H.E. Troiani, A.A. Pasa, T.B. Creczynski-Pasa, A.H. Silva, P. Gurman, L. Colombo, G.F. Goya, A. Lamagna, R.D. Zysler, In vitro and in vivo experiments with iron oxide nanoparticles functionalized with DEXTRAN or polyethylene glycol for medical applications: Magnetic targeting, Journal of Biomedical Materials Research Part B-Applied Biomaterials, 102 (2014) 860-868.

[310] N. Schleich, C. Po, D. Jacobs, B. Ucakar, B. Gallez, F. Danhier, V. Preat, Comparison of active, passive and magnetic targeting to tumors of multifunctional paclitaxel/SPIO-loaded nanoparticles for tumor imaging and therapy, Journal of Controlled Release, 194 (2014) 82-91.

[311] M.G. Krukemeyer, V. Krenn, M. Jakobs, W. Wagner, Mitoxantrone-Iron Oxide Biodistribution in Blood, Tumor, Spleen, and Liver-Magnetic Nanoparticles in Cancer Treatment, Journal of Surgical Research, 175 (2012) 35-43.

[312] Y. Bao, T. Wen, A.C.S. Samia, A. Khandhar, K.M. Krishnan, Magnetic nanoparticles: material engineering and emerging applications in lithography and biomedicine, Journal of Materials Science, 51 (2016) 513-553.

[313] H.-C. Huang, S. Barua, G. Sharma, S.K. Dey, K. Rege, Inorganic nanoparticles for cancer imaging and therapy, Journal of Controlled Release, 155 (2011) 344-357.

[314] W.C. Zamboni, V. Torchilin, A.K. Patri, J. Hrkach, S. Stern, R. Lee, A. Nel, N.J. Panaro, P. Grodzinski, Best Practices in Cancer Nanotechnology: Perspective from NCI Nanotechnology Alliance, Clinical Cancer Research, 18 (2012) 3229-3241.

[315] S.E. Lee, K.J. Choi, G.K. Menon, H.J. Kim, E.H. Choi, S.K. Ahn, S.H. Lee, Penetration Pathways Induced by Low-Frequency Sonophoresis with Physical and Chemical Enhancers: Iron Oxide Nanoparticles versus Lanthanum Nitrates, Journal of Investigative Dermatology, 130 (2010) 1063-1072.

[316] B. Baroli, M.G. Ennas, F. Loffredo, M. Isola, R. Pinna, M.A. Lopez-Quintela, Penetration of metallic nanoparticles in human full-thickness skin, Journal of Investigative Dermatology, 127 (2007) 1701-1712.

[317] O. Ziv-Polat, M. Topaz, T. Brosh, S. Margel, Enhancement of incisional wound healing by thrombin conjugated iron oxide nanoparticles, Biomaterials, 31 (2010) 741-747.

[318] P. Rucker, F.M. Torti, S.V. Torti, Role of H and L subunits in mouse ferritin, Journal of Biological Chemistry, 271 (1996) 33352-33357.

[319] E. Alphandery, S. Faure, O. Seksek, F. Guyot, I. Chebbi, Chains of Magnetosomes Extracted from AMB-1 Magnetotactic Bacteria for Application in Alternative Magnetic Field Cancer Therapy, Acs Nano, 5 (2011) 6279-6296.

[320] J. Nissim, Intravenous iron (M.D. thesis), University of London, London, 1949.

[321] G.W. Richter, THE CELLULAR TRANSFORMATION OF INJECTED COLLOIDAL IRON COMPLEXES INTO FERRITIN AND HEMOSIDERIN IN EXPERIMENTAL ANIMALS - A STUDY WITH THE AID OF ELECTRON MICROSCOPY, Journal of Experimental Medicine, 109 (1959) 197-&.

[322] A.S. Arbab, L.B. Wilson, P. Ashari, E.K. Jordan, B.K. Lewis, J.A. Frank, A model of lysosomal metabolism of dextran coated superparamagnetic iron oxide (SPIO) nanoparticles: implications for cellular magnetic resonance imaging, NMR in Biomedicine, 18 (2005) 383-389.

[323] Wahajuddin, S. Arora, Superparamagnetic iron oxide nanoparticles: magnetic nanoplatforms as drug carriers, International Journal of Nanomedicine, 7 (2012) 3445-3471.

[324] O. Lunov, T. Syrovets, C. Roecker, K. Tron, G.U. Nienhaus, V. Rasche, V. Mailaender, K. Landfester, T. Simmet, Lysosomal degradation of the carboxydextran

shell of coated superparamagnetic iron oxide nanoparticles and the fate of professional phagocytes, Biomaterials, 31 (2010) 9015-9022.

[325] K.C. Briley-Saebo, L.O. Johansson, S.O. Hustvedt, A.G. Haldorsen, A. Bjornerud, Z.A. Fayad, H.K. Ahlstrom, Clearance of iron oxide particles in rat liver - Effect of hydrated particle size and coating material on liver metabolism, Investigative Radiology, 41 (2006) 560-571.

[326] M.-Y. Hua, H.-L. Liu, H.-W. Yang, P.-Y. Chen, R.-Y. Tsai, C.-Y. Huang, I.C. Tseng, L.-A. Lyu, C.-C. Ma, H.-J. Tang, T.-C. Yen, K.-C. Wei, The effectiveness of a magnetic nanoparticle-based delivery system for BCNU in the treatment of gliomas, Biomaterials, 32 (2011) 516-527.

[327] H. Arami, K.M. Krishnan, Intracellular performance of tailored nanoparticle tracers in magnetic particle imaging, Journal of Applied Physics, 115 (2014) 17B306.

[328] E. Okon, D. Pouliquen, P. Okon, Z.V. Kovaleva, T.P. Stepanova, S.G. Lavit, B.N. Kudryavtsev, P. Jallet, BIODEGRADATION OF MAGNETITE DEXTRAN NANOPARTICLES IN THE RAT - A HISTOLOGIC AND BIOPHYSICAL STUDY, Laboratory Investigation, 71 (1994) 895-903.

[329] K. Briley-Saebo, A. Bjornerud, D. Grant, H. Ahlstrom, T. Berg, G.M. Kindberg, Hepatic cellular distribution and degradation of iron oxide nanoparticles following single intravenous injection in rats: implications for magnetic resonance imaging, Cell and Tissue Research, 316 (2004) 315-323.

[330] K. Briley-Saebo, S.A. Hustvedt, A. Haldorsen, A. Bjornerud, Long-term imaging effects in rat liver after a single injection of an iron oxide nanoparticle based MR contrast agent, Journal of Magnetic Resonance Imaging, 20 (2004) 622-631.

[331] J.H. Jensen, H.Y. Tang, C.L. Tosti, S.V. Swaminathan, A. Nunez, K. Hultman, K.U. Szulc, E.X. Wu, D. Kim, S. Sheth, T.R. Brown, G.M. Brittenham, Separate MRI Quantification of Dispersed (Ferritin-like) and Aggregated (Hemosiderin-like) Storage Iron, Magnetic Resonance in Medicine, 63 (2010) 1201-1209.

[332] E. Sarac, N. Haroon, J. John, D. Gemmel, SAFETY AND EFFICACY OF INTERCHANGE FROM FERRLECIT TO FERAHEME IN OUTPATIENT DIALYSIS POPULATION, American Journal of Kidney Diseases, 59 (2012) A74-A74.

[333] S. Shanehsazzadeh, M.A. Oghabian, F.J. Daha, M. Amanlou, B.J. Allen, Biodistribution of ultra small superparamagnetic iron oxide nanoparticles in BALB mice, Journal of Radioanalytical and Nuclear Chemistry, 295 (2013) 1517-1523.

[334] M. Ahmd, K. Rashid, M. Nadeem, K. Masood, S. Ali, M. Nafees, N. Gull, Mumtaz-ul-Haq, N. Ibrahim, A. Saeed, A. Qureshy, F. Aleem, H. Naseer, S. Mehmood, S.W. Hyder, A Simple Method to Prepare Aqueous Dispersion of Iron Oxide Nanoparticles and Their Biodistribution Study, Journal of Colloid Science and Biotechnology, 1 (2012) 201-209.

[335] R. Chakravarty, H.F. Valdovinos, F. Chen, C.M. Lewis, P.A. Ellison, H. Luo, M.E. Meyerand, R.J. Nickles, W. Cai, Intrinsically Germanium-69-Labeled Iron Oxide Nanoparticles: Synthesis and In-Vivo Dual-Modality PET/MR Imaging, Advanced Materials, 26 (2014) 5119-5123.

[336] B. Freund, U.I. Tromsdorf, O.T. Bruns, M. Heine, A. Giemsa, A. Bartelt, S.C. Salmen, N. Raabe, J. Heeren, H. Ittrich, R. Reimer, H. Hohenberg, U. Schumacher, H. Weller, P. Nielsen, A Simple and Widely Applicable Method to Fe-59-Radiolabel Monodisperse Superparamagnetic Iron Oxide Nanoparticles for In Vivo Quantification Studies, Acs Nano, 6 (2012) 7318-7325.

[337] H.T. Wang, R. Kumar, D. Nagesha, R.I. Duclos, S. Sridhar, S.J. Gatley, Integrity of In-111-radiolabeled superparamagnetic iron oxide nanoparticles in the mouse, Nuclear Medicine and Biology, 42 (2015) 65-70.

[338] P. Bourrinet, H.H. Bengele, B. Bonnemain, A. Dencausse, J.M. Idee, P.M. Jacobs, J.M. Lewis, Preclinical safety and pharmacokinetic profile of ferumoxtran-10, an ultrasmall superparamagnetic iron oxide magnetic resonance contrast agent, Investigative Radiology, 41 (2006) 313-324.

[339] J.A. Tate, A.A. Petryk, A.J. Giustini, P.J. Hoopes, In vivo biodistribution of iron oxide nanoparticles: an overview, SPIE Proceedings, 7901 (2011) 1-9.

[340] J.M. Berg, J.L. Tymoczko, L. Stryer, Biochemistry, 5th ed., W H Freeman, New York, 2002.

[341] X.L. Zhang, C.S. Liu, Y. Yuan, X.Q. Shan, Y. Sheng, F. Xu, Reduction and Suppression of Methemoglobin Loaded in the Polymeric Nanoparticles Intended for Blood Substitutes, Journal of Biomedical Materials Research Part B-Applied Biomaterials, 87B (2008) 354-363.

[342] A. Hanini, A. Schmitt, K. Kacem, F. Chau, S. Ammar, J. Gavard, Evaluation of iron oxide nanoparticle biocompatibility, International Journal of Nanomedicine, 6 (2011) 787-794.

[343] C. Geers, G. Gros, Carbon dioxide transport and carbonic anhydrase in blood and muscle, Physiological Reviews, 80 (2000) 681-715.

[344] X.Q. Yang, H. Hong, J.J. Grailer, I.J. Rowland, A. Javadi, S.A. Hurley, Y.L. Xiao, Y.A. Yang, Y. Zhang, R. Nickles, W.B. Cai, D.A. Steeber, S.Q. Gong, cRGD-functionalized, DOX-conjugated, and Cu-64-labeled superparamagnetic iron oxide nanoparticles for targeted anticancer drug delivery and PET/MR imaging, Biomaterials, 32 (2011) 4151-4160.

[345] L.L.C. Estevanato, L.M. Lacava, L.C.F. Carvalho, R.B. Azevedo, O. Silva, F. Pelegrini, S.N. Bao, P.C. Morais, Z.G.M. Lacava, Long-Term Biodistribution and Biocompatibility Investigation of Dextran-Coated Magnetite Nanoparticle Using Mice as the Animal Model, Journal of Biomedical Nanotechnology, 8 (2012) 301-308.

[346] B. Chertok, A.J. Cole, A.E. David, V.C. Yang, Comparison of Electron Spin Resonance Spectroscopy and Inductively-Coupled Plasma Optical Emission Spectroscopy for Biodistribution Analysis of Iron-Oxide Nanoparticles, Molecular Pharmaceutics, 7 (2010) 375-385.

[347] A.J. Giustini, R. Ivkov, P.J. Hoopes, Magnetic nanoparticle biodistribution following intratumoral administration, Nanotechnology, 22 (2011).

[348] M. Thaler, S. Roy, A. Fornara, M. Bitsche, J. Qin, M. Muhammed, W. Salvenmoser, G. Rieger, A.S. Fischer, R. Glueckert, Visualization and analysis of superparamagnetic iron oxide nanoparticles in the inner ear by light microscopy and energy filtered TEM, Nanomedicine-Nanotechnology Biology and Medicine, 7 (2011) 360-369.

[349] R.T.M. de Rosales, R. Tavare, A. Glaria, G. Varma, A. Protti, P.J. Blower, Tc-99m-Bisphosphonate-Iron Oxide Nanoparticle Conjugates for Dual-Modality Biomedical Imaging, Bioconjugate Chemistry, 22 (2011) 455-465.

[350] L. Maurizi, U. Sakulkhu, A. Gramoun, J.P. Vallee, H. Hofmann, A fast and reproducible method to quantify magnetic nanoparticle biodistribution, Analyst, 139 (2014) 1184-1191.

[351] J. Zhuang, K.L. Fan, L.Z. Gao, D. Lu, J. Feng, D.L. Yang, N. Gu, Y. Zhang, M.M. Liang, X.Y. Yan, Ex Vivo Detection of Iron Oxide Magnetic Nanoparticles in Mice Using Their Intrinsic Peroxidase-Mimicking Activity, Molecular Pharmaceutics, 9 (2012) 1983-1989.

[352] H. Ding, F. Wu, Image Guided Biodistribution and Pharmacokinetic Studies of Theranostics, Theranostics, 2 (2012) 1040-1053.

[353] P.J. Hoopes, A.A. Petryka, B. Gimib, A.J. Giustini, J.B. Weaver, J. Bischof, R. Chamberlaine, M. Garwoode, In Vivo Imaging and Quantification of Iron Oxide Nanoparticle Uptake and Biodistribution, Proceeding of SPIE, 8317 (2012) 83170R83171-83170R-83179.

[354] R.M. Ferguson, A.P. Khandhar, H. Arami, L. Hua, O. Hovorka, K.M. Krishnan, Tailoring the magnetic and pharmacokinetic properties of iron oxide MPI tracers, Biomedical Engineering, 58 (2013) 493-507.

[355] L.M. Bauer, S.F. Situ, M.A. Griswold, A.C.S. Samia, Magnetic Particle Imaging Tracers: State-of-the-Art and Future Directions, The Journal of Physical Chemistry Letters, 6 (2015) 2509-2517.

[356] H. Mok, O. Veiseh, C. Fang, F.M. Kievit, F.Y. Wang, J.O. Park, M.Q. Zhang, pH-Sensitive siRNA Nanovector for Targeted Gene Silencing and Cytotoxic Effect in Cancer Cells, Molecular Pharmaceutics, 7 (2010) 1930-1939.

[357] M. Bellusci, A. La Barbera, F. Padella, M. Mancuso, A. Pasquo, M.G. Grollino, G. Leter, E. Nardi, C. Cremisini, P. Giardullo, F. Pacchierotti, Biodistribution and acute toxicity of a nanofluid containing manganese iron oxide nanoparticles produced by a mechanochemical process, International Journal of Nanomedicine, 9 (2014) 1919-1929.

[358] L.F. Gamarra, A.J. daCosta-Filho, J.B. Mamani, R.d.C. Ruiz, L.F. Pavon, T.T. Sibov, E.D. Vieira, A.C. Silva, W.M. Pontuschka, E. Amaro, Jr., Ferromagnetic resonance for the quantification of superparamagnetic iron oxide nanoparticles in biological materials, International Journal of Nanomedicine, 5 (2010) 203-211.

[359] N. Raabe, E. Forberich, B. Freund, O.T. Bruns, M. Heine, M.G. Kaul, U. Tromsdorf, L. Herich, P. Nielsen, R. Reimer, H. Hohenberg, H. Weller, U. Schumacher, G. Adam, H. Ittrich, Determination of liver-specific r2* of a highly monodisperse USPIO by 59Fe iron core-labeling in mice at 3 T MRI, Contrast Media & Molecular Imaging, 10 (2015) 153-162.

[360] J.F. Zeng, B. Jia, R.R. Qiao, C. Wang, L.H. Jing, F. Wang, M.Y. Gao, In situ In-111-doping for achieving biocompatible and non-leachable In-111-labeled Fe3O4 nanoparticles, Chemical Communications, 50 (2014) 2170-2172.

[361] D. Bargheer, A. Giemsa, B. Freund, M. Heine, C. Waurisch, G.M. Stachowski, S.G. Hickey, A. Eychmueller, J. Heeren, P. Nielsen, The distribution and degradation of radiolabeled superparamagnetic iron oxide nanoparticles and quantum dots in mice, Beilstein Journal of Nanotechnology, 6 (2015) 111-123.

[362] E.-J. Cha, E.S. Jang, I.-C. Sun, I.J. Lee, J.H. Ko, Y.I. Kim, I.C. Kwon, K. Kim, C.-H. Ahn, Development of MRI/NIRF 'activatable' multimodal imaging probe based on iron oxide nanoparticles, Journal of Controlled Release, 155 (2011) 152-158.

[363] S.P. Foy, R.L. Manthe, S.T. Foy, S. Dimitrijevic, N. Krishnamurthy, V. Labhasetwar, Optical Imaging and Magnetic Field Targeting of Magnetic Nanoparticles in Tumors, Acs Nano, 4 (2010) 5217-5224.

[364] S.H. Crayton, D.R. Elias, A. Al Zaki, Z. Cheng, A. Tsourkas, ICP-MS analysis of lanthanide-doped nanoparticles as a non-radiative, multiplex approach to quantify biodistribution and blood clearance, Biomaterials, 33 (2012) 1509-1519.

[365] P.C. Naha, A. Al Zaki, E. Hecht, M. Chorny, P. Chhour, E. Blankemeyer, D.M. Yates, W.R.T. Witschey, H.I. Litt, A. Tsourkas, D.P. Cormode, Dextran coated bismuth-iron oxide nanohybrid contrast agents for computed tomography and magnetic resonance imaging, Journal of Materials Chemistry B, 2 (2014) 8239-8248.

[366] M. Li, J. Reineke, Physiologically Based Pharmacokinetic Modeling for Nanoparticle Toxicity Study, Nanotoxicity: Methods and Protocols, Methods in Molecular Biology, 926 (2012) 369-382.

[367] S. Wada, L. Yue, K. Tazawa, I. Furuta, H. Nagae, S. Takemori, T. Minamimura, New local hyperthermia using dextran magnetite complex (DM) for oral cavity: experimental study in normal hamster tongue, Oral Diseases, 7 (2001) 192-195.

[368] S. Puntarulo, Iron, oxidative stress and human health, Molecular Aspects of Medicine, 26 (2005) 299-312.

[369] S.J.H. Soenen, M. De Cuyper, Assessing iron oxide nanoparticle toxicity in vitro: current status and future prospects, Nanomedicine, 5 (2010) 1261-1275.

[370] V. Monge-Fuentes, M.P. Garcia, M.C.H. Tavares, C.R.A. Valois, E.C.D. Lima, D.S. Teixeira, P.C. Morais, C. Tomaz, R.B. Azevedo, Biodistribution and biocompatibility of DMSA-stabilized maghemite magnetic nanoparticles in nonhuman primates (Cebus spp.), Nanomedicine, 6 (2011) 1529-1544.

[371] T.K. Jain, M.K. Reddy, M.A. Morales, D.L. Leslie-Pelecky, V. Labhasetwar, Biodistribution, clearance, and biocompatibility of iron oxide magnetic nanoparticles in rats, Molecular Pharmaceutics, 5 (2008) 316-327.

[372] R. Mejias, S. Perez-Yaguee, L. Gutierrez, L.I. Cabrera, R. Spada, P. Acedo, C.J. Serna, F.J. Lazaro, A. Villanueva, M. del Puerto Morales, D.F. Barber, Dimercaptosuccinic acid-coated magnetite nanoparticles for magnetically guided in vivo delivery of interferon gamma for cancer immunotherapy, Biomaterials, 32 (2011) 2938-2952.

[373] S.B. Chaves, L.M. Lacava, Z.G.M. Lacava, O. Silva, F. Pelegrini, N. Buske, C. Gansau, P.C. Morais, R.B. Azevedo, Light microscopy and magnetic resonance characterization of a DMSA-coated magnetic fluid in mice, Ieee Transactions on Magnetics, 38 (2002) 3231-3233.

[374] R. Mejias, S. Perez-Yaguee, A.G. Roca, N. Perez, A. Villanueva, M. Canete, S. Manes, J. Ruiz-Cabello, M. Benito, A. Labarta, X. Batlle, S. Veintemillas-Verdaguer, M. Puerto Morales, D.F. Barber, C.J. Serna, Liver and brain imaging through dimercaptosuccinic acid-coated iron oxide nanoparticles, Nanomedicine, 5 (2010) 397-408.

[375] J.H. Feng, H.L. Liu, L.M. Zhang, K. Bhakoo, L.H. Lu, An insight into the metabolic responses of ultra-small superparamagnetic particles of iron oxide using metabonomic analysis of biofluids, Nanotechnology, 21 (2010).

[376] J.H. Feng, H.L. Liu, K.K. Bhakoo, L.H. Lu, Z. Chen, A metabonomic analysis of organ specific response to USPIO administration, Biomaterials, 32 (2011) 6558-6569.

[377] E.J. Park, H. Kim, Y. Kim, J. Yi, K. Choi, K. Park, Inflammatory responses may be induced by a single intratracheal instillation of iron nanoparticles in mice, Toxicology, 275 (2010) 65-71.

[378] G. Masselli, G. Gualdi, MR Imaging of the Small Bowel, Radiology, 264 (2012) 333-348.

[379] J. Wang, B. Chen, N. Jin, G. Xia, Y. Chen, Y. Zhou, X. Cai, J. Ding, X. Li, X. Wang, The changes of T lymphocytes and cytokines in ICR mice fed with Fe3O4 magnetic nanoparticles, International Journal of Nanomedicine, 6 (2011) 605-610.

[380] M. Kumari, S. Rajak, S.P. Singh, S.I. Kumari, P.U. Kumar, U.S.N. Murty, M. Mahboob, P. Grover, M.F. Rahman, Repeated Oral Dose Toxicity of Iron Oxide Nanoparticles: Biochemical and Histopathological Alterations in Different Tissues of Rats, Journal of Nanoscience and Nanotechnology, 12 (2012) 2149-2159.

[381] K.R. Di Bona, Y. Xu, P.A. Ramirez, J. DeLaine, C. Parker, Y. Bao, J.F. Rasco, Surface charge and dosage dependent potential developmental toxicity and biodistribution of iron oxide nanoparticles in pregnant CD-1 mice, Reproductive Toxicology, 50 (2014) 36-42.

[382] P.L. McCormack, Ferumoxytol In Iron Deficiency Anaemia in Adults With Chronic Kidney Disease, Drugs, 72 (2012) 2013-2022.

[383] S. Motoyama, K. Ishiyama, K. Maruyama, K. Narita, Y. Minamiya, J.-i. Ogawa, Estimating the Need for Neck Lymphadenectomy in Submucosal Esophageal Cancer Using Superparamagnetic Iron Oxide-Enhanced Magnetic Resonance Imaging: Clinical Validation Study, World Journal of Surgery, 36 (2012) 83-89.

[384] S.P.S. Howarth, T.Y. Tang, R. Trivedi, R. Weerakkody, J. U-King-Im, M.E. Gaunt, J.R. Boyle, Z.Y. Li, S.R. Miller, M.J. Graves, J.H. Gillard, Utility of USPIO-enhanced MR imaging to identify inflammation and the fibrous cap: A comparison of symptomatic and asymptomatic individuals, European Journal of Radiology, 70 (2009) 555-560.

[385] H. Bernd, E. De Kerviler, S. Gaillard, B. Bonnemain, Safety and Tolerability of Ultrasmall Superparamagnetic Iron Oxide Contrast Agent Comprehensive Analysis of a Clinical Development Program, Investigative Radiology, 44 (2009) 336-342.

[386] Rienso (ferumoxytol): summary of product characteristics, in, London: Takeda Global Research and Development Centre (Europe) Ltd, June 2012.

[387] S. Fishbane, W.K. Bolton, W.C. Winkelmayer, W. Strauss, Z. Li, B.J.G. Pereira, Factors affecting response and tolerability to ferumoxytol in nondialysis chronic kidney disease patients, Clinical Nephrology, 78 (2012) 181-188.

[388] D. Hasan, N. Chalouhi, P. Jabbour, A.S. Dumont, D.K. Kung, V.A. Magnotta, W.L. Young, T. Hashimoto, H.R. Winn, D. Heistad, Early Change in Ferumoxytol-Enhanced Magnetic Resonance Imaging Signal Suggests Unstable Human Cerebral Aneurysm A Pilot Study, Stroke, 43 (2012) 3258-3265.

[389] Schiller B., Bhat P., Sharma A., e. al., Safety of Feraheme (ferumoxytol) in hemodialysis patients at 3 dialysis chains over a 1-year period [abstract no. FR-PO1573 plus poster], in: American Society of Nephrology Kidney, Philadelphia (PA), 2011.

[390] Amy Barton Pai, A.O. Garba, Ferumoxytol: a silver lining in the treatment of anemia of chronic kidney disease or another dark cloud?, Journal of Blood Medicine, 3 (2012) 77-85.

[391] J. Nissim, Histological appearance following intravenous saccharated iron oxide and the factors governing precipitation of the compound in vivo, Guy's Hospital Reports, 102 (1953) 164-179.

[392] R.M. Ferguson, K.R. Minard, A.P. Khandhar, K.M. Krishnan, Optimizing magnetite nanoparticles for mass sensitivity in magnetic particle imaging, Medical Physics, 38 (2011) 1619-1626.

[393] Y.I. Frenkel, Kinetic Theory of Liquids, Dover, New York, 1955.

[394] M.I. Shilomis, Magnetic fluids, Soviet Physics Uspekhi, 17 (1974) 153-169.

[395] L. Néel, Théorie du traînage magnétique des ferromagnétiques en grains fins avec application aux terres cuites, Annales de Geo- physique, 5 (1949) 99-136.

[396] L. Néel, Influence des fluctuations thermiques sur l'aimantation de grains ferromagnétiques très fins., Séance du académie des sciences, 228 (1949) 664-666.

[397] A.P. Khandhar, R.M. Ferguson, J.A. Simon, K.M. Krishnan, Tailored magnetic nanoparticles for optimizing magnetic fluid hyperthermia, Journal of Biomedical Materials Research Part A, 100A (2012) 728-737.

[398] S. Kalele, R. Narain, K.M. Krishnan, Probing temperature-sensitive behavior of pNIPAAm-coated iron oxide nanoparticles using frequency-dependent magnetic measurements, Journal of Magnetism and Magnetic Materials, 321 (2009) 1377-1380.

[399] R. Narain, M. Gonzales, A.S. Hoffman, P.S. Stayton, K.M. Krishnan, Synthesis of monodisperse biotinylated p(NIPAAm)-coated iron oxide magnetic nanoparticles and their bioconjugation to streptavidin, Langmuir, 23 (2007) 6299-6304.

[400] A.P. Khandhar, R.M. Ferguson, K.M. Krishnan, Monodispersed magnetite nanoparticles optimized for magnetic fluid hyperthermia: Implications in biological systems, Journal of Applied Physics, 109 (2011) 07B310.

[401] A.P. Khandhar, R.M. Ferguson, J.A. Simon, K.M. Krishnan, Enhancing cancer therapeutics using size-optimized magnetic fluid hyperthermia, Journal of Applied Physics, 111 (2012) 07B306.

[402] M.D. Mitchell, H.L. Kundel, L. Axel, P.M. Joseph, Agarose as a tissue equivalent phantom material for NMR imaging, Magnetic Resonance Imaging, 4 (1986) 263-266.

[403] J. Narayanan, J.-Y. Xiong, X.-Y. Liu, Determination of agarose gel pore size: Absorbance measurements vis a vis other techniques, Journal of Physics: Conference Series 28 (2006) 83–86.

[404] R. Chantrell, J. Popplewell, S. Charles, Measurements of particle size distribution parameters in ferrofluids, IEEE Transactions on Magnetics, 14 (1978) 975-977.

[405] W.F. Brown, Thermal fluctuations of a single-domain particle, Physical Review, 130 (1963) 1677-1686.

[406] H. Arami, R.M. Ferguson, A.P. Khandhar, K.M. Krishnan, Size-dependent ferrohydrodynamic relaxometry of magnetic particle imaging tracers in different environments, Medical Physics, 40 (2013) 071904.

[407] I. Schmale, J. Rahmer, B. Gleich, J. Borgert, J. Weizenecker, Point Spread Function Analysis of Magnetic Particles, in: T.M. Buzug, J. Borgert (Eds.) Magnetic Particles Imaging, Springer, Germany, 2012, pp. 279–284.

[408] A. Mengast, R.M. Ferguson, W. Grogger, F. Hofer, K.M. Krishnan, (Unpublished Results).

[409] K.M. Krishnan, Iron-L3, 2 near-edge fine structure studies, Ultramicroscopy, 32 (1990) 309-311.

[410] T. Knopp, J. Rahmer, T.F. Sattel, S. Biederer, J. Weizenecker, B. Gleich, J. Borgert, T.M. Buzug, Weighted iterative reconstruction for magnetic particle imaging, Physics in Medicine and Biology, 55 (2010) 1577-1589.

[411] T. Knopp, S. Biederer, T.F. Sattel, M. Erbe, T.M. Buzug, Prediction of the Spatial Resolution of Magnetic Particle Imaging Using the Modulation Transfer Function of the Imaging Process, IEEE Transactions on Medical Imaging, 30 (2011) 1284-1292.

[412] B. Gleich, J. Weizenecker, J. Borgert, Theory, simulation and experimental results of the acoustic detection of magnetization changes in superparamagnetic iron oxide, BMC Med Imaging, 11 (2011) 16-21.

[413] A.M. Rauwerdink, J.B. Weaver, Viscous effects on nanoparticle magnetization harmonics, Journal of Magnetism and Magnetic Materials, 322 (2010) 609-613.

[414] F. Ludwig, T. Wawrzik, T. Yoshida, N. Gehrke, A. Briel, D. Eberbeck, M. Schilling, Optimization of Magnetic Nanoparticles for Magnetic Particle Imaging, IEEE Transactions on Magnetics 48 (2012) 3780-3783.

[415] A.M. Rauwerdink, J.B. Weaver, Harmonic phase angle as a concentration-independent measure of nanoparticle dynamics, Medical Physics, 37 (2010) 2587-2592.

[416] R.W. Chantrell, A. Bradbury, J. Popplewell, S.W. Charles, Agglomerate formation in a magnetic fluid, Journal of Applied Physics, 53 (1982) 2742-2744.

[417] E.C. Stoner, E.P. Wohlfarth, A mechanism of magnetic hysteresis in hetrogeneous alloys (reprinted from Philosophical Transaction Royal Society-London, Vol 240, pg 599-642, 1948), IEEE Transactions on Magnetics, 27 (1991) 3475-3518.

[418] P.B. Laxton, J.C. Berg, Colloid Aggregation Arrested by Caging within a Polymer Network, Langmuir, 24 (2008) 9268-9272.

[419] M.Q. Zhu, E. Chang, J.T. Sun, R.A. Drezek, Surface modification and functionalization of semiconductor quantum dots through reactive coating of silanes in toluene, Journal of Materials Chemistry, 17 (2007) 800-805.

[420] M.K. Yu, J. Park, Y.Y. Jeong, W.K. Moon, S. Jon, Integrin-targeting thermally cross-linked superparamagnetic iron oxide nanoparticles for combined cancer imaging and drug delivery, Nanotechnology, 21 (2010).

[421] J. Weizenecker, B. Gleich, J. Rahmer, J. Borgert, Micro-magnetic simulation study on the magnetic particle imaging performance of anisotropic mono-domain particles, Physics in Medicine and Biology, 57 (2012) 7317-7327.

[422] G.C. Baltazar, S. Guha, W. Lu, J. Lim, K. Boesze-Battaglia, A.M. Laties, P. Tyagi, U.B. Kompella, C.H. Mitchell, Acidic Nanoparticles Are Trafficked to Lysosomes and Restore an Acidic Lysosomal pH and Degradative Function to Compromised ARPE-19 Cells, PLOS One, 7 (2012) e49635.

[423] H. Arami, R.M. Ferguson, A.P. Khandhar, A. Tomitaka, K.M. Krishnan, Role of biofunctionalization and tracer cross-linking in magnetic particle spectrometry, in: International Workshop on Magnetic Particle Imaging (IWMPI 2013) , art. no. 6528378, IEEE Xplore, Berkeley, US, 2013.

[424] B. Zheng, T. Vazin, P.W. Goodwill, A. Conway, A. Verma, E.U. Saritas, D. Schaffer, S.M. Conolly, Magnetic Particle Imaging tracks the long-term fate of in vivo neural cell implants with high image contrast, Scientific Reports, 5 (2015) 14055(14051-14058).

[425] J.W.M. Bulte, H. Boeve, K.M. Krishnan, H. Arami, P. Walczak, B. Gleich, J. Borgert, J. Rahmer, Non-Invasive Hot Spot Imaging of Transplanted Stem Cells using Magnetic Particle Imaging, Tomography, In Press.

[426] A. Antonelli, C. Sfara, J. Rahmer, B. Gleich, J. Borgert, M. Magnani, Red blood cells as carriers in magnetic particle imaging, Biomedical Engineering-Biomedizinische Technik, 58 (2013) 517-525.

[427] R.M. Ferguson, A.P. Khandhar, C. Jonasson, J. Blomgren, C. Johansson, K.M. Krishnan, Size-dependent relaxation properties of monodisperse magnetite nanoparticles measured over seven decades of frequency by AC Susceptometry, IEEE Transactions on Magnetics, 49 (2013) 3441-3444.

[428] O. Veiseh, F.M. Kievit, J.W. Gunn, B.D. Ratner, M.Q. Zhang, A ligand-mediated nanovector for targeted gene delivery and transfection in cancer cells, Biomaterials, 30 (2009) 649-657.

[429] A. Schade, E. Delyagina, D. Scharfenberg, A. Skorska, C. Lux, R. David, G. Steinhoff, Innovative Strategy for MicroRNA Delivery in Human Mesenchymal Stem Cells via Magnetic Nanoparticles, International Journal of Molecular Sciences, 14 (2013) 10710-10726.

[430] H.-S. Cho, Z. Dong, G.M. Pauletti, J. Zhang, H. Xu, H. Gu, L. Wang, R.C. Ewing, C. Huth, F. Wang, D. Shi, Fluorescent, Superparamagnetic Nanospheres for Drug Storage, Targeting, and Imaging: A Multifunctional Nanocarrier System for Cancer Diagnosis and Treatment, Acs Nano, 4 (2010) 5398-5404.

[431] C.G. Hubert, S. Hansen, M. Stroud, J. Parrish-Novak, J. Olson, Tumor paint provides near-infrared fluorescence detection of tumor tissue in mouse models of skin cancer, Journal of Nuclear Medicine, 54 (2013) 10-11.

[432] S. Hansen, M. Stroud, J. Parrish-Novak, C. Jochheim, J. Olson, Evaluation of candidate near-infrared dyes for clinical translation of a tumor paint, Journal of Nuclear Medicine, 54 (2013) 24-24.

[433] D.W. Hwang, H.Y. Ko, J.H. Lee, H. Kang, S.H. Ryu, I.C. Song, D.S. Lee, S. Kim, A Nucleolin-Targeted Multimodal Nanoparticle Imaging Probe for Tracking Cancer Cells Using an Aptamer, Journal of Nuclear Medicine, 51 (2010) 98-105.

[434] J.J. Konkle, P.W. Goodwill, O.M. Carrasco-Zevallos, S.M. Conolly, Projection Reconstruction Magnetic Particle Imaging, IEEE Transactions on Medical Imaging, 32 (2013) 338-347.

[435] P.W. Goodwill, J.J. Konkle, B. Zheng, E.U. Saritas, S.M. Conolly, Projection X-Space Magnetic Particle Imaging, IEEE Transactions on Medical Imaging, 31 (2012) 1076-1085.

[436] C.C. Lu, L.R. Bhatt, H.Y. Jun, S.H. Park, K.Y. Chai, Carboxyl-polyethylene glycol-phosphoric acid: a ligand for highly stabilized iron oxide nanoparticles, Journal of Materials Chemistry, 22 (2012) 19806-19811.

[437] T. Wang, F.M. Kievit, O. Veiseh, H. Arami, Z.R. Stephen, C. Fang, Y. Liu, R.G. Ellenbogen, M. Zhang, Targeted cell uptake of a noninternalizing antibody through conjugation to iron oxide nanoparticles in primary central nervous system lymphoma, World Neurosurgery, 80 (2013) 134-141.

[438] W. Chen, D.P. Cormode, Z.A. Fayad, W.J.M. Mulder, Nanoparticles as magnetic resonance imaging contrast agents for vascular and cardiac diseases, Wiley Interdisciplinary Reviews-Nanomedicine and Nanobiotechnology, 3 (2011) 146-161.

[439] A. Tomitaka, H. Arami, S. Gandhi, K.M. Krishnan, Lactoferrin conjugated iron oxide nanoparticles for targeting brain glioma cells in magnetic particle imaging, Nanoscale, 7 (2015) 16890-16898.

[440] C.J. Foltz, M. Ullman-Cullere, Guidelines for assessing the health and condition of mice, Lab Animal, 28 (1999) 28-32.

[441] C.R. Sun, K. Du, C. Fang, N. Bhattarai, O. Veiseh, F. Kievit, Z. Stephen, D.H. Lee, R.G. Ellenbogen, B. Ratner, M.Q. Zhang, PEG-Mediated Synthesis of Highly Dispersive Multifunctional Superparamagnetic Nanoparticles: Their Physicochemical Properties and Function In Vivo, Acs Nano, 4 (2010) 2402-2410.

[442] C. Sun, O. Veiseh, J. Gunn, C. Fang, S. Hansen, D. Lee, R. Sze, R.G. Ellenbogen, J. Olson, M. Zhang, In vivo MRI detection of gliomas by chlorotoxin-conjugated superparamagnetic nanoprobes, Small, 4 (2008) 372-379.

[443] R. Misri, K. Saatchi, U.O. Hafeli, Nanoprobes for hybrid SPECT/MR molecular imaging, Nanomedicine, 7 (2012) 719-733.

[444] H.T. Hai, H.T. Yang, H. Kura, D. Hasegawa, Y. Ogata, M. Takahashi, T. Ogawa, Size control and characterization of wustite (core)/spinel (shell) nanocubes obtained by decomposition of iron oleate complex, Journal of Colloid and Interface Science, 346 (2010) 37-42.

[445] B.P. Pichon, O. Gerber, C. Lefevre, I. Florea, S. Fleutot, W. Baaziz, M. Pauly, M. Ohlmann, C. Ulhaq, O. Ersen, V. Pierron-Bohnes, P. Panissod, M. Drillon, S. Begin-Colin, Microstructural and Magnetic Investigations of Wustite-Spinel Core-Shell Cubic-Shaped Nanoparticles, Chemistry of Materials, 23 (2011) 2886-2900.

[446] A. Shavel, L.M. Liz-Marzan, Shape control of iron oxide nanoparticles, Physical Chemistry Chemical Physics, 11 (2009) 3762-3766.

[447] H.T. Hai, H. Kura, M. Takahashi, T. Ogawa, Facile synthesis of Fe3O4 nanoparticles by reduction phase transformation from gamma-Fe2O3 nanoparticles in organic solvent, Journal of Colloid and Interface Science, 341 (2010) 194-199.

[448] K. Woo, J. Hong, S. Choi, H.W. Lee, J.P. Ahn, C.S. Kim, S.W. Lee, Easy synthesis and magnetic properties of iron oxide nanoparticles, Chemistry of Materials, 16 (2004) 2814-2818.

[449] H. Wei, O.T. Bruns, O. Chen, M.G. Bawendi, Compact zwitterion-coated iron oxide nanoparticles for in vitro and in vivo imaging, Integrative Biology, 5 (2013) 108-114.

[450] K. Cheng, S.H. Sun, Recent advances in syntheses and therapeutic applications of multifunctional porous hollow nanoparticles, Nano Today, 5 (2010) 183-196.